Imperial College London

Coherent Dynamics of Trapped Ions Within and Outside the Lamb-Dicke Regime

By

Manoj Kumar Joshi

Thesis submitted in partial fulfilment of the requirements for the degree of Doctor of Philosophy

Department of Physics · Imperial College London

April 2018

Declaration

The studies discussed in this thesis are carried out by me unless it is referenced accordingly.

The copyright of this thesis rests with the author and is made available under a Creative Commons Attribution Non-Commercial no Derivatives licence. Researchers are free to copy, distribute or transmit the thesis on the condition that the attribute it, that they do not use it for commercial purposes and that the do not alter, transform or build upon it. For any reuse or redistribution, researchers must make clear to other the licence terms of this work.

Abstract

From subatomic particles to macromolecules, quantum mechanics has a deep impact in understanding the interactions and nature of such constituents of matter. The paradoxical observations of entanglement in quantum systems is used in quantum computations. Ion traps are among the leading platforms which provide clean and highly controllable quantum systems. This thesis presents the study of quantum coherence aiming to devise and test coherent control with trapped ions in a Penning trap.

Our apparatus contains one or more calcium ions that are confined in space using DC electric and magnetic fields. Doppler cooling and resolved sideband cooling of trapped ions are carried out to perform high fidelity quantum control. The ions are prepared in their motional ground state via a multi-stage resolved sideband cooling technique. The cooling methods are first verified through simulations. The axial mean phonon numbers for a single ion are measured to be 0.03 ± 0.01 and 0.012 ± 0.009 at 187 kHz and 420 kHz axial frequencies, respectively. The heating rate is measured to be 2.5 ± 0.5 phonons/s, which is consistent with the previous measurements in our system. Similarly, the radial motional modes of a single ion are cooled to $\langle n_+ \rangle < 0.4$ and $\langle n_- \rangle < 0.6$ from mean phonon numbers corresponding to each mode of around 100. Preliminary studies are carried out of the axial motional modes of a 1D chain and 2D planar crystals, extending sideband cooling to small ICC's in a Penning trap.

Coherent control is examined in our system and the optical coherence time and motional coherence time are estimated to be approximately 1 ms and 0.5 s, respectively. Furthermore, a single ion is prepared outside the Lamb-Dicke regime via a sideband heating technique and coherent studies are performed in such a regime via a laser beam.

Acknowledgements

I would like to express my great appreciation to my supervisor Richard Thompson for his tremendous guidance and help throughout my PhD. During my 3.5 years at Imperial, I had fabulous time working with him. Special thanks to Richard for helping me at the writing stage of my PhD and his valuable comments and discussion. The insightful interactions with Richard have shaped my thinking as an independent researcher. I also wish to thank Danny Segal for his very short yet impressive interaction at the beginning of my PhD. Sadly Danny passed away right after I started my PhD but his enthusiasm and love for physics left a great impact on me.

I am also very thankful to my colleagues: Joe Goodwin, Graham Stutter, Pavel Hrmo, Vincent Jarlaud and Ollie Corfield. It would be an injustice without especially thanking Pavel and Vince for being friendly with me in both scientific and social adventures in past years. Further thanks go to Jake Lishman and Florian Mintert for their theoretical support and discussion in the final year of my PhD. I thank to all MSc, MRes, MSci and summer students who worked with me for their valuable contribution to the experiment.

I wish to acknowledge the help provided by the technical and administrative staff of QOLS group: Brian Willey, Judith Baylis, Sanja Maricic and Marcia Salviato. Many thanks to international office people for helping me regarding the visa application.

My special thanks are extended to Myungshik Kim and Doug Plato for managing the FQT program at Imperial College and their efforts on engaging us in various scientific and extracurricular activities, which were crucial for us. I wish to acknowledge the financial support from the People Programme (Marie Curie Actions) of European Union's Seventh Framework Programme (FP7/2007-2013) under REA grant agreement no 31723. I would like to acknowledge all the members of FQT programme for their direct or indirect support.

As a part of Marie Curie Actions network program, I worked in Yb-ion clock experiment at National Physical Laboratory (NPL, UK) for four months under the supervision of Prof Patrick Gill and Rachel Godun. I would like to greatly appreciate the effort by Prof. Patrick Gill and

Dr Rachel Godun for arranging my secondment at NPL. In regards to the illustration of laser diagrams presented in this thesis are reproduced with the help of “gw optics" library. I would like to acknowledge Alexander Franzen for providing such a great library for optics components.

Thanks to all my friends from London: Javier, Quentin, Dylan, Taran, David, Indi, Xiaxi, Mike, Jimmy, Seb, Kyle, Fredi, Sid, Alba, Cristina and many more for providing a great company during my stay in London. Thanks to Dr Satyajith, Dr Jagatap and Dr Rao for helping me during my BARC era. I would like to thank my friends from India: Nilanjal, Mahesh, Chinmay, Sanjay, Moumita, Priyanka, Jagdish, Devraj and and many others.

I am grateful to my mummy, babu and my siblings; Gita di, Pushpa Di and Dheeru for their unconditional love and support throughout my life. Special thanks to my wife Lata for her love and constant support during these years, without her support, I would not have thought of coming to London. Finally, I would like to thank all my friends, family members, mentors who helped me directly or indirectly.

Contents

Abstract **4**

Acknowledgements **5**

1 Introduction **18**

2 Theory of ion trapping and laser-ion interaction in a Penning trap **24**

2.1 Motion of charged particles inside a Penning trap 24

2.1.1 Classical dynamics of a single trapped ion 24

2.1.2 Energy of motion in a Penning trap 27

2.2 Trapping of multiple ions in a Penning trap 29

2.2.1 Classical dynamics of two trapped ions 29

2.2.2 Hamiltonian of a two-ion Coulomb crystal 34

2.2.3 Ion Coulomb crystals in a Penning trap 35

2.3 Quantum dynamics of an ion in a Penning trap 37

2.3.1 A 3-D quantum harmonic oscillator 37

2.3.2 Fock space representation of harmonic oscillator states 40

2.3.3 A coherent state of harmonic motion 40

2.3.4 A squeezed state of motion 41

2.4 Interaction of trapped atomic ions with a laser field 41

2.4.1 Laser-ion interaction Hamiltonian for a single trapped ion 41

2.4.2 Interaction of a trapped ion with a resonant laser field 45

2.4.3 Lamb-Dicke regime 46

2.4.4 Interactions with a non-resonant laser field 46

2.4.5 Laser-ion interaction for a two-ion Coulomb crystal 48

3 Laser cooling of ions in a Penning trap **51**

3.1 Doppler cooling in a Penning trap . . . 51
3.2 Axialisation . . . 55
3.3 Sideband cooling . . . 58

4 Experimental apparatus and techniques 62
4.1 Atomic structure of a calcium ion . . . 62
4.1.1 Zeeman effect . . . 63
4.1.2 Magnetically induced transitions in a Penning trap . . . 65
4.1.3 Transition strengths . . . 66
4.1.4 Polarisations of the laser induced transitions . . . 67
4.2 Loading of ions . . . 68
4.3 Trapping apparatus . . . 69
4.3.1 SPECtrap . . . 69
4.3.2 Magnetic field . . . 70
4.3.3 Axialisation drive . . . 70
4.3.4 Anharmonicity and misalignment effects in the Penning trap . . . 72
4.3.5 AC and DC compensations . . . 73
4.4 Optical system . . . 74
4.4.1 External-cavity diode lasers . . . 74
4.4.2 Layout of the optical system . . . 77
4.4.3 Laser frequency stabilisation . . . 79
4.5 Stabilisation of spectroscopy laser system . . . 81
4.5.1 Laser frequency stabilisation . . . 81
4.5.2 Frequency drifts and linewidth measurement with a trapped ion . . . 83
4.5.3 Intensity stabilisation of the spectroscopy laser . . . 85
4.6 Optical control and detection system . . . 87
4.6.1 Trap optics . . . 87
4.6.2 Radial beam viewer and control . . . 88
4.6.3 Detection efficiency and background measurement . . . 89
4.7 Experimental control . . . 91

5 Simulation studies of sideband cooling of trapped ions in a Penning trap 94
5.1 Theory of resolved-sideband cooling of a trapped calcium ion . . . 94
5.1.1 A three-level atom . . . 95

5.1.2 Additional effects in a Penning trap 98
5.1.3 Transformation of a six-level system into a two-level equivalent 101
5.2 Population dynamics in motional states of a trapped ion interacting with the laser radiation 102
5.2.1 Comparison of resonant and off-resonant excitation rates 102
5.2.2 Description of the simulation methods 103
5.2.3 Optimisation of sideband cooling laser parameters 105
5.3 Sideband cooling outside the L-D regime 106
5.3.1 Problems with the large value of the L-D parameter 106
5.3.2 Optimisation of cooling sequence 108
5.3.3 Simulation of cooling dynamics for a single ion 110
5.3.4 Cooling dynamics of a two-ion Coulomb crystal 112
5.4 Sideband heating to outside the L-D regime 116
5.5 Summary 118

6 Experimental realisation of ground state cooling in a Penning trap 119
6.1 Ground state cooling of the axial motion of a trapped calcium ion 119
6.1.1 Sideband cooling at a low trapping potential 120
6.1.2 Sideband cooling at a high trapping potential 123
6.1.3 Cooling dynamics of the axial motion 124
6.2 Demonstration of ground state cooling of radial motional modes of a calcium ion in a Penning trap 127
6.2.1 Radial Doppler spectrum 127
6.2.2 Ground state cooling of the radial motion 129
6.2.3 Effect of the axialisation field 132
6.3 Sideband cooling of a two-ion Coulomb crystal 133
6.3.1 Sideband cooling of a two-ion chain in a Penning trap 134
6.3.2 Sideband cooling of a two-ion planar crystal 136
6.4 Sideband cooling of a multi-ion Coulomb crystal 139
6.4.1 Ground state cooling of a three-ion Coulomb crystal 140
6.4.2 Sideband cooling of a five-ion Coulomb crystal 142
6.4.3 Sideband cooling of a ten-ion Coulomb crystal 143
6.5 Sideband heating: preparing an ion outside the L-D regime 144
6.6 Adiabatic ground state cooling of a trapped ion in a Penning trap 146

6.7 Summary . . . 149

7 Coherent control using trapped atomic ions 150

7.1 Quantum coherence in a two-level trapped atomic ion . . . 150

7.1.1 Demonstration of Rabi oscillations with a trapped calcium ion in a Penning trap . . . 150

7.1.2 Decay of the visibility . . . 152

7.2 Source of errors/dephasing in the optical qubit . . . 154

7.2.1 Decoherence due to radiative decay of the metastable state . . . 155

7.2.2 Decoherence due to magnetic field noise . . . 155

7.2.3 Decoherence due to frequency or phase noise in the probe laser . . . 155

7.2.4 Laser intensity noise . . . 156

7.2.5 Thermal dephasing . . . 157

7.2.6 Pulse-timing error . . . 157

7.2.7 Loss of information in optical qubits . . . 158

7.2.8 Estimation of qubit coherence time for our system . . . 158

7.3 Estimation of optical coherence time with Ramsey interference experiment . . . 159

7.4 Enhancement of optical coherence time . . . 161

7.4.1 Spin-echo . . . 161

7.4.2 Theory of dynamical decoupling in quantum systems . . . 164

7.4.3 Experimental demonstration of the UDD scheme . . . 167

7.5 Demonstration of spin-coherence with multiple ions . . . 167

7.5.1 Two-ion chain . . . 167

7.5.2 Two-ion planar crystal . . . 170

7.5.3 Three-ion planar crystal . . . 171

7.5.4 Multi-ion planar crystals . . . 172

7.6 Coherent evolution of population between motional states . . . 172

7.6.1 Demonstration of $n = 0$ and $n = 1$ superposition . . . 173

7.6.2 Demonstration of the $n = 0$ and $n = 2$ superposition . . . 175

7.6.3 Demonstration of the phonon-echo with a trapped ion system . . . 176

7.6.4 Demonstration of 0-1-2 motional superposition . . . 178

7.6.5 Motional superposition of high-n motional states . . . 181

7.7 Experimental demonstration of coherent state of motion . . . 186

7.7.1 Demonstration of a forced harmonic oscillator using a trapped ion system 188
7.7.2 Experimental demonstration of a squeezed state of motion 191
7.8 Dephasing of the motional superposition 194
7.8.1 Stability of the trap power supply 194
7.8.2 Heating rate measurements 194
7.8.3 Heating rates of a single ion 195
7.8.4 Heating rates with a two-ion chain 197
7.9 Summary 197

8 Conclusion **199**
8.1 Summary of thesis achievements 199
8.2 Applications 201
8.3 Outlook 201

Bibliography **203**

A Quantum dynamics of a harmonic oscillator **217**
A.1 Axial motion 217
A.2 Radial motion 218

B Electric quadrupole transitions **220**

C Circuit diagram for intensity noise eater **221**

D Calibration of trap frequency and ion spacing in our apparatus **223**

E Distribution functions and excited state probabilities **225**

F Squeezed state miscellany **226**

List of Figures

2.1 Ideal Penning trap 25
2.2 Classical trajectory of a single ion 28
2.3 Two-ion orientation 31
2.4 Stability of two ions 34
2.5 Motional states in a Penning trap 39
2.6 Motional states coupled through laser beam 45

3.1 Schematic of radial Doppler cooling 53
3.2 Radial mean phonon number as a function of ω_z 56
3.3 Cooling in the presence of axialisation 57
3.4 Simulation of magnetron Doppler cooling 59
3.5 Schematic of resolved sideband cooling 60
3.6 Different branches during sideband cooling 60

4.1 Energy level diagram of a $^{40}Ca^{+}$ 63
4.2 Dipole and quadrupole transitions 68
4.3 SPECtrap 71
4.4 Ring segments 72
4.5 Laser diode 75
4.6 Gain curve of an ECDL 76
4.7 Layout of the optical system 78
4.8 Transfer cavity locking system 80
4.9 Transfer cavity modes 81
4.10 Layout of the 729-nm laser system 83
4.11 Ring down measurement 83

4.12 Linewidth measurement . . . 84
4.13 Carrier frequency drift . . . 85
4.14 Noise eater schematic . . . 86
4.15 Measurement of intensity noise . . . 87
4.16 Trap assembly, laser beams and optical components . . . 88
4.17 Webcam based radial beam viewer. . . . 89
4.18 PMT count histogram . . . 90
4.19 $J-$mixing . . . 91
4.20 Experimental control . . . 92
4.21 Pulse sequence . . . 93

5.1 SBC energy level diagram . . . 95
5.2 SBC in a Penning trap . . . 99
5.3 Absorption spectrum . . . 103
5.4 Off-resonant excitation rate . . . 103
5.5 Trap frequency dependent excitation rate . . . 104
5.6 Ground state occupancy . . . 105
5.7 Sideband cooling dynamics . . . 106
5.8 Sideband strength . . . 107
5.9 SBC with different sidebands . . . 108
5.10 Sideband strength at 150 kHz . . . 109
5.11 Normalised cooling strength . . . 110
5.12 Simulation of SBC at 420 kHz . . . 111
5.13 Simulation of SBC at 150 kHz . . . 111
5.14 Simulated $\langle n \rangle$ as a function ω_z . . . 112
5.15 Contour plots for two ions . . . 114
5.16 Simulated cooling dynamics of a two-ion chain . . . 115
5.17 Simulated cooling dynamics of a two-ion disc . . . 116
5.18 Sideband heating . . . 117
5.19 Sideband heating dynamics . . . 118

6.1 Doppler spectrum of a single ion at 187 kHz . . . 120
6.2 Axial sideband strength at 187 kHz . . . 122

6.3 Spectrum after population trapping . . . 122
6.4 Axial spectrum after SBC of a single ion at 187 kHz . . . 123
6.5 Axial spectrum at 420 kHz . . . 124
6.6 Dip-spectrum . . . 125
6.7 Repumping rate . . . 126
6.8 Axial cooling dynamics of a single ion . . . 127
6.9 Radial Doppler spectrum . . . 129
6.10 Magnetron sidebands of the carrier . . . 129
6.11 Modified cyclotron sidebands . . . 130
6.12 Contour plots for the radial modes . . . 131
6.13 Radial spectroscopy after sideband cooling . . . 131
6.14 Radial windowed spectra after sideband cooling . . . 132
6.15 Axialisation peaks in a radial spectrum . . . 133
6.16 EMCCD image of two ions . . . 134
6.17 Axial Doppler spectrum of a two-ion chain . . . 135
6.18 Axial spectrum of a two-ion chain after sideband cooling . . . 135
6.19 Axial Doppler spectrum of a two-ion planar disc . . . 137
6.20 PMT data histogram of two ions . . . 137
6.21 Axial spectrum of a two-ion planar disc after SBC . . . 138
6.22 Rotation frequency measurement of a two-ion planar disc . . . 139
6.23 Windowed spectrum of a two-ion disc . . . 139
6.24 ICC images . . . 140
6.25 Three ions in a Penning trap . . . 141
6.26 Axial modes of a three-ion planar disc . . . 141
6.27 Axial spectrum of a three-ion disc after SBC . . . 142
6.28 Five ions in a Penning trap . . . 142
6.29 Axial spectrum of a five-ion disc . . . 143
6.30 Ten ions in a Penning trap . . . 143
6.31 Axial spectrum of a ten-ion disc . . . 144
6.32 Excitation strength for sideband heating . . . 145
6.33 Spectra after sideband heating . . . 146
6.34 Rabi oscillations after sideband heating . . . 146
6.35 Adiabatic switching circuit . . . 147

6.36 Time constant of the adiabatic switch 147
6.37 Axial spectra before and after adiabatic switching 148
6.38 Measured cooling limit after adiabatic switching 149

7.1 Laser sequence for a Rabi oscillation experiment 151
7.2 Doppler Rabi oscillations 152
7.3 Rabi oscillations after sideband cooling 152
7.4 Damped Rabi flops 153
7.5 Rabi flops for reduced laser intensity 153
7.6 Rabi flops for population trapping case 154
7.7 Simulated Rabi flop visibility 157
7.8 Simulated Rabi flops for various values of laser power 159
7.9 Bloch representation of a Ramsey experiment 160
7.10 Ramsey fringes after sideband cooling of a single ion 161
7.11 Spin echo 162
7.12 Phase scan plots for a spin echo experiment 163
7.13 Schematic of a UDD method 166
7.14 Simulated qubit frequency variation for the UDD scheme 166
7.15 Time dynamics after employing the UDD scheme 167
7.16 Experimental demonstration of the UDD scheme 168
7.17 Carrier Rabi oscillations of a two-ion chain after sideband cooling 168
7.18 Ramsey fringes for a two-ion chain 169
7.19 Phase scan plot of a two-ion chain 169
7.20 Blue sideband Rabi flops of a two-ion chain 170
7.21 Rabi flops for a two-ion disc 171
7.22 Three-ion Rabi oscillation 172
7.23 Multi-ion Rabi flops 173
7.24 Pulse sequence for the 0-1 superposition 174
7.25 Motional visibility plot for the 0-1 superposition 175
7.26 Motional free-precession plot 175
7.27 Motional coherence time measurement for 0-2 superposition 176
7.28 Pulse sequence for motional spin-echo experiment 177
7.29 Motional phase scan plots 177

7.30 Experimental plot for motional spin-echo . . . 178
7.31 Pulse sequence used in 0-1-2 superposition . . . 179
7.32 Experimental plots showing 0-1-2 superposition . . . 180
7.33 Visibility of the 0-1-2 superposition . . . 181
7.34 High-n motional superposition . . . 183
7.35 Free-precession plots after creating a high-n superposition . . . 184
7.36 Visibility at $n \sim 150$ . . . 185
7.37 Visibility at $n \sim 288$ . . . 185
7.38 Pulse sequence for preparing a coherent state of motion . . . 187
7.39 Rabi flops after preparing into a coherent state . . . 188
7.40 $P(n)$ after preparing in coherent state . . . 188
7.41 Collapse and revival of population . . . 189
7.42 Axial spectrum after preparing in a coherent state of motion . . . 190
7.43 Rabi flops after preparing at $\langle n \rangle = 49$ . . . 191
7.44 Spectra for driven oscillator demonstration . . . 192
7.45 Forced and damped harmonic oscillator . . . 193
7.46 Squeezed state of motion . . . 193
7.47 $P(n)$ for a squeezed state of motion . . . 194
7.48 Trap power supply stability measurement . . . 195
7.49 Heating rate along the axial direction . . . 196
7.50 Heating rate along the radial direction . . . 196
7.51 Heating rates for a two-ion chain . . . 197

8.1 Alternative sideband cooling scheme . . . 202

C.1 Electronic circuit for the 729-nm noise eater system. . . . 222

D.1 Trap frequency calibration . . . 223
D.2 EMCCD calibration . . . 223
D.3 Two-ion rotation speed calibration from an EMCCD image . . . 224

F.1 Calculated $P(n)$ for squeezed state of motion . . . 226
F.2 Frequency analysis of the squeezed state data . . . 227

List of Tables

4.1 First and second order Zeeman shifts 64

5.1 Momentum distribution after emission of a photon 101
5.2 Transition rates 102

6.1 Pulse sequence for multi-stage cooling of radial modes 130
6.2 Sideband cooling sequence for a two-ion chain. 136

Chapter 1

Introduction

Quantum mechanics has been successfully used to describe many fundamental physical and chemical phenomena. The nature of matter ranging from subatomic particles to macro-molecules can only be understood using quantum theories. Recently, however, quantum mechanical advancements have cultivated new research directions and their possible use in technological advancements, in particular “quantum computation" and “quantum simulation". A new line of thought to compute otherwise intractable, fundamental processes was presented by Feynman and Benioff [1] in the early 1980’s. Richard Feynman once stated the importance of a quantum computation in one of his famous articles [2],

> “Can quantum systems be probabilistically simulated by a classical computer? .... the answer is certainly, No! This is called the hidden-variable problem: it is impossible to represent the results of quantum mechanics with a classical universal device."

Since then various theories and experimental models have been presented to describe such computations using a well-controlled quantum system.

A *qubit* is a quantum counterpart of a classical information bit. It is formed by two quantum states of an atom or a photon. Spooky nature of quantum mechanics differentiates a quantum gate from its classical equivalent. The exponential rise in qubit operations with the number of qubits in a quantum information processor exhibits its superiority over others. Notably, Shor’s algorithm in a quantum computer has been shown to be the most efficient and the fastest way to factorise a large prime number, which can be used to break currently existing encryption protocols [3]. There has been a lot of research in the field of quantum information theory in the past few decades [4]. In recent years, NMR systems, superconducting circuits, trapped atoms, trapped ions and several other systems have shown tremendous progress towards the experimental realisation of a quantum information processor and a quantum simulator [5–7].

Current quantum systems lack the full processing power due to both their vulnerability to decoherence effects and their limited scalability. Various “Quantum error correction" (QEC) models

have been developed in past years to protect such systems against decoherence effects [8–10]. In order to devise a “fault-tolerant quantum computer", many experimental demonstrations of QEC have been conducted in recent years [11–14]. In order to resolve the scalability issues, there have been proposals for preparing an entangled system with a large number of qubits in it, and interconnecting such multiple systems via photonic channels [15]. Furthermore, in trapped ion systems, proposals have been made to devise multiple trapping zones on a common device, and shuttling the ions between different zones in order to create entanglement using optical sources [16–18].

Laser-cooled trapped atomic ions have been widely used in the past several decades to examine quantum mechanical models [19]. More recently, such systems have been used to verify quantum algorithms in order to realise the basic building blocks of a quantum computer [20, 21]. A single trapped ion system manifests an ideal realisation of a quantum harmonic oscillator. Deterministic experimentation with a single atom or electron was once unimaginable. Nowadays, however, coherent control with one or a few atomic ions is a routine process. In current systems, the internal and external states of an ion can be manipulated with very high fidelity, which is essential for “fault-tolerant computing" with quantum systems [22].

In trapped ion systems, the trapping mechanism enables us to interrogate atomic ions for a very long time and allows repetitive measurements on the same particle. Additionally, laser cooling brings the ions to rest and reduces many unwanted transition broadening effects. Such systems are very useful for developing a deeper comprehension of the underlying physics of a singly ionised isolated atom. Laser cooling of multiple trapped ions held in a common trapping system forms a special state of matter called an “Ion Coulomb Crystal" (ICC) [23]. In such a state, the trapping force is balanced by the repulsive Coulomb force among the trapped ions and an equilibrium state is achieved. Such systems are extensively used to perform quantum simulations on spin systems [24, 25].

Historically, in early 20^{th} century, Frans M. Penning added a magnetic field in a discharge tube to enhance the lifetime of electrons. This idea was later utilised by Hans G. Dehmelt and built the first ion trap using magnetic field along with a static electric quadrupole potential. Another type of trap was developed by Wolfgang Paul, who used a time-varying electric quadrupole potential to confine the charged particles. For the developments of trapping and detection of trapped ions, in 1989 Paul and Dehmelt shared half of the Nobel prize award, with the other half going to Norman Ramsey [26]. Initial trap geometries were not particularly suitable for laser-based studies. Various forms of ion trap geometries have been generated since then for better optical access or for some specific applications [27, 28]. A linear geometry of trap electrodes is particularly useful for realising a linear chain of ions and their individual addressing to realise quantum gates [29]. In these traps, the anharmonicity in the confining potential is reduced by an appropriate design of the trap electrodes [30]. On the other hand, cylindrical Penning traps are used to contain non-neutral plasmas [31, 32] and many beamline based studies [33].

Laser cooling of atoms or atomic ions was first proposed, independently, by Hänsch et al. [34] and Wineland et al. [35]. The first experimental demonstration was carried out by Neuhauser

et al. [36] and Wineland et al. [37]. The initial demonstrations were based on Doppler cooling of bound atomic ions and these studies led to the first realisation of ICCs [38], and laser cooling and trapping of free atoms [39]. The Doppler cooling mechanism relies on the fact that if a red-detuned laser beam illuminates a cloud of atoms, then due to the Doppler effect the probability of photon absorption is maximised for the atoms moving in the opposite direction to the laser beam. The emission of absorbed photons takes place in random directions, hence on average the atoms lose their energy along the direction of the laser beam. However, at the same time the atoms moving in the direction of the laser beam, do not absorb photons and hence remain unaffected. In an ion trap, the periodic motion brings the ions into resonance during half of their period and eventually the ions are cooled to their Doppler limits [40].

Doppler cooling methods limit the ultimate temperature to a few hundreds of μK (depending on the Doppler limit of the specific transition), which is not sufficient for many high precision and quantum gate experiments, hence other cooling methods are employed to achieve cooling beyond the Doppler limit. In trapped ion systems, the second stage of laser cooling is performed using optical or microwave pumping methods in the “tightly confined regime". The most popular methods of ground state cooling are resolved-sideband cooling, “Electromagnetically-induced transparency" (EIT) cooling and “Raman sideband cooling" [41–44]. The first demonstration of ground state cooling through resolved sideband cooling was performed on an Hg^{+} ion trapped in a Paul trap [41]. Ground state cooling of the axial motion of a calcium ion in a Penning trap was carried out by Goodwin et al. [45]. More recently, ground state cooling of an 18-ion chain has been achieved with the EIT method [46]. Often, the ground state cooling of ions is essential for high fidelity gate operations [47]. In principle, a Mølmer-Sørensen type gate [48] does not require ground state cooling, as long as the system is prepared in the “Lamb-Dicke Regime" (LDR). However, the ground state cooling has shown improvements in the gate performance [49].

Soon after the first proposal of a quantum gate using trapped ions by I. Cirac and P. Zoller [47], the first experimental demonstration of the “Cirac Zoller" (CZ) gate using a single ground state cooled ion was carried out by Monroe et al. in 1995 [50]. In this paper, they demonstrated the “controlled-NOT" (c-NOT) gate via two-qubit states realised with both internal and external states of a single trapped ion. However, the first demonstration of the CZ c-NOT gate using two trapped ions with individual ion addressing was achieved by Schmidt-Kaler et al. in 2003 [51]. A quantum logic gate with hot ions was proposed by A. Sørensen and K. Mølmer in 1999 [48] and such gates are known as “Mølmer-Sørensen" (MS) gates after them. These gates do not require the ions to be in the motional ground state or individual addressing of ions, thus they are readily easy to implement. For this type of gate, a bichromatic laser beam, detuned from red and blue sidebands of the transition, is used to illuminate both ions, simultaneously [52].

There is another type of gate which is demonstrated using two laser beams producing a standing wave pattern which provides a state-dependent force on each ion. The state-dependent force imparts different phase to each internal state of the ions, which provides basic gate operation in such systems. Such gates are called geometrical phase gates and they do not require ions to be

cooled to their motional ground state [53]. Leibfried et al. in 2003 demonstrated a geometrical phase gate with two Be^+ ions trapped in a linear Paul trap [54] by using two laser beams, far detuned from the transition, forming a standing wave pattern along the trap axis. The detuning of the laser beams from each other is chosen such that it is near to one of the two motional modes.

Trapped ion systems are routinely used to prepare highly coherent states due to the low dispersion of their wavepackets and the precise control of the quantum states of a trapped ion. A “coherent state" of motion of a harmonic oscillator is realised by applying a displacement force on a ground state cooled trapped ion [55]. The displacement force is created by applying a bichromatic radiation field [49] or by applying a classical driving force on a ground state cooled ion [55]. The probability distribution among the phonon states is described in terms of a Poissonian distribution function [56]. In quantum systems, the coherent state of motion is identified by observing collapse and subsequently revival of the quantum coherence. Recently a large coherent state of motion, up to 10000 phonon states, has been realised by rapidly changing the trap potential [57] and shows a great level of quantum control for such a high amplitude coherent state. The “Schrödinger cat" state is of much interest in quantum information processing and also is of fundamental interest. The first demonstration of a cat state using a trapped ion was carried out by Monroe et al. [58]. In this paper, they show a superposition of spatially separated classical like wavepackets using a trapped Be^+ ion. A state-dependent displacement is used to create a coherent superposition of two coherent states of a harmonic oscillator.

In recent years, a lot of progress has been made in the direction of quantum simulation using trapped ions [19]. Preliminary simulations are carried out by mimicking the interactions of a “problem" quantum system in a well-controlled quantum system (“simulator"). This is done by engineering the required interaction Hamiltonian in terms of the system Hamiltonian, which is then employed on the simulator system and the outcome of the system is considered as the simulation result. Quantum dynamics and engineering of many body systems is of interest nowadays and trapped ion systems have been used in such research [59]. Exotic frustration in spin systems has already been simulated in three spin systems [25] by engineering the interaction via optical forces. Such systems are known as “analogue quantum simulators" [60]. The other type of simulator is called “digital quantum simulator", where the qubit states are idealised as digital bits and the elementary quantum gate operations are translated from required interactions. However, the required goal of the functionality of such devices has not been achieved yet, but some preliminary experiments have been performed with trapped ions [61, 62].

Most of the studies mentioned so far require high-level coherent control using lasers or microwave radiation, with minimal decoherence in the system. In reality, there are always decoherence effects, which limit the coherent control [63]. In trapped ion systems, the “T2 type" or so-called dephasing effects are responsible for causing decoherence in the system [52, 63]. Currently, due to the rapid growth of ultra-stable laser sources and availability of proper shielding of laboratory noise sources, one can achieve very long qubit coherence times in such systems. In some cases, the qubit coherence time has been extended up to 10 minutes by applying “dynam-

ical decoupling schemes" to eliminate the effects of de-phasing mechanisms [64]. On the other hand, trapped ion systems also require a high level of motional coherence in the system, which is provided by the trapping sources [65]. In ion traps, there are various mechanisms, such as electric field noise in the trap supply and patch potentials on the trap electrodes, which cause heating of a ground state cooled ion [66]. Recently, sub-hertz heating rates have been measured in room temperature ion traps [45, 67].

This brief review shows the usefulness and scope of trapped ion systems in order to perform fundamental studies and simulations with high fidelity. Importantly, trapped ion systems are distinguished from other systems due to their well-isolated platform and highly controllable coherent manipulation. The purpose of this thesis is to describe and devise coherent control with one or more trapped ions in a Penning trap. Planar spin systems are ideal to simulate quantum magnetism. The outstanding use of a Penning trap is to demonstrate large sized planar crystals [32], which are naturally suitable for studies of spin-spin interactions. The Bollinger group from NIST Boulder showed simulations of “Ising-type interactions" with hundreds of trapped Be^+ ions in a Penning trap [24], which naturally form a crystalline triangular lattice structure. This thesis presents studies of sideband cooling of small size ICCs in a Penning trap, which opens the future possibilities of quantum simulation and quantum computation using such ICCs. Quantum error correction using five qubits in a Penning trap has already been proposed by Goodwin et al. in reference [10]. Low heating rates measured in our trap can be useful for high precision and long interrogation time studies.

In this thesis, I present scientific studies that have been carried out in the Penning trap that is currently situated in the ion-trapping laboratory at Imperial College London. The thesis is structured as follows. In chapter 2, the theory of ion trapping in a Penning trap will be discussed. In the same chapter, I will elaborate the motion of one and two trapped ions, and their motional modes along the axial and radial directions. A brief discussion of quantum dynamics of trapped ions will be carried out in a subsequent section. Spectroscopy and laser cooling of the trapped ions requires a deep understanding of the laser-ion interaction, which is carried out in section 4 of the chapter.

Chapter 3 describes laser cooling of trapped ions in a Penning trap. Doppler cooling is a prerequisite for our studies, hence the theory of Doppler cooling in a Penning trap is discussed in detail in this chapter. The second stage of cooling, resolved sideband cooling, is briefly discussed in a later section of the chapter. Chapter 4 contains the description of the experimental apparatus and the introduction of the calcium ion energy level diagram. In chapter 5, numerical simulation studies of sideband cooling outside the Lamb-Dicke regime are presented. Chapter 6 contains experimental results of sideband cooling of an ion along the axial and radial directions. Experimental results of sideband cooling of a two-ion chain and planar configurations are discussed in the same chapter. The chapter also contains results of sideband cooling of a three-ion, a five-ion and a ten-ion Coulomb crystal. In the end of chapter 6, I present the results of sideband heating and adiabatic cooling of a single ion in our trap.

The coherent control of trapped ions in the Penning trap is presented in chapter 7. Firstly, in this chapter, I present the studies of the optical coherence of ground state cooled trapped calcium ions. The discussion of different decoherence effects and their role is discussed in this chapter too. Furthermore, I present the studies of motional superposition and motional coherence of a ground state cooled ion. Finally, in chapter 8 I conclude the experimental findings and discuss future aspects of the current research work.

The main challenges that we faced while working with our Penning trap are caused by a very strong magnetic field and working outside the L-D regime. The strong magnetic field requires multiple laser frequencies to laser cool the ions and being outside the L-D regime calls for a multistage sideband cooling sequence. These two issues have been tackled in this thesis and subsequently ground state cooling has been investigated. The scientific studies shown in this thesis seek to improve coherent control with ion Coulomb crystals in Penning traps. The results can be used for sympathetic cooling of particles which can not be directly laser-cooled [68] or quantum simulations in Penning traps [69]. The experimental work presented here is performed jointly by me, Pavel Hrmo and Vincent Jarlaud. Most of the experimental data were taken by all three of us together. The experimental apparatus was inherited from previous students who worked in our group. A number of modifications were carried out in order to perform new studies in our system. Even though the experimental data are shared between three of us, the data analysis was carried out independently. Each person had a different aspect to highlight in his thesis and the studies are presented in three different themes. Some of the studies, in particular, simulation studies of sideband cooling and development of noise eating system, were carried out entirely by me. Additionally, I actively participated in data taking of all the key results presented in this thesis. The experimental work of sideband cooling of two-ion chain and planar crystals has been published in a peer-reviewed journal. The published work can be found in reference [70]. Additionally, two more papers are being prepared based on the work presented in this thesis.

Chapter 2

Theory of ion trapping and laser-ion interaction in a Penning trap

Trapped ion systems have been found extremely useful to study and manipulate quantum properties. Initial work by Hans Dehmelt and Wolfgang Paul paved the foundation of ion trapping, which nowadays is being regularly used to perform precision measurements and coherent manipulation with atomic ions. Understanding of classical and quantum dynamics of ions in a trap is very important for us in order to manipulate the quantum states of a trapped ion. In this chapter, I will give a brief overview of dynamics of atomic ions in a Penning trap. I will first describe the motion of a single ion in a Penning trap and its quantum treatment. Subsequently, I will discuss the case of multiple ions and then I will formulate their motional frequencies. In the latter part of the chapter, I will describe the laser-ion interaction and I will set up the equations for coherent manipulation using a laser field.

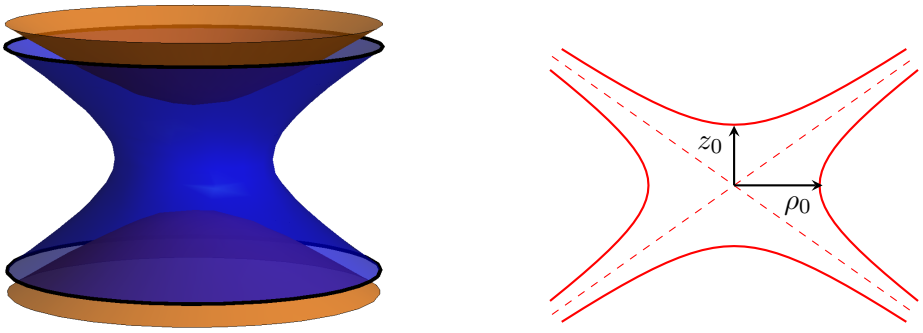
2.1 Motion of charged particles inside a Penning trap

2.1.1 Classical dynamics of a single trapped ion

Understanding of laws of classical electrodynamics gives the basic notion of how charges can be held in space or can be moved from one place to another by means of their interaction with electric or magnetic fields. By satisfying Laplace's equation in the vacuum ($\nabla^2\Phi = 0$), one can find the lowest order polynomial of the electric potential, quadrupolar potential, which can provide confinement to charged particles in space. However, the confinement of charged particles in all three-dimensions (3D) is not possible by means of only static electric fields. From Earnshaw's theorem, it is also clear that one cannot maintain a stable equilibrium entirely with static electric fields [71].

In the mid 20^{th} century, Wolfgang Paul and others came up with the idea of ion trapping

by means of a time-varying electric potential. Initially, the trapping was only demonstrated in two dimensions and such traps were used for the purpose of mass filtering [72]. Later, the trap electrodes were modified in order to generate a 3D quadrupolar potential within the enclosed volume. The traps which use a time-varying electric field to confine the ions are known as Paul traps named after Wolfgang Paul. Concurrently, Hans Dehmelt came up with another type of trap which used static magnetic fields in conjunction a with DC quadrupole potential to confine the ions. These types of traps are known as Penning traps named after Francis Michel Penning, who modified the existing electric discharge tubes of that time by introducing an axial magnetic field to them, which enhanced the discharge current output. The present thesis describes an experimental demonstration of coherent control using trapped ions in a Penning trap; hence I will be describing the theory of ion trapping focussed on Penning traps.



(a) (b)

Figure 2.1: Figure (a) shows a side view of an ideal Penning trap. A DC potential is applied to the end-caps (in orange colour) while keeping the ring electrode (in blue colour) at the ground potential. The magnetic field is applied along the trap axis (say along the $z-$axis). Figure (b) shows the cross-sectional view of the ideal Penning trap.

A Penning trap uses a static quadrupole potential (DC) and an axial magnetic field to confine the ions in all 3 directions. The DC potential (U_{dc}) is applied to the end-caps while connecting the ring electrode to the ground potential. The electrodes are shaped in order to provide a quadrupole potential within the volume enclosed. Ideally, the electrodes are chosen such that their shapes exactly match with the equipotential curves, essential to confine the ions. A side view of an ideal trap is shown in figure 2.1 (a). Electrodes in orange are called “end-caps" and the central electrode (in blue) is called “ring electrode". Vertical cross-section of the trap electrodes is shown in figure 2.1 (b). In order to generate a quadrupolar potential, the Penning trap electrodes are shaped through hyperboloid revolution along the z-axis, satisfying the geometry condition [73]

$$\frac{\rho^2}{\rho_0^2} - \frac{z^2}{z_0^2} = 1, \quad \frac{z^2}{z_0^2} - \frac{\rho^2}{\rho_0^2} = 1, \tag{2.1}$$

where $\rho = \sqrt{x^2 + y^2}$ and $\rho_0^2 = 2z_0^2$. The potential inside the enclosed volume is given by,

$$\Phi = U_{dc}\frac{(2z^2 - x^2 - y^2)}{2d_0^2}, \tag{2.2}$$

where $d_0 = \sqrt{2z_0^2}$ is the characteristic trap dimension.

In a Penning trap, for a positively charged particle, the DC potential creates a confining force in the axial direction (z-axis). However, an outward force in the radial plane (xy-plane) is generated by the same field, thus leads to the de-confinement in the xy-plane. In order to confine a charged particle in the radial plane, a homogeneous axial magnetic field is added which rotates the ion in the plane, therefore 3D trapping is realised.

The equation of motion of a charged particle, with charge Q and mass m, in a Penning trap is given as

$$m\frac{d^2\mathbf{r}}{dt^2} = -Q\nabla\Phi + Q(\mathbf{v} \times \mathbf{B}), \tag{2.3}$$

where $\mathbf{v}$ is the velocity of the charged particle at a time t and $\mathbf{B} = (0, 0, B_0)$ is a homogeneous axial magnetic field. The equations of motion in the Cartesian coordinates are expressed as

$$\ddot{x} = \tfrac{1}{2}\omega_z^2 x + \omega_c\dot{y}, \tag{2.4}$$
$$\ddot{y} = \tfrac{1}{2}\omega_z^2 y - \omega_c\dot{x}, \tag{2.5}$$
$$\ddot{z} = -\omega_z^2 z, \tag{2.6}$$

where $\omega_c = \frac{|Q|B_0}{m}$ is the pure cyclotron frequency. The motion along the axial direction is simple harmonic type and is expressed as

$$z(t) = A_z\cos(\omega_z t + \phi_z), \tag{2.7}$$

where A_z is the amplitude and ϕ_z is the phase of the motion. For a positively charged particle, the axial motional frequency is given as $\omega_z = \sqrt{\frac{2|Q|U_{dc}}{md_0^2}}$. A charged particle in the radial plane moves in the presence of electric and magnetic fields (essentially an $\mathbf{E} \times \mathbf{B}$ field), thus the equations of motion are coupled in the x and y coordinates. Elegantly, the motion in the radial plane can be analytically solved by making a coordinate transformation into a rotating frame. A frame rotating at $\omega_c/2$ (at half the pure cyclotron frequency) decouples the motion and transforms the equations of motion as

$$\ddot{x'} = -(\tfrac{1}{4}\omega_c^2 - \tfrac{1}{2}\omega_z^2)x', \tag{2.8}$$
$$\ddot{y'} = -(\tfrac{1}{4}\omega_c^2 - \tfrac{1}{2}\omega_z^2)y', \tag{2.9}$$

which makes a 2D isotropic harmonic oscillator. The frequencies of motion in the rotating frame are given as $\pm\sqrt{\frac{1}{4}\omega_c^2 - \frac{1}{2}\omega_z^2}$. These differential equations give rise to

$$x'(t) = x'_0\cos(\omega_1 t + \phi'_x),$$
$$y'(t) = y'_0\sin(\omega_1 t + \phi'_y), \tag{2.10}$$

where $\omega_1 = \sqrt{(\frac{1}{4}\omega_c^2 - \frac{1}{2}\omega_z^2)}$ and $x'_0, y'_0, \phi'_x, \phi'_y$ are the parameters indicating amplitude and phase of motion in the rotating frame[1].

The characteristic frequency, ω_1, plays an important role in understanding the motion of trapped ions in a Penning trap. In the rotating frame, it creates a confining force, $F_{trap} = -m\omega_1^2 x'$, which is harmonic and keeps the ions confined in the radial plane. The motion of an ion in the laboratory frame, after making coordinate transformation, is expressed as

$$x(t) = A_- \cos(\omega_- t + \phi_-) + A_+ \cos(\omega_+ t + \phi_+), \tag{2.11}$$

$$y(t) = -A_- \sin(\omega_- t + \phi_-) - A_+ \sin(\omega_+ t + \phi_+), \tag{2.12}$$

where A_+, A_-, ϕ_+ and ϕ_- are parameters indicating amplitude and phase of the motion in the laboratory frame of reference, which will be set by the initial position and velocity of the trapped ion. The characteristic frequencies of motion in this frame are indicated as

$$\omega_\pm = \frac{1}{2}\omega_c \pm \omega_1, \tag{2.13}$$

where ω_+ is called “modified cyclotron frequency" and ω_- is called “magnetron frequency". In a Penning trap, the stable confinement in 3D is only realised if the frequencies satisfy the condition [73]

$$\omega_c^2 - 2\omega_z^2 > 0, \quad QU_{dc} > 0. \tag{2.14}$$

For a positively charged particle, the above condition limits the highest value of the potential that can be applied to the trap electrodes and that is expressed $U_{max} = \frac{QB^2 d_0^2}{4m}$.

For the visualisation purpose, the trajectory of an ion in the radial plane is shown in figure 2.2 (a). The parameters for this plot are chosen to be $A_+ = 0.3$ and $A_- = 1$ in arbitrary units and frequencies of motion are assumed to be $\omega_+ = 0.907\omega_c$ and $\omega_- = 0.093\omega_c$. Note that the motion in the radial plane is composed of two types of circular motion, namely magnetron and modified cyclotron. The trajectory in the rotating frame is an ellipse with the semi-major axis and semi-minor axis to be $A_+ + A_-$ and $A_- - A_+$, where the initial phases are assumed to be $\phi_- = \phi_+ = 0$. In this figure, different curves correspond to trajectories in the rotating frame at different values of amplitude of motion. From curve I to IV the parameters (A_-, A_+) are taken to be (0,1.3), (1,0.3), (0.45,0.85) and (0.65, 0.65) respectively.

2.1.2 Energy of motion in a Penning trap

The energy of motion in a Penning trap can be derived from the Hamiltonian formalism. The Hamiltonian of a charged particle interacting with electric and magnetic fields is expressed as

$$H = \frac{1}{2m}(\mathbf{p} - Q\mathbf{A})^2 + Q\Phi \tag{2.15}$$

[1]The solution is chosen in cosine and sin forms, which is arbitrary but this choice simplifies the solutions of equations of motion while transforming into the laboratory frame. The choice of the amplitudes and phases of motion is also arbitrary at this point but can be set by initial conditions.

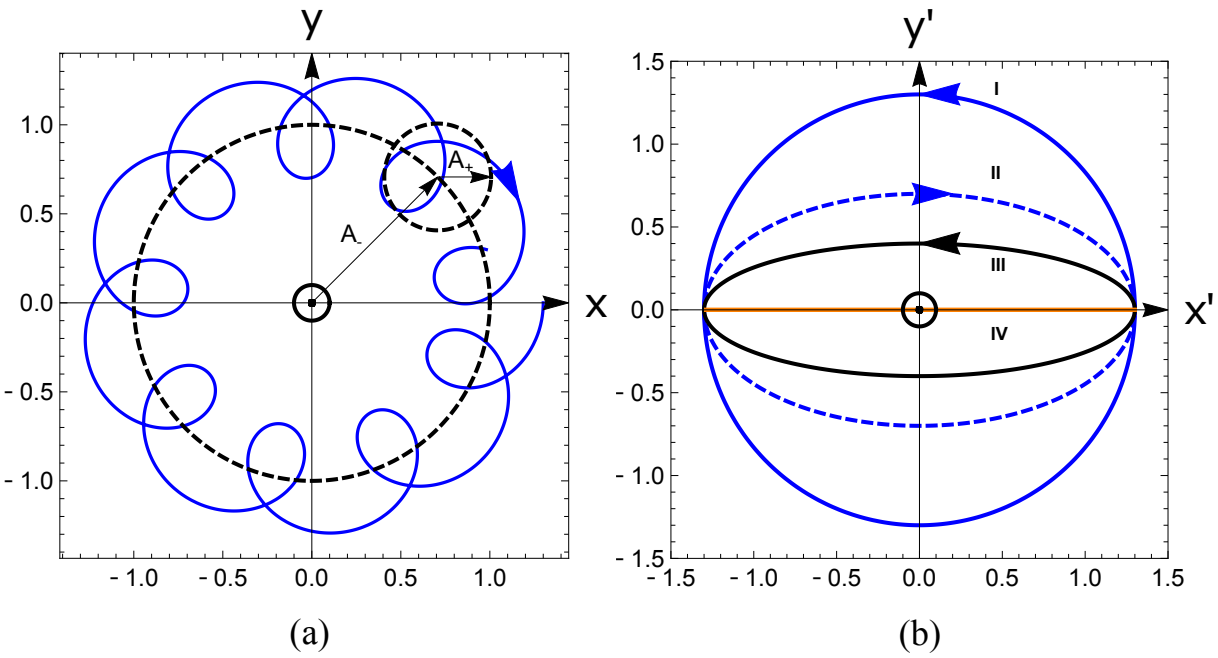


Figure 2.2: Trajectories of motion for an ion in a Penning trap, (a) in the laboratory frame, (b) in the rotating frame. Please refer the text for a detailed description. The dotted line in figure (b) corresponds to the laboratory motion shown in figure (a).

where $\mathbf{p} = m\mathbf{v} + Q\mathbf{A}$ is the total generalised momentum and $\mathbf{A} = \frac{B_0}{2}(-y, x, 0)$ is the vector potential associated with the applied magnetic field. The potential Φ is the quadrupole potential generated by the trap electrodes, which has been discussed in a previous section. The motion of an ion in the radial plane and in the axial direction can be treated independently. After following the separation of variable method, the Hamiltonian corresponding to the axial motion can be expressed as

$$H_z = \frac{1}{2}m\dot{z}^2 + \frac{1}{2}m\omega_z^2 z^2. \tag{2.16}$$

Similarly, the Hamiltonian for the radial motion can be written as

$$H_{rad} = \frac{1}{2m}\left(p_x + \frac{QB_0 y}{2}\right)^2 + \frac{1}{2m}\left(p_y - \frac{QB_0 x}{2}\right)^2 - \frac{QU_{dc}}{2d_0^2}\left(x^2 + y^2\right), \tag{2.17}$$

where p_x, p_y are the associated momentum along the x-axis and y-axis respectively and the rest of the parameters have usual meaning. The above expression can be further simplified to

$$H_{rad} = \frac{1}{2m}\left(p_x^2 + p_y^2\right) + \frac{1}{2}m\omega_1^2\left(x^2 + y^2\right) - \frac{1}{2}\omega_c(xp_y - yp_x) \tag{2.18}$$

where $\omega_1 = \frac{1}{2}\sqrt{\omega_c^2 - 2\omega_z^2}$.

The total energy motion along the axial direction is expressed as

$$KE_z + PE_z = \frac{1}{2}m\dot{z}^2 + \frac{1}{2}m\omega_z^2 z^2 = \frac{1}{2}m\omega_z^2 A_z^2, \tag{2.19}$$

and the total energy of the radial motion is given as

$$KE_{rad} + PE_{rad} = \frac{1}{2}m\left(\dot{x}^2 + \dot{y}^2\right) - \frac{QU_{dc}}{2d_0^2}(x^2 + y^2). \tag{2.20}$$

After replacing the position coordinates and their derivatives from equation 2.11 and 2.12, the expression for the radial energy simplifies to

$$KE_{rad} + PE_{rad} \quad = \quad \frac{1}{2}m\left(A_-^2\omega_-^2 + A_+^2\omega_+^2\right) - \frac{1}{4}m\omega_z^2\left(A_-^2 + A_+^2\right). \tag{2.21}$$

where A_i is the amplitude of the motion along a specific direction, $i = +, -$ and z corresponding to the mod-cyclotron, magnetron and axial motion, respectively.

Consequently, the total energy of an ion in a Penning trap can be written as

$$E = \frac{1}{2}m\omega_z^2 A_z^2 + m\omega_1(A_+^2\omega_+ - A_-^2\omega_-), \tag{2.22}$$

where the term with a negative sign indicates negative energy of the magnetron motion in a Penning trap. Evidently, the motion will have maximum energy if the magnetron radius is minimum, suggesting that the amplitude for the magnetron motion can be reduced if some energy is added to the motion. This specific issue in Penning traps leads to the complexity while performing Doppler cooling of trapped ions and it will be discussed in section 3.1.

2.2 Trapping of multiple ions in a Penning trap

2.2.1 Classical dynamics of two trapped ions

The classical treatment of motion of a single trapped ion is a trivial problem and can be solved analytically without making any approximations. Insertion of another ion in the trap leads to the Coulomb repulsion term, which adds another restriction while dealing the equations of motion. The equations of motion of two ions, with same charge (Q) and mass (m), in a Penning trap are expressed as

$$m\ddot{\mathbf{r}}_\mathbf{1} \quad = \quad -Q\nabla\Phi_{(r_1)} + Q\mathbf{v_1} \times \mathbf{B} + \frac{1}{4\pi\epsilon_0}\frac{Q^2(\mathbf{r_1} - \mathbf{r_2})}{|(r_1 - r_2)|^3}, \tag{2.23}$$

$$m\ddot{\mathbf{r}}_\mathbf{2} \quad = \quad -Q\nabla\Phi_{(r_2)} + Q\mathbf{v_2} \times \mathbf{B} + \frac{1}{4\pi\epsilon_0}\frac{Q^2(\mathbf{r_2} - \mathbf{r_1})}{|(r_1 - r_2)|^3}, \tag{2.24}$$

where $r_1(x_1, y_1, z_1)$ and $r_2(x_2, y_2, z_2)$ are the position coordinates of ion-1 and ion-2, respectively. The equations can be further simplified by transforming into the centre of mass (COM) and relative coordinates. Let us define the COM coordinates, $(X, Y, Z) = (\frac{x_1+x_2}{2}, \frac{y_1+y_2}{2}, \frac{z_1+z_2}{2})$ and the relative coordinates $(x, y, z) = (x_1 - x_2, y_1 - y_2, z_1 - z_2,)$. The transformed equations of

motion in relative and COM coordinates can be written as

$$\begin{aligned}
\ddot{x} &= \frac{1}{2}\omega_z^2 x + \omega_c \dot{y} + \frac{1}{4\pi\epsilon_0 m}\frac{2Q^2 x}{|r_{12}|^3}, \\
\ddot{y} &= \frac{1}{2}\omega_z^2 y - \omega_c \dot{x} + \frac{1}{4\pi\epsilon_0 m}\frac{2Q^2 y}{|r_{12}|^3}, \\
\ddot{z} &= -\omega_z^2 z + \frac{1}{4\pi\epsilon_0 m}\frac{2Q^2 z}{|r_{12}|^3}, \\
\ddot{X} &= \frac{1}{2}\omega_z^2 X + \omega_c \dot{Y}, \\
\ddot{Y} &= \frac{1}{2}\omega_z^2 Y - \omega_c \dot{X}, \\
\ddot{Z} &= -\omega_z^2 Z,
\end{aligned} \tag{2.25}$$

where r_{12} is the relative distance between the ions. The above transformation eliminates the non-linear term ($1/|r_{12}|^3$ term) from the equations of motion for the COM mode, but the relative motion still contains the non-linear term. The characteristic frequencies for the COM motion come to be ω_z, ω_+ and ω_-, which are identical to the single ion frequencies.

In order to solve the motion in the relative coordinates, we will make a few assumptions and reduce the equations to simpler forms. From the conservation of energy and angular momentum, we can assume that at equilibrium a perfect inversion symmetry around the trap centre can be realised; provided that the atoms have identical mass. Additionally, if the amplitude of motion of an individual ion around its equilibrium position is much smaller than the distance between the two ions, then we can rewrite the equation of motion for relative position coordinate, $i = r, z$, in terms of $\delta_i = i - 2i_0$, where $2i_0$ is the equilibrium separation of ions [2]. In a Penning trap, if two ions are trapped and laser-cooled then they align themselves either along the magnetic field axis (an axial chain) or rotate in the plane perpendicular to the magnetic field axis (as shown in figure 2.3). The COM motion in both cases will be identical to its equivalent single counterpart. In order to formulate the motional frequencies for the relative motion, I will describe both crystal orientations solely by assuming two specific cases.

Relative motion of a two-ion chain in a Penning trap

First I will discuss the case where the ions form a 1D chain along the magnetic field axis. If the ions are laser-cooled the amplitude of motion can be assumed to be much smaller than the separation between the ions and the motion can be re-written in terms of a differential position coordinate (δ_z). In order to solve the relative motion of a 1D chain problem, let us first define the total potential energy along the axial direction

$$U_{\text{Tot}} = \frac{1}{4\pi\epsilon_0}\frac{Q^2}{z} + \frac{1}{4}m\omega_z^2 z^2. \tag{2.26}$$

[2] The parameters $2z_0$ and $2r_0$ denote the equilibrium distances between ions for a chain and planar configurations and should not be confused with trap parameters.

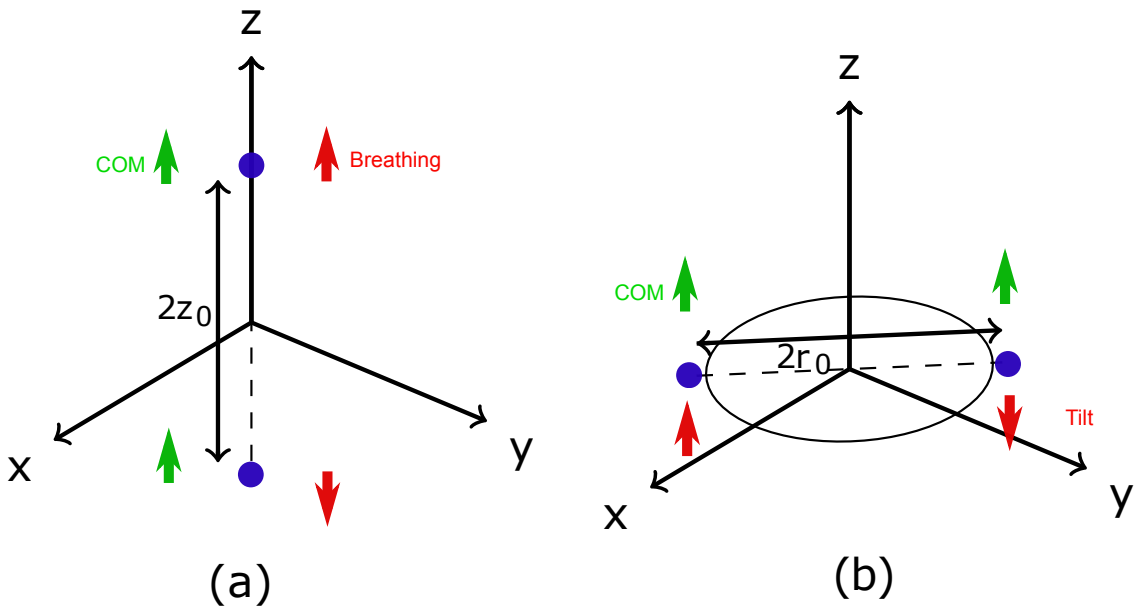


Figure 2.3: Two possible orientations of a two-ion Coulomb crystal in a Penning trap, (a) a two-ion chain and (b) a two-ion planar crystal rotating about the trap axis.

After taking a Taylor expansion around the equilibrium position of ions, the expression of the potential energy simplifies to

$$U_{\text{Tot}} = \frac{1}{4\pi\epsilon_0}\frac{Q^2}{(2z_0)} - \frac{1}{4\pi\epsilon_0}\frac{Q^2(z-2z_0)}{(2z_0)^2} + \frac{1}{4\pi\epsilon_0}\frac{Q^2(z-2z_0)^2}{(2z_0)^3} + \ldots \\ + \frac{1}{4}m\omega_z^2(2z_0)^2 + \frac{1}{2}m\omega_z^2(2z_0)(z-2z_0) + \frac{1}{4}m\omega_z^2(z-2z_0)^2 \tag{2.27}$$

where $2z_0$ is the equilibrium separation of ions. At equilibrium it can be assumed that $\frac{\partial U_{\text{Tot}}}{\partial z}|_{z=2z_0} = 0$, which gives

$$\frac{1}{4\pi\epsilon_0}\frac{Q^2}{(2z_0)^2} = m\omega_z^2(z_0), \tag{2.28}$$

and from this expression the equilibrium distance between the ions ($2z_0$) can be calculated. The above equation states that at equilibrium the Coulomb repulsion is cancelled out by the trapping force. After ignoring the position independent terms in the expression of the total energy (U_{Tot}), the expression reduces to

$$U_{\text{Tot}} = \frac{1}{4\pi\epsilon_0}\frac{Q^2\delta_z^2}{(2z_0)^3} + \frac{1}{4}m\omega_z^2\delta_z^2, \tag{2.29}$$

which will give rise to a harmonic potential around their equilibrium position. Therefore, the equation of motion along the axial direction simplifies as

$$\ddot{\delta_z} = -3\omega_z^2\delta_z, \tag{2.30}$$

with a new characteristic motional frequency, $\sqrt{3}\omega_z$, of the relative motion.

Similarly, the radial motion of an axial chain can be expressed by directly replacing the

Coulomb force term from equation 2.28. Subsequently, the radial equations of motion are simplified to

$$\begin{aligned} \ddot{x} &= \tfrac{3}{2}\omega_z^2 x + \omega_c \dot{y}, \\ \ddot{y} &= \tfrac{3}{2}\omega_z^2 y - \omega_c \dot{x}. \end{aligned} \tag{2.31}$$

These equations can be solved in the same way as the radial equations of motion for a single ion. The solution of radial equations of motion in a chain configuration gives rise to the characteristic frequencies

$$\begin{aligned} \omega_{+S} &= \omega_c/2 + \sqrt{\omega_1^2 - \omega_z^2}, \\ \omega_{-S} &= \omega_c/2 - \sqrt{\omega_1^2 - \omega_z^2}, \end{aligned} \tag{2.32}$$

where ω_c, ω_z and ω_1 are the characteristic frequencies of motion of a single ion.

The relative motional modes of a two-ion chain are termed as “breathing modes" and the terminology will be used in this thesis on many occasions. Evidently, from equation 2.32, we come to a conclusion that the ions will stay in as a chain as long as $\omega_1 \geq \omega_z$. Importantly, this condition is only valid if the separation of two ions is greater than the amplitude of motion in the radial plane. However, if the ions rotate in the radial plane (in a perpendicular to $\mathbf{B}$) the stability condition will be determined by the rotation frequency of the crystal. This case will be discussed in the following subsection.

Relative motion of a planar two-ion crystal

In a situation where two ions align themselves in the radial plane, the analytical solution of the relative motion would be a little bit trickier due to the rotation of the crystal. Since the ions in the radial plane rotate due to the presence of crossed electric and magnetic fields, it becomes necessary to consider the effect of the rotation of the crystal. In this situation also, the main task will be to eliminate the non-linear term from the equations of motion (equation 2.25). Let us assume that the ions form a Coulomb crystal and the motion of each individual ion is locked with respect to the other ion. Suppose the spacing of the ions is $r_{12} = 2r_0$ and it is larger than the amplitude of the relative motion. Let us also assume that in the laboratory frame, the rotation frequency of the crystal is ω_r.

In this case, the equilibrium condition will be established for the radial motion as the Coulomb force greatly affects the motion along that direction. From the single ion case, we know that radial trapping force in the rotating frame is given by $m\omega_1^2 r$, where r is $\sqrt{x^2 + y^2}$. For a two-ion planar crystal, the additional pseudo force in the rotating frame arises from the coordinate transformation and is known as Coriolis force. If we make transformation into the rotating frame, the new centrifugal force is given as $F_{cent} = m(\omega_r - \omega_c/2)^2 r$. At equilibrium, the trapping force should be cancelled out by the repulsion term and the centrifugal force; hence it is obvious to

write

$$\frac{1}{4\pi\epsilon_0}\frac{Q^2}{(2r_0)^2} = m(\omega_1^2 - (\omega_r - \omega_c/2)^2)r_0, \tag{2.33}$$

where the first term on the right hand side is due to the trapping force and second term is the equivalent centrifugal force in the rotating frame.

The axial motion of a planar crystal will be solved by simply replacing the Coulomb term from above equation in the equation of motion 2.25. The resultant equation of motion is given as

$$\ddot{z} = -\omega_z^2 z + (\omega_1^2 - (\omega_r - \omega_c/2)^2)z, \tag{2.34}$$

which gives the motional frequency of the “tilt" motion to be

$$\omega_{\text{tilt}} = \sqrt{\omega_z^2 - \left(\omega_r(\omega_c - \omega_r) - \tfrac{1}{2}\omega_z^2\right)}, \tag{2.35}$$

where the second term gives rise to an effective trap frequency in the radial plane, $\omega_{eff} = \sqrt{\left(\omega_r(\omega_c - \omega_r) - \frac{1}{2}\omega_z^2\right)}$.

The out-of-phase motion in the radial direction can be interpreted in terms of two types of motion, first is due to small displacement about their equilibrium positions (it can be also treated as vibration in the rotating frame) and second is due to pure rotation of the crystal. After making the harmonic approximation of the Coulomb potential, the equations of motion in the rotating frame can be written as

$$\ddot{\delta_r} = -\omega_1^2\delta_r - \frac{1}{2\pi\epsilon_0}\frac{Q^2\delta_r}{m(2r_0)^3}, \tag{2.36}$$

$$\ddot{r_{12}} = -(\omega_r - \omega_c/2)^2 r_{12}, \tag{2.37}$$

where $\delta_r = r_{12} - 2r_0$ is the small change in radial position from their equilibrium spacing. From equation 2.33 and 2.36 the motion in the radial plane is expressed as

$$\ddot{\delta_r} = -\omega_1^2\delta_r - 2(\omega_1^2 - (\omega_r - \omega_c/2)^2)\delta_r, \tag{2.38}$$

$$\ddot{r_{12}} = -(\omega_r - \omega_c/2)^2 r_{12}, \tag{2.39}$$

which gives the frequencies $\omega_v = \sqrt{3\omega_1^2 - (\omega_r - \omega_c/2)^2}$ and $(\omega_r - \omega_c/2)$. In the laboratory frame the vibration will still remain same and the rotation frequency will be ω_r or $\omega_r + \omega_c$. The frequency component $\omega_r + \omega_c$ will be disregarded from the stability condition of a planar crystal which will be discussed in the following section.

Stability conditions for a two-ion Coulomb crystal

The stability of a two-ion crystal is also determined by the trapping parameters and is indicated by equation 2.14. However, the two types of structures (chain and planar crystals) are observed

at specific trapping conditions. These structures can be changed from one to the other by varying the trap frequency and/or rotation frequency of the crystal. A planar crystal is observed if the “tilt" mode frequency lies between $0 \leq \omega_{\text{tilt}} \leq \omega_z$. More intuitively, a planar crystal is not stable if $\omega_{\text{eff}} > \omega_z$ (see equation 2.35 for more details) and eventually it makes a two-ion chain.

The stability condition of a two-ion crystal can also be illustrated in terms of the rotation frequency of the crystal and is indicated in figure 2.4. The area outside the red curve in the figure implies that the crystal is not stable if the rotation frequency is ever higher than the single-ion modified cyclotron frequency or if it is lower than the single-ion magnetron frequency at a non-zero axial frequency. However, within the enclosed area of red curve and $\omega_z = 0$ line, the crystal will be always stable. A planar crystal will be realised for the parameters in the red region of the plot and a chain is realised when the parameters are chosen from the brown region of the plot. The plot has been generated for two calcium-40 ions trapped in a 1.9 T Penning trap. A dashed vertical line is drawn at $\omega_z \sim 300$ kHz, which implies that above this frequency, one can only observe a planar structure. If the axial frequency is less than 300 kHz, the chain will be observed if the rotation frequency lies between the black curve and $\omega_z = 0$ line. The intersection point of the dashed vertical line and dashed horizontal line ($\omega_r = \omega_c/2$) indicates the Brillouin flow point, where maximum density of the system will be obtained.

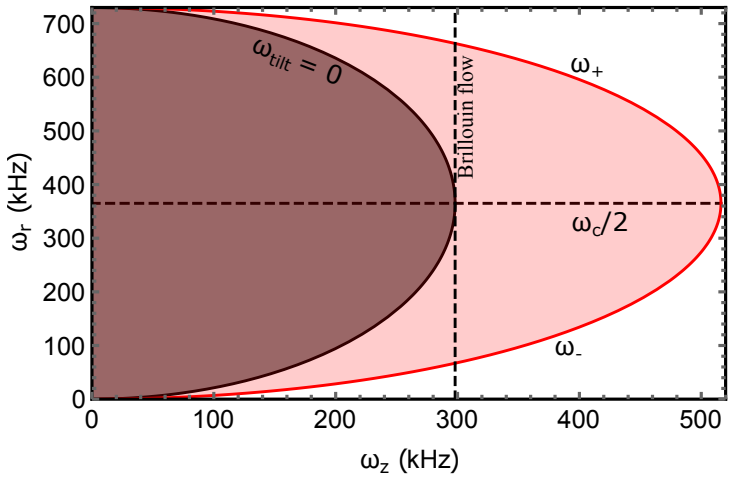


Figure 2.4: Figure illustrating stability condition of a two-ion Coulomb crystal in a Penning trap against trapping frequency and rotation frequency of the crystal. A chain structure of a two-ion crystal is realised for the parameter values that lie within the black curve and $\omega_z = 0$. Similarly, a planar structure is realised when parameters lie within red curve and black curve.

2.2.2 Hamiltonian of a two-ion Coulomb crystal

The Hamiltonian for two ions, of same masses (m) and charges (Q), trapped in a Penning trap is given as

$$H = \frac{(\mathbf{p_1} - Q\mathbf{A})^2}{2m} + \frac{(\mathbf{p_2} - Q\mathbf{A})^2}{2m} + \frac{QU_{dc}}{2d_0^2}(2z_1^2 - x_1^2 - y_1^2) + \frac{QU_{dc}}{2d_0^2}(2z_2^2 - x_2^2 - y_2^2) + \frac{Q^2}{4\pi\epsilon_0|r_1 - r_2|}, \tag{2.40}$$

where $\mathbf{p_1}$ and $\mathbf{p_2}$ are the generalised momentum of ion 1 and 2 respectively. The Hamiltonian can be further reduced to a simpler form by assuming two laser cooled ions and writing the motion in terms of the relative coordinates. The Hamiltonian along the axial direction in COM and breathing/tilt modes is written as

$$H_z = \frac{P_{\text{com}}^2}{2M} + \frac{p_{re}^2}{2\mu} + \tfrac{1}{2}m\omega_{\text{com}}^2 Z^2 + \tfrac{1}{2}m\omega_{re}^2 z^2, \tag{2.41}$$

where $M = 2m$ is the combined mass and $\mu = m/2$ is the reduced mass of the two-ion Coulomb crystal. Similarly, the momentum in terms of relative coordinates will be P_{com} for the COM motion and p_{re} for the stretch/tilt mode of motion.

2.2.3 Ion Coulomb crystals in a Penning trap

When multiple ions are trapped together in an ion trap, at equilibrium the trapping force is cancelled out by interionic Coulomb repulsion. At equilibrium, the ions form a minimum energy configuration and a regular structure is observed. Such regular structures are commonly seen in ion traps when laser cooling of atomic ions is carried out and they are known as Ion Coulomb Crystals (ICCs) [23]. The structural property of ICCs is purely determined by the trapping parameters (i.e parameters governing the trapping strength). Such systems are easy to control and thus they are used for the purpose of quantum simulations and computations.

In Penning traps, the ICCs rotate about the magnetic field axis forming a crystal structure in the rotating frame. The rotation frequency can be controlled by the trapping parameters and the laser beam parameters such as beam position, intensity and detuning from the transition. Tuning of the axial and radial confining forces can be used to change the crystal structure from a 2D planar crystal to 3D crystals and finally a 1D chain [32]. A simplest 1D chain is realised when the axial confining force is weaker than the equivalent confining force in the radial direction. Conversely, the planar ICCs are realised when radial trapping force is much weaker than the axial trapping force.

In ion traps, the trapping force emulates the presence of oppositely charged species with a uniform density. Coexistence of the trapped atomic ions along with the fictitious oppositely charged species resembles a plasma. Hence, this is often referred to a “non-neutral plasma" or a “single component plasma". The behaviour of such systems is determined by a parameter Γ, which is called the Coupling parameter and is defined as a ratio of electrostatic potential energy and associated thermal energy of the trapped ions. The coupling parameter is given as

$$\Gamma = \frac{e^2}{4\pi\epsilon_0 a_0 k_B T} \tag{2.42}$$

where a_0, the Wigner-Seitz radius, is the average distance between the nearest neighbour atomic ions [23]. The parameter a_0 relates to the trapped ion number density (n) through $\frac{4\pi a_0^3 n}{3} = 1$. The parameter Γ determines the physical state of a system, whether it is a gaseous or crystalline type. The crystallisation occurs only for a high value of Γ. Typically for an infinite system,

$\Gamma > 178$ is essential, which is feasible with Doppler cooled trapped atomic ions.

The normal modes of a multi-ion Coulomb crystal

With increasing number of ions, the motion of trapped ions is no longer solvable without making any approximations. In a multi-ion crystal (typically for more than two ions), the motional frequencies cannot be formulated analytically. The normal modes of a one-dimensional chain have been discussed in reference [74]. In general, Penning traps are not very suitable for a one-dimensional chain. Typically, for more than two ions, a chain orientation is achieved at a low trapping potential, i.e. at a low motional frequency along the axial direction [32]. In this case, it is almost impossible to ground state cool the motion along the axial direction. On the other hand, in a Penning trap, the ions tend to align in the radial plane at high axial trapping voltages, forming planar crystals. Such crystals are interesting as they do not possess any micro-motion like in an RF trap and they can be used to study/simulate multi-spin systems [24].

In an N-ion Coulomb crystal system, there are $3N$ possible motional modes, out of which at least N modes can be interrogated through a laser beam propagating along the axial direction. In order to simplify the equations of motion, we can evaluate the equations in the rotating frame of the crystal. Following the treatment of a single ion, the Lagrangian of an N-ion crystal can be written as

$$L = \sum_{i}^{N} \left(\frac{p_i^2}{2m} - \frac{1}{4}\omega_z^2(2z_i^2 - x_i^2 - y_i^2) + m\omega_c(x_i\dot{y_i} - y_i\dot{x_i}) - \sum_{j\neq i}^{N} \frac{1}{8\pi\epsilon_0}\frac{Q^2}{r_{ij}} \right). \tag{2.43}$$

At equilibrium, it can be assumed that the amplitude of motion is small in comparison to the equilibrium spacing of ions, hence we can write $r_i = r_i^0 + \delta r_i(t)$, where $\delta r_i(t) << r_i^0$. If the ions are rotating at a frequency ω_r, then in the rotating frame the Lagrangian can be written as

$$\begin{aligned} L = \sum_{i}^{N} \Bigg[& \frac{(p_i')^2}{2m} + m\omega_c(x_i\dot{y_i} - y_i\dot{x_i}) - \frac{1}{2}m\omega_z^2(z_i')^2 \\ & + \left(\frac{1}{4}m\omega_z^2 + \frac{1}{2}m\omega_r^2 - QB_z\omega_r\right)\left((x_i')^2 + (y_i')^2\right) - \sum_{j\neq i}^{N} \frac{1}{8\pi\epsilon_0}\frac{Q^2}{r_{ij}} \Bigg] \end{aligned} \tag{2.44}$$

where x', y' and z' are position coordinates in the rotating frame of reference.

In order to calculate the eigenvalues and eigenvectors of the classical motion, the action $S = \int L dt$ must be minimised. Expanding the Lagrangian around the equilibrium position (r_i^0), we can find a stiffness matrix (**K**), which can be used to calculate the frequency of motion. In the scope of the current work, I would like to restrict the studies to axial modes of planar crystals. Elements of the stiffness matrix for the axial modes of a planar crystal are given by

[75]

$$K_{ij}^{zz} = \begin{cases} m\omega_z^2 - \sum_{k\neq j}^{N} \frac{1}{4\pi\epsilon_0} \frac{Q^2}{(r_{jk}^0)^3}, & i = j \\ \frac{1}{4\pi\epsilon_0} \frac{Q^2}{(r_{ij}^0)^3}, & i \neq j \end{cases} \tag{2.45}$$

where r_{ij}^0 is the equilibrium distance between ion i and j. At any point, the equilibrium distance between the ions can be calculated by equating the trapping force with the Coulomb repulsion, centripetal and Coriolis force. A load equation in terms of the stiffness matrix is given as

$$\mathbf{K^{zz}Z} = \mu\mathbf{Z}, \tag{2.46}$$

where $\mathbf{Z} = (z_1, ...z_N)$ is the eigenvector and μ is the corresponding eigenvalue. The eigenvalues and eigenvectors can be calculated by transferring the load equation into normal modes, which is possible by appropriate diagonalisation of the stiffness matrix.

2.3 Quantum dynamics of an ion in a Penning trap

2.3.1 A 3-D quantum harmonic oscillator

A harmonic oscillator is a well-studied problem in quantum mechanics. Trapped ion systems are considered as an ideal realisation of the quantum harmonic oscillator. Previously, I have defined a Hamiltonian for an ion in a Penning trap to describe the classical motion (equations 2.16 and 2.18). The equivalent quantum Hamiltonian for the axial and radial motion is given as [3]

$$\begin{aligned} H_z &= \frac{p_z^2}{2m} + \frac{1}{2}m\omega_z^2 z^2, \\ H_{rad} &= \frac{p_x^2 + p_y^2}{2m} + \frac{1}{2}m\omega_1^2(x^2 + y^2) - \frac{1}{2}\omega_c L_z, \end{aligned} \tag{2.47}$$

where $L_z = xp_y - yp_x$ is an angular momentum operator and ω_z, ω_1 and ω_c are the characteristic motional frequencies of a single ion. Note that the Hamiltonian in the radial plane (H_{rad}) is similar to an isotropic 2D harmonic oscillator Hamiltonian. For simplicity we will make transformation into cylindrical coordinates (ρ, ϕ and z), where $x = \rho\cos(\theta)$ and $y = \rho\sin(\theta)$. After adapting the separation of variable method, the wave-function will be defined as

$$\psi(\rho, \phi, z) = \Xi(\rho, \phi)Z(z), \tag{2.48}$$

and we can define two individual wave equations corresponding to the axial and radial motion. In order to simplify the Hamiltonian, let us define the raising ($a^\dagger$) and lowering (a) operators in

[3] In the quantum mechanical treatment of the Hamiltonian, the position and momentum coordinates of the ion will be taken in operator forms [40].

the following manner

$$
\begin{aligned}
x &= \sqrt{\frac{\hbar}{m\omega_1}}(a_x^\dagger + a_x)/\sqrt{2}, && (2.49)\\
y &= \sqrt{\frac{\hbar}{m\omega_1}}(a_y^\dagger + a_y)/\sqrt{2}, && (2.50)\\
z &= \sqrt{\frac{\hbar}{m\omega_z}}(a_z^\dagger + a_z)/\sqrt{2}, && (2.51)\\
p_x &= i\sqrt{\hbar m\omega_1}(a_x^\dagger - a_x)/\sqrt{2}, && (2.52)\\
p_y &= i\sqrt{\hbar m\omega_1}(a_y^\dagger - a_y)/\sqrt{2}, && (2.53)\\
p_z &= i\sqrt{\hbar m\omega_z}(a_z^\dagger - a_z)/\sqrt{2}, && (2.54)\\
a_+ &= (a_x + ia_y)/\sqrt{2}, && (2.55)\\
a_- &= (a_x - ia_y)/\sqrt{2}, && (2.56)\\
a_+^\dagger &= (a_x^\dagger - ia_y^\dagger)/\sqrt{2}, && (2.57)\\
a_-^\dagger &= (a_x^\dagger + ia_y^\dagger)/\sqrt{2}, && (2.58)
\end{aligned}
$$

where $a^\dagger_{+/-/z}, a_{+/-/z}$ are the raising and lowering operator for magnetron/modified cyclotron/axial motion.

The Hamiltonian and angular momentum components in operator form can be written as

$$
\begin{aligned}
H_z &= (a_z^\dagger a_z + \tfrac{1}{2})\hbar\omega_z,\\
H_{rad} &= (a_+^\dagger a_+ + \tfrac{1}{2})\hbar\omega_+ - (a_-^\dagger a_- + \tfrac{1}{2})\hbar\omega_-,\\
L_z &= (a_-^\dagger a_- - a_+^\dagger a_+)\hbar && (2.59)
\end{aligned}
$$

Note that the radial Hamiltonian contains a negative energy term, suggesting a negative energy contribution due to the magnetron motion. The corresponding eigenvalues of motion in the axial and radial direction are given as

$$
\begin{aligned}
E_z &= (n_z + \frac{1}{2})\hbar\omega_z, && (2.60)\\
E_{+-} &= (n_+ + \frac{1}{2})\hbar\omega_+ - (n_- + \frac{1}{2})\hbar\omega_-, && (2.61)
\end{aligned}
$$

where respective oscillators states n_z, n_+ and n_- are positive integers. After following the normal algebra for the angular momentum operator L_z, the eigenvalue is deduced as $(n_- - n_+)\hbar$.

In order to deduce the wavefunction corresponding to these harmonic oscillator states, I will follow the operator method as discussed in reference [76, 77]. The full algebraic analysis can be found in appendix A.1, which leads to the expression of the axial wave function as

$$
Z(z) = \frac{1}{\sqrt{n_z! 2^{n_z} z_1 \sqrt{\pi}}} H_{n_z}\left(\frac{z}{z_1}\right)\exp\left(-\frac{z^2}{2z_1^2}\right), \qquad (2.62)
$$

where $z_1 = \sqrt{\frac{\hbar}{m\omega_z}}$.

Now let us find the wavefunction corresponding to the radial motional modes. I have already defined the operator form of the radial Hamiltonian, the expression becomes a 2D harmonic oscillator with new raising and lowering operators denoting two types of rotations. The transformation from the raising and lowering operators of the motion in the Cartesian coordinate system to a new one denoting the rotational motion gives a better realisation of quantum dynamics in a Penning trap. The new operators are equivalent to the operators of left and right circularly-polarised quanta of light [76]. The detailed derivation of the radial wave function is discussed in appendix A.2. The expression in operator form is given as

$$\Xi_{n_+,n_-}(\rho,\phi) = \frac{1}{r_1\sqrt{\pi n_+! n_-!}}(a_-^\dagger)^{n_-}(a_+^\dagger)^{n_+}e^{-\frac{\rho^2}{2r_1^2}}, \tag{2.63}$$

where $a_+^\dagger/a_+$ and $a_-^\dagger/a_-$ are the raising/lowering operators for the modified cyclotron and magnetron motion, respectively. After following the definition of $a_+^\dagger$ and $a_-^\dagger$, as mentioned in appendix A.2, it is straight forward to construct the radial wavefunction. The final expression of the wavefunction in terms of Hermite and Laguerre polynomials is given as

$$\psi_{n_+,n_-,n_z} = \frac{1}{\pi^{3/4}r_1 z_1^{1/2}\sqrt{2^{n_z}n_z!}}\sqrt{\frac{n_<!}{n_>!}}\left(\frac{\rho}{r_1}\right)^{|s|}L_{n_<}^{|s|}\left(\frac{\rho^2}{r_1^2}\right)e^{-\frac{\rho^2}{2r_1^2}-\frac{z^2}{2z_1^2}}e^{is\theta}H_{n_z}\left(\frac{z}{z_1}\right) \tag{2.64}$$

where $n_<$ ($n_>$) is the smaller (larger) quantum number among n_+ and n_- motional quantum numbers, and $s = n_- - n_+$ is an integer denoting eigenvalues of the angular momentum operator (L_z). The corresponding energy level diagram for the motional states of an ion in an ideal Penning trap is shown in figure 2.5. The energy spacing is arbitrarily chosen and for simplicity the ground state energy is ignored.

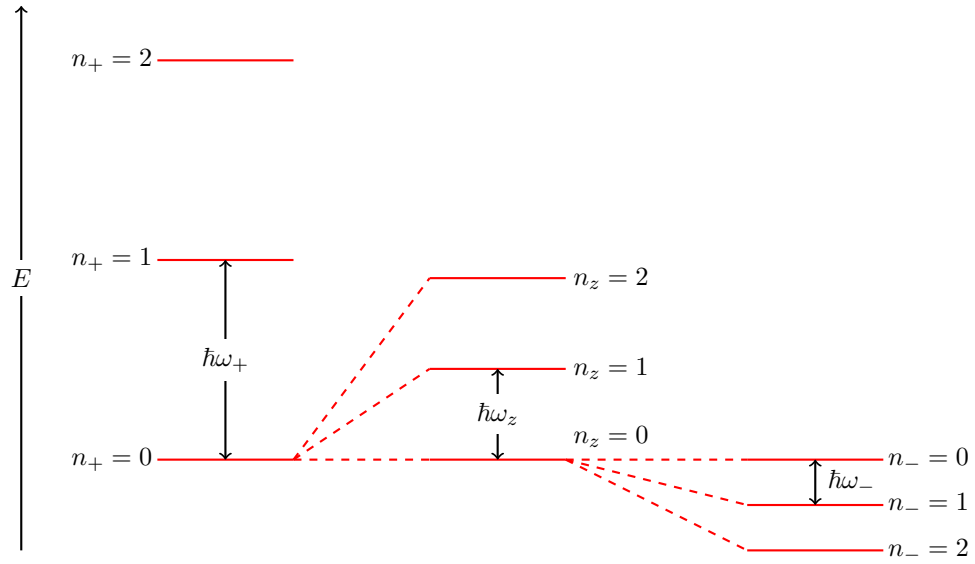


Figure 2.5: The energy level diagram showing quantum harmonic energy levels corresponding to a single ion in a Penning trap ($\omega_+ > \omega_z > \omega_-$). Each motional state n_+ comprises the infinite number of states for axial and magnetron motional states.

2.3.2 Fock space representation of harmonic oscillator states

Harmonic oscillator state vectors can be represented by a complete orthonormal set of vectors { $|n\rangle$ }, where n is the quantum number associated with the harmonic oscillator energy level. This representation of the harmonic oscillator state vector is called Fock-space representation and the state vectors are called the “Fock" states. In this representation, the raising and lowering operators can be used to construct the state vectors from the ground state wave-function $|0\rangle$,

$$|n\rangle = \frac{1}{n!}(a^\dagger)^n |0\rangle . \tag{2.65}$$

The state vectors and operators mentioned here follow the definition of the Hilbert space [76].

2.3.3 A coherent state of harmonic motion

Another very interesting state of motion is termed as a coherent state. The coherent state is a minimal uncertainty wave-packet derived by Erwin Schrödinger while searching for solutions which could bridge quantum and classical theories. Such a state was later introduced to quantum optics by Glauber to represent the states of electromagnetic fields [56]. A coherent state of a harmonic oscillator is denoted by $|\alpha\rangle$ and is always an eigenstate of the lowering operator (a), hence $a|\alpha\rangle = \alpha|\alpha\rangle$. A coherent state is constructed by applying a displacement operator ($D(\alpha)$) on the ground state vector $|0\rangle$ of the harmonic oscillator and it is defined as

$$|\alpha\rangle = D(\alpha)|0\rangle , \tag{2.66}$$

where $D(\alpha)$ in operator form is $e^{\alpha a^\dagger - \alpha^* a}$. After expanding the displacement operator $D(\alpha)$, the coherent state is expressed as

$$|\alpha\rangle = e^{-\frac{\alpha\alpha^*}{2}} \sum_{k=0}^{\infty} \frac{\alpha^k}{k!} |0\rangle . \tag{2.67}$$

A coherent state of motion corresponds to the classical motion of the equivalent harmonic oscillator with the amplitude of motion $|\alpha|$. In the Fock-space representation, a coherent state is a superposition of the number states $|k\rangle$ and hence the probability distribution in terms of number states is expressed as

$$P_k = |\langle\alpha|k\rangle|^2 = \frac{|\alpha|^{2k}}{k!} e^{-|\alpha|^2}, \tag{2.68}$$

which is equivalent to a Poisson distribution function with the mean value $|\alpha|^2$. In a later section, I will discuss how can we realise a coherent state with the trapped ions after interrogating them with laser radiation.

2.3.4 A squeezed state of motion

Similarly, a squeezed state or vacuum squeezed state of motion is constructed by applying the squeezing operator $S(\xi) = e^{\frac{\xi(a^\dagger)^2}{2} - \frac{\xi^* a^2}{2}}$ to the ground state $|0\rangle$ of a harmonic oscillator. Often the squeezing operator is accompanied by a Displacement operator $D(\alpha)$ and the generated state is called a displaced-squeezed state of motion. The population distribution of a vacuum squeezed state of motion is given as [78]

$$P_{2k} = \frac{(2k)! \tanh^{2k}(r)}{\left(2^k k!\right)^2 \cosh(r)} \; \forall \; k = 0 \text{ to } \infty \tag{2.69}$$

with $\xi = e^{2r}$. In later chapters, I will show an experimental demonstration of the squeezed state of motion.

2.4 Interaction of trapped atomic ions with a laser field

In order to perform high fidelity quantum control with atomic species, a system that is clean and well isolated from any surrounding perturbations is required. Atomic ions held inside a vacuum chamber provide an ideal and a clean quantum system. Trapped ion systems in conjunction with lasers are routinely being used to perform high-fidelity quantum computation and simulations. In order to perform coherent control with trapped atomic ions using lasers, we need to solve the Schrödinger equation for the laser-ion interaction. A time-dependent solution of the Schrödinger equation for the laser-ion interaction Hamiltonian is generally used to understand the time evolution of population between atomic and motional states.

2.4.1 Laser-ion interaction Hamiltonian for a single trapped ion

In order to set up the Schrödinger equation for a trapped ion, interacting with laser radiation, we will need to find the required Hamiltonian. The full Hamiltonian of a trapped ion interacting with laser radiation is given as

$$H = H_e + H_{\mathrm{m}} + H_{int}, \tag{2.70}$$

where H_e is the atomic part and H_{m} is the motional part of the Hamiltonian. The term H_{int} is due to the interaction of the atomic ion with the electromagnetic radiation.

Let us first discuss the atomic part of the Hamiltonian (H_e). At this stage, we will assume that the internal states of the atomic ion are already quantised and the atomic states are denoted by a total angular quantum number J. Additionally, if the atomic ion is held in a magnetic field, the internal states of the ion get further split into Zeeman sub-levels (m_j). [4] In the current

[4] Here we are setting up the framework for a calcium ion in a Penning trap, where the fine structure states are denoted by (j), which further split into sub-levels m_j due to a strong magnetic field. So we can assume that the two-level system is composed of $|g\rangle = |J, m_j\rangle$ and $|e\rangle = |J', m_j'\rangle$.

description, we are interested in the time evolution of a two-level system interacting with a near-resonant electromagnetic field. Hence, we can ignore the other atomic levels and we will assume that $|\mathrm{g}\rangle = |j, m_j\rangle$ and $|\mathrm{e}\rangle = |j', m_j'\rangle$ make a two-level quantum system. The Hamiltonian corresponding to a free two-level atom in state vector representation is given as

$$\begin{aligned} H_e &= E_e |e\rangle \langle e| + E_g |g\rangle \langle g| , \\ &= \frac{\hbar\omega_0}{2} |e\rangle \langle e| - \frac{\hbar\omega_0}{2} |g\rangle \langle g| , \end{aligned} \tag{2.71}$$

where $|g\rangle$ and $|e\rangle$ are state vectors of the ground state and excited state, respectively. The time-independent solution of the Schrödinger equation ($H_0 |\psi_i\rangle = E_i |\psi_i\rangle$) of a two-level atom has eigenvector $|g\rangle$ and $|e\rangle$ with eigenvalues $-\hbar\omega_0/2$ and $\hbar\omega_0/2$ [5]. The Hamiltonian in Pauli-spin matrix representation further simplifies to [79]

$$H_e = \frac{\hbar\omega_0}{2}\sigma_z, \tag{2.72}$$

where $\sigma_z = |e\rangle \langle e| - |g\rangle \langle g|$, is one of the Pauli spin matrices defined for a spin-1/2 system.

Initially, we will discuss the motion along one axis only (say along the axial direction) and the description for the remaining two axes can be simply extended in a similar manner. From the previous discussion of the harmonic oscillator problem, the Hamiltonian for a harmonic oscillator is given as

$$H_{mech} = \left(a^\dagger a + \frac{1}{2}\right)\hbar\omega_m, \tag{2.73}$$

where ω_m is the frequency of the harmonic oscillator and a and $a^\dagger$ are the corresponding raising and lowering operators.

A two-level atom can be considered as a dipole oscillator with atomic dipole moment $\mathbf{D}$, interacting with a time-varying electric field $\mathbf{E} = E_0\hat{x}\cos(\omega_L t - kz)$ of the electromagnetic radiation. Here, E_0 is the amplitude and ω_L is the frequency of the radiation. The interaction Hamiltonian of the system is given as

$$H_{int} = -\mathbf{E}\cdot\mathbf{D} = -E_0\hat{x}\cos(\omega_L t - kz)\cdot\mathbf{D} \tag{2.74}$$

$$= -\tfrac{E_0}{2}(e^{i(\omega_L t - kz)} + e^{-i(\omega_L t - kz)})\hat{x}\cdot\mathbf{D}, \tag{2.75}$$

where the electric field vector is assumed to be oriented along the x-axis and the wave is assumed to be travelling along the z-axis. The scalar product $\hat{x}\cdot\mathbf{D}$ for a two-level system can be further expressed in state vector form [79],

$$\hat{x}\cdot\mathbf{D} \equiv \langle \mathrm{e}|\, \hat{x}\cdot\mathbf{D}\, |\mathrm{g}\rangle\, (|\mathrm{e}\rangle \langle \mathrm{g}| + |\mathrm{g}\rangle \langle \mathrm{e}|). \tag{2.76}$$

Subsequently, introducing the derived Pauli spin matrices, $\sigma_+ = |\mathrm{e}\rangle \langle \mathrm{g}|$ and $\sigma_- = |\mathrm{g}\rangle \langle \mathrm{e}|$, which indicate the transitions up ($|g\rangle \to |e\rangle$) or down ($|e\rangle \to |g\rangle$) when operating on states $|g\rangle$

[5] In order to simplify the expressions I have assumed that the zero of the energy lies at the middle point of the levels $|g\rangle$ and $|e\rangle$.

and $|e\rangle$ [76]. Also from the description of a two-level atom, the matrix product $-\frac{E_0}{\hbar}\langle \mathrm{e}|\,\hat{x}\cdot\mathbf{D}\,|\mathrm{g}\rangle$ is denoted by the parameter Ω and it is called the Rabi frequency. The Rabi frequency in a two-level system is a characteristic frequency at which the population density oscillates between the ground and excited states. The interaction Hamiltonian further simplifies as

$$H_{int} = \frac{\hbar\Omega}{2}(\sigma_+ + \sigma_-)(e^{i(\omega_L t - kz)} + e^{-i(\omega_L t - kz)}). \tag{2.77}$$

Note that the above interaction Hamiltonian corresponds to the atom's atomic dipole interacting with a plane electromagnetic wave. A similar treatment can be found in Appendix B for the electric quadrupole transitions when the Rabi frequency is redefined in terms of the tensor product of the electric quadrupole moment of the atom and electric field vector of the electromagnetic radiation.

Now we can solve the dynamics of the population between states $|g\rangle$ and $|e\rangle$ due to a time-varying electromagnetic field. The simplest description of time evolution between the states can be established via transforming into the interaction picture [76]. In the interaction picture, the time dependence of the population between the atomic states is studied by transforming the state vectors into time-dependent state vectors and operators, via a suitable unitary operation. Let us define the unitary operator as $U = e^{-iH_0 t/\hbar}$, where $H_0 = H_e + H_m$, which operates on the interaction Hamiltonian given in equation 2.77 and the transformation is given as

$$\tilde{H}_{int} = U^\dagger H_{int} U. \tag{2.78}$$

After performing normal algebraic operation, the interaction Hamiltonian in the interaction picture converts to

$$\tilde{H}_{int} = \frac{\hbar\Omega}{2}\left(\sigma_+ e^{i\omega_0 t} + \sigma_- e^{-i\omega_0 t}\right)\left(e^{i\omega_L t}e^{iH_m t/\hbar}e^{-ikz}e^{-iH_m t/\hbar} + e^{-i\omega_L t}e^{iH_m t/\hbar}e^{ikz}e^{-iH_m t/\hbar}\right). \tag{2.79}$$

We can also rewrite the spatial part of the electric field (e^{ikz}) in terms of its interaction picture equivalent. This transformation is equivalent to transferring the harmonic oscillator time dependence to the electromagnetic field. This transformation resembles the situation where the atom is assumed to be at rest and the electromagnetic field is frequency modulated at the frequency of the harmonic oscillator. The expression of the interaction Hamiltonian can be further simplified by taking the rotating-wave approximation. The rotating wave approximation can be made when the atom is weakly coupled to the radiation ($\Omega \ll \omega_0$) and the laser frequency is tuned near to resonance ($|\omega_L - \omega_0| \ll \omega_0$). In this case, the rapidly oscillating terms of the Hamiltonian can be neglected, thus the interaction picture Hamiltonian simplifies to

$$\tilde{H}_{int} = \frac{\hbar\Omega_0}{2}\left(\sigma_+ e^{-i\delta t}e^{i\eta(\tilde{a^\dagger}+\tilde{a})} + \sigma_- e^{i\delta t}e^{-i\eta(\tilde{a^\dagger}+\tilde{a})}\right) \tag{2.80}$$

where δ $(=\omega_L - \omega_0)$ is the laser detuning and $\tilde{a}$ $(= ae^{i\omega_z t})$ is the lowering operator in the interaction picture. We have also introduced a term $\eta(= k\sqrt{\hbar/2m\omega_z})$, which appears when we rewrite the spatial part of the electric field in terms of the raising and lowering operators. The

parameter η is called the Lamb-Dicke parameter, which is essentially the product of the size of the ground state wave-function ($\sqrt{\hbar/(2m\omega_z)}$) of the harmonic oscillator and the wave vector of the light field $k = (2\pi/\lambda)$. The parameter η also determines the coupling strength between the internal and external states of the atom. The external states of the atom are the motional states due to the harmonic motion inside the trap, denoted by a state vector $|n\rangle$, where n is harmonic oscillator quantum number.

The generalised state vector of a two-level trapped atomic ion can be defined as an "outer product" ($\otimes$) of the basis states ($|g\rangle, |e\rangle$) and the motional states $|n\rangle$ accounting for the trapping. In the interaction picture, the time-dependent state vector is defined as

$$|\psi_{int}\rangle = \sum_{n=0}^{\infty} C_n(t)\,|g,n\rangle + D_n(t)\,|e,n\rangle\,, \tag{2.81}$$

where $C_n(t)$ and $D_n(t)$ are the time-dependent coefficients and $|g/e,n\rangle = |g/e\rangle \otimes |n\rangle$, is the time independent state vector of a trapped ion. The time-dependent coefficients can be calculated by solving the time-dependent Schrödinger equation in the interaction picture, $\tilde{H}_{int}\,|\psi_{int}\rangle = i\hbar\frac{\mathrm{d}|\psi_{int}\rangle}{\mathrm{d}t}$. Here I will rewrite the Schrödinger equation in the coefficients form giving the final expression as

$$\dot{C}_n(t) = -i^{1-|n'-n|}\frac{\Omega_{n',n}}{2}e^{i\Delta t}D_{n'}(t), \tag{2.82}$$

$$\dot{D}_{n'}(t) = -i^{1+|n'-n|}\frac{\Omega_{n,n'}}{2}e^{-i\Delta t}C_n(t), \tag{2.83}$$

where $\Delta = \omega_L - \omega_0 - l\omega_z$ is the detuning from the l^{th} sideband (i.e. $l = n' - n$). Depending upon the laser detuning from the transition ($|e\rangle \leftrightarrow |g\rangle$), a laser field couples to a particular motional state of the atomic level ($|e\rangle$), and so called red (if $l < 0$) or blue (if $l > 0$) sidebands are generated in a spectrum. The parameter $\Omega_{n',n} = \Omega_0|\,\langle n'|\,e^{i\eta(a+a^\dagger)}\,|n\rangle\,|$ determines the coupling strength between the states $|n\rangle$ and $|n'\rangle$, and is called the Rabi frequency of the l^{th} sideband. The Rabi frequency ($\Omega_{n',n}$) is also written as a function of generalised Laguerre polynomial ($L_n^{|l|}(\eta^2)$) [56, 79]

$$\Omega_{n',n} = \Omega_0 e^{-\eta^2/2}\eta^{|l|}\sqrt{\frac{n_<!}{n_>!}}L_{n_<}^{|l|}(\eta^2). \tag{2.84}$$

where $n_< = n$, $n_> = n + l$ for $l \geq 0$ and vice-versa for $l < 0$. Finally the coupled equations 2.82 and 2.83 can be solved analytically and are expressed in a matrix form as

$$\begin{bmatrix} D_{n'}(t) \\ C_n(t) \end{bmatrix} = \mathcal{M}_{n',n}\begin{bmatrix} D_{n'}(0) \\ C_n(0) \end{bmatrix}, \tag{2.85}$$

where the transformation matrix is given as [79]

$$\mathcal{M}_{n',n} = \begin{bmatrix} e^{-\frac{i\Delta t}{2}}\left\{\cos(\frac{\tilde{\Omega}t}{2}) + i\frac{\Delta}{\tilde{\Omega}}\sin(\frac{\tilde{\Omega}t}{2})\right\} & -i\frac{\Omega_{n',n}}{\tilde{\Omega}}e^{i\left(|n'-n|\frac{\pi}{2}-\frac{\Delta t}{2}\right)}\sin(\frac{\tilde{\Omega}t}{2}) \\ -i\frac{\Omega_{n',n}}{\tilde{\Omega}}e^{-i\left(|n'-n|\frac{\pi}{2}-\frac{\Delta t}{2}\right)}\sin(\frac{\tilde{\Omega}t}{2}) & e^{\frac{i\Delta t}{2}}\left\{\cos(\frac{\tilde{\Omega}t}{2}) - i\frac{\Delta}{\tilde{\Omega}}\sin(\frac{\tilde{\Omega}t}{2})\right\} \end{bmatrix}. \tag{2.86}$$

In the above equation, we have defined a new Rabi frequency $\tilde{\Omega} = \sqrt{\Omega_{n',n}^2 + \Delta^2}$, which denotes the Rabi frequency of the system incorporating the laser detuning from a particular sideband. From equation 2.85 and 2.86, we can interpret the time-evolution of the population between states $|g, n\rangle$ and $|e, n'\rangle$.

2.4.2 Interaction of a trapped ion with a resonant laser field

From the previous discussion, we know that the interaction between the laser and a two-level atom trapped in a harmonic trapping potential creates various resonances. These resonances are well resolved if $\omega_z \gg \Omega_0$ and $\omega_z \gg \Gamma_e$, where Γ_e is the natural decay rate of the atomic state $|e\rangle$. A carrier ($\Delta n = 0$) of the transition is seen when the laser is tuned to the exact frequency spacing of the two-level atom (i.e. $\omega_L = \omega_0$). In this case, the motional state of the atom remains unchanged. In contrast, when the laser is red detuned by an integer multiple of the motional frequency (ω_z); the resonances are called red sidebands. Similarly, the resonances are called blue sidebands if the laser is blue detuned from the transition by integer multiples of the motional frequency. A schematic of motional states of a two-level atom is shown in figure 2.6, where the black arrow, red arrow and blue arrow indicate the carrier, red sideband and blue sideband transitions, respectively.

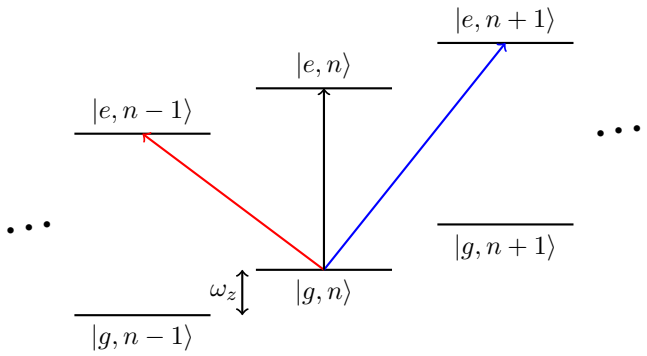


Figure 2.6: Figure shows motional states coupled to the atomic energy levels of a two-level atom. Respective transitions are denoted as carrier ($l = 0$) in black, red sideband ($l < 0$) in red and blue sideband ($l > 0$) in blue.

If the atom is assumed to be in the ground atomic state ($|g, n\rangle$), then the population in the excited state ($|e, n'\rangle$) as a function of the laser interaction time is given as $\sin^2(\Omega_{n',n}t/2)$. In this case, the laser-induced population dynamics shows a pure sinusoidal oscillation at a period determined by $2\pi/\Omega_{n',n}$. On the other hand, if the atom is assumed to be in a thermal equilibrium with a reservoir then the population between the harmonic oscillator states follows a thermally-distributed occupation probability function. In this case, the occupation probability in a particular motional state (n) is determined by an expression given as [79]

$$p(n) = \frac{\langle n \rangle^n}{(\langle n \rangle + 1)^{n+1}} \tag{2.87}$$

where $\langle n \rangle$ is the mean motional state number. The time evolution of the population for a particular sideband $(n' - n)$ for a thermal trapped ion system is expressed as

$$P_{e,n'-n}(t) = \sum_{n=0}^{\infty} p(n) \sin^2(\Omega_{n',n} t/2), \tag{2.88}$$

where the excitation probability will be a statistical mixture of various sinusoidal functions, each with a different oscillation period; hence the outcome is not expected to be sinusoidal.

2.4.3 Lamb-Dicke regime

So far we have considered a general case of sideband excitation, but it is possible to simplify the expressions for the interaction Hamiltonian (equation 2.80) and the coupling strength (equation 2.84), for the situation where the ratio of spatial spread of the wave-function of a trapped atom is much smaller than the wavelength of the electromagnetic field. Essentially, if $\eta\sqrt{\langle (a^\dagger + a)^2 \rangle} = \eta\sqrt{2n+1} \ll 1$, the higher order terms in the interaction Hamiltonian can be neglected and the Hamiltonian can be written in a simpler form. The regime where the above-mentioned condition holds is called the “Lamb-Dicke regime" or simply LDR. The interaction Hamiltonian in this regime is therefore expressed as

$$\tilde{H}_{int} \approx \frac{\hbar\Omega_0}{2} \left(\sigma_+ e^{-i\delta t} \{1 + i\eta(\tilde{a}^\dagger + \tilde{a})\} + H.c. \right), \tag{2.89}$$

where higher order terms of η are neglected. In this situation only up to first order terms of η are significant, hence only up to first order resonances should be visible. The excitation strength of the carrier, first red and first blue sidebands can be approximated as

$$\Omega_{car} = \left(1 - \eta^2(n + \frac{1}{2})\right) \Omega_0, \tag{2.90}$$

$$\Omega_{rsb} = \sqrt{n}\eta\Omega_0, \tag{2.91}$$

$$\Omega_{bsb} = \sqrt{n+1}\eta\Omega_0, \tag{2.92}$$

respectively. The Lamb-Dicke approximation is a very important handle to set-up the laser-ion interaction terms for a quantum gate operation such as in the Mølmer-Sørensen [48] and Cirac-Zoller gates [47].

2.4.4 Interactions with a non-resonant laser field

If the laser is not tuned to the carrier transition then the AC-Stark effect shifts the atomic energy level from its original position [80]. The effect is prominent while exciting the motional sidebands, where the excitation strength is weaker than the carrier transition and requires high laser power in order to observe the resonances. It is crucial to compensate for the AC-Stark shift [81] and off-resonant excitations in order to perform coherent dynamics on a motional side-

band[6]. After assuming the laser field is detuned from the carrier transition by $\delta = \omega_L - \omega_0$, the Hamiltonian for a free two-level atom with the Rabi frequency Ω_0 in the rotating wave picture (dressed state representation) can be written as

$$\tilde{H}_{\text{Stark}} = \frac{\hbar\delta}{2}\sigma_z + \frac{\hbar\Omega_0}{2}(\sigma_+ + \sigma_-). \tag{2.93}$$

In principle, it is possible to choose a basis a where the state vector rotates at the frequency of the electromagnetic radiation, which eliminates the time dependence of the Hamiltonian [80]. In this representation, the eigenvalues of the system come to be

$$\begin{aligned} E_{\text{Stark}} &= \pm\sqrt{\frac{\hbar^2\Omega_0^2}{4} + \frac{\hbar^2\delta^2}{4}}, \\ &= \pm\left(\frac{\hbar\delta}{2} + \frac{\hbar\Omega_0^2}{4\delta}\right) \text{ when } \delta \gg \Omega_0. \end{aligned} \tag{2.94}$$

In the dressed state representation, the extra frequency shift, which arises due to the light shift, is $\frac{\Omega_0^2}{2\delta}$ for the case when $\delta \gg \Omega_0$. However, when the detuning is zero, the energy levels in the dressed state picture split into two eigenstates $\pm\Omega_0/2$. The splitting of energy levels in the presence of a resonant field is called the Autler-Townes splitting [82]. Note that the calculated shift in a far-detuned case is proportional to the square of the Rabi frequency of the transition, hence the shift for the sidebands will be insignificant due to the weak coupling. If the laser parameters are chosen such that the detuning is small or the Rabi frequency is large then the shift will be significant and must be taken into account while performing any coherent control using laser radiation. In our system, the typical Rabi frequency of the 729-nm transition is 40 kHz and the motional frequency is $100 - 400$ kHz, for which the AC-Stark shift will be $8 - 2$ kHz. In this situation, if the motional sidebands are interrogated with the laser radiation then radiation will shift the carrier transition; hence the sidebands transitions will shift as well. In our system, the effects are more prominent while performing sideband cooling, where the 854-nm laser radiation also shifts the $D_{5/2}$ energy level by typically 40 kHz.

Apart from the shift in the transition frequency due to a non-resonant laser field, a part of the population is sometimes excited, undesirably, by the nearby sidebands while the laser is tuned to a desired motional sideband. This happens due to the finite excitation strength of a particular motional sideband near the relevant transition. For example, the off-resonant carrier excitation probability (directly from equation 2.80) for a detuning Δ is

$$P_e(t) = \frac{\Omega_0^2}{\Omega_0^2 + \Delta^2}\sin^2\left(\frac{t\sqrt{\Omega_0^2 + \Delta^2}}{2}\right). \tag{2.95}$$

Typically, at $\omega_z = 2\pi \times 400$ kHz, $\Omega_0 = 2\pi \times 40$ kHz and $\Delta = \pm\omega_z$ the off-resonant carrier excitation gives 0.5% amplitude oscillation at a frequency $\sim \omega_z$. The off-resonant excitation leads to poor fidelity of the coherent control in trapped atomic ion systems. In order to get high

[6]The prominent effect will be seen when a laser is tuned to the first red or first blue sideband. In this case, the AC-Stark effect moves the carrier from its actual frequency position, thus the sidebands also move.

fidelity operations one needs to avoid or compensate for off-resonant excitations.

2.4.5 Laser-ion interaction for a two-ion Coulomb crystal

In order to analyse the spectrum for the two-ion case, it important to discuss the interaction between the laser beam and trapped ions. In this case, the sideband interaction is not straightforward due to the entanglement between internal and external states of the ions. Suppose each ion is a two-level atomic system, where the internal states of the j^{th} ion are denoted by $|\mathrm{e}_j\rangle$ and $|\mathrm{g}_j\rangle$. For identical ions, the motional Hamiltonian is expressed as

$$H_m = \frac{p_1^2}{2m} + \frac{1}{2}m\omega_z^2 z_1^2 + \frac{p_2^2}{2m} + \frac{1}{2}m\omega_z^2 z_2^2 + \frac{1}{4\pi\epsilon_0}\frac{q^2}{r_{12}}, \tag{2.96}$$

where p_j and z_j are the momentum and position coordinates of the j^{th} ion. Similarly, the electronic part of the Hamiltonian in the two-ion case is expressed as

$$H_e = \frac{\hbar\omega_0}{2}(\sigma_z^{(1)} + \sigma_z^{(2)}). \tag{2.97}$$

After following the previous discussion of the laser-ion interaction, the Hamiltonian is given as

$$H_I = \sum_{j=1}^{2} \frac{\hbar\Omega_0}{2}(e^{i(\omega_l t - kz_j)} + e^{-i(\omega_l t - kz_j)})(\sigma_+^{(j)} + \sigma_-^{(j)}), \tag{2.98}$$

where the parameters retain the same meaning as discussed in chapter 2. The quantum treatment of the motion will be used to describe the motional part of the Hamiltonian, which will be expressed in terms of COM and breathing modes. The motional part of the Hamiltonian in terms of the axial normal modes is expressed as

$$H_m = \hbar\omega_z(a^\dagger a + 1/2) + \hbar\omega_b(b^\dagger b + 1/2), \tag{2.99}$$

where a and b are the lowering operators for the COM and the breathing modes, respectively.

The total Hamiltonian of the system is given as $H = H_e + H_m + H_I$. After transforming into the interaction picture using a unitary operator ($U_0 = e^{i(H_m + H_e)t/\hbar}$), the interaction part of the Hamiltonian becomes

$$\begin{aligned}\hat{H}_I &= U_0^\dagger H_I U_0, \\ &= e^{-iH_m t/\hbar} e^{-iH_e t/\hbar} \sum_{j=1}^{2} \frac{\hbar\Omega_0}{2}(e^{i(\omega_l t - kz_j)} + e^{-i(\omega_l t - kz_j)}) \\ &\times (\sigma_+^{(j)} + \sigma_-^{(j)}) e^{iH_m t/\hbar} e^{iH_e t/\hbar},\end{aligned} \tag{2.100}$$

where I assume that both ions simultaneously interact with the laser field of frequency ω_l. The

above expression further simplifies to

$$\begin{aligned}\hat{H}_I = \frac{\hbar\Omega_0}{2}\sum_{j=1}^{2}\big[(\sigma_+^{(j)}e^{-\omega_0 t} + \sigma_-^{(j)}e^{i\omega_0 t})e^{-iH_m t/\hbar} \\ \times (e^{-ikz_j}e^{i\omega_l t} + e^{ikz_j}e^{-i\omega_l t})e^{iH_m t/\hbar}\big].\end{aligned} \tag{2.101}$$

At this stage we can replace the position coordinates z_1 and z_2 with their normal mode counterparts. Let us define the normal coordinates, $Z_c = (z_1 + z_2)/2$ and $Z_b = z_1 - z_2$. After making the above replacement and adapting the rotating wave approximation, the interaction Hamiltonian is expressed as

$$\begin{aligned}\hat{H}_I &= \frac{\hbar\Omega_0}{2}\sum_{j=1}^{2}\left[(\sigma_+^{(j)}e^{-i\delta t})e^{-iH_m t/\hbar}e^{-ik(2Z_c+(-1)^j Z_b)}e^{iH_m t/\hbar}\right] + h.c. \\ &= \frac{\hbar\Omega_0}{2}\sum_{j=1}^{2}\sigma_+^{(j)}e^{-i\delta t}e^{-iH_m t/\hbar}\left[e^{-i\eta_c(a^\dagger+a)}e^{-i(-1)^j\eta_b(b^\dagger+b)}\right]e^{iH_m t/\hbar} + h.c.\end{aligned} \tag{2.102}$$

where η_c and η_b are the L-D parameters corresponding to the COM and breathing modes, and $\delta = \omega_l - \omega_0$. The L-D parameters are defined as $\eta_c = \eta_0/\sqrt{2}$ and $\eta_b = \eta_0/\sqrt{2\sqrt{3}}$ [83] for the COM and breathing modes, respectively. After replacing the raising and lowering operators, $a^\dagger$ and a, with their interaction-picture version $\tilde{a}^\dagger$ and $\tilde{a}$, and making the rotating wave approximations, the interaction Hamiltonian simplifies to

$$\hat{H}_I = \frac{\hbar\Omega_0}{2}\sum_{j=1}^{2}\sigma_+^{(j)}e^{-i\delta t}[e^{-i\eta_c(\tilde{a}^\dagger+\tilde{a})}e^{-i(-1)^j\eta_b(\tilde{b}^\dagger+\tilde{b})}] + h.c.. \tag{2.103}$$

Let us insert the motional states projection operator $|n\rangle\langle n|$. The Hamiltonian is then expressed as

$$\hat{H}_I = \frac{\hbar\Omega}{2}\sum_{n,n,k',k}\sum_{j=1}^{2}\sigma_+^{(j)}e^{-i\delta t}\left[|n'\rangle\langle n'|\, e^{-i\eta_c(\tilde{a}^\dagger+\tilde{a})}\,|n\rangle\langle n|\,|k'\rangle\langle k'|\, e^{-i(-1)^j\eta_b(\tilde{b}^\dagger+\tilde{b})}\,|k\rangle\langle k|\right] + h.c., \tag{2.104}$$

where n and k are used to indicate the motional states corresponding to the COM and the breathing motional modes. The middle part of the above equation will be replaced by $\Omega_{n',n}e^{-i\Delta n\omega_z}\times \Omega_{k',k}e^{-i\Delta k\omega_b}$, where $\Omega_{n',n}$ and $\Omega_{k',k}$ are defined as the normalised Rabi strengths for the respective sidebands. The interaction Hamiltonian can then be further simplified to

$$\hat{H}_I = \frac{\hbar\Omega}{2}\sum_{j=1}^{2}\sigma_+^{(j)}e^{-i\delta t}[|n'\rangle\langle n|\,\Omega_{n',n}e^{-i\Delta n\omega_z}\,|k'\rangle\langle k|\,\Omega_{k',k}e^{-i\Delta k\omega_B}(-1)^j] + h.c. \tag{2.105}$$

where $\Delta n = n' - n$ and $\Delta k = k' - k$.

From the above Hamiltonian, the time evolution of the population between the internal

and external states of two ions can be determined by solving with respect to appropriate basis vectors. Let us assume that the basis vectors for the blue sideband for the COM motion are $|g_1, g_2, n, k\rangle$, $|e_1, g_2, n+1, k\rangle$, $|g_1, e_2, n+1, k\rangle$ and $|e_1, e_2, n+2, k\rangle$, then the wave function for the blue sideband is defined as

$$|\psi\rangle = C_1 |g_1, g_2, n, k\rangle + C_2 |e_1, g_2, n+1, k\rangle + C_3 |g_1, e_2, n+1, k\rangle + C_4 |e_1, e_2, n+2, k\rangle , \quad (2.106)$$

where C_l is the coefficient of the respective basis state. The interaction Hamiltonian in the matrix form for the above state vectors is expressed as

$$H_{BSB} = \frac{i\Omega_0\hbar}{2}\Omega_k, k \begin{pmatrix} 0 & e^{-\mathrm{i}\Delta_1 t}\Omega_{n+1,n} & e^{-\mathrm{i}\Delta_2 t}\Omega_{n+1,n} & 0 \\ -e^{\mathrm{i}\Delta_1 t}\Omega_{n,n+1} & 0 & 0 & e^{-\mathrm{i}\Delta_2 t}\Omega_{n+2,n+1} \\ -e^{-\mathrm{i}\Delta_2 t}\Omega_{n,n+1} & 0 & 0 & e^{-\mathrm{i}\Delta_1 t}\Omega_{n+2,n+1} \\ 0 & -e^{\mathrm{i}\Delta_2 t}\Omega_{n+1,n+2} & -e^{\mathrm{i}\Delta_1 t}\Omega_{n+1,n+2} & 0 \end{pmatrix} \quad (2.107)$$

which can be used to numerically solve the Schrödinger equation for the blue sideband of the transition to give the time evolution after the laser interaction time t. The similar treatment can be employed for the other sidebands as well. The state vectors for the carrier transition can be written as $|g_1, g_2, n, k\rangle$, $|e_1, g_2, n, k\rangle$, $|g_1, e_2, n, k\rangle$ and $|e_1, e_2, n, k\rangle$, The interaction Hamiltonian in matrix form is written as

$$H_{Car} = \frac{\Omega_0\hbar}{2}\Omega_{k,k}\Omega_{n,n} \begin{pmatrix} 0 & e^{-\mathrm{i}\Delta_1 t} & e^{-\mathrm{i}\Delta_2 t} & 0 \\ e^{\mathrm{i}\Delta_1 t} & 0 & 0 & e^{-\mathrm{i}\Delta_2 t} \\ e^{\mathrm{i}\Delta_2 t} & 0 & 0 & e^{-\mathrm{i}\Delta_1 t} \\ 0 & e^{\mathrm{i}\Delta_2 t} & e^{\mathrm{i}\Delta_1 t} & 0 \end{pmatrix} \quad (2.108)$$

where $\Delta_1 = \omega_l - \omega_0^{(1)}$ and $\Delta_2 = \omega_l - \omega_0^{(2)}$. At this stage, the time-dependent Schrödinger equation will be used to calculate the excitation probability between the excited and ground state of the ion. For the carrier transition, the excited state probability of both ions $P(e_1, e_2)$ comes to be $P(e_1) \times P(e_2)$, hence each ion can be treated independent to each other. However, the same does not apply to the sideband transitions, where the entanglement between the internal and external states must be taken into account. In this case, the only possible method to solve the time-dependent Schrödinger for the above described Hamiltonian is through numerical ways. The sideband cooling results of a two-ion chain and a two-ion disc will be analysed using this method. After making proper adjustments of the L-D parameter and the motional frequencies, the above treatment will be applicable for the planar case too.

Chapter 3

Laser cooling of ions in a Penning trap

Laser cooling utilises radiation pressure as a resistive force on an atom to bring it to rest. Laser cooling of atoms or atomic ions was first proposed in 1975 independently by Hänsch et al. [34] and Wineland et al. [35]. The first experimental realisation of laser cooling was carried out with trapped atomic ions in 1978 by Neuhauser et al. [36] and Wineland et al. [37]. Since then laser cooling is routinely used to prepare ultra-cold atomic systems. Doppler cooling is one of the most used laser cooling techniques to slow down the motion of neutral atoms or atomic ions, especially for pre-cooling purposes. In Doppler cooling, the red-detuned laser photons preferentially get absorbed by the atoms which are moving in the opposite direction of the laser beam propagation. In this case, the Doppler effect provides a frequency shift to the atomic transition and brings the atomic transition in resonance with the laser photons. Eventually, continuous absorption and re-emission cycles cool the atoms to their Doppler limit ($\hbar\gamma/2k_B$) [84]. In this chapter, I will discuss Doppler laser cooling and sideband cooling of ions in a Penning trap.

3.1 Doppler cooling in a Penning trap

In trapped ion systems, due to the additional trapping fields, Doppler cooling is not as simple as for a free atom. In particular, in a Penning trap, Doppler cooling needs to consider the effect of the electric de-trapping force in the radial direction. In this case, a simple red-detuned laser beam, which is used to reduce the kinetic energy of the ion, increases the magnetron radius and eventually the ion goes into a big magnetron orbit around the trap centre. However, with proper beam positioning and detuning of the Doppler cooling laser beam, one can reduce the magnetron radius and eventually the ion can be brought to rest at the trap centre. A detailed description of laser cooling in a Penning trap is given by Itano et al. [40]. In this section, I will follow their methodology to illustrate the laser cooling in a Penning trap and I will also derive an expression for the Doppler cooling limit of trapped ions in a Penning trap.

In this review of Doppler cooling, I will assume a weak binding case, $\omega_z \ll \gamma_s \ll \omega_0$, where

ω_z is the motional frequency, γ_s is the natural linewidth of the transition and ω_0 is the transition frequency of the atom. For simplicity, I will also treat the laser cooling with two individual laser beams, one along the magnetic field axis and one along the axis perpendicular to the magnetic field. This scenario is analogous to Doppler cooling of trapped ions in our laboratory, where we cool radial and axial motion with two individual laser beams.

Let us assume that the electric field component of the electromagnetic wave travelling along the unit vector $\mathbf{k}/k$ is $\mathbf{E} = E_0\hat{\epsilon}\cos(\omega_L t - \mathbf{k}\cdot\mathbf{r})$. If an atomic ion absorbs a photon with momentum $\hbar\mathbf{k}$ followed by re-emission at $\hbar\mathbf{k}'$, then each scattering event will change the momentum of the ion by $\hbar(\mathbf{k}-\mathbf{k}')$. Thus, the change in the velocity is $\Delta\mathbf{v} = \hbar(\mathbf{k}-\mathbf{k}')/m$. Suppose A_j is the amplitude of motion before the scattering event (at time t) and A'_j is the amplitude after the scattering event (at time t_i). The change in the amplitude of motion after the scattering event is given as

$$\Delta A_z^2 = \left(\frac{\Delta v_z}{\omega_z}\right)^2 - \frac{2A_z\Delta v_z}{\omega_z}\sin(\omega_z t_i + \phi_z), \tag{3.1}$$

$$\Delta A_-^2 = \frac{(\Delta v_x)^2 + (\Delta v_y)^2}{4\omega_1^2} + \frac{A_-}{\omega_1}\left[\Delta v_x \sin(\omega_- t_i + \phi_-) + \Delta v_y \cos(\omega_- t_i + \phi_-)\right], \tag{3.2}$$

$$\Delta A_+^2 = \frac{(\Delta v_x)^2 + (\Delta v_y)^2}{4\omega_1^2} - \frac{A_+}{\omega_1}\left[\Delta v_x \sin(\omega_+ t_i + \phi_+) + \Delta v_y \cos(\omega_+ t_i + \phi_+)\right]. \tag{3.3}$$

The above equations have been derived from equations 2.7, 2.11, 2.12 and their time derivatives. From equation 3.1, it may be concluded that the motion along the axial direction can be reduced if the change in the velocity is negative, or more precisely if $\mathbf{\Delta v_z}$ is opposite to the direction of motion. Similarly, for the modified cyclotron motion, the square of the amplitude decreases if the change in velocity is opposite to the direction of the circular motion. However, the square of the amplitude for the magnetron motion decreases only if the change in velocity is in the direction of motion (when $\mathbf{v}_-$ and $\mathbf{\Delta v}_-$ are parallel to each other).

For the modified cyclotron and axial motion, cooling requirement can be met if the ion is compelled to absorb the photons only when the ion moves opposite to the laser beam propagation. This can be achieved with a red-detuned laser beam with the wave-vector along the axis of motion. The Doppler effect allows the absorption only if the motion is opposite to the direction of laser propagation. Furthermore, we will see that the magnetron motion can be cooled with the same beam that is used to cool the modified cyclotron motion provided the beam is placed slightly off-centre on the radial plane.

In principle, the motion in all three directions can be cooled with a single non-uniform laser beam, provided the laser beam forms an oblique angle to the magnetic field axis [40]. However, throughout this thesis, I will consider two non-uniform laser beams. We will see that the beam along the x-axis should be able to cool the magnetron and modified cyclotron motion simultaneously. Let us assume a Gaussian-shaped laser beam is used to cool the axial motion and the laser propagation is along the axial direction. If the amplitude of the radial motion is much smaller than the axial beam waist (w_z), then the beam along the axial direction can be assumed to have

a uniform intensity I_{z0}. To accomplish laser cooling of the magnetron and modified cyclotron modes, a non-uniform laser beam with offset y_0, laser frequency ω_L and a peak intensity I_{x0} is considered to be travelling along the wave-vector $\mathbf{k}_x = k_x\hat{x}$. Again if the amplitude of the radial motion is much smaller than the beam waist (w_x), the intensity profile can be approximated to $I(y) = I_{x0}(1+y/y_0)$. A schematic of a laser beam with some offset from the trap centre is shown in figure 3.1.

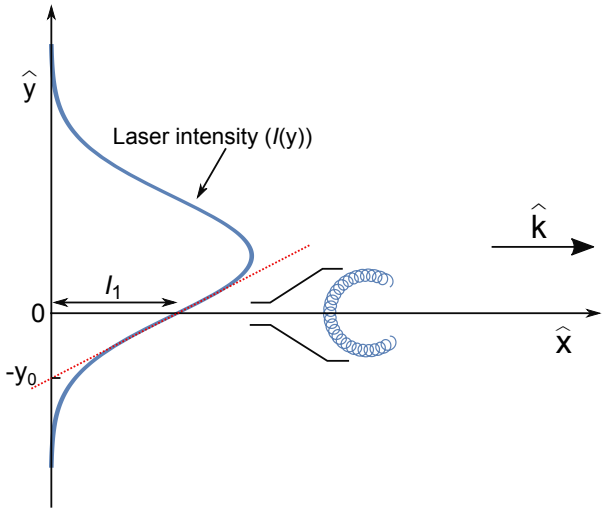


Figure 3.1: Figure showing ion motion in the radial plane and red-detuned beam offset from the trap centre and its profile. The beam offset method is adapted to cool both radial modes simultaneously.

The interaction of electromagnetic radiation with a two-level atom has been well studied before and it can also be found in the previous chapter. Suppose a two-level trapped ion interacts with a laser photon with wave-vector $\mathbf{k}$ and detuning $\delta_L(=\omega_L-\omega_0)$ through a dipole-allowed transition. The photon scattering rate of the ion, moving at a velocity $\mathbf{v}$, is given as

$$R = \frac{s_0|\hat{\epsilon}_L\cdot\hat{\mathbf{D}}|^2\gamma_s^3/2}{(1+s_0)\gamma_s^2+4(-\mathbf{k}\cdot\mathbf{v}+\delta_L)^2}, \tag{3.4}$$

where γ_s is the transition rate and $s_0(=I/I_s)$ is the saturation parameter of the atom. For the low saturation case, where the intensity (I) is assumed to be well below the saturation intensity $I_s = \frac{\pi hc\gamma_s}{3\lambda^3}$, the steady-state scattering rate is given as

$$R = \frac{s_0|\hat{\epsilon}_L\cdot\hat{\mathbf{D}}|^2\gamma_s^3/2}{\gamma_s^2+4(-\mathbf{k}\cdot\mathbf{v}+\delta_L)^2}, \tag{3.5}$$

$$= \frac{I}{\hbar\omega_l}\frac{\sigma_0\gamma_s^2}{(\gamma_s^2+4(\delta_L-\mathbf{k}\cdot\mathbf{v})^2}. \tag{3.6}$$

In the above equation, $\sigma_0 = \frac{3\lambda^2}{2\pi}|\hat{\epsilon}_L\cdot\hat{\mathbf{D}}|^2$ and ϵ_L is the polarisation direction of the laser beam. Subsequently, the average rate of change of the square of the amplitude can be expressed in terms of the product of amplitude squared and the respective scattering rates. After multiplying

both terms together, the rate of change of the square of the amplitude is expressed as

$$\frac{\mathrm{d}\langle A_z^2\rangle}{\mathrm{d}t} = \frac{I_{z0}}{\hbar\omega_{Lz}}\left\langle \frac{\sigma_{z0}\gamma_s^2\Delta A_z^2}{\gamma_s^2+4(\delta_L-\mathbf{k_z}\cdot\mathbf{v})^2}\right\rangle + \frac{I_{x0}}{\hbar\omega_{Lx}}\left\langle \left(1+\frac{y}{y_0}\right)\frac{\sigma_{x0}\gamma_s^2\Delta A_z^2}{\gamma_s^2+4(\delta_L-\mathbf{k_x}\cdot\mathbf{v})^2}\right\rangle, \tag{3.7}$$

$$\frac{\mathrm{d}\langle A_i^2\rangle}{\mathrm{d}t} = \frac{I_{x0}}{\hbar\omega_{Lx}}\left\langle \left(1+\frac{y}{y_0}\right)\frac{\sigma_{x0}\gamma_s^2\Delta A_i^2}{\gamma_s^2+4(\delta_L-\mathbf{k_x}\cdot\mathbf{v})^2}\right\rangle + \frac{I_{x0}}{\hbar\omega_{Lx}}\left\langle \frac{\sigma_{x0}\gamma_s^2\Delta A_i^2}{\gamma_s^2+4(\delta_L-\mathbf{k_z}\cdot\mathbf{v})^2}\right\rangle, \tag{3.8}$$

where i indicates the magnetron and modified cyclotron motion. The second term in the equations is inserted there to account for the recoil effects on the atom due to the scattering of photons from the other laser beam. After taking the Taylor expansion in the limit of $(\mathbf{k}\cdot\mathbf{v})^2 \ll \gamma_s^2+4\delta_L^2$, the above equations simplify to

$$\frac{\mathrm{d}\langle A_z^2\rangle}{\mathrm{d}t} = R_z\left\langle\left(1+\frac{8\delta_L(\mathbf{k}_z\cdot\mathbf{v})}{\gamma_s^2+4\delta_L^2}\right)\Delta A_z^2\right\rangle + R_x\left\langle\left(1+\frac{y}{y_0}\right)\left(1+\frac{8\delta_L(\mathbf{k}_x\cdot\mathbf{v})}{\gamma_s^2+4\delta_L^2}\right)\Delta A_z^2\right\rangle, \tag{3.9}$$

$$\frac{\mathrm{d}\langle A_i^2\rangle}{\mathrm{d}t} = R_x\left\langle\left(1+\frac{y}{y_0}\right)\left(1+\frac{8\delta_L(\mathbf{k}_x\cdot\mathbf{v})}{\gamma_s^2+4\delta_L^2}\right)\Delta A_i^2\right\rangle + R_z\left\langle\left(1+\frac{8\delta_L(\mathbf{k}_z\cdot\mathbf{v})}{\gamma_s^2+4\delta_L^2}\right)\Delta A_i^2\right\rangle, \tag{3.10}$$

where $R_{(j=z,+,-)} = \frac{I_{j0}}{\hbar\omega_{Lj}}\frac{\sigma_{j0}\gamma_s^2}{\gamma_s^2+4\delta_L^2}$. After making substitutions from equations 3.1, 3.2 and 3.3, the rate equations are rewritten as

$$\frac{\mathrm{d}\langle A_z^2\rangle}{\mathrm{d}t} = 8R_z\frac{\hbar k_z^2\delta_L}{m(\gamma_s^2+4\delta_L^2)}\langle A_z^2\rangle + \frac{R_z\hbar^2k_z^2}{m^2\omega_z^2}\left\{1+(1+R_x/R_z)f_{sz}\right\}, \tag{3.11}$$

$$\frac{\mathrm{d}\langle A_+^2\rangle}{\mathrm{d}t} = \frac{R_x\hbar k_x}{2m\omega_1 y_0}\langle A_+^2\rangle + \frac{4R_x\delta_L\hbar k_x^2\omega_+\langle A_+^2\rangle}{m\omega_1(\gamma_s^2+4\delta_L^2)} + R_x\frac{\hbar^2k_x^2}{4m^2\omega_1^2}\left\{1+(1+R_z/R_x)(f_{sx}+f_{sy})\right\}, \tag{3.12}$$

$$\frac{\mathrm{d}\langle A_-^2\rangle}{\mathrm{d}t} = -\frac{R_x\hbar k_x}{2m\omega_1 y_0}\langle A_-^2\rangle - \frac{4R_x\delta_L\hbar k_x^2\omega_+\langle A_-^2\rangle}{m\omega_1(\gamma_s^2+4\delta_L^2)} + R_x\frac{\hbar^2k_x^2}{4m^2\omega_1^2}\left\{1+(1+R_z/R_x)(f_{sx}+f_{sy})\right\}, \tag{3.13}$$

where f_{sx}, f_{sy} and f_{sz} are parameters to account for the re-emitted photon distribution along the x, y and z directions, respectively.

From the above equations, it is apparent that by proper choice of laser detuning and beam offset, one can achieve simultaneous cooling of motion in all three directions with only two laser beams. We can see that, in equation 3.11, if the detuning (δ_L) is negative the first term shows the reduction of the mean square amplitude of the axial motion. In contrast, the positive sign of the second term leads to heating of the motion, which is due to recoil effects. Similarly, the second term in equation 3.12 is responsible for cooling of the modified cyclotron mode. Other than that, the first and third terms show heating caused by the gradient cooling and recoil effects. The magnetron motion will be cooled by the gradient term (first term in equation 3.13). However, the detuning and recoil terms will cause heating of the magnetron motion. In order to achieve the simultaneous cooling of the magnetron and modified cyclotron modes one needs to satisfy

$$\omega_- < -\frac{\gamma_s^2+4\delta_L^2}{8k_x y_0\delta_L} < \omega_+, \tag{3.14}$$

which holds only for the negative detuning ($\delta_L < 0$) and the positive beam offset ($y_0 > 0$). If the laser is red-detuned by $\gamma_s/2$ from the transition (at half the transition linewidth) then the equilibrium mean square amplitude of the motional modes come to be

$$\langle A_z^2 \rangle = \frac{5\hbar\gamma_s}{6m\omega_z^2}, \tag{3.15}$$
$$\langle A_+^2 \rangle = \frac{7\hbar\gamma_s}{12m\omega_1\omega_+}\left[1 - \frac{\gamma_s}{2k_x y_0 \omega_+}\right]^{-1},$$
$$\langle A_-^2 \rangle = \frac{7\hbar\gamma_s}{12m\omega_1\omega_-}\left[\frac{\gamma_s}{2k_x y_0 \omega_-} - 1\right]^{-1},$$

where $f_{sx} = f_{sy} = f_{sz} = 1/3$ are the emission cross sections in the radial and axial directions respectively for an electric dipole allowed transition, between Zeeman sub-levels of excited and ground states $\Delta m_j = 0, \pm 1$. Therefore the mean phonon number for radial motion and axial motion after Doppler cooling is given as

$$\langle n_z \rangle = \frac{5\gamma_s}{12\omega_z}, \tag{3.16}$$
$$\langle n_+ \rangle = \frac{7\gamma_s}{12\omega_+}\left[1 - \frac{\gamma_s}{2k_x y_0 \omega_+}\right]^{-1}, \tag{3.17}$$
$$\langle n_- \rangle = \frac{7\gamma_s}{12\omega_-}\left[\frac{\gamma_s}{2k_x y_0 \omega_-} - 1\right]^{-1}, \tag{3.18}$$

where $\langle n_z \rangle$, $\langle n_+ \rangle$ and $\langle n_- \rangle$ are the mean phonon numbers corresponding to the axial, modified cyclotron and magnetron modes, respectively. The theoretical limit of $\langle n \rangle$ of the radial motion in our Penning trap is calculated using the above expressions and corresponding plots are shown in figure 3.2. The cooling limits are calculated for $y_0 = 20$ μm and 1.9 T magnetic field. At a given value of y_0, the $\langle n_+ \rangle$ increases but very slowly with increasing ω_z. On the other hand, the Doppler limit for the negative energy mode rises exponentially with the increasing value of ω_z and this is noted in figure 3.2. Note that at ω_z = 200 kHz, $\langle n_- \rangle$ is calculated to be roughly 2000, which corresponds to tens of μm spread in the radial plane. Such a large spread is not used for any experimental studies in our apparatus. In principle, $\langle n_- \rangle$ can be reduced by choosing a tightly focused laser beam (smaller y_0). A plot showing $\langle n \rangle$ at $y_0 = 10$ μm indicates that the magnetron mean phonon number can be reduced by an order of magnitude. The current thesis shows the results of cooling with the laser beam waist of w_0 = 100 μm ($y_0 = 50$ μm). Experimentally, at this beam waist, cooling can be achieved only for $\omega_z < 100$ kHz. For higher values of ω_z, an alternative cooling method is employed alongside the gradient Doppler cooling method. This alternative way of laser cooling will be discussed in the following section.

3.2 Axialisation

Alternatively, it is possible to laser cool the magnetron motion when a time-varying quadrupole potential is applied in the radial plane, at the cyclotron frequency (ω_c). In this technique, the time-varying quadrupole potential couples both radial motional modes and eventually the

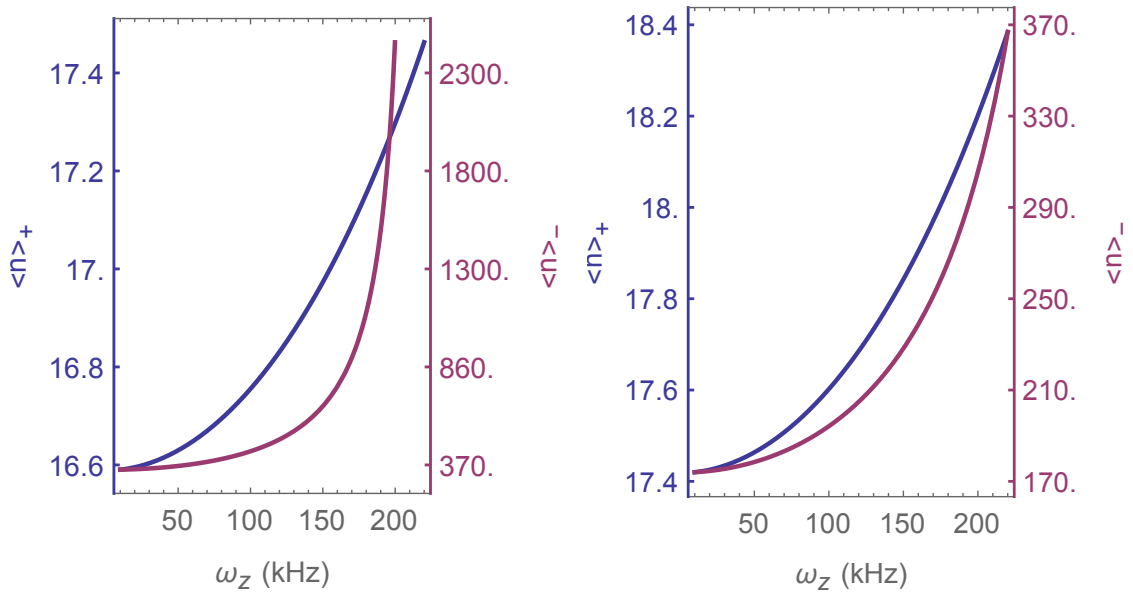


Figure 3.2: A plot showing $\langle n_+ \rangle$ and $\langle n_- \rangle$ as a function of applied axial frequency at $y_0 = 20$ μm (left) and $y_0 = 10$ μm (right).

coupling reduces the amplitude of the magnetron mode when the modified cyclotron mode is laser-cooled. The technique is called axialisation. This technique was initially employed in Penning traps to avoid ion loss during buffer gas cooling of trapped ions [85, 86]. A detailed description of axialisation based cooling is given in reference [87]. In this section, I will review the axialisation technique for laser cooling and I will set up the equations of motion for an ion in the presence of a Doppler cooling laser along with the axialisation fields.

In this technique, the ring electrode is split into four segments and a time-varying potential is applied to each electrode while maintaining the opposite phase with adjacent electrodes. This creates a quadrupole potential in the radial plane, which is expressed as

$$\phi = \frac{V_{rf}}{2r_0^2}(x^2 - y^2)\cos\omega_c t, \tag{3.19}$$

where V_{rf} is the amplitude and r_0 is the characteristic trap dimension (radius of the ring electrode). The principle of axialisation-based cooling can be understood more elegantly in a rotating frame (ω_r). In the rotating frame, the axialisation potential is expressed as

$$\phi = \frac{V_{rf}}{4r_0^2}(r')^2\{\cos(2\theta' + (2\omega_r - \omega_c)t) + \cos(2\theta' + (2\omega_r + \omega_c)t)\}, \tag{3.20}$$

where r' and θ' are the cylindrical position coordinates in the rotating frame of reference. Interestingly, if the angular frequency of the rotating frame is assumed to be $\omega_c/2$, the first term in the expression becomes static and the second term varies at $2\omega_c$ frequency. The time-varying part of the potential can be dropped by making rotating wave approximations.

Also from the previous chapter, we know that the radial motion in this rotating frame can

be treated as a 2D isotropic simple harmonic oscillator with angular frequency $\omega_1 = \sqrt{\frac{\omega_c^2}{4} - \frac{\omega_z^2}{2}}$. The actual rotation due to the magnetron motion and modified cyclotron motion in the rotating frame can be treated as two clockwise and anticlockwise rotations at $\pm\omega_1$ frequencies. Intuitively, the sum of these frequencies in the rotating frame is zero. Therefore the situation can be correlated to the static part of the potential in equation 3.20 and it can be said that the axialisation potential couples both rotations in the rotating frame.

The sum of the modified cyclotron and magnetron frequencies is nothing but the true cyclotron frequency in the laboratory frame, hence the axialisation field (at $\omega_c = \omega_+ + \omega_-$) becomes in resonance with the coupled modified cyclotron motion and magnetron motion. This coupling becomes more interesting if there is a damping term due to laser cooling, which eventually reduces the overall radial motion. A numerical solution of radial motion in a Penning trap in the presence of the axialisation potential and damping due to Doppler cooling is shown in figure 3.3. Note that the reduction of amplitude of both modes depicts simultaneous cooling of both modes. This technique allows us to cool the radial motion in the regime where gradient laser cooling does not work efficiently.

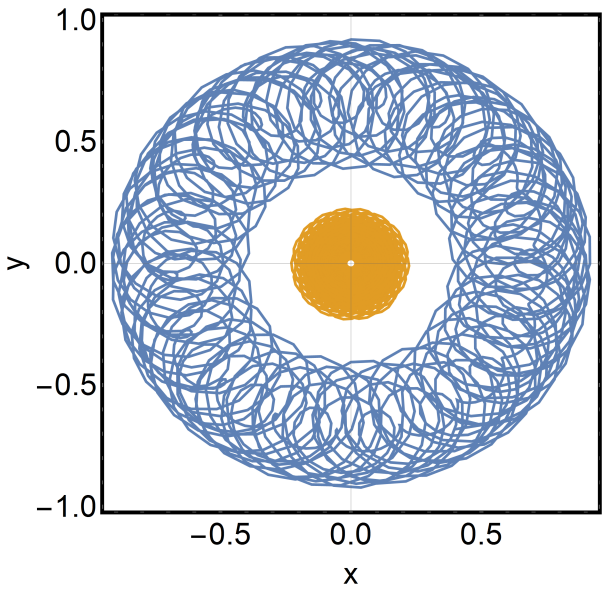


Figure 3.3: Simulated trajectories of the radial motion showing the reduction of the motion of an ion in the presence of axialisation field and Doppler cooling laser radiation in a Penning trap. Blue trajectory corresponds to the motion at an initial time and orange corresponds to at 500 μs time. The simulated plot is for illustration purpose and the parameters are chosen from our general experimental conditions.

Studies of laser cooling in the presence of an additional axialisation field have been carried out by various people [85–87]. They predict cooling in the presence of the axialisation field, even in the regime where gradient cooling shows poor behaviour. So far no direct expression for the cooling limit in the presence of the axialisation has been found. In principle, the cooling limit can be calculated by following the approach adopted by Itano et al. [40], where they find an analytical expression by solving the rate equations for the amplitude of the motion. But in the presence of the axialisation field, the equations become inseparable, hence it is difficult to find

an analytical expression for the cooling limit. In order to find out the cooling limit, a numerical approach can be viable.

In order to infer the cooling limit, let us assume that the laser beam is travelling along the x-axis. The equations of motion of the radial motion in the presence of the axialisation field and the Doppler cooling laser can be written as

$$\frac{\mathrm{d}x}{\mathrm{d}t} = v_x(t) + \zeta_x(t), \tag{3.21}$$

$$\frac{\mathrm{d}v_x}{\mathrm{d}t} = \frac{1}{2}\omega_z^2 x + \omega_c v_y(t) + \gamma v_x(t) - \frac{qV_{rf}}{mr_0^2} x\cos(\omega_c t/2), \tag{3.22}$$

$$\frac{\mathrm{d}y}{\mathrm{d}t} = v_y(t) + \zeta(t), \tag{3.23}$$

$$\frac{\mathrm{d}v_y}{\mathrm{d}t} = \frac{1}{2}\omega_z^2 y - \omega_c v_x(t) + \frac{qV_{rf}}{mr_0^2} y\cos(\omega_c t/2), \tag{3.24}$$

where V_{rf} is the amplitude of the axialisation potential. Here I have introduced new time-dependent parameters $\zeta_x(t)$ and $\zeta_y(t)$, which represent stochastic scattering of photons and are responsible for heating of ions. At the same time, Doppler cooling of the ions is incorporated in terms of a velocity dependent force ($m\gamma v_x$), where γ is the parameter defined as

$$\gamma = R_x \frac{\hbar k}{m} \frac{8\delta_l k}{\Gamma_s^2 + 4\delta_l^2}, \tag{3.25}$$

where all the parameters have the same meaning as discussed previously.

For the known stochastic parameters, the above mentioned coupled equations can be solved numerically and a cooling limit can be estimated. However, it is difficult to find these parameters, thus I will adopt a Monte-Carlo method to estimate the cooling limit. In the Monte-Carlo method, the stochastic time-dependent part will be assigned to a random number generator, weighted to the photon scattering rate of a trapped calcium ion. A plot showing ion amplitude of motion in the presence of an axialisation field is shown in figure 3.4 and cooling of both radial modes is illustrated.

3.3 Sideband cooling

In the previous section, I have described laser cooling in a weak binding regime, where cooling is performed on a broad linewidth atomic transition and hence the motional states are not resolved. These cooling methods limit the ion temperature to the Doppler limit which is set by the transition linewidth ($T_{Dop} \sim \frac{\hbar\Gamma}{2k_B}$). The temperature, in this case, is found to be much higher than the actual recoil limit ($T_{rec} \sim \frac{\hbar^2 k^2}{2mk_B}$), which is the lowest temperature achievable with a quanta of light. There are many ways to achieve sub-Doppler cooling of a free or bound atom using lasers such as Sisyphus cooling [88, 89], EIT cooling [90], resolved sideband cooling [44] etc.. In this thesis I will only discuss the resolved sideband cooling method. Resolved sideband cooling only applies to the trapped atoms/ions, where the trapping of atoms causes them to

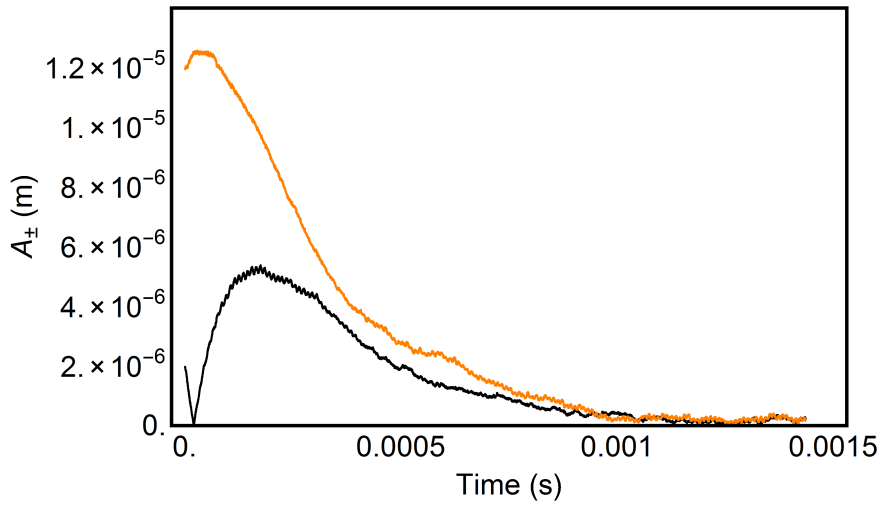


Figure 3.4: Figure showing the reduction of radial motion amplitudes in the presence of axialisation field and Doppler cooling laser beam. The magnetron mode (orange curve) and the cyclotron mode (black curve), are found to average out to the same mean amplitude of motion. Simulation is carried at 100 V of trapping potential and 2 V of axialisation amplitude.

move in a harmonic manner. This manifests itself as motional states superimposed with the internal state of the atom. The motion of an ion in a Penning trap is a harmonic type and its quantum dynamics are described in section 2.3.

The resolved sideband cooling technique is employed in the strong-binding regime, which is observed when $\omega_z \gg \Omega_0 \gg \Gamma_s$. In this regime, the sidebands are well separated and individual sidebands can be targeted with laser or microwave radiation. This condition can be achieved in a tightly confined trapped ion system along with a laser tuned to a quadrupole atomic transition. Resolved sideband cooling is generally performed after the ion has undergone Doppler cooling, where the mean phonon number is limited by the Doppler limit as shown in equation 3.15. In tightly confined systems, the mean phonon number, after Doppler cooling, can be less than ten. If the condition of resolved sidebands is met, the spectroscopy reveals sidebands in the spectrum. Interestingly, if the laser is tuned to one of these sidebands then the phonon state of the system can be changed by the laser transition. If the laser is tuned to the first red sideband, the absorption and re-emission process removes one phonon in each cycle and after repeating this process the ion can be ultimately cooled to the ground state of the harmonic motion. Once the ion reaches the motional ground state, the laser does not resonate with any motional states and hence the transition ceases. A schematic of sideband cooling is shown in figure 3.5 for a two-level system.

Experimental realisation of ground state cooling of trapped atomic ion was first demonstrated by Diedrich et al. [41]. Since then a lot of progress has been made in this direction. Electromagnetically induced transparency (EIT) is another efficient method to cool multiple ions, where

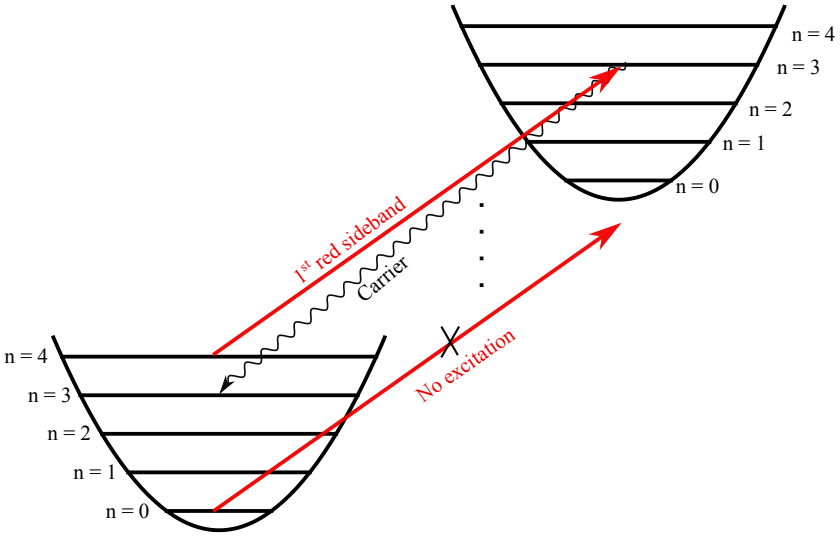


Figure 3.5: A schematic of resolved sideband cooling: each absorption followed by an emission removes a photon from the system and a repetitive process brings the ion to the motional ground state.

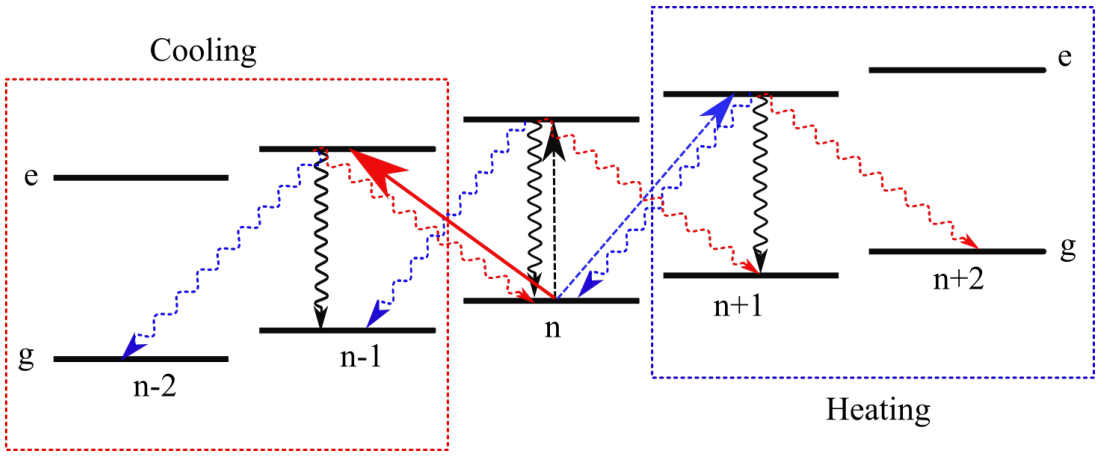


Figure 3.6: Absorption and spontaneous emission of photons in the system with large L-D parameter. See text for more details.

multiple sidebands can be targeted at the same time. Recently, the ground state cooling of an ion in a Penning trap along the axial direction has been demonstrated by Goodwin et al. [91]. In this paper, they employed resolved-sideband cooling along the axial direction on a trapped calcium ion. In general, cooling is efficient if the ion is within the L-D regime after Doppler cooling. The L-D regime is a specific regime of trapped ion system where the spread of the wave function of a trapped ion is considered to be smaller than the wavelength of the electromagnetic radiation that is used to probe it, that is mathematically $\sqrt{2n+1}\eta \ll 1$ where η is called the L-D parameter. If the L-D parameter is small then the re-emission of a photon maintains the phonon state and hence cooling is efficient. However, beyond the Lamb-Dicke regime, cooling is not efficient due to the diffusion of population among the various other motional quantum numbers

during spontaneous emission of the photon [92], which causes heating of the ion.

For a large L-D parameter, the ion may encounter off-resonant excitations during the absorption processes. These processes can increase the phonon number and unnecessarily heat the ion. A schematic of absorption and emission processes during resolved sideband cooling of a trapped ion with a large L-D parameter is illustrated in figure 3.6, where the red solid arrow indicates resonant absorption of a photon when the laser is tuned to the first red sideband. The arrows in black and blue depict the off-resonant excitation of a photon. The emission processes are denoted by squiggly arrows, with corresponding colours indicating the change in trap frequency after the emission of the photon.

Chapter 4

Experimental apparatus and techniques

In this chapter, I will describe the experimental apparatus used to acquire the data presented in this thesis. The experimental apparatus includes a Penning trap, 1.9 T superconducting magnet, vacuum system, diode laser system for Doppler cooling and spectroscopy of trapped ions, ultra-stable optical cavities for locking purposes, an Nd-YAG laser system for ion generation, photo-multiplier tubes (PMT's), "electron-multiplying CCD" (EMCCD), computer control for the experimental apparatus and data acquisition, and various electronic and optical devices that are used to run the experiment. The apparatus was designed by previous PhD students and post-docs working in our group, even before my arrival at Imperial. After I joined some of the modifications were carried out by me and other colleagues working during these years of my PhD. For the sake of completeness, I will describe the whole experimental apparatus and I will properly cite the contributions of the other people. Finally, I will describe the experimental techniques that are used to perform the current studies.

4.1 Atomic structure of a calcium ion

A two-level atomic system is an ideal choice in order to perform quantum simulations and computations. A two-level atom provides a simple system which fulfils the basic requirements to perform any qubit operation. Out of many atomic species, there are only a few elements which have an atomic structure suitable for laser manipulation. A singly ionised positive calcium ion resembles alkali type elements, which have a single outer electron. The optically active single electron of a Ca^+ ion makes it the simplest system to manipulate and perform laser spectroscopy. More specifically ^{40}Ca is the most abundant isotope in the natural sample of calcium. Additionally, due to its zero nuclear spin, the isotope is highly suitable for optical-based quantum information experiments [7].

Our group works with $^{40}Ca^+$ ions trapped in a Penning trap. A partial energy level diagram

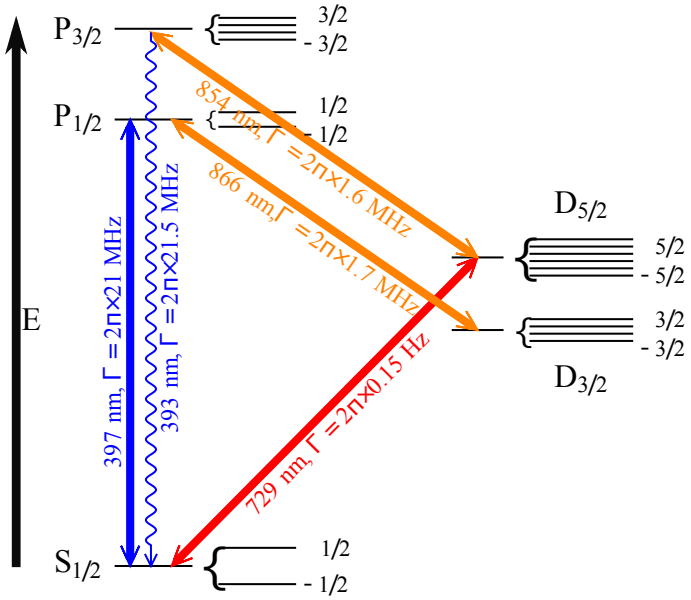


Figure 4.1: Relevant electronic level structure of a $^{40}Ca^{+}$ ion (energy spacing is not scaled). Transition rates, Zeeman shifted energy spacing of the levels and laser wavelength of the required transitions are taken from ref. [74]

of a $^{40}Ca^{+}$ ion is shown in figure 4.1. It has zero nuclear spin, hence it has no hyperfine energy levels, which reduces the complexity of the experiment. The specific transitions of interest are denoted by red, blue and orange colour arrows and squiggly lines. Spectroscopy is performed on a narrow linewidth $S_{1/2} \leftrightarrow D_{5/2}$ transition. Doppler cooling is performed on the $S_{1/2} \leftrightarrow P_{1/2}$ transition. The system requires repumping lasers at 854 nm and 866 nm as indicated in figure 4.1.

4.1.1 Zeeman effect

Due to the presence of a strong magnetic field, in a Penning trap, the atomic states of a trapped ion are further split into sub-levels, which are termed “Zeeman sublevels". The theory of the “anomalous Zeeman effect" can be used to determine the energy spacing between these sub-levels. The interaction Hamiltonian of a bound electron in the presence of a magnetic field is given as

$$\boldsymbol{H_B} = -\boldsymbol{\mu} \cdot \mathbf{B}, \tag{4.1}$$

where μ is the magnetic moment of the trapped ion. The magnetic moment in terms of orbital momentum (**L**) and spin momentum (**S**) is expressed as $\mu = -\mu_B(g_L\mathbf{L} + g_S\mathbf{S})$, where μ_B is the Bohr magnetron and “g" is the g-factor of the electron. For a bound electron, the spin and orbital g-factors are $g_S = 2.002319 \approx 2$ and $g_L = 1$. Additionally, the bound electron experiences spin-orbit coupling (**L-S** coupling), thus L and S are no longer good quantum numbers; hence, the

description of the atomic model shall be denoted in terms of the total angular quantum number (**J**). After assuming the magnetic field along the axial direction (along the z-axis), the Zeeman Hamiltonian is expressed

$$H_B = \frac{g_j \mu_B J_z B_0}{\hbar}, \tag{4.2}$$

where g_J is the Landè g-factor and $J_z (= L_z + S_z)$ is the component of the total angular momentum along the magnetic field direction. The first order energy shift due to the Zeeman effect can be calculated by Perturbation theory and it is expressed as

$$\Delta E = \frac{g_J \mu_B B_0}{\hbar} \langle \psi_{J,m_j} | J_z | \psi_{J,mj} \rangle , \tag{4.3}$$

$$= g_J \mu_B m_j B_0. \tag{4.4}$$

The Landè g-factor for the atomic states can be expressed in terms of angular quantum numbers J, L and S and is given as

$$g_J = g_L \frac{J(J+1) - S(S+1) + L(L+1)}{2J(J+1)} + g_S \frac{J(J+1) + S(S+1) - L(L+1)}{2J(J+1)}. \tag{4.5}$$

Similarly, the second-order Zeeman shift from perturbation theory is given as

$$\Delta E_k^{(2)} = \sum_{k \neq n} \left(\frac{\mu_B B_0}{\hbar} \right)^2 \frac{| \langle \psi_k | g_L L_z + g_S S_z | \psi_n \rangle |^2}{E_n^{(0)} - E_k^0}, \tag{4.6}$$

which can be easily calculated via the Clebsch-Gordan coefficients method [93, 94]. The first and second-order Zeeman shifts for a calcium ion in a 1.9 T magnetic field have been calculated and are given in table 4.1.

Atomic level	1^{st} order Zeeman Shift $\Delta\nu^{(1)}$ (GHz)	2^{nd} order Zeeman Shift $\Delta\nu^{(2)}$ (MHz)
$S_{1/2}, m_j = \pm\frac{1}{2}$	± 26.623	0
$P_{1/2}, m_j = \pm\frac{1}{2}$	± 8.854	-23.5
$P_{3/2}, m_j = \pm\frac{3}{2}$	± 53.216	0
$P_{3/2}, m_j = \pm\frac{1}{2}$	± 17.739	+23.5
$D_{3/2}, m_j = \pm\frac{3}{2}$	± 31.892	-62
$D_{3/2}, m_j = \pm\frac{1}{2}$	± 10.631	-93
$D_{5/2}, m_j = \pm\frac{5}{2}$	± 79.808	0
$D_{5/2}, m_j = \pm\frac{3}{2}$	± 47.885	+62
$D_{5/2}, m_j = \pm\frac{1}{2}$	± 15.962	+93

Table 4.1: Table showing the first and second-order Zeeman shifts for the atomic states of a $^{40}Ca^+$ ion at 1.9 T magnetic field.

In order to perform laser cooling and spectroscopy on a trapped calcium ion, it is important to set the laser frequencies to a certain precision. After describing the energy level diagram of a calcium ion, I will describe the transitions of interest in our system. In our system, the required

laser transitions and their use can be summarised as follows:

- In a calcium ion system, Doppler cooling is performed on the $S_{1/2} \leftrightarrow P_{1/2}$ transition, which is a dipole-allowed transition. In our case, the transition falls within the "weak-binding regime", which is the regime where the motional frequency of the trapped ion (typically < 1 MHz) is much smaller than the linewidth of the transition (22 MHz). In our system, the transition is induced by a 397-nm diode laser system. Moreover, the transition requires two laser frequencies due to the Zeeman shifts in a Penning trap. In our case, the S state is split into two sublevels $m_j = -1/2$ and $m_j = 1/2$, which are $\sim$ 53.24 GHz apart from each other. The $P_{1/2}$ state is also split into $m_j = 1/2$ and $m_j = -1/2$ with energy spacing of 17.7 GHz. The transition is bridged by two separate laser beams tuned to the $S_{1/2,-1/2} \leftrightarrow P_{1/2,1/2}$ and $S_{1/2,1/2} \leftrightarrow P_{1/2,-1/2}$ transitions, respectively. The frequency spacing of these transitions is $\approx$ 71 GHz, which is not possible to bridge by any electro-optic modulators (EOMs).

- During Doppler cooling, the population from the $P_{1/2}$ state often decays to the metastable state $D_{3/2}$ through a dipole allowed transition and also to the metastable state $D_{5/2}$ through a weak magnetically induced transition [95]. The population from these metastable states is re-pumped by the frequency-modulated 866-nm and 854-nm laser beams. The frequency modulation of these laser beams is essential for the re-pumping of the population from the Zeeman sub-levels of the metastable states. In our experiment, frequency modulation is carried out by a single EOM for both laser beams.

- Spectroscopy and sideband cooling of a calcium ion our trap is performed on the $S_{1/2,-1/2} \leftrightarrow D_{5/2,-3/2}$ quadrupole transition, which occurs at 729 nm. The laser frequency is finely tuned by an acousto optic modulator (AOM).

4.1.2 Magnetically induced transitions in a Penning trap

From the dipole allowed transition rules [96], in normal operating conditions, transition between the $P_{1/2}$ and $D_{5/2}$ states is forbidden. In this case, the transition can only take place through a magnetic quadrupole or an electric octupole (M2/E3) rule. The transition rates in such cases are a few orders of magnitude smaller than that of the dipole allowed case. But in the presence of a strong magnetic field, various J levels get mixed together and thus the transition becomes allowed. The transition rate, in this case, depends upon the strength of the magnetic field [93].

Once the population decays to the metastable states, it gets trapped there for the lifetime of the metastable states, which is 1 second for a calcium D state. The decay of the population to these states eventually stops Doppler cooling. In order to speed-up the process, the metastable level needs to be recycled by another laser beam tuned to the $D_{5/2} \leftrightarrow P_{3/2}$ transition, which is carried out by an 854-nm laser beam. The magnetically induced transition rates for a calcium-40 ion has been studied before by Crick et al. [93].

At a moderate magnetic field, the decay rate (transitions/T^2/s) of the $P_{1/2}$ state to the metastable state $D_{5/2}$ state is given as [91]

$$\Gamma_{j\text{-mixing}} = \Gamma_s \times 4.2 \times 10^{-7} B_0^2 \tag{4.7}$$

where Γ_s is the scattering rate of the $S_{1/2} \leftrightarrow P_{1/2}$ transition. Γ_s depends upon the incident laser intensity and the detuning from the transition. In our system, these transitions are unavoidable and limit the detection efficiency of the qubit while performing the state readout. I will discuss this issue in section 4.6.3.

4.1.3 Transition strengths

For a trapped calcium ion, Doppler cooling is performed on a dipole allowed transition, hence a low power laser is sufficient to perform cooling. The repumping is performed on another dipole-allowed transition. The expression for the Rabi frequency for these transitions has been derived by James et al. [74] and it is given as

$$\Omega_0^{(E1)} = \sqrt{\frac{3I_0 e^2 (2j'+1)\Gamma}{2\epsilon_0 \hbar^2 c^2 \alpha k^3}} \sum_{q=-1}^{1} \begin{pmatrix} j & 1 & j' \\ -m_j & q & m'_j \end{pmatrix} c_i^{(q)} \epsilon_i, \tag{4.8}$$

where the coefficients $c_i^{(q)}$ are the normalised spherical vectors given in the appendix of reference [74] and I_0 is the intensity of the laser beam. The parameter α is the fine structure constant and Γ is the decay rate of the excited state. The matrix term is called a 3-j symbol, which can be calculated with “Mathematica" [97].

Similarly, the expression for the Rabi frequency of a quadrupole transition can be written as

$$\Omega_0^{(E2)} = \sqrt{\frac{15I_0 e^2 (2j'+1)\Gamma}{2\epsilon_0 \hbar^2 c^2 \alpha k^3}} \sum_{q=-2}^{2} \begin{pmatrix} j & 1 & j' \\ -m_j & q & m'_j \end{pmatrix} c_{ij}^{(q)} \epsilon_i n_j. \tag{4.9}$$

Now, from these equations, it is possible to derive the required laser powers to achieve a low saturation dipole allowed transition rate. In our experiment, typically 4 μW of power in each 397-nm laser beam with 100 μm beam waist satisfies the low saturation conditions. Similarly, the 854-nm beams and 866-nm laser beams have 0.6 mW and 6 mW of power with a 200 μm beam waist at the trap centre. The low saturation requirement is very important for the 397-nm beam to achieve Doppler cooling, however the 854-nm and 866-nm laser beams do not require the power to be below the saturation limit. The quadrupole transition is induced by a 729-nm laser beam with approximately 150 μm beam waist and 30 mW power at the trap centre.

4.1.4 Polarisations of the laser induced transitions

In a Penning trap, due to the magnetic field, a transition may require a specific polarization of the light field to stimulate the specific resonance. The magnetic field, in this case, acts as a tool to set the quantisation axis of the system. The dependency of the transition strength on the polarisation axis can be seen from the Rabi frequency formula as given in equation 4.8 and 4.9. For a $^{40}Ca^{+}$ ion, we are mainly interested in a dipole or a quadrupole transition. Moreover, we are interested in two specific directions of laser beam propagation, first parallel to the magnetic field axis and second perpendicular to the magnetic field axis. Specifically, in the first case when the laser beam is parallel to the magnetic field axis (along the axial direction) the π ($\Delta m = 0$) transition cannot be induced. However, in the second case, when the laser beam is perpendicular to the magnetic field axis (in the radial plane), then both $\sigma^{\pm}$ ($\Delta m = \pm 1$) and π transitions can be induced. In both directions of laser propagation, plane polarised light can be used to stimulate the required transition. Furthermore, the relevant transitions in a calcium ion system are elaborated as follows.

- The $S_{1/2} \leftrightarrow P_{1/2}$ transition: Doppler cooling is performed on this transition. Cooling requires a closed cycle and hence at least two laser beams resonant with the $\Delta m_j = +1$ and $\Delta m_j = -1$ transitions are required. Along the axial direction, this can be excited with linearly polarised light with any arbitrary polarisation angle. However, in the radial direction, the same transitions can only be excited by linearly polarised light with polarisation angle perpendicular to the magnetic field direction.

- The $D_{3/2} \leftrightarrow P_{1/2}$ transition: Decay of the population to the $D_{3/2}$ state from the $P_{1/2}$ state during Doppler cooling is re-pumped by an 866-nm laser beam. The relevant transitions are shown in figure 4.2 (b). Multiple Zeeman sublevels are repumped by a frequency modulated laser beam. In our experiment, an axial laser beam with “linear polarisation" (LP) is sufficient to induce the $\sigma_{\pm}$ transitions. Ideally a σ^{+} or σ^{-} transition is induced by a right circularly polarised (RCP) or left circularly polarised (LCP) laser field. Even though an LP laser field is used in our experiment, often a problem occurs due to the presence of a circular polarisation component in the field. It becomes more important when the laser beam is passed through an optical fibre and the thermal fluctuations in the fibre change the strength of the RCP or LCP component, which alters the scattered photon rate. In order to avoid any circularity of the laser field, we clean the polarisation with a “polarising beamsplitter" (PBS) cube placed in the beam path.

- The $D_{5/2} \leftrightarrow P_{3/2}$ transition: The magnetically-induced population decay to the $D_{5/2}$ state is repumped via a laser beam at 854 nm. Frequency modulation is carried out to induce all the transitions between Zeeman sublevels. The relevant transition channels are indicated in figure 4.2 (c). These transitions are also induced by propagating a linearly polarised laser beam along the axial direction. In order to avoid the same polarisation issues, the beam is again passed through a PBS, enabling an LP laser field to induce the transition.

- The $S_{1/2} \leftrightarrow D_{5/2}$ transition: The quadrupole transition is used for spectroscopy and side-

band cooling purposes. The transition is induced by an LP laser beam travelling along either the axial or the radial directions, depending upon studies of interest. The relevant transition is indicated in figure 4.2 (d). For axial spectroscopy, linearly polarised light can excite the transition with the polarisation axis anywhere in the xy-plane. However, when the laser beam propagates in the radial plane, the transition requires a polarisation component along the direction perpendicular to the magnetic field axis. In both cases LP light is used with an angle perpendicular to the magnetic field direction.

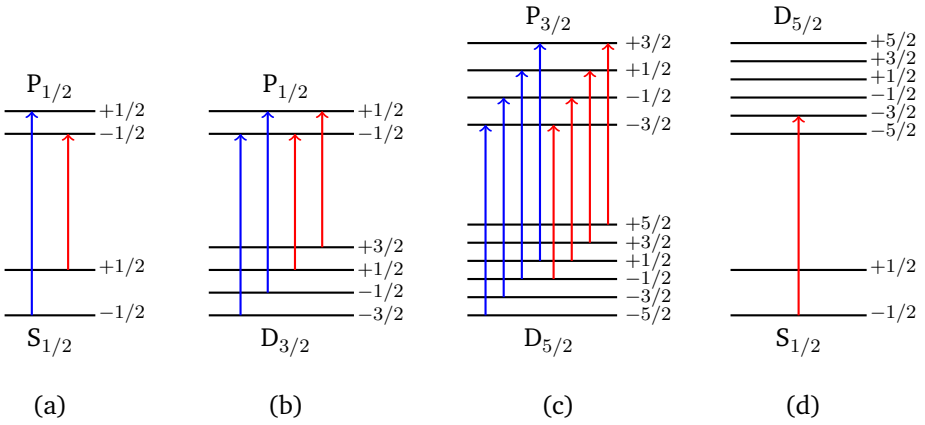


Figure 4.2: Relevant dipole and quadrupole transitions for a calcium ion in the presence of a magnetic field. The σ^+ transitions are shown in blue and the σ^- are shown in red.

4.2 Loading of ions

In most cases, atomic ions are generated by the impact of an energetic electron beam or by a laser beam with the atomic vapour of the required element [73]. Electron impact ionisation is not element or isotope specific, hence it can generate a variety of ions in the trap vicinity, which is not suitable in many experiments. Moreover, element specific ionisation is carried out by a resonant photo-ionisation method, where multiple laser beams are simultaneously used to create the ionisation. In this case, the first laser beam excites the atom to its excited state, from where the second laser beam creates ionisation by exciting the electron to the continuum.

The other way to create atomic ions is a non-resonant multiphoton ionisation method, where an intense laser beam is used to ionise the atomic vapour. This method is also not element or isotope specific but does not require photons with a specific frequency. However, if the atomic vapour is generated from an enriched sample of the required elements, the intense laser beam can create photo-ionisation with two or sometimes three photons. In our laboratory, the calcium ions are created with the help of a frequency doubled (SHG) Nd-YAG[1] laser beam interacting with the atomic beam of calcium atoms.

The neutral beam of calcium atoms is produced by the resistive heating of a calcium sample

[1] Continuum Surelite II

(“oven") situated near the trap electrodes. Ionisation occurs through the absorption of three simultaneous photons of 532 nm wavelength. The YAG system generates 5 ns laser pulses at a 10 Hz repetition rate. Typically, the average power output of the laser beam at 532-nm is 0.5 W, which is sufficient for our purpose. The laser beam is focused at the trap centre in order to enhance the ionisation yield and to generate the ions at the trap centre. Typically, the method loads a few tens of ions during 10-30 seconds loading time. To enhance the production of ions, the oven is kept on for a minute before the laser beam is passed through the trap centre. Once ionisation occurs, the trap, which is continuously on during the loading of ions, captures the ions. The cooling lasers, which are set to the right detuning from the transition, then cool the ions to the trap centre which are then detected by observing the fluorescence.

Often, we just need one or two ions in the trap. The extra ions produced in the trap are ejected by turning off the trap potential for a short time. This is done by connecting the end-cap electrodes to the ground potential for a few tens of μs. During this time, due to the Coulomb repulsion, the ions push each other away from the trap centre and eventually some of the ions hit the trap electrodes and are neutralised. If the trap potential is quickly switched back to the normal operating potential, then the remaining ions come back to the trap centre. This method is called the “pulsing technique" and a home built apparatus with an Arduino micro-controller is currently being used for this purpose. More details about the pulsing apparatus can be found in the thesis of Graham Stutter [98]. In order to trap the required number of ions, multiple short ejection pulses are used. There is no specific recipe to control the number of ions in our apparatus. But generally, with re-pumping lasers tuned to the required detuning, a short loading of $\sim$ 15 s is sufficient to load less than 10 ions near the trap centre, which are later pulsed down to one or two ions.

4.3 Trapping apparatus

4.3.1 SPECtrap

The basic principle of ion trapping has been described in chapter 2. The trap geometry used for ion trapping in our laboratory is a modified version of a classical 3D quadrupole trap. The trapping device uses in a cylindrical geometry and is shown in figure 4.3. The modified geometry of the trap electrodes provides greater optical access to the ions. It is an open end-cap trap geometry formed with various hollow cylinders stacked together while maintaining a common axis. The trap is called “SPECtrap" and details about it can be found in reference [99]. The characteristic trap dimension d_0 is estimated to be 18.6 mm. Corresponding calibration is shown in appendix D.

Furthermore, the ring electrode is split into four equal segments to provide a quadrupole radial potential for the axialisation technique. The SPECtrap also contains a pair of compensation electrodes, which can be used to reduce the anharmonicity in the trapping potential. Apart from that, there are two electrodes intended for use as capture electrodes in accelerator based heavy

ion precision experiments at GSI Darmstadt. In the current experiment, the capture and compensation electrodes are used to nullify any stray electric fields. The electrodes are connected to just above the ground potential (approximately ± 100 mV) to cancel any offset potential in the trapping zone. A DC potential is applied between the end-caps and the ring electrode, which are indicated in the schematic of the trap geometry. In order to provide trapping in the radial plane, the trap axis (i.e. the axis of the cylindrical electrodes) is aligned with the magnetic field direction.

The trap is held inside a vacuum chamber and then it is electrically connected through vacuum compatible wires to feed-throughs connecting to external coaxial cables. The vacuum chamber is continuously pumped via a Varion ion-pump running at a 40 l/s pumping rate, which maintains the vacuum below 1×10^{-9} mbar pressure. The optical access is provided by various quartz windows connected to the vacuum chamber. The chamber allows six-way orthogonal access to the trap centre. The axial laser beam passes through the bottom quartz window and comes out from the top window after passing through the trap centre. In the radial plane, optical access is provided by two pairs of 4 mm holes, which are drilled orthogonal to each other. A diagonally opposite pair of holes is used to collect the scattered photons from the trapped ions and the remaining two holes are used to pass the radial laser beam through the trap centre.

4.3.2 Magnetic field

A Penning trap requires a uniform magnetic field at the trap centre for the confinement of the ions. In our trap apparatus, the magnetic field is provided by a 100-mm diameter open bore superconducting magnet manufactured by "Magnex Scientific Ltd."[2]. According to the cryostat instruction manual, at 41 A persistent current one can produce a field of 1 T. The cryostat has a room temperature bore to insert the trap assembly. The magnet in our laboratory currently creates a 1.9 T magnetic field. The open bore system reduces the external thermal loading effects, hence the consumption of the cryogens is low. The system consumes approximately 100 litres of liquid helium in four months. The trap assembly is inserted from the bottom of the bore and held along the axis of the cryostat. The trap assembly is raised enough so that the turning point of the magnetic field overlaps with the trap centre, which provides a uniform magnetic field along the trap axis. More details about the magnetic field variation and its optimisation can be found in references [98, 99].

4.3.3 Axialisation drive

The theory of axialisation has been briefly discussed in section 3.2. For efficient radial cooling, the ring electrode is split into four segments. A time-varying electric potential is then applied to each segment of the ring electrode, at the cyclotron frequency of the ions. In order to couple the magnetron and modified cyclotron modes, the phase difference between each adjacent electrode

[2]Operating manual for 2.5 Tesla magnet system, Magnex Scientific Ltd. (1995).

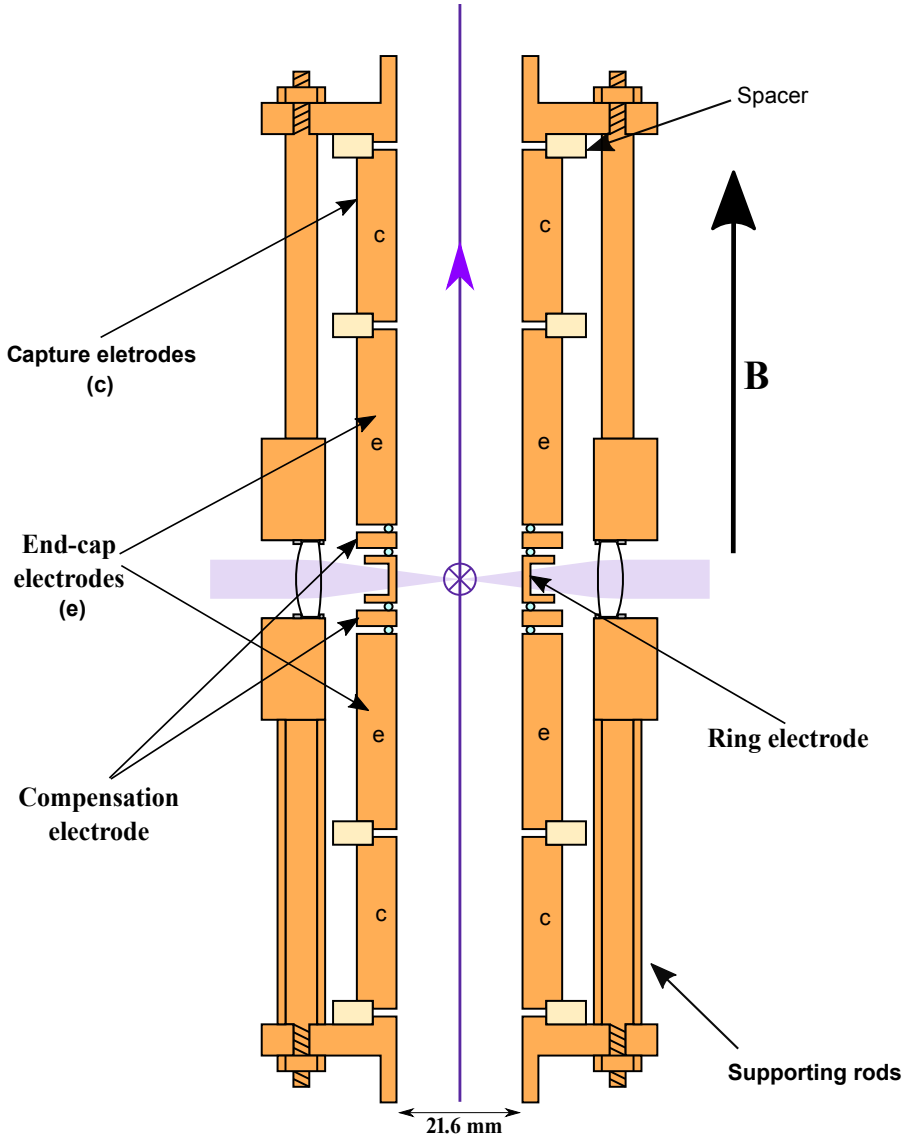


Figure 4.3: A schematic cross-section view of the SPECtrap. The axial laser beam path is indicated with a violet arrow and the radial laser beam passes along the axis perpendicular to the plane of the page. Optical detection is carried out by two high numerical aperture lenses shown on the left and right sides of the trap geometry. The detected photon paths are indicated with violet cones [32].

is kept at π radians. In our experiment, for a single ion, we usually apply ~ 300 mV amplitude potential at each electrode. The voltage is generated using an HP 3325B function generator. The appropriate phase is assigned by a home built electronic circuit developed by Joe Goodwin [91]. Additionally, the home built circuit allows us to individually change the amplitude of the AC potential, which enables us to match the AC null of the axialisation drive with the trap centre. Otherwise, any AC offset adds micro-motion to the ion at the drive frequency.

In order to compensate for any DC offset in the radial plane, due to electrode misalignment or patch potentials, a small DC offset (typically < 100 mV) is applied to each segment of the ring electrode.

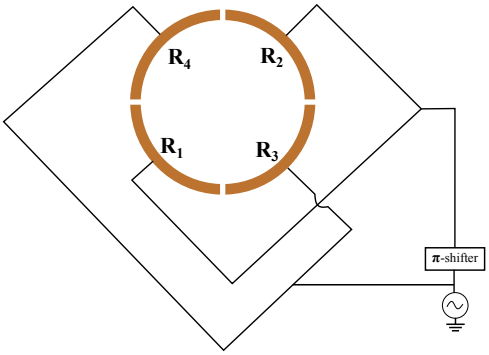


Figure 4.4: A cross-sectional view of our SPECTrap showing four segments of the ring electrode. Appropriate AC signal with correct phase is applied to each segment to couple the magnetron and modified cyclotron motion.

A cross-sectional view of the segmented ring electrode is shown in figure 4.4. Appropriate phase is essential to avoid any unwanted effects of micromotion. In practice, due to the passive electrical components in the system, the phase difference between the segments is not exactly 0 or π. I have carried out an exact phase measurement of the AC signal that is applied to the individual electrodes. The measured phase differences between R_1 and the rest of the segments are $-3°$, $175°$ and $177°$ for R_2, R_3 and R_4, respectively. This slight difference in the phase affects the purity of the axialisation potential and can be minimised by adjusting the AC amplitude at each segment. Experimentally, AC compensation is carried out by varying the AC potential at each segment from the axialisation drive while looking at the ion spread on an EMCCD. A more intelligent way is to compensate for the AC potential while looking at the axialisation sidebands in the spectrum of the trapped ion. However, for most of our studies, we found out that the camera based compensation trick is sufficient.

4.3.4 Anharmonicity and misalignment effects in the Penning trap

In order to satisfy the trapping condition, it is necessary to produce a quadrupole potential within the enclosed volume of the trap electrodes. A pure quadrupole potential can only be generated by a set of electrodes shaped from hyperboloids of revolution (as shown in figure 2.1), but this geometry provides very little optical access. The SPECtrap, discussed in the previous section, allows more optical access at the cost of anharmonicity due to the non-hyperbolic shaped electrodes. The anharmonicity in a cylindrical Penning trap can be reduced by adjusting the height and the radius of the trap electrodes. In the SPECtrap, the relationship between the height and radius of the electrodes is maintained such that it maximises the quadrupole component of the potential around the trap centre. Moreover, the anharmonicity can be further reduced by applying a small potential on the compensation electrodes.

The anharmonicity, in a cylindrical type Penning trap, is still problematic for large ion clouds. In our experiments, we mostly work with a small number of ions, hence the anharmonicity is not a big problem for us. More importantly, any stray field affects the ion motion, which is compensated by the set of compensation electrodes that were initially designed for anharmonicity removal. Additionally, in a Penning trap, it is also crucial to align the trap axis along the magnetic field direction in order to avoid any misalignment induced instabilities or artefacts [100]. These artefacts are important in order to minimise the uncertainties in precision measurements [101]. In our experiments, these effects lead to coupling of the motional modes and the appearance of some resonance peaks while performing spectroscopy. The presence of these resonance peaks affects the coherent control of the trapped ions.

4.3.5 AC and DC compensations

The motional frequency of a trapped ion depends upon the potential applied to the trap electrodes. In reality, a small stray field can change the motional frequency or sometimes couples the motional modes which is undesirable in many experiments [102, 103]. In our experiments, the compensation is essential to eliminate any coupling between motional modes, which otherwise show resonances in optical spectroscopy. On the other hand, the AC compensation (for axialisation frequencies) is essential to minimise micromotion of the trapped ion.

In practice, the DC offset can be precisely cancelled out by applying some small DC voltages on the compensation electrodes (C_1 or C_2 electrodes along the axial direction) and on the R_2 and R_3 segments of the ring electrode. The effect due to the external DC voltage offset can be seen in terms of the change in the ion's position while changing the trap potential. Ideally, a laser-cooled single ion should stay at the null of the trapping field, i.e. the trap centre, for all values of trapping potential. But due to the external electric field, the trap centre is not truly the DC null. Especially, at low trapping voltages, the effects are apparent.

In an uncompensated trap, if the trapping voltage is changed from a high value to a low value the ion moves from one place to the other due to the offset fields. At a high trap potential, the effect of the offset is nullified thus the ion position corresponds to the ideal situation. However, at a low trapping potential, the effect of the offset starts dominating and eventually the ion moves to the point of potential null. In practice, in order to eliminate the effects, the ion position is marked at sufficiently high trapping voltages (typically at 250 V), where the trap centre overlaps with the DC null. Subsequently, at a low trapping potential (say at 10 V), the ion position is recorded again and the compensation voltages are adjusted to place the ion to its original position. The process is repeated until the offset effects are nullified in all the directions.

In our system, the axial compensation is carried out with the C_1 and C_2 compensation electrodes. Ideally, only one compensation electrode is enough to compensate the axial offset, therefore the voltage is applied to C_1. In the radial plane, a small DC voltage is applied to R_3 while R_4 is connected to the ground potential. This technique works very well if the ion movement is in the plane of view of the EMCCD. The movement of the ion along the other axis in the radial

plane is not visible on the EMCCD, hence, the adjustment cannot be made with this technique. However, for coarse adjustments, the PMT signal can be used as a reference of the ion position assuming that the optical arrangement is such that the PMT sees the photons coming from the trap centre. In this case, if the ion changes its position then its movement is noted by observing the change in the fluorescence level and the potential on the R_1 or R_2 segments is varied to correct for any offset.

After correcting for the DC offset, the AC compensation is carried out to reduce driven motion of a trapped ion due to the axialisation field. The axialisation field is much weaker than the trapping field but often can cause serious micromotion induced artefacts. In practice, some misalignments of the electrodes causes micromotion at the ion. The AC compensation is carried out by adjusting the axialisation potential to each segment, independently. For the adjustment, a live image of an ion is viewed through an EMCCD and the spread due to the micromotion is reduced. In our system, the amplitude of the axialisation potential is controlled by an electronic circuit that also provides DC compensation control. More details can be found in Joe Goodwins's thesis from our group.

4.4 Optical system

Laser-cooled trapped ions are extensively used to perform high-precision experiments and optical quantum gates. In a Penning trap, the laser cooling requires multiple laser frequencies, hence the system requires many laser sources and optoelectronic components to generate multiple frequencies. The current apparatus has a total of five main lasers in the ECDL configuration, an Nd-YAG laser and a reference He-Ne laser. At various stages, these lasers were optimised and realigned according to the requirements. In this section, I will describe the laser system and its arrangement, laser frequency generation and stabilisation of laser frequencies.

4.4.1 External-cavity diode lasers

In our laboratory, all five main lasers are external cavity diode lasers (ECDL) systems. A schematic of an ECDL system is shown in figure 4.5. An ECDL comprises an optical diode, a collimating lens and a grating which is controlled via a piezoelectric device attached to it. Typically, one end of the optical diode used in an ECDL is coated with an anti-reflecting material (AR) to reduce losses. The other end of the diode is left with a highly reflective (HR) material.

The optical cavity in an ECDL is produced by placing a grating a few cm away from the front of the optical diode, which acts as the first mirror. The HR surface of the diode acts as the second mirror of the optical cavity. In a Littrow configuration, the grating is mounted such that the first order Bragg diffracted beam goes back into the diode and lasing is realised by stimulated emission in the diode medium. The 0^{th} order beam of the ECDL is taken as the laser output used in the experiments [104]. A schematic of ECDL in the Littrow configuration is shown in figure

4.5. The Bragg equation for the laser output in a Littrow configuration is given by

$$2d\sin(\theta) = m\lambda, \tag{4.10}$$

where d is the groove spacing of the grating and λ is the wavelength of the light. The angle θ is defined as the angle between an incident laser beam and the normal axis drawn on the grating surface. Generally, to enhance the laser output at a particular frequency, a “blazed" type grating is used in an ECDL, which enhances the optical output of the required grating mode.

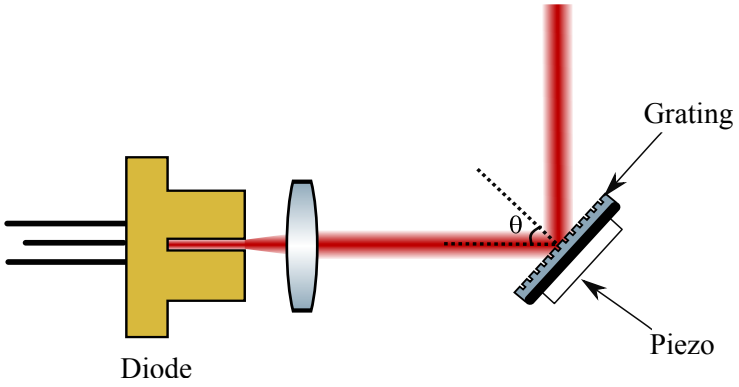


Figure 4.5: A schematic of an ECDL laser in the Littrow configuration is shown above. The first order grating mode is fed back to the diode medium to create stimulated emission of a single frequency mode. The 0^{th} order reflection is finally used for the laser output.

Generally, the frequency tunability of an ECDL is limited but it provides a very narrow linewidth laser output, which is vital for optical quantum control of atoms and molecules. The frequency of a diode laser depends upon the band-gap of the semiconductor material that is used to construct the diode. The frequency of a specific diode laser, within a certain limit, can be varied by changing the temperature or the injection current.

Typical sensitivity of an ECDL with the injection current is $\sim$ 3GHz/mA and with the temperature is $\sim$30 GHz/K [106]. The laser frequency of an ECDL can be tuned by altering the grating angle as shown in equation 4.10. Furthermore, the frequency can be tuned by changing the cavity spacing, i.e. by applying some voltage on piezoelectric transducer attached to the back of the grating (as shown in figure 4.5). The cavity spacing changes the mode spacing in an optical cavity which changes the wavelength of the laser. A schematic of ECDL modes and respective frequency spacing is shown in figure 4.6.

397-nm laser sources

Two DL100 ECDL’s manufactured by Tui-Optics (now Toptica) are currently being used to excite σ^+ and σ^- transitions between S and P atomic levels of a calcium ion. Each laser is customised in the Littrow arrangement and currently provides 6 mW power at $\sim$ 396.847 nm. The frequency difference between these two lasers is kept at $\sim$ 71 GHz, which bridges the frequency difference

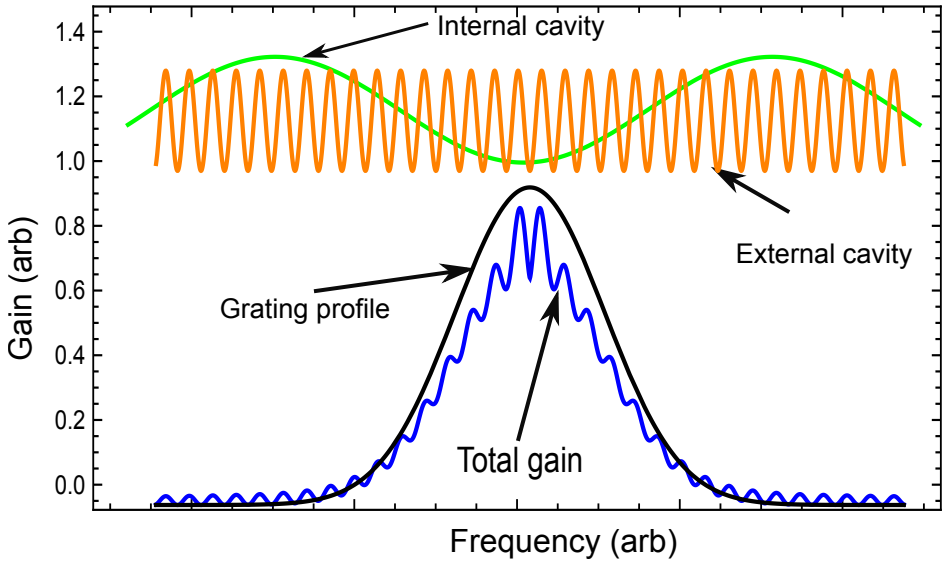


Figure 4.6: Gain curve of an ECDL diode laser. Figure adapted from reference [105].

between the Zeeman shifted sublevels. Each laser diode is actively temperature stabilised and firmly held on a vibration-free optical table, which passively reduces the short term frequency noise and reduces the linewidth to $\sim$ 10 MHz. Furthermore, these lasers are locked to a pair of low finesse optical cavities via a PDH locking method to increase short-term frequency stability upto 2-3 MHz. Long-term frequency stability is provided by a high finesse transfer cavity, which is actively stabilised using a He-Ne reference laser. The locking system stabilises the cavity with the He-Ne source, which subsequently stabilises the ECDL frequencies. The laser locking method and its performance will be discussed in section 4.4.3.

Re-pumping laser sources

Two home built ECDLs, at 854 nm and 866 nm, are used for repumping. The laser head is temperature stabilised by an active feedback loop and firmly placed on an optical table. As these two lasers do not directly affect Doppler cooling performance, their linewidth requirement is not that stringent. Typically, a few MHz linewidth laser sources can comply with the repumping requirement. It is very important that the lasers do not drift in the long term. In order to stabilise long-term drifts, the lasers are locked to another transfer cavity which is locked to the He-Ne reference source (the same one used for the 397-nm transfer cavity). The frequency stabilised output of both ECDL's is then passed through a "fibre electro-optic modulator" (EOM) to produce optical sidebands on each laser beam, which is then used to excite all the Zeeman sublevels.

Spectroscopy laser

Spectroscopy of a trapped calcium ion is performed at 729 nm by inducing S-D clock transitions. The natural linewidth of the transition is $2\pi \times 0.15$ Hz [107]. This clock transition requires a narrow linewidth laser source, at least narrower than the frequency spacing of the motional sidebands. The clock transition in our laboratory is excited by a home-built ECDL system. It is used to excite a quadrupole transition, hence it requires a high power source, typically a few tens of mW power at the trap centre. The ECDL produces 20 mW of optical power measured after the laser system, but typically half of the power is attenuated during frequency stabilisation and beam transport, and thus has insufficient power. In order to boost the laser output, the beam is passed through a tapered amplifier (TA) system, which enhances the laser power by a factor of ~ 30. The laser power is further attenuated during various intermediate steps, such as passing through fibres and AOM's. Ultimately, the power that reaches to the trap is $\sim$ 40 mW. The optical system used for the spectroscopy of a calcium ion is discussed in figure 4.10.

4.4.2 Layout of the optical system

The layout of the optical system and laser beam transport is shown in figure 4.7. The layout of the system is divided into three main blocks. The first block is for Doppler cooling laser sources and it comprises two 397-nm laser sources procured from Tui-Optics. The layout also shows the PDH locking system for both lasers. Two AOM's in double pass configuration provide switching of the laser beams according to experimental requirements. The beams are finally divided into two branches to induce transitions from the axial and radial directions.

A pair of ECDL's at 854 nm and 866 nm are shown in the layout of the second block. The 854-nm laser is passed through a double pass AOM system to provide switching control for the laser beam. The 866-nm laser beam does not have an AOM in its beam path and is left on continuously . The frequency stabilised output of both beams is simultaneously sent to a fibre EOM, which induces frequency modulation (FM) on both beams. The EOM driver frequencies are chosen such that all the Zeeman sublevels are repumped by the common FM output of both beams. The combined laser beam is then passed to the trap centre propagating along the axial direction.

The third block of the laser layout is used for the spectroscopy of trapped ions. In this layout, I show the frequency controlling AOM and beam path for the laser output. The AOM is operated in a single pass configuration. The single pass configuration was changed from double pass when modifying the system to produce a bichromatic output. The bichromatic beam (two laser frequencies in the same beam) is used for the demonstration of a coherent state of motion. We noticed that the double pass configuration is not suitable for the bichromatic operation, hence the arrangement was changed.

The switching control of various laser beams is carried out by AOMs. An AOM utilises an RF field at typically a few hundreds of MHz to create a deflected first order output at $\omega_l \pm \omega_{rf}$,

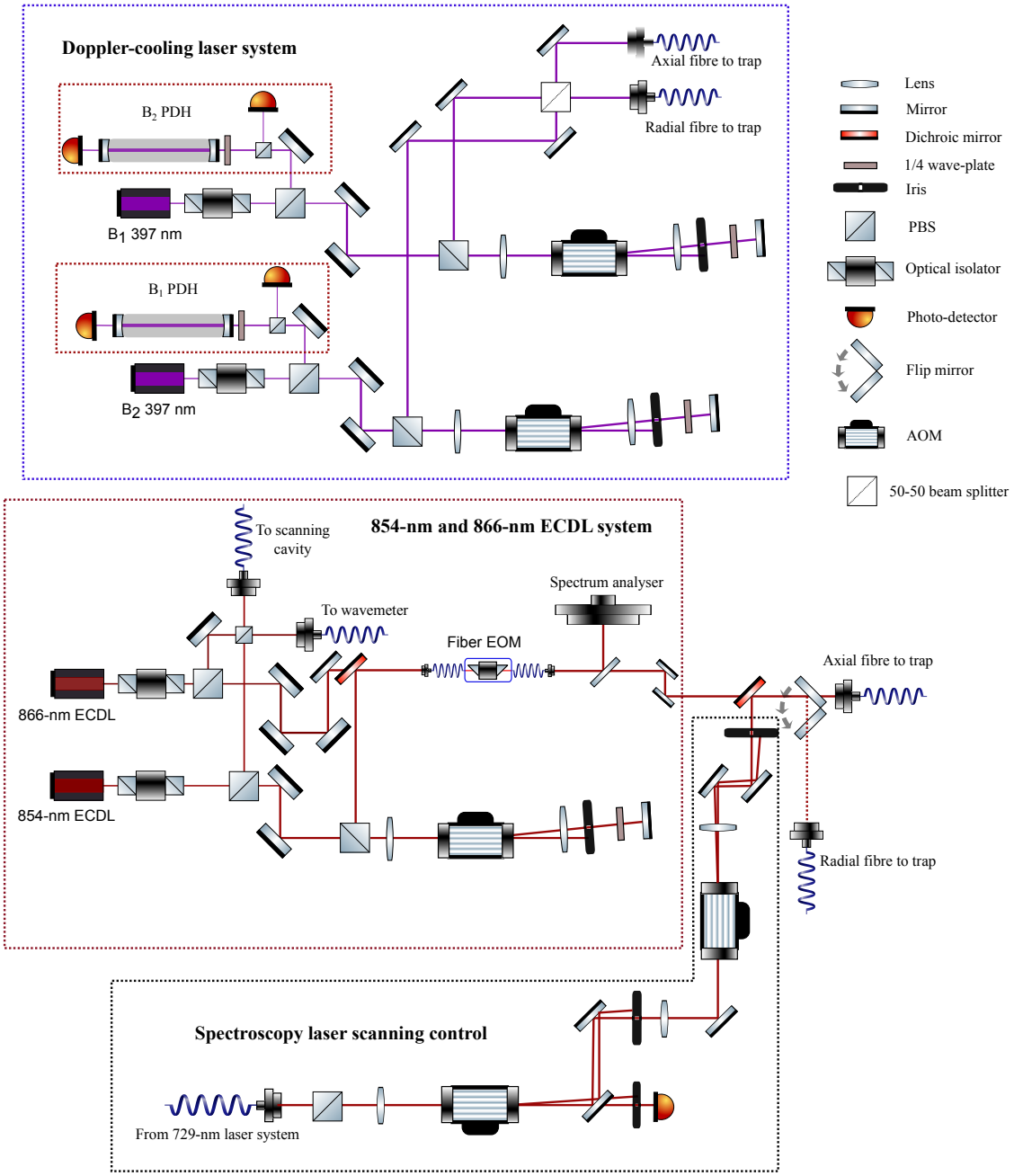


Figure 4.7: A layout of the optical system and beam path for the calcium ion system.

where ω_l is the input light frequency and ω_{rf} is the RF. In our experiments, it is essential to be able to switch on and off the beam output depending upon requirements for either Doppler cooling or state preparation etc.. Various laser sequences and controls are described in section 4.7.

4.4.3 Laser frequency stabilisation

All five ECDL's mentioned previously are locked to their respective reference cavities or transfer cavities in some cases. Here, I will discuss the methodologies and performances of these stabilisation systems.

Pound-Drever-Hall system for 397-nm laser sources

Both 397-nm laser sources (Doppler cooling lasers) are locked to a pair of low finesse ($F \sim 30$) optical cavities via the Pound-Drever-Hall (PDH) locking mechanism. The locking system was built by G. Stutter [98]. Each cavity provides short-term stability for the respective laser source. Both cavities consist of a pair of mirrors separated by ~ 10 cm with the help of two Zerodur glass spacers. The whole system is kept inside a vacuum chamber, which provides thermal isolation for both cavities. The error signal is generated by modulating the injection current of each laser diode at $\sim$ 10 MHz. Reflected output of the optical cavities is measured with two fast photo detectors. The first order intensity independent error signal is then sent to a loop filter to filter out the 10 MHz modulation and then feeds back to the laser diode to control the frequency drifts. The locking system narrows the linewidth of the laser below 0.5 MHz from 10 MHz. A piezoelectric transducer allows us to adjust the length of the cavity to lock the laser to a suitable cavity mode.

Transfer cavity locking system for Doppler and repumping lasers

Slow drift of the Doppler cooling lasers is removed by locking the laser sources to a transfer cavity (scanning cavity). The transfer cavity contains a high finesse cavity ($\mathcal{F} > 600$) in a confocal configuration. A brass cylinder is used as a spacer, which separates the mirrors by 15 cm. The spacing between the mirrors is varied by applying some voltage to a stack of "piezoelectric transducers" (PZT) attached to each mirror. The transfer cavity is locked to a He-Ne reference laser, which stabilises the length of the cavity against any thermal or mechanical fluctuations. This locking system makes a master and slave configuration, where a master laser beam (He-Ne output) and two slave laser beams (two 397-nm laser beams) are sent through a single optical cavity. The transmitted output of the cavity is then separated by a dichroic mirror and detected on two separate photodetectors, which are used as error signals. A schematic of the transfer cavity locking system is shown in figure 4.8.

The error signals are generated by scanning the length of the cavity, where consecutive longitudinal transmission peaks of the reference laser and slave lasers are detected. The length of the cavity is changed by varying the PZT voltage of one PZT stack by ~ 0.6 times the He-Ne laser wavelength. This produces two consecutive longitudinal transmission peaks of the reference laser at $\lambda/2$ spacing. The spacing of these peaks is used as a reference for the cavity spacing. After locking the cavity, the slave lasers are locked in a similar manner. The schematic of the

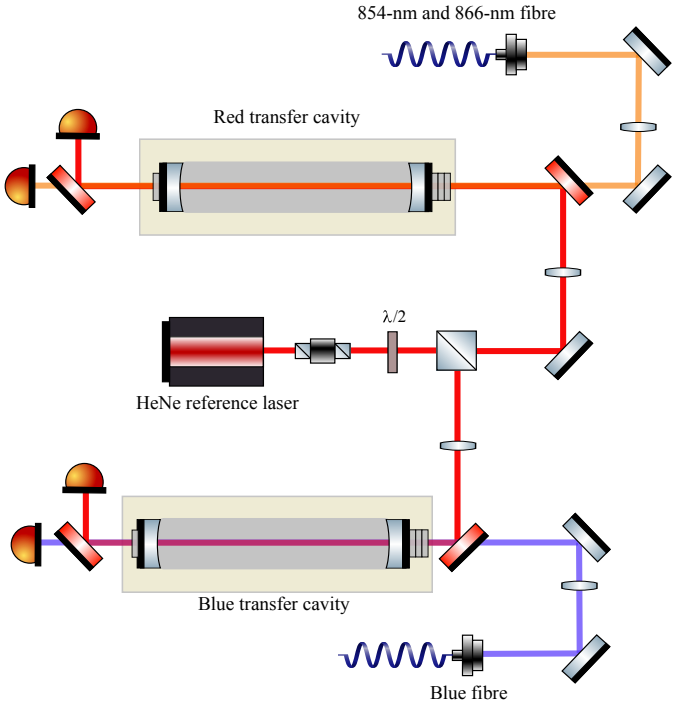


Figure 4.8: Schematic for a transfer cavity (scanning cavity) locking system for 397-nm laser sources.

transmission peaks for the master-slave configuration lock is shown in figure 4.9. The PZT voltage is varied linearly with time (indicated in green) and corresponding peaks appear at different PZT voltages, labelled for the respective laser wavelengths. The peak position indicates that for the specific laser frequency the cavity resonance condition is met at the relevant mirror spacing. If at any time the slave laser frequency changes, the peak position shifts from its previous place, and the feedback system immediately corrects for any frequency change.

The feedback control is carried out by an Arduino, which continuously monitors the transmission peak positions and feeds a control signal to the cavity PZT stack and the slave laser frequency controller. More detail about the scanning cavity locking system can be found in the MRes and PhD theses of Joe Goodwin. In order to passively stabilise the scanning cavity system, the cavity spacer and mirrors are further sealed and actively temperature locked (stability below 1 mK) to avoid any thermally induced refractive index variation. This arrangement removes any frequency drift caused by thermally induced optical path length variation of the laser beams inside the cavity.

A similar transfer cavity locking system is used for 854-nm and 866-nm laser sources. The system contains another slightly lower finesse optical cavity ($\mathcal{F}_{633} \sim 35$), and both lasers are

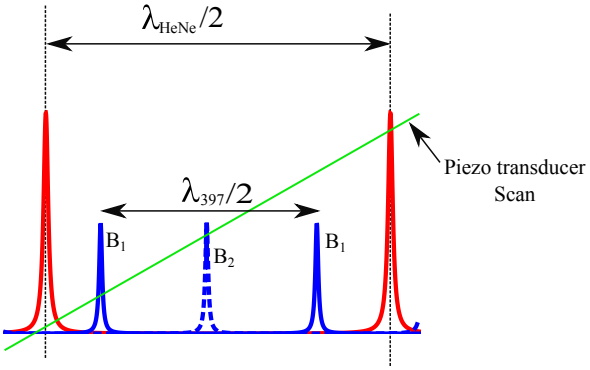


Figure 4.9: Reference laser and a pair of 397-nm laser transmission peaks after passing them through the transfer cavity. The cavity is stabilised with the help of red peaks. The slave lasers are then locked with respect the red peaks.

locked with respect to the master laser transmission peaks. The locking mechanism is similar to that is used for 397-nm laser sources.

Reference He-Ne laser system

As previously mentioned, the transfer cavity locking system requires a He-Ne reference laser. The laser has two orthogonal modes at different frequencies and different polarisations. The mode amplitude, in this case, is temperature sensitive. The laser system is actively temperature stabilised by generating an error signal from the relative intensities of these two orthogonal He-Ne modes. The transfer cavities are locked to one of these modes. The He-Ne system was developed by D. Crick [93] and is stabilised to $\sim$ 0.5 MHz laser linewidth. The slow drifts are also reduced to 0.5 MHz/day. The reference laser system performance is sufficiently good to stabilise the Doppler cooling and repumping lasers.

4.5 Stabilisation of spectroscopy laser system

In a $^{40}Ca^{+}$ ion system, the S $\leftrightarrow$ D clock transition is induced by a narrow linewidth 729-nm laser source. In order to resolve the motional states, the laser linewidth must be smaller than the motional mode spacing. In this section, I will describe the locking system and performance of the 729-nm laser source.

4.5.1 Laser frequency stabilisation

A single mode ECDL system at 729 nm is frequency stabilised through a high finesse reference optical cavity ($\mathcal{F} \approx 60000$). The reference cavity contains a pair of high reflectivity mirrors separated by a 10 cm long ultra-low expansion glass spacer (ULE) and the mirrors are held in

a confocal arrangement. The high finesse cavity acts as reference resonator. As the resonance frequency of an optical cavity depends upon the spacing between the mirrors, it is important to stabilise the spacing. The ULE glass itself has a very low thermal expansion coefficient (CTE $\approx 0 \pm 30$ ppb/C within $\pm 15^{\circ}$ C of the zero crossing point), hence, up to some level, the system is tolerant against thermal fluctuations. In order to enhance the stability, it is advised to temperature stabilise the ULE spacer close to its zero crossing point to reduce the thermal effects.

In our case, the reference cavity is actively temperature stabilised at 14.6° C via a thermoelectric cooler (TEC) and a servo lock which controls the TEC current. The locking system controls the TEC current depending upon thermal fluctuations. The cavity is kept below room temperature ($24 \pm 2^{\circ}$ C), hence only cooling of the cavity is essential. The reference cavity is kept inside a vacuum chamber and is continuously evacuated with an ion-pump maintaining below 10^{-7} mbar pressure inside the chamber. This additional precaution reduces the optical path length variation due to the ambient temperature or pressure fluctuations. Otherwise, any change in temperature or pressure changes the refractive index of the air, hence, the optical path length of the light passing through the cavity changes.

The locking approach is based on the PDH technique. If an unstable laser beam is passed through the stable reference cavity, the transmitted or reflected light output varies with the laser frequency. The locking method requires the light to be frequency modulated in order to eliminate intensity-based fluctuation of the transmitted or reflected output. The error signal is produced by the reflection output signal of the frequency-modulated laser beam. A detailed description of the locking method can be found in various references [32, 108]. In our system, the frequency sidebands are created with an EOM. The EOM is driven by a local oscillator at 13.47 MHz frequency. Subsequently, the reflected beam from the cavity mirrors is detected on a fast photodetector. The detected signal is then mixed with the local oscillator signal (at 13.47 MHz) with appropriate phase. The mixer output is then passed through a low pass filter. The generated control signal is then used to alter the injection current to correct for any laser frequency noise. Additionally, the transmission signal is used to control the grating PZT position inside the ECDL system to avoid any frequency offset. A schematic of the spectroscopy ECDL and locking system along with the tapered amplifier system is shown in figure 4.10.

The performance of the laser frequency lock mainly relies on the finesse of the reference cavity. As a rule-of-thumb, the laser linewidth decreases by increasing the finesse ($\mathcal{F}$) of the cavity. In our laboratory, the cavity is manufactured by REO[3] and claimed to have $\mathcal{F} = 250000$. Moreover, the finesse of the cavity has been measured through a cavity ring-down technique, very recently. The ring-down output of the cavity is measured via a fast photodetector and it is shown in figure 4.11. The estimated decay time from the fit comes to be 6.4 μs, which gives $\mathcal{F} \approx 60000$. This reduction in cavity performance is attributed to the degradation of the coating of the mirrors with time. The linewidth of the cavity resonance at this finesse is estimated to be 25 kHz, which locks the laser to below 1 kHz linewidth.

[3] www.reoinc.com

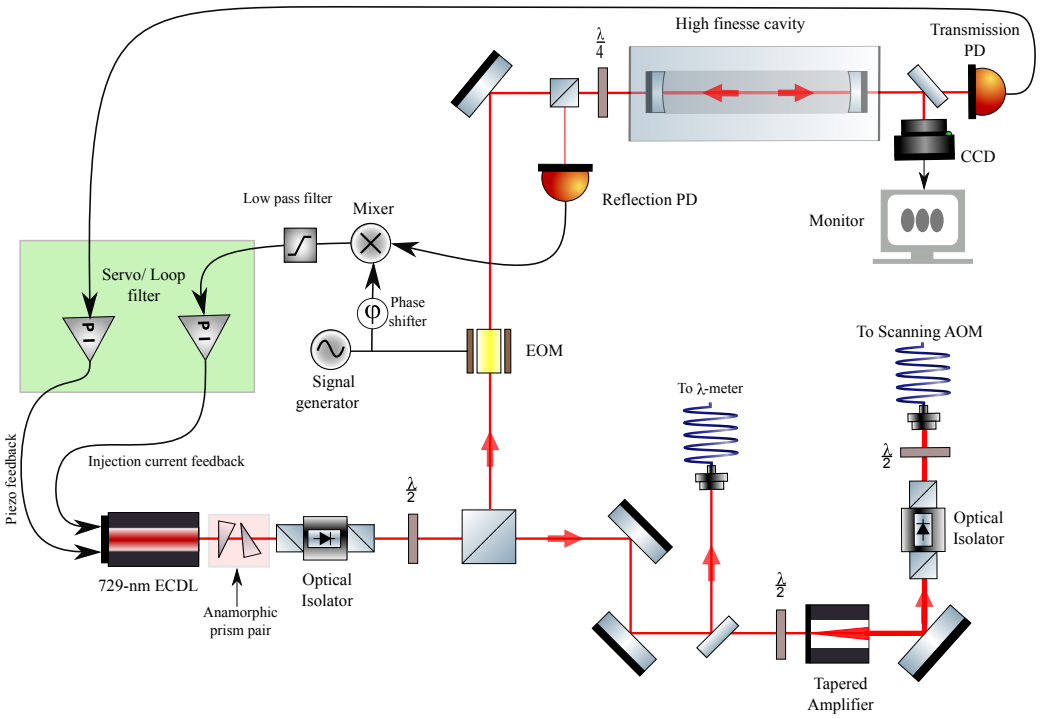


Figure 4.10: The figure shows the optical layout of the 729-ECDL system.

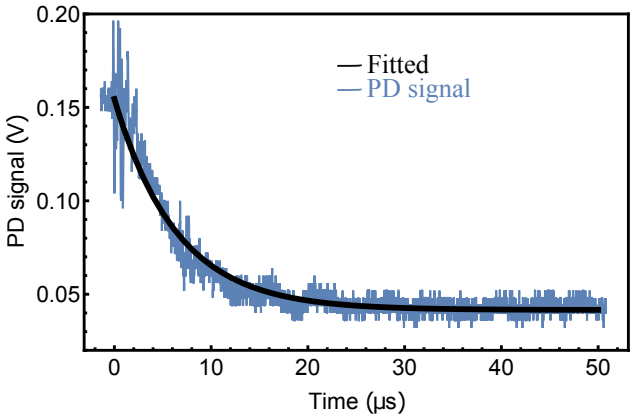


Figure 4.11: The ring-down output of the ultra-stable cavity that is used to stabilise the 729-nm laser.

4.5.2 Frequency drifts and linewidth measurement with a trapped ion

The linewidth of a laser source is defined as the width of the optical power spectrum. In practice, it is not possible to measure the linewidth of a narrow-linewidth laser source with an optical spectrum analyser. Instead, a direct linewidth measurement is carried out with two laser sources, a reference laser and an unknown laser. If these two laser beams are detected on a photodetector then the full width at half maximum (FWHM) of the beat output gives the sum of the linewidth

of both lasers. In order to precisely measure the linewidth, the reference laser linewidth must be narrower than the unknown laser source. The main problem with this method is to find a narrow linewidth laser source. In our laboratory, the direct measurement of the 729-nm laser is not possible due to the unavailability of any narrow-linewidth laser source.

In order to measure the linewidth of the 729-nm laser, we perform spectroscopy on a quadrupole transition of a trapped calcium ion. Ideally, the quadrupole transition of a single trapped calcium ion can be treated as a high Q factor resonance system. The natural linewidth of the S-D transition is 0.16 Hz, hence it acts as an ideal reference system for the linewidth measurements. In our system, a ground state cooled calcium ion is interrogated with the 729-nm laser and a spectrum is recorded. Power broadening of the transition is avoided by performing the spectroscopy with a low-intensity laser beam. The laser power is reduced below 1% of its normal operational value. The spectrum of the carrier transition of a ground state cooled calcium ion is shown in figure 4.12. The fitting is conducted with a Lorentzian function and the FWHM is estimated to be 530 $\pm$30 Hz. The estimated value suggests that the laser linewidth is 530 Hz. As the estimated value may have some contributions from magnetic field noise in the system, therefore the actual laser linewidth will be less than 530 Hz.

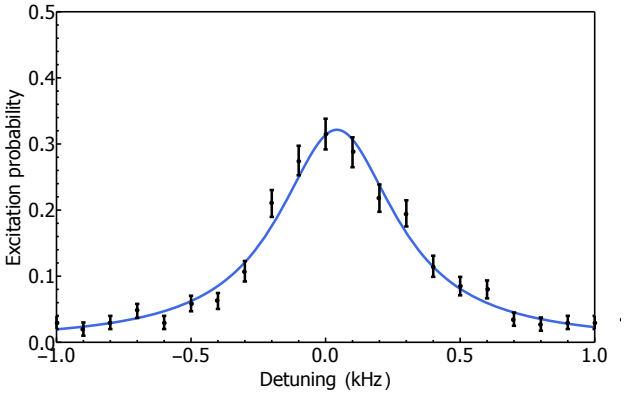


Figure 4.12: A spectrum shows the lineshape of a calcium ion transition, using the 729-nm laser source. For the current experiment, sideband cooling is performed for 21 ms and the laser interaction is carried out for 3 ms.

In future, a direct measurement of the laser linewidth could be carried out through a self-heterodyne technique discussed in reference [109]. This technique relies on a beat output of two parts of the same laser beam, one part is passed through an AOM and the other part is delayed by passing it through a long optical fibre. The purpose is to provide enough delay between two parts of the laser beam so that the beat note becomes uncorrelated. Thus the width of the beat note spectrum refers to a true laser linewidth.

The linewidth of a laser takes account of any fast frequency or phase noise in the system. However, the system might have some drifts, leading to a slow change in the laser frequency. The slow drifts of the laser frequency limit the ability to perform the required coherent manipulation. The drifts are mainly caused by mechanical or thermal effects to the reference cavity or laser source. In the current system, the reference cavity is temperature stabilised up to 0.2 mK, which

corresponds to $\Delta f \approx 60$ Hz. Additionally, frequency drift is caused by the relaxation of the cavity spacer due to its ageing. In order to estimate the drifts, we perform a direct measurement of the frequency variation using a single trapped calcium ion. Such a plot indicating carrier frequency drift of the system with time is shown in figure 4.13. The plot contains the data for 7 months, between October 2015 and May 2016. The carrier frequency shown in the plot corresponds to the actual DDS frequency. The frequency must be doubled for the calculation due to the double-pass configuration of the AOM. The fitting suggests that we have roughly 1.45 kHz drift per day. It is attributed to the combined effects of the magnetic field variation and the change in the cavity spacing due to the creeping of the ULE spacer with time. In our experiments, we correct for these drifts by experimentally measuring the carrier frequency before running any coherent control. Sometimes, during the day the carrier frequency needed to be recorded multiple times and appropriate corrections are made. In our experiments, the carrier frequency change is observed up to 5 kHz during the course of a couple hours. The exact reason of carrier drift is not known to us for now.

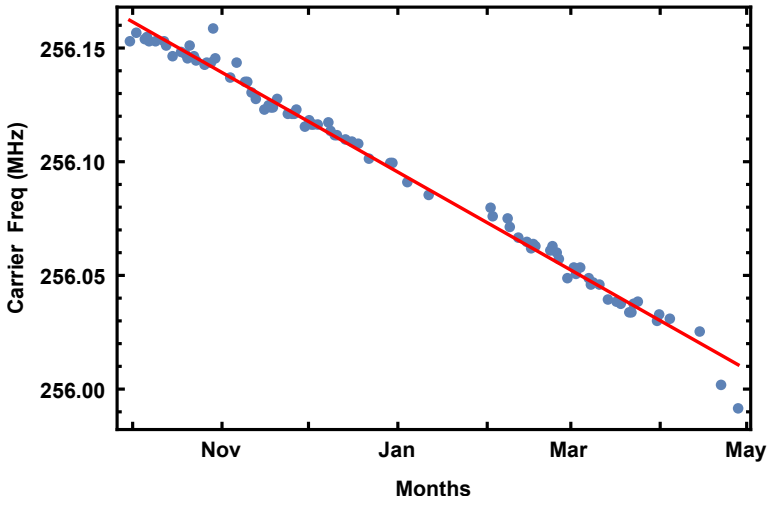


Figure 4.13: The figure shows the variation of carrier frequency with time. Blue data points indicated experimentally recorded carrier frequency values and red is the fitted curve to these data points.

4.5.3 Intensity stabilisation of the spectroscopy laser

In addition to the frequency stability, controlled coherent manipulation of atomic ions requires a constant intensity of the spectroscopy laser beam at the ion. In our laser system, the major source of intensity noise is introduced due to thermal and mechanical effects at the laser head. Additionally, the laser beam is guided through an optical fibre and any thermal effects will change the intensity or the polarisation of the laser beam. Specifically, an optical fibre introduces polarisation noise in the laser field, which eventually turns into the intensity noise if it is passed through a PBS.

Usually, the laser intensity is stabilised via a feedback control system along with an optical

component that can control the output beam intensity. The simplest method is to send a laser beam through an AOM and vary the RF power to the AOM for any intensity fluctuations. Here, I will describe a home built intensity noise-eater system that is used for the spectroscopy laser source. The feedback system uses a proportional-integral (PI) electronic circuit, which generates a control signal for a frequency generator. The frequency generator eventually controls the RF power, which controls the intensity of the laser beam by controlling the first order output of the AOM. A schematic of the intensity noise eating system is shown in figure 4.14. The circuitry that is used to generate the control signal is shown in appendix C.

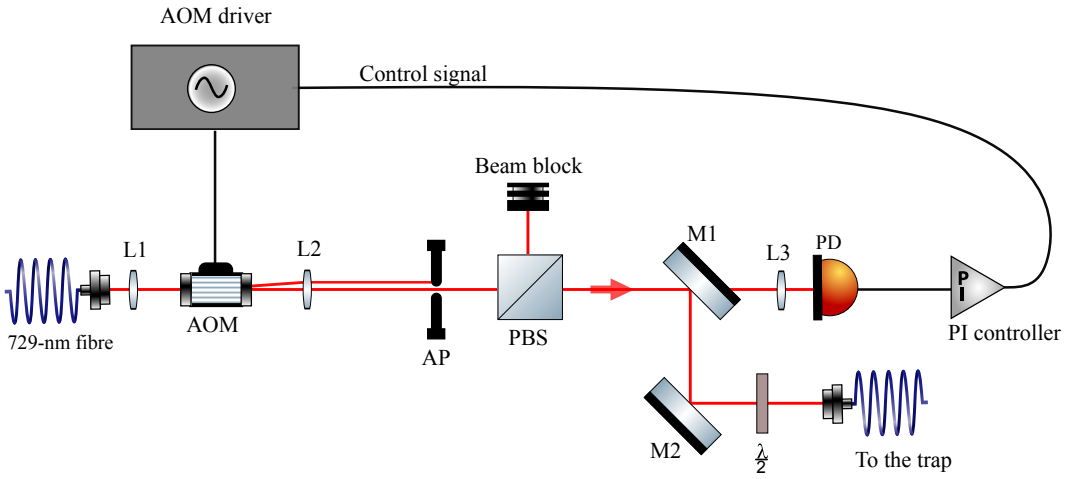


Figure 4.14: A schematic of the noise-eater system that is used to stabilize the 729-nm laser output. The mirror M1 is a leaky mirror and typically leaks 1% of the total power. The 0^{th} order output of the AOM is sent to a photo detector after passing through M1. The control signal is generated by a PI controller which subsequently modulates the output of the AOM driver.

The performance of the intensity lock is analysed by noting the power fluctuation of the laser output. The power fluctuation of the spectroscopy laser beam is measured with a power meter, before and after implementing the intensity stabilisation system. The measured noise is roughly 10 $\%$ of the total power without implementing the feedback system. The time variation of the laser power is shown in figure 4.15. After installing the feedback system the intensity noise is reduced to $< 0.2\%$, which corresponds to roughly 0.1% Rabi frequency noise of the transition. In our experiments, fast intensity noise limits the optical coherence time of the qubit. Similarly, the slow drift affects coherent control by introducing error in the laser pulses. In our experiment, we are more interested in the slow intensity noise, because each data point in the spectrum takes tens of seconds.

In the current feedback system, the main limiting factor is the stable reference signal which is used to create the error signal in the PI controller circuit. The current system has a voltage reference source stable up to 0.1%, which is good enough for the required intensity fluctuations. Also, the AOM bandwidth is 1 MHz, hence any intensity noise faster than 1 μs cannot be eliminated through this system. The mechanical or thermal effects are slow hence the locking system provides good stabilisation against these effects. The output laser power is always smaller than that of the input value because of the losses and the first order deflection. In order to account

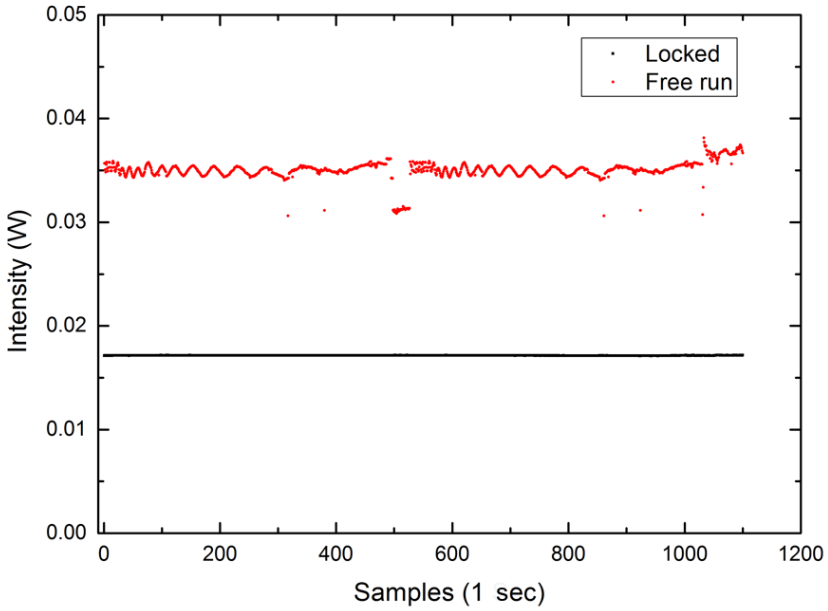


Figure 4.15: The figure presents the intensity fluctuation readout of the 729-nm laser source. The intensity is locked to approximately half of its initial value to account for the larger drifts. The curve in red corresponds to the readout without implementing the feedback control and the curve in black corresponds to the readout with feedback control.

for larger intensity variation, the intensity is locked to approximately 50 to 70 % of the total intensity.

4.6 Optical control and detection system

4.6.1 Trap optics

A description of the laser system and stabilisation has been given in the previous section. The experimental control of the laser beams is carried out by various AOM's on the optical table, which are later sent to a breadboard near to the trapping assembly via polarisation maintaining (PM) fibres. At the breadboard, various laser beams are mixed together and focused through their respective lenses. The focused beams are then sent to the trap centre from the axial and radial directions. A complete schematic of the optical arrangement at the trap is shown in figure 4.16. Two separate 397-nm laser beams are used to perform Doppler cooling in the axial and radial directions. A dichroic mirror is used to mix the 397-nm laser beams with the repump/spectroscopy laser beams which then propagate along the axial direction. Additionally, while performing radial spectroscopy, the spectroscopy laser beam is mixed with the 397-nm radial beam and sent to the trap. The ionisation laser beam is focused to the trap centre via a lens and propagates along the axial direction from above the trap.

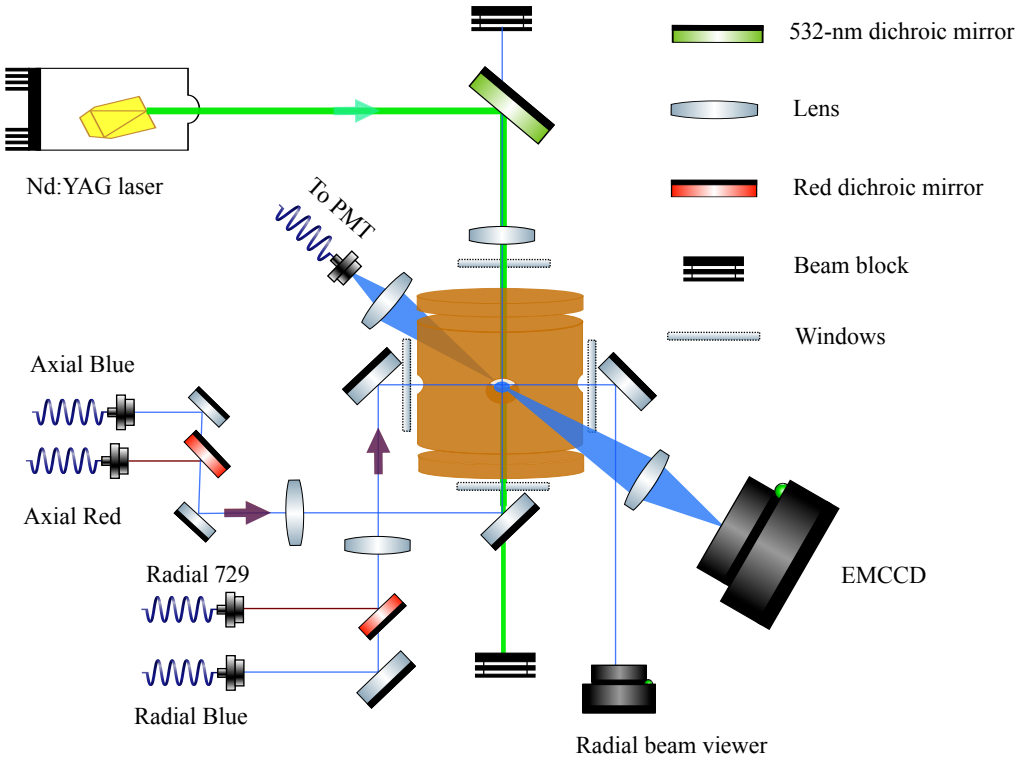


Figure 4.16: The figure shows layout of the trap assembly, laser beam propagation and various optical components used in the system. The mirrors guiding the fluorescence signal are not shown in the figure for simplicity.

The scattered photons from the ions are collected through two high numerical aperture lenses placed next to two diagonally opposite holes in the ring electrode and then guided with the help of mirrors and other optical components. Due to the strong magnetic field, it is not possible to place the PMT's or the EMCCD anywhere close to the trap assembly. Hence, the scattered light is focused onto two multimode fibres and then sent to the PMTs located elsewhere. The EMCCD requires preservation of spatial information of the ions. Hence, a fibre cannot be used to guide the light to a distant location. Instead, a periscopic optical setup is used to guide the scattered light. The system was designed by Jieyi Liu [110] and Graham Stutter[98].

4.6.2 Radial beam viewer and control

Efficient Doppler cooling of the radial motion in a Penning trap requires a good control of laser beam pointing at the ions. The radial beam is steered by a piezo-controlled mirror. The beam position is then viewed on a webcam located on the breadboard collecting the beam from its exit path. The webcam-based viewer for the radial beam pointing replaces the previous quad-photodiode system developed by Sandeep Mavadia. The viewer was assembled by me and uses standard MATLAB coding to provide the user interface. The reassembled webcam along with

the viewer is shown in figure 4.17. The piezo-controlled mirror steering system is procured from “Newport" and is controlled by the experimental computer.

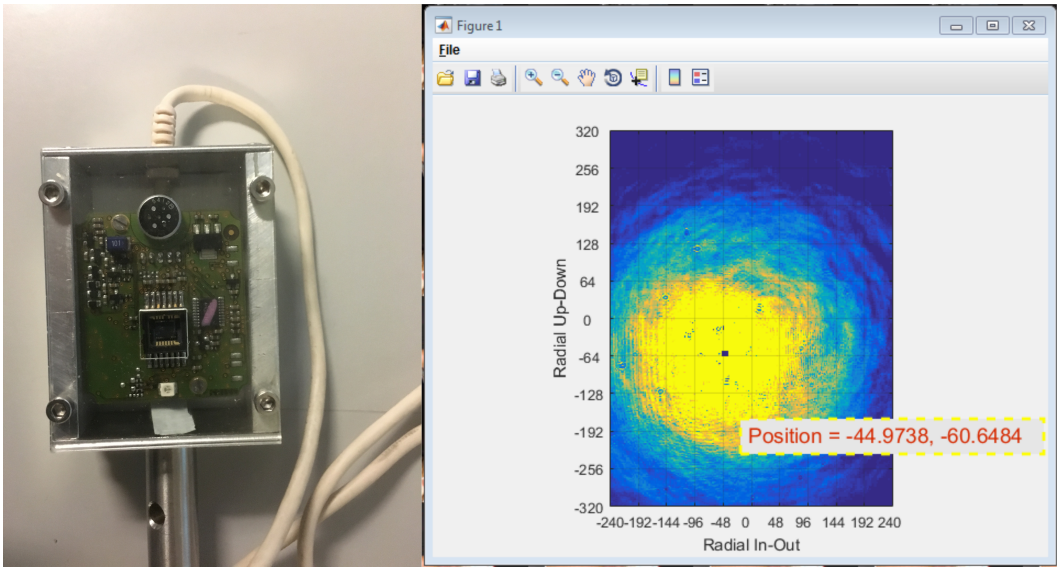


Figure 4.17: Webcam based radial beam viewer.

4.6.3 Detection efficiency and background measurement

Two PMTs operating in photon counting mode are used to detect the fluorescence of the trapped ions. The quantum efficiency of each PMT is roughly 20%. Due to the limited numerical aperture lenses and propagation losses in optical fibres, the collection efficiency of the optical detection is not very good. Each PMT, on an average, detects only 0.7 photons out of $\sim 10^4$ photons that are scattered in one ms.

State readout of the ion is carried out by looking at the collected photon distribution. During spectroscopy, depending upon the excitation probability, the ion is shelved in the metastable state or it stays in the ground state. The readout of ion the state is then carried out by illuminating the ion with the 397-nm laser beams. Depending upon its occupancy in the ground state or excited state, either fluorescence or just the background counts are recorded by the PMTs. During detection time, the current detection scheme allows us to generate a histogram of collected photons.

The state readout involves setting a threshold to distinguish the bright or dark events. A histogram of collected photons for 10 ms of detection time is shown in figure 4.18. Evidently, the photon distribution follows two distinct peaks, each with Poisson type statistics. These peaks correspond to either the “bright" state of the ion (fluorescing) or the “dark" state of the ion (not fluorescing). Ideally, the dark state would have zero photons, but due to the background photons the distribution peaks around a non-zero value. The background counts are mainly detected due to the direct scattering/reflection of the 397-nm laser beams when they pass through apertures or windows in the trap assembly. Especially, the radial laser beam passes through two

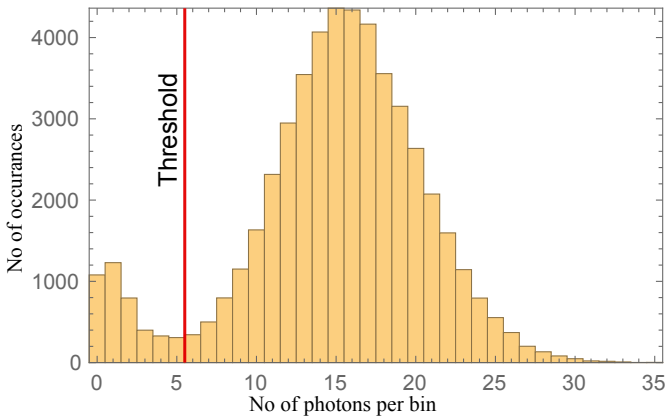


Figure 4.18: Distribution of PMT counts during 10 ms detection time.

4-mm apertures in the ring electrode, which generates the majority of background counts in our system. The overlap between background counts and fluorescence counts introduces some error during state detection, which is unavoidable.

Additionally, in a Penning trap, the state detection inherits some extra error due to the J-mixing effect. Due to this effect, the transition $P_{1/2} \rightarrow D_{5/2}$ is not strictly forbidden, thus the ion can decay to the $D_{5/2}$ state during detection time and will then become dark. The error becomes unavoidable if the probability of bright to dark transition is finite. A simulated histogram of photons during state readout is shown in figure 4.19. In this simulated plot, the parameters are considered to be relevant to our system. The expression for the J-mixing rate can be found in Sandeep Mavadia's thesis. For typical experimental conditions, J-mixing adds up to 4% error in the state readout. Apart from that, approximately 1% error is introduced by the tail of the bright distribution adding to the dark distribution.

The J-mixing error can be reduced by decreasing the background counts, because in that case the threshold can be set to a lower value. In order to reduce the dark counts, we have introduced an AOM to attenuate the radial beam power during the readout of the ion. The majority of florescence counts are generated by the axial beam, thus reducing the radial power does not affects the count rate. However, radial Doppler cooling is essential for the experiments, hence it is kept on for Doppler cooling. By doing so, during readout, the radial 397-nm beam power is reduced to 4 μW from 12 μW, hence the background counts are reduced by factor of three. A similar trick was adapted during the radial spectroscopy, where the axial Doppler cooling laser intensity was initially reduced in order to get better Doppler cooling of the radial motion. Later, the axial power was increased for the readout sequence, which increased the bright counts, hence increasing the readout fidelity.

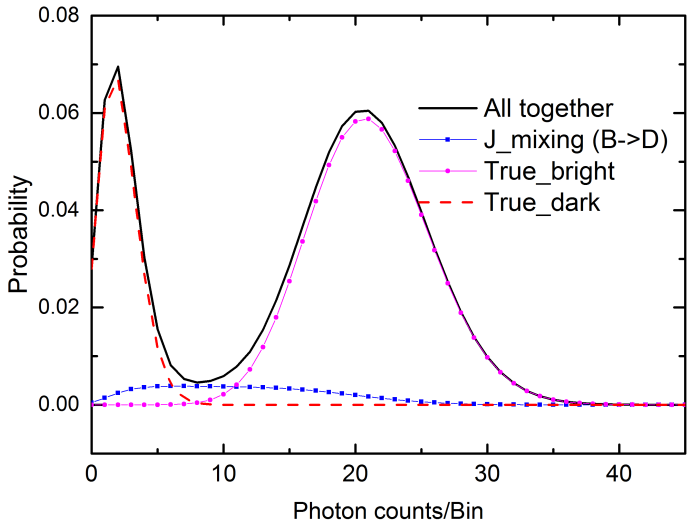


Figure 4.19: A simulated plot of photon counts during state detection of a trapped calcium ion. The blue line corresponds to the detected photons due to J-mixing events, which impose error during state detection of the ion.

4.7 Experimental control

A field-programmable gate array (FPGA) is used to control the various RF switches and the optical detection of trapped ions. The laser beams are toggled via AOMs, which respond according to the outputs of the RF switches. A layout of experimental control using an FPGA system is shown in figure 4.20. The FPGA provides various TTL signals for the Doppler cooling lasers, 854-nm laser and the 729-nm laser outputs. The 866-nm laser beam is continuously sent to the trap and does not impose any restriction while performing coherent control of the trapped ions. The Doppler cooling and repumping laser beams are diffracted by three AOM's in double pass configurations, which are powered by three VCO's each providing a fixed amplitude RF at 80 MHz drive frequency.

The current FPGA control system does not provide any frequency selectivity for the laser outputs. The Doppler cooling and repumping laser beams as such do not require automated frequency control, but for spectroscopy, it is essential to have frequency control of the laser output. Frequency control of the spectroscopy laser is provided by a scanning AOM, whose first order diffracted output is frequency shifted from the incoming laser beam. The frequency shift, in this case, is equal to the frequency of the RF signal fed to the AOM. A direct digital synthesis (DDS) generator provides a variable frequency RF signal to control the scanning AOM output. An Arduino is used to control the frequency, phase and amplitude of the DDS at the call of the experimental computer. The Arduino sends the required tuning words to the DDS, which accordingly changes the parameters of the RF signal.

The computer control of the DDS through the Arduino takes roughly half a second. This long

communication time is not a problem while performing spectroscopy because each frequency point itself takes roughly 15 seconds to record the respective information. More importantly, fast control of the laser frequency during the coherent manipulation of trapped ions is provided by toggling the DDS output between various profiles. The parameters for these profiles are set according to the user requirement at the beginning of the experimental run.

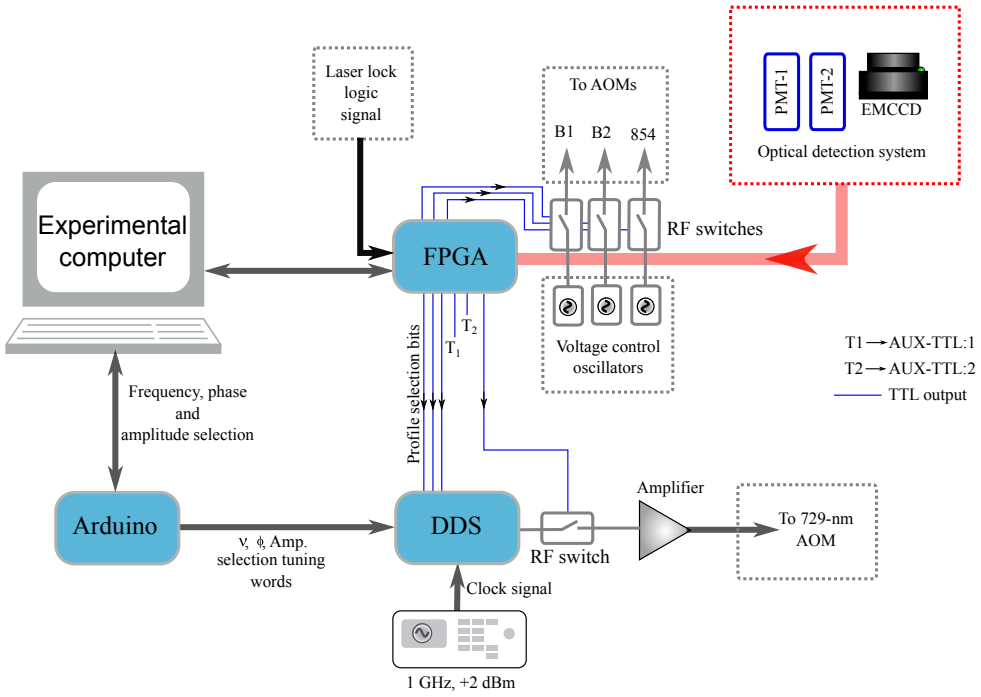


Figure 4.20: Schematic of the experimental control system.

The computer interface to the FPGA is provided by a C# coded framework. The majority of the C# framework is the same as described in previous theses, references [32, 91, 98], but has been modified many times since the original code was written. The framework allows us to compile and upload the required pulse sequences to the FPGA memory. The FPGA control is designed to read the instructions from the experimental computer in order to set the pulse timing, type of operation and references to the TTL pins. The required information is coded into a 24-bit phrase, which is then sent to the FPGA via a USB cable and uploaded into the FPGA memory. More detail about the experimental control can be found in reference [32, 91].

The laser sequence and instructions vary from one experimental run to the other. We often generate these sequences through the spectroscopy control pane designed to run the experiment. Typical laser sequences for spectroscopy after Doppler cooling and sideband cooling are shown in figure 4.21. Some of the experimental sequences will be described in later chapters.

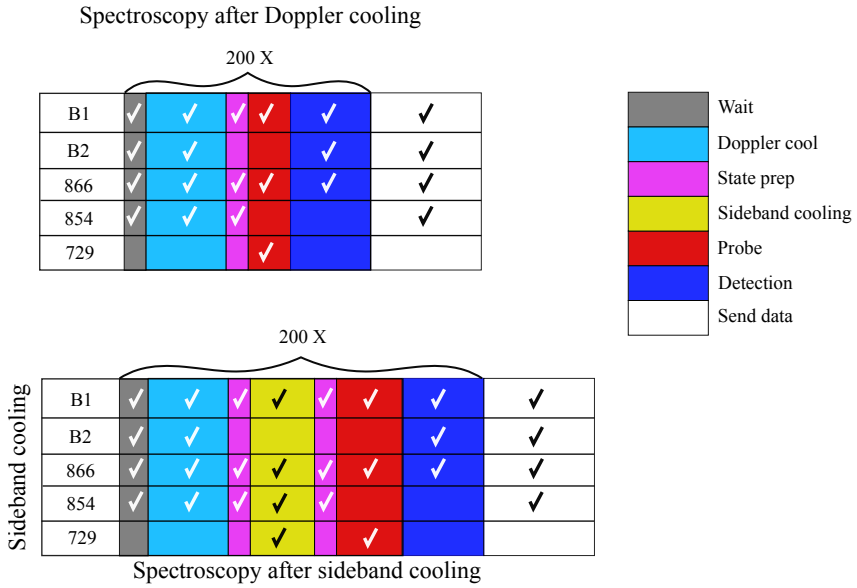


Figure 4.21: Layout of laser sequences for spectroscopy after Doppler cooling and sideband cooling of trapped ions.

Chapter 5

Simulation studies of sideband cooling of trapped ions in a Penning trap

Resolved-sideband cooling is a technique to prepare trapped atoms or atomic ions in their vibrational ground state. The technique generates an ideal quantum system in which high fidelity operations can be carried out. Often, a narrow linewidth laser beam or microwave radiation is used to manipulate the motional and electronic states of trapped atomic ions [44, 111]. In this chapter, I will present simulation studies of the resolved sideband cooling of trapped ions in a Penning trap. Such simulation studies have not been performed before, especially for the case where the system lies far outside the L-D regime. In the situation when the system lies outside the L-D regime, various mechanisms affect the sideband cooling rate and it leads to a poor occupation in the ground state of motion. It is important to consider two aspects while performing resolved sideband cooling; the highest achievable ground state occupancy and cooling time. More importantly, the highest possible occupancy in the ground state for the shortest cooling time is of paramount importance for us; hence the optimisation of the cooling parameters is necessary. Preliminary simulations of sideband cooling in a Penning trap are discussed by F. Beck [112] in her master's thesis. The work discussed in my thesis shows extension of her work.

5.1 Theory of resolved-sideband cooling of a trapped calcium ion

In our Penning trap, the highest trap frequency is limited by the fixed value of the applied magnetic field (which is currently set to 1.9 T). At this magnetic field, a trapped calcium ion can have $\omega_z < 515$ kHz, $\omega_- < 365$ kHz and $\omega_+ < 729$ kHz. For these frequencies, the system lies outside the L-D regime after Doppler cooling. Specifically, these operating conditions motivated us to perform simulation studies. The main focus of these studies will be to optimise the cooling dynamics for trapped calcium ions. However, the studies can be extended to any other system of similar trapping conditions.

5.1.1 A three-level atom

For sideband cooling of a calcium ion, we are mainly interested in the $S_{1/2}$, $P_{3/2}$ and $D_{5/2}$ atomic levels. Such a three-level atomic system is illustrated in figure 5.1. The parameters such as Rabi frequency, spontaneous decay rate and laser detuning are indicated by Ω_i, Γ_i and Δ_i, respectively. The index i is used to indicate 729-nm, 854-nm and 393-nm transitions. Sideband cooling of a calcium ion in an RF trap is exactly identical to this scheme. However, in a Penning trap, due to the presence of the magnetic fields, it is no longer a three-level atomic system. For simplicity, I will retain the three-level atomic model in our studies and I will make appropriate adjustments to the model in order to incorporate the additional complexity.

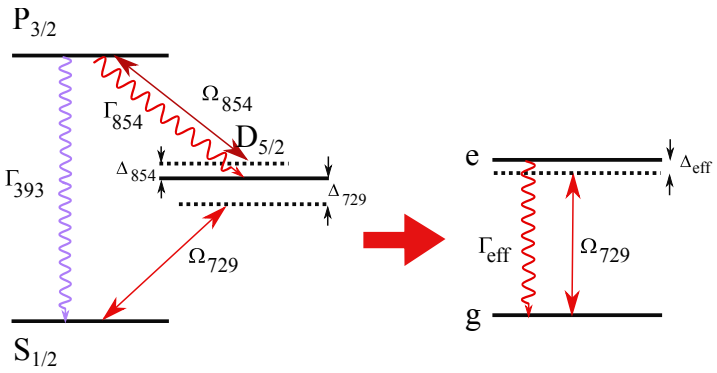


Figure 5.1: Partial energy level diagram of a calcium ion with required transitions involved in the resolved sideband cooling (left). An equivalent two-level schematic is shown in the right side.

The time evolution of the population in an atomic system is described by a master equation [113]

$$\frac{d\rho(t)}{dt} = -i\left[H(t), \rho(t)\right] + \mathcal{L}\rho(t), \tag{5.1}$$

where ρ is the density matrix for the atomic system[1]. The spontaneous decay term is denoted by $\mathcal{L}$, the Liouvillian operator, and is expressed as

$$\mathcal{L}\rho = \frac{\Gamma}{2}(2\sigma_-\tilde{\rho}\sigma_+ - \sigma_+\sigma_-\rho - \rho\sigma_+\sigma_-), \tag{5.2}$$

where Γ is the spontaneous decay rate of the excited state and $\sigma_+(= |e\rangle\langle g|)$, $\sigma_-(= |g\rangle\langle e|)$ are Pauli spin matrices. In our system, the Liouvillian term will correspond to the 393-nm decay and 854-nm absorption, as indicated in figure 5.1. The momentum transfer to the trapped ion, during the emission of the photons, is taken care of by $\tilde{\rho}$ and is expressed as

$$\tilde{\rho} = \frac{1}{2}\int_{-1}^{1} d(\cos\theta)\mathcal{W}(\cos\theta)e^{ik\cos\theta r}\rho e^{-ik\cos\theta r}, \tag{5.3}$$

[1]For the sake of simplicity, $\hbar$ will be omitted by assuming it to be 1.

where the term $\mathcal{W}(\cos\theta)$ is used to account for the angular distribution of the emitted photons about the quantisation axis and k is the wave-vector amplitude of the emitted photons. For uniformly distributed photons, the angular distribution function $\mathcal{W}(\cos\theta)$ is unity. On the other hand, for the dipole allowed transitions ($\Delta m_j = \pm 1$) the term is expressed as $\mathcal{W}(\cos\theta) = \frac{3}{4}(1+\cos^2\theta)$.

For the sake of simplicity, the three-level system will be reduced to a two-level equivalent. The laser absorption and decay between the atomic levels D and P will be included in the form of an effective decay rate Γ_{eff} of the $D_{5/2}$ level. In the limit of low saturation, Γ_{eff} is expressed as [114]

$$\Gamma_{\text{eff}} = \frac{\Omega_{854}^2}{4\Delta_{854}^2 + (\Gamma_{393}+\Gamma_{854})^2}\Gamma_{393}, \tag{5.4}$$

where Ω_i, Δ_i and Γ_i are the transition parameters as indicated in figure 5.1. It is also important to incorporate the light-shift caused by the 854-nm laser light, which shifts the $D_{5/2}$ level from its actual position; hence the detuning of the 729-nm laser changes. The new detuning of the 729-nm transition for the reduced two-level atom is given as

$$\Delta_{\text{eff}} = \Delta_{729} - \Delta_{854}\frac{\Omega_{854}^2}{4\Delta_{854}^2 + (\Gamma_{393}+\Gamma_{854})^2}. \tag{5.5}$$

It may be argued that the population decay from the $P_{3/2}$ level is instantaneous; hence the atomic coherence can be neglected while making the reduction of the three-level atom into a two-level equivalent [115]. The new two-level system parameters are denoted as Ω_0, Γ_{eff} and Δ_{eff} and are indicated in figure 5.1. The master equation for the new system can be written as

$$\begin{aligned}\frac{d\rho(t)}{dt} &= -i\frac{\Omega_0}{2}\left[|g\rangle\langle e| + |e\rangle\langle g|, \rho\right] - i\Delta_{\text{eff}}\left[|e\rangle\langle e|, \rho\right] \\ &\quad + \frac{\Gamma_{\text{eff}}}{2}(2|g\rangle\langle e|\tilde{\rho}|e\rangle\langle g| - |e\rangle\langle e|\rho - \rho|e\rangle\langle e|).\end{aligned} \tag{5.6}$$

In this equation, the element $\tilde{\rho}$ takes account of the momentum transfer due to the absorption of the 854-nm laser photons.

Let us now add the motional states in the two-level atomic system. In a two-level trapped atom, the laser-induced coupling between internal and external states is given by

$$\Omega_{n,n'} = \Omega_0 \langle n'| e^{-i\eta(a+a^\dagger)} |n\rangle, \tag{5.7}$$

where a and $a^\dagger$ are the raising and lowering operators for the harmonic states and η is the L-D parameter as defined in chapter 2. The rate equation for the population evolution between

internal and external states (from $n' \rightarrow n'' \rightarrow n$) is derived as [116] [2]

$$\begin{aligned}\frac{\mathrm{d}}{\mathrm{d}t}\langle n|\,\rho_{ee}\,|n'\rangle &= -(-i\delta n\,\omega_z + \Gamma_{eff})\,\langle n|\,\rho_{ee}\,|n'\rangle \\ &- i\frac{\Omega_0}{2}\sum_{n''}\left(\tilde{\Omega}^*_{n,n''}\,\langle n''|\,\rho_{ge}\,|n'\rangle - \tilde{\Omega}_{n'',n'}\,\langle n|\,\rho_{eg}\,|n''\rangle\right),\end{aligned} \tag{5.8}$$

$$\begin{aligned}\frac{\mathrm{d}}{\mathrm{d}t}\langle n|\,\rho_{gg}\,|n'\rangle &= i\delta n\,\omega_z\,\langle n|\,\rho_{gg}\,|n'\rangle \\ &- i\frac{\Omega_0}{2}\sum_{n''}\left(\tilde{\Omega}_{n,n''}\,\langle n''|\,\rho_{eg}\,|n'\rangle - \tilde{\Omega}^*_{n'',n'}\,\langle n''|\,\rho_{ge}\,|n\rangle\right) \\ &+ \Gamma_{\text{eff}}\sum_{n'',n'''}\langle n''|\,\rho_{ee}\,|n'''\rangle\,\frac{1}{2}\int_{-1}^{1}\mathrm{d}(\cos\theta)\tilde{\Omega}_{n,n''}(\eta_s\cos\theta)\mathcal{W}(\cos\theta)\tilde{\Omega}_{n''',n'}(\eta_s\cos\theta),\end{aligned} \tag{5.9}$$

$$\begin{aligned}\frac{\mathrm{d}}{\mathrm{d}t}\langle n|\,\rho_{eg}\,|n'\rangle = \frac{\mathrm{d}}{\mathrm{d}t}\langle n'|\,\rho_{12}\,|n\rangle^* &= -i(-\delta n\,\omega_z + \Delta_{\text{eff}} - i\frac{\Gamma_{\text{eff}}}{2})\,\langle n|\,\rho_{eg}\,|n'\rangle \\ &-i\frac{\Omega_0}{2}\sum_{n''}\left(\tilde{\Omega}_{n,n''}\,\langle n''|\,\rho_{gg}\,|n'\rangle - \tilde{\Omega}^*_{n'',n'}\,\langle n|\,\rho_{ee}\,|n''\rangle\right),\end{aligned} \tag{5.10}$$

where $\tilde{\Omega}_{n,n'}(=\Omega_{n,n'}/\Omega_0)$ is redefined for normalised Rabi strength for transitions between motional states n to $n'(=n+\delta n)$ of the trapped ion. The diffusion term is simplified as $\tilde{\Omega}(\eta_s\cos\theta)$, where η_s is the L-D parameter of the emitted photons and is multiplied by $\cos\theta$ to account for the geometrical contribution of the momentum transfer. For sideband cooling simulation, the main interest is to estimate the change in phonon number, hence the time evolution of the population between atomic states will be neglected. Arguably, during sideband cooling, the population from state $|e\rangle$ decays into $|g\rangle$ at a rate $\Gamma_{\text{eff}} >> \Omega_{n,n'}$; therefore an adiabatic elimination of the excited state is possible [83]. The resultant rate equation for the population evolution between the phonon states is expressed as

$$\begin{aligned}\frac{\mathrm{d}P_n}{\mathrm{d}t} = \Gamma_{eff}\Bigg(&-\sum_{n'}\frac{|\Omega_{n,n'}|^2}{4(\Delta_{\text{eff}}-\delta_n\omega_z)^2+\Gamma^2_{\text{eff}}+2|\Omega_{n,n'}|^2}P_n \\ &+\sum_{n',n''}\frac{|\Omega_{n',n''}|^2}{4(\Delta_{\text{eff}}-\delta_{n'}\omega_z)^2+\Gamma^2_{\text{eff}}+2|\Omega_{n',n''}|^2}\frac{1}{2}\int_{-1}^{1}\mathrm{d}(\cos\theta)|\tilde{\Omega}_{n,n''}(\eta_s\cos\theta)|^2\mathcal{W}(\cos\theta)P_{n''}\Bigg).\end{aligned} \tag{5.11}$$

This is equivalent to considering the whole system as a one-level atom. The validity of the simplified rate equation is discussed by Morigi et. al. in their work [83], where they found it to be consistent with quantum Monte Carlo simulations.

At this stage, we can also neglect the atomic coherence, which arguably does not affect

[2] I am omitting the steps that are taken while transforming the Master equation in an optical Bloch equation, which is carried out by tracing out the required components after making inner product in terms of internal state vectors ($|e\rangle$ and $|g\rangle$). The required terms are traced out from the matrix multiplication and are written in the form of the optical Bloch equation. Once the optical Bloch equations for internal states of the atom are derived, the equations are rewritten for external states by taking an outer product with the external states ($|n\rangle$ and $|n'\rangle$). Please refer to reference [116] for more details.

the cooling dynamics. After collecting the terms for population entering into the state $|n\rangle$ and leaving from the state $|n\rangle$, the rate equation of the population at the phonon state $|n\rangle$ can be written as

$$\begin{aligned}\frac{\mathrm{d}P_n}{\mathrm{d}t} &= -\sum_{n''\neq n}\sum_{n'}\frac{\Gamma_{\text{eff}}|\Omega_{n,n'}|^2}{\Gamma_{\text{eff}}^2+4(\Delta_{\text{eff}}-\delta_n\omega_z)^2+2|\Omega_{n,n'}|^2}\mathcal{D}_{n'\to n''}P_n \\ &\quad+\sum_{n''\neq n}\sum_{n'}\frac{\Gamma_{\text{eff}}|\Omega_{n'',n'}|^2}{\Gamma_{\text{eff}}^2+4(\Delta_{\text{eff}}-\delta_{n'}\omega_z)^2+2|\Omega_{n'',n'}|^2}\mathcal{D}_{n'\to n}P_{n''}, \end{aligned} \tag{5.12}$$

where

$$\mathcal{D}_{n'\to n''}=\frac{1}{2}\int_{-1}^{1}\mathrm{d}(\cos\theta)|\tilde{\Omega}_{n',n''}(\eta_s\cos\theta)|^2\mathcal{W}(\cos\theta), \tag{5.13}$$

is called the diffusion function which accounts for the population spread between the motional states during the spontaneous emission of photons. In order to calculate the diffusion function, the total probability of spread in all possible directions must be normalised to unity, thus

$$\frac{1}{2}\int_{-1}^{1}\mathrm{d}(\cos\theta)\mathcal{W}\cos\theta=1 \tag{5.14}$$

must hold for all possible transitions [3]. The diffusion function, as expressed in equation 5.13, is impossible to solve analytically, however, it is possible to replace it with a simpler expression. In these simulations, I will directly replace the expression as

$$\mathcal{D}_{n'\to n''}=|\tilde{\Omega}_{n',n''}(\eta_g)|^2, \tag{5.15}$$

where η_g is the normalised L-D parameter weighted over the angular spread. The equivalent expression has also been used in reference [117]. After following the above discussion, the weighted L-D parameter for uniformly distributed photons is given as $\eta_g=\eta_s/\sqrt{3}$ [116]. More detailed discussion of the L-D parameter will be given in a later section.

5.1.2 Additional effects in a Penning trap

The additional atomic levels involved in sideband cooling of a calcium ion in a Penning trap are indicated in figure 5.2. The transitions during sideband cooling of calcium are summarised as follows:

- The 729-nm excitation: The resonant transition between $m_j=-1/2$ of the ground state and $m_j=-3/2$ of the excited state is the main sideband cooling transition. Each resonant excitation event alters the phonon number depending upon the sideband chosen. Additionally, off-resonant excitation to the nearby sideband also alters the phonon number. The

[3] Here the expression 5.14 is integrated over angle θ about the quantization axis. In reality, it must be integrated over the solid-angle Ω, which takes the spread of the angle ϕ in the radial plane. The expression still holds as I have normalised the function $\mathcal{W}(\cos\theta)$ to account for the angle ϕ. At a later stage, where I will integrate the expression over solid angle, the function will have a prefactor of $1/2\pi$ to normalise it.

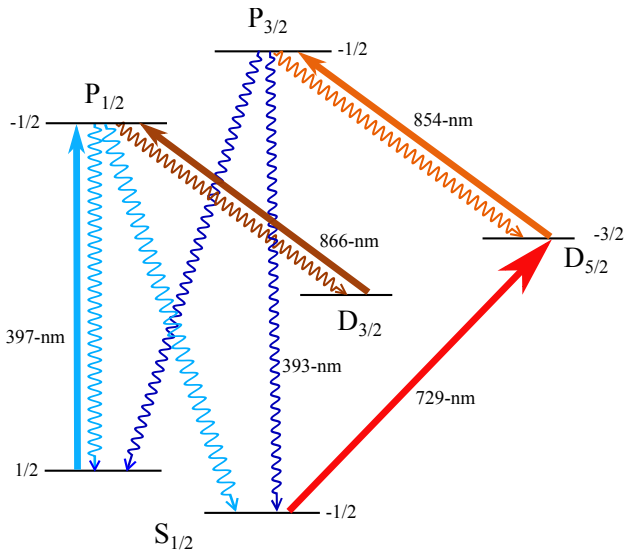


Figure 5.2: Partial level structure of a calcium ion in trapped in a Penning trap. The transitions that take place during sideband cooling are indicated as solid and squiggly arrows.

resonant and off-resonant excitation strengths depend upon the Rabi frequency and the L-D parameter η_{729} [4] of the transition. In the simulations, the cooling laser beam will be assumed to be travelling along the direction of interest, so that while discussing the case of axial cooling the beam will be assumed to propagate along the axial direction, and hence no geometrical correction is required.

- The 854-nm excitation: In our system, the 854-nm laser off-resonantly quenches the $D_{5/2}$ level and populates the $m_j = -1/2$ sub-level of the $P_{3/2}$ atomic level, through a dipole allowed-transition. The off-resonant excitation rate for the 854-nm transition is taken into account through the effective decay rate (as indicated in equation 5.4). However, the spread of population due to the excitation events will be inserted separately in the form of diffusion function. The diffusion function for this transition is given as $|\tilde{\Omega}_{n',n}(\eta_{854})|^2$, where η_{854} is the L-D parameter for the aforementioned transition. In the simulations, we will assume that the 854-laser beam is travelling in the axial direction only, which resembles the experimental situation in our case. The L-D parameter along the axial and radial directions for this transition will be η_{854} and zero, respectively.

- The spontaneous emission: In a Penning trap, the population from $-1/2$ sub-level of the $P_{3/2}$ level takes two routes to populate the $-1/2$ sub-level of the $S_{1/2}$ level. In the first route, the population directly decays to the $-1/2$ sub-level with a 2/3 probability. In the second route, the remaining population initially decays to the $+1/2$ sub-level of the ground state followed by a resonant excitation at 397 nm wavelength to $-1/2$ sub-level of the $P_{1/2}$ level and eventually populates the $-1/2$ sub-level of the ground state. This

[4] I am writing the L-D parameter as η_i, where "i" corresponds to the wavelength of the associated transition. In order to calculate the L-D parameter, one must express $\eta = k\sqrt{\frac{\hbar}{2m\omega_z}}$ by substituting the corresponding values of the wavelength of the radiation and the frequencies of the corresponding motional mode.

additional step takes a few μs to reach to the ground state. We will neglect the time evolution during this step but we will incorporate the diffusion of the population between motional levels during this additional step. The diffusion function will be assumed to be $|\tilde{\Omega}_{n,n'}(\eta_g)|^2$, where η_g is the weighted L-D parameter for the intermediate steps before it reaches the $-1/2$ sub-level of the ground state.

The L-D parameter to account for the spontaneous emission events

During spontaneous emission of the photons, the ion receives a momentum kick which changes its phonon state and thus causes heating. The change in the phonon state along a specific direction, during this event, depends upon the emission pattern and the wavelength of the emitted photons. For a dipole allowed transition, the emission pattern is not spherically symmetric about the quantisation axis, thus the contribution will be different along the axial direction that the radial plane. Previously, various studies have been carried out to calculate the component of diffusion along a specific direction and the discussion can be found in references [40, 117, 118]. Following their approach, here, I calculate the average component of momentum distribution for the S-P transition. This momentum transfer will then be normalised in the form of the L-D parameter and finally, the contribution will be incorporated in the form of the diffusion function (which has been given in equation 5.15).

The normalised L-D parameter for spontaneous decay relates to the geometric factor associated with the momentum distribution along the direction of interest [116, 117]. From the definition of the L-D parameter, $\eta^2 \propto p^2$, where p is the momentum of the absorbed or emitted photons. The mean distribution function for the momentum is actually $\langle p(\theta)^2 \rangle$, hence the square of the effective L-D parameter must be normalised with the mean component of the momentum distribution along the direction of interest. The component of the momentum distribution along a specific direction ($\hat{x}$) is given as

$$\tilde{\mathcal{D}}_{\mathrm{C}} = \frac{1}{2}\int_{-1}^{1} \mathrm{d}(\cos\theta)\hat{x}^2 \mathcal{W} \cos\theta, \tag{5.16}$$

where $\hat{x}$ is expressed as $\sin\theta\cos\phi$, $\sin\theta\sin\phi$ and $\cos\theta$ for the component along the x, y and z axes, respectively. Therefore, the η_g is expressed as

$$\eta_g = \eta_s \sqrt{\tilde{\mathcal{D}}_{\mathrm{C}}}, \tag{5.17}$$

where η_s is the L-D parameter for the emitted photons and it is expressed as $k\sqrt{\frac{\hbar}{2m\omega_z}}$.

After getting the general characteristic of the transitions, we can derive the expressions for the L-D parameters for a trapped calcium ion in a Penning trap. In a Penning trap, the additional decay channels appear due to the multiple Zeeman sub-levels. The decay pattern for a dipole allowed transition varies if it is a σ ($\Delta m_j = \pm 1$) or π ($\Delta m_j = 0$) transition. The normalised decay patterns and the component of diffusion coefficients for a calcium ion in the magnetic field

Atomic transition	m_j	$\mathcal{W}(\cos\theta)$	Probability	$\tilde{\mathcal{D}}_C$ Axial	$\tilde{\mathcal{D}}_C$ Radial
$P_{1/2} \leftrightarrow S_{1/2}$	$\frac{1}{2} \rightarrow \frac{1}{2}$ or $-\frac{1}{2} \rightarrow -\frac{1}{2}$	$\frac{3}{4\pi}\sin^2\theta$	$1/6$	$1/5$	$2/5$
	$\frac{1}{2} \rightarrow -\frac{1}{2}$ or $-\frac{1}{2} \rightarrow \frac{1}{2}$	$\frac{3}{8\pi}(1+\cos^2\theta)$	$1/3$	$2/5$	$3/10$
$P_{3/2} \leftrightarrow S_{1/2}$	$\frac{3}{2} \rightarrow \frac{1}{2}$ or $-\frac{3}{2} \rightarrow -\frac{1}{2}$	$\frac{3}{8\pi}(1+\cos^2\theta)$	$1/4$	$2/5$	$3/10$
	$\frac{1}{2} \rightarrow \frac{1}{2}$ or $-\frac{1}{2} \rightarrow -\frac{1}{2}$	$\frac{3}{4\pi}\sin^2\theta$	$1/6$	$1/5$	$2/5$
	$\frac{1}{2} \rightarrow -\frac{1}{2}$ or $-\frac{1}{2} \rightarrow \frac{1}{2}$	$\frac{3}{8\pi}(1+\cos^2\theta)$	$1/12$	$2/5$	$3/10$

Table 5.1: Table showing components of momentum distribution along and perpendicular to the magnetic field axis during transitions between atomic levels P and S of a calcium ion.

are given in table 5.1. Moreover, the normalised L-D parameter will be elaborated as follows:

- The $P_{3/2} \rightarrow S_{1/2}$ spontaneous decay: The emission pattern for the transition from $m_j = -1/2$ sub-level of the $P_{3/2}$ atomic state to $m_j = \pm 1/2$ sub-levels of the ground state is not isotropic about the quantisation axis. In this situation, the parameter $\tilde{\mathcal{D}}_C$ is given as $4/15$ and $11/30$ along the axial and radial directions, respectively. The associated L-D parameters are calculated to be $\sqrt{4/15}\eta_s$ and $\sqrt{11/30}\eta_s$ for the motion along the axial and radial directions. In this transition 2/3 of the population directly decays to $m_j = -1/2$ sublevel of the ground electronic state but remaining population takes another route.

- The $P_{1/2} \leftrightarrow S_{1/2}$ transition: The remaining 1/3 population from $m_j = -1/2$ sub-level of the ground electronic state is recycled by a pair of 397-nm laser beams, along with the axial and radial directions. The L-D parameter for this transition can also be calculated by assessing the steps involved and substituting the parameters from the above table. For the simulation, we will assume that the ion is equally illuminated by the axial and radial directions. The weighted L-D parameter, in this case, comes out to be $0.707\eta_{397}$ for the absorption process. Similarly, the L-D parameter for the emission process comes out to be $0.57\eta_{397}$ [5].

- The partial decay of the population from $P_{1/2}$ to $D_{5/2}$ and $D_{3/2}$ is negligible, therefore the diffusion during the emission and absorption effects from this process will not be taken into account in the simulations.

5.1.3 Transformation of a six-level system into a two-level equivalent

Following Marzoli's approach to designing a two-level atom [114], I will reduce a six-level atomic system into a two-level equivalent. It may be argued that the other atomic levels are barely occupied during sideband cooling; hence the adiabatic elimination of some of the atomic levels is valid. The effective re-pumping rate formalism, as indicated in equation 5.4, is also

[5] While calculating the L-D parameter, I have assumed that all the processes are taking place in series. This is even correct for the 397-nm recycling transition if the diffusion probabilities are calculated by carefully normalising for the corresponding transitions.

valid along the same line of reason. The main interest in performing the simulation is to design a cooling sequence which can allow us to achieve a minimum mean phonon number for the shortest cooling time. The cooling dynamics can be computed from equation 5.12. After inserting the relevant diffusion functions for intermediate branches, the new diffusion function is expressed as

$$\mathcal{D}_{n',n''} = \sum_{p}\sum_{m}\sum_{l} |\tilde{\Omega}_{n',l}(\eta_{854a})|^2 |\tilde{\Omega}_{l,m}(\eta_{393d})|^2 |\tilde{\Omega}_{m,p}(\eta_{397a})|^2 |\tilde{\Omega}_{p,n''}(\eta_{397d})|^2, \tag{5.18}$$

where η_i is the L-D parameter for aforementioned four diffusion branches. The summations over p, m and l take into account all motional states to which the diffusion could take place during sideband cooling.

5.2 Population dynamics in motional states of a trapped ion interacting with the laser radiation

5.2.1 Comparison of resonant and off-resonant excitation rates

The rate equation description is found to be valid in low saturation limits for sideband cooling, i.e. $\Omega_{n,n'} \ll \Gamma_{\text{eff}}$ [83]. In order to introduce the saturation effects, I have inserted $2\Omega^2_{n,n'}$ term in the denominator of the Lorentzian function and it is shown in equation 5.12. Simulated absorption spectra for a calcium ion, at 420 kHz axial frequency with and without saturation effects are shown in figure 5.3. In the presence of the saturation term, the absorption strength is reduced, which is expected due to the coherent oscillation of probability between the excited and ground states of the ion due to the driving field; hence we expect it to slow the cooling dynamics. The typical laser parameters that are used for the simulation of the absorption spectrum are shown in table 5.2.

$\Gamma_{854} \approx 2\pi \cdot 1.58$ MHz	$\Gamma_{\text{eff}} \approx 2\pi \cdot 40$ kHz
$\Gamma_{866} \approx 2\pi \cdot 1.3$ MHz	$\Omega_{729} \approx 2\pi \cdot 40$ kHz
$\Gamma_{393} \approx 2\pi \cdot 21.5$ MHz	$\Gamma_{729} \approx 2\pi \cdot 0.15$ Hz
$\Gamma_{397} \approx 2\pi \cdot 21.2$ MHz	$\omega_z \approx 2\pi \cdot 100 - 500$ kHz

Table 5.2: Typical transition parameters used for the simulation [98, 107].

Additionally, due to off-resonant excitation during sideband cooling, the ultimate mean phonon number is expected to be higher after sideband cooling. The off-resonant excitation strength of the carrier and the first blue sideband of the transition as a function of phonon number (n) is shown in figure 5.4 at 420 kHz motional frequency. It can be seen that at 420 kHz ion oscillation frequency, the off-resonant excitation is not problematic. However, we expect some issues due to the off-resonant excitation at a lower motional frequency, which ultimately limits the lowest achievable mean phonon number. The frequency dependence of the off-resonant excitation is shown in figure 5.5. In this figure, the simulation assumed that the population is

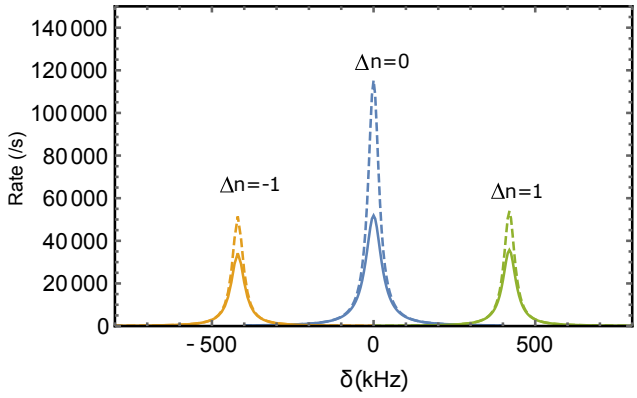


Figure 5.3: A calculated absorption spectrum of a calcium ion at 420 kHz axial frequency for the red, blue and the carrier transitions at the Doppler limit. The solid curves and dashed curves indicate “with" and “without" the saturation term in the absorption spectrum expression.

initialised in the $n = 1$ motional state and the cooling laser is resonant with the first red sideband of the transition. The simulated curve in blue corresponds to the off-resonant excitation of the carrier transition. This transition does not change the phonon number during absorption. However, when the ion decays back to the ground state during recycling it may change the phonon number and hence can lead to unwanted heating. Similarly, the off-resonant excitation to the blue sideband (shown in green) is estimated to be negligible at this trap frequency. It contributes significantly at very low motional frequencies (< 150 kHz).

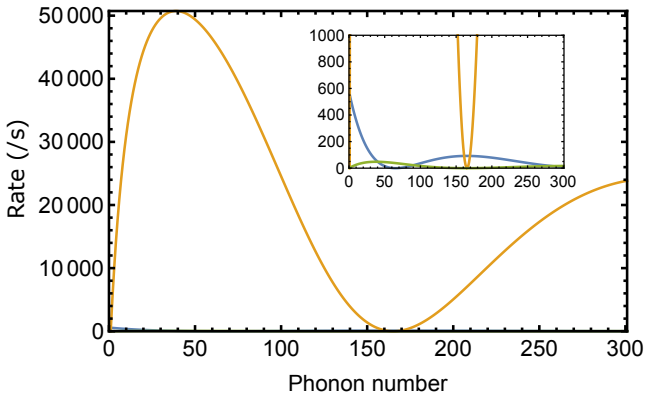


Figure 5.4: Off-resonant excitation rate for the carrier transition (in blue) and the first blue sideband transition (in green) as a function of phonon number (n) at 420 kHz ion oscillation frequency when the 729-nm laser is tuned to the first red sideband of the transition (in orange).

5.2.2 Description of the simulation methods

In this thesis, I have used two types of simulation approaches. The first approach is based on numerical methods where the rate equation is solved for a given set of laser and trap parameters. However, the approach becomes cumbersome if a large number of phonon states are taken into account in the simulations. Also, the approach is intractable if the simulations are carried out for more than one motional mode. The second approach is based on a Monte-Carlo method,

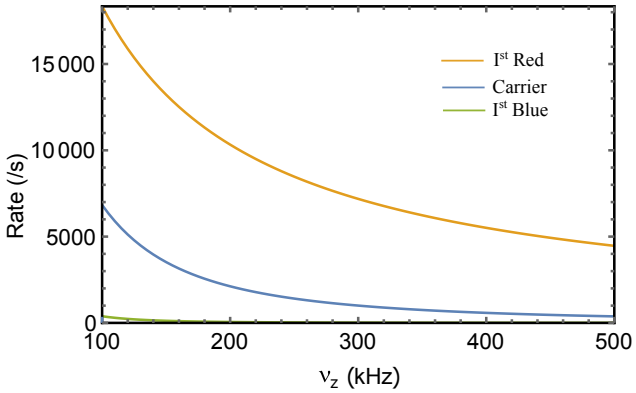


Figure 5.5: The simulated resonant and off-resonant excitation rates as a function of ion oscillation frequency is shown above. Unwanted effects are more prominent at the lower value motional frequencies.

where a random number is assigned for the transitions to different motional states with a known transition probability. Both approaches are discussed in the following.

Rate equation approach

Unlike previous studies in references [114, 119], the rate equation approach described here (as given in equation 5.12) is not restricted to the L-D regime. The analytical solution of the rate equation is not possible due to the complicated diffusion function; hence a numerical simulation will be carried out. In my thesis, the simulations are carried out in “Mathematica". The numerical simulations are performed in three steps;

1) Initialise the population in each motional state by assuming a thermal distribution after Doppler cooling. The expression for the Doppler limit has been indicated in equation 3.15.

2) Calculate the resonant or off-resonant excitation rates for a range of phonon numbers which are assumed to make the transition to their nearby phonon states (say $\Delta n = \pm 5$). The expression for the excitation rate is given in equation 5.12.

3) Calculate the diffusion coefficients for the relevant spontaneous transitions. The expression in terms of normalised L-D parameter is given in equation 5.16. The relevant values for the L-D parameters have been calculated and shown in section 5.1.2.

4) The final step is to perform numerical integration of the rate equations for each phonon state and estimate the population at each time.

Monte-Carlo approach

A Monte-Carlo approach is often a suitable alternative when the rate equation method is analytically intractable. A pseudo random number generator can be used to simulate the cooling

dynamics with given sets of instructions. As the transitions in atomic systems take place through discrete jumps, solving such systems via a Monte-Carlo approach resembles the actual experiments quite well.

1. The state is initialised into a phonon state sampled from the Doppler cooled Fock state distribution.

2. Uniform random numbers are sampled to check for the sideband cooling excitation followed by the repumping transition.

3. The time is updated for each transition.

4. Steps 2-3 are repeated the desired number of times corresponding to the cooling length being simulated.

5. Steps 1-4 are repeated 10000 times.

5.2.3 Optimisation of sideband cooling laser parameters

Before carrying out the simulation for the actual cooling dynamics, I would like to optimise the cooling and repumping laser parameters. For this, I would assume the axial ion oscillation frequency to be 420 kHz ($\eta_{729} = 0.15$). At this frequency, the effects of being outside the Lamb-Dicke regime are not significant. The initial mean phonon number following Doppler cooling is calculated to be 21. These studies will be used later to optimise the cooling sequence. The simulated populations outside the motional ground state ($n = 0$) after sideband cooling at various values of the effective repumping rates are shown in figure 5.6. In practice the effective repumping rate can be varied by changing Ω_{854} or δ_{854} in equation 5.4 but in the simulation, I simply changed the values and made the corrections for the AC Stark shift as expressed in equation 5.5. The simulation is carried out at 40 kHz Rabi frequency for the 729-nm transition.

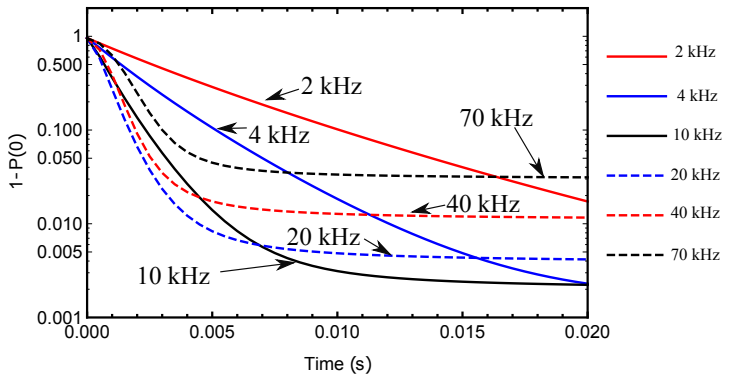


Figure 5.6: Simulated population outside the $n = 0$ state as a function of cooling time for different repumping rates. The simulations are carried out at a motional frequency of 420 kHz and Rabi frequency of 40 kHz.

The simulations show that the highest ground state occupancy can be achieved with a combination of longer cooling times and an effective repumping rate low enough to limit off-resonant excitation, but sufficient to overcome any heating processes. If short cooling times are required, then the optimal repumping rate should be around or above 20 kHz. But one can only achieve an occupation probability of 99.5% at this re-pumping rate. In order to achieve a lower mean phonon number one has to reduce the repumping rate. Realistically, one can achieve the ground state occupation probability to 99.7 % after 20 ms of cooling at a repumping rate of ~ 10 kHz. In another study, we find an optimum 729-nm absorption rate, which comes out to be roughly 40 kHz (see figure 5.7) at this trap frequency. In the simulation, the repumping rate is assumed to be 10 kHz and the motional frequency is assumed to be 420 kHz.

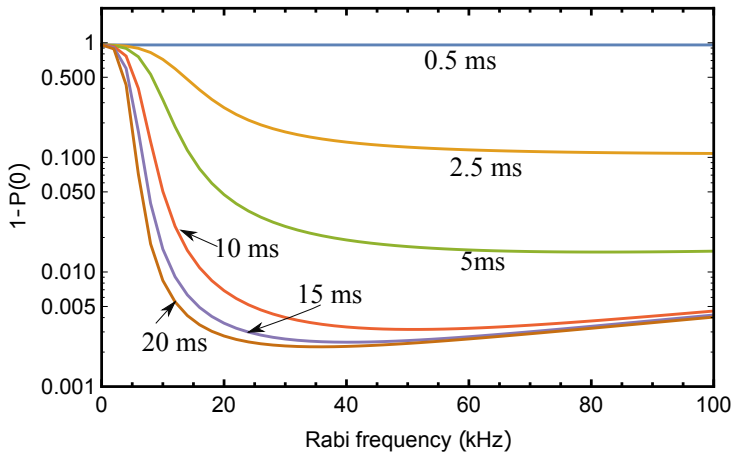


Figure 5.7: The figure shows population outside $n = 0$ phonon state as a function of Rabi frequency at different cooling times. The repumping rate is chosen to be 10 kHz and the motional frequency is chosen to be 420 kHz for this set of studies.

5.3 Sideband cooling outside the L-D regime

The main focus of these simulations is to optimise the cooling dynamics for a system where the L-D parameter value is large.

5.3.1 Problems with the large value of the L-D parameter

Sideband cooling of trapped ions outside the L-D regime is complicated by the fact that the red sideband strength is not proportional to $\sqrt{n}$ for all the phonon numbers. Especially for some of the phonon numbers, the sidebands see almost zero excitation strength, hence the cooling rate is found to be close to zero for the population in these states, which leads to “population trapping". The effect of population trapping has been previously discussed in references [92, 117] and it was identified as a reason for the poor ground state occupancy [45]. Here I attempt to show the effect of such “dark states" (sideband minima) while performing sideband cooling in our system. A simulated sideband strength at 300 kHz motional frequency for a calcium ion as a function

of phonon state is shown in figure 5.8. The L-D parameter at this frequency is calculated to be η_{729} =0.17 with a mean phonon number after Doppler cooling of 32. In this case, the first red sideband strength approaches zero around $n \sim 117$, where the population trapping would be expected. In our system at this trap parameters, 0.5% of the population is expected to lie above the first dark state after Doppler cooling. Furthermore, if the system lies outside the L-D regime, the diffusion heating is worse.

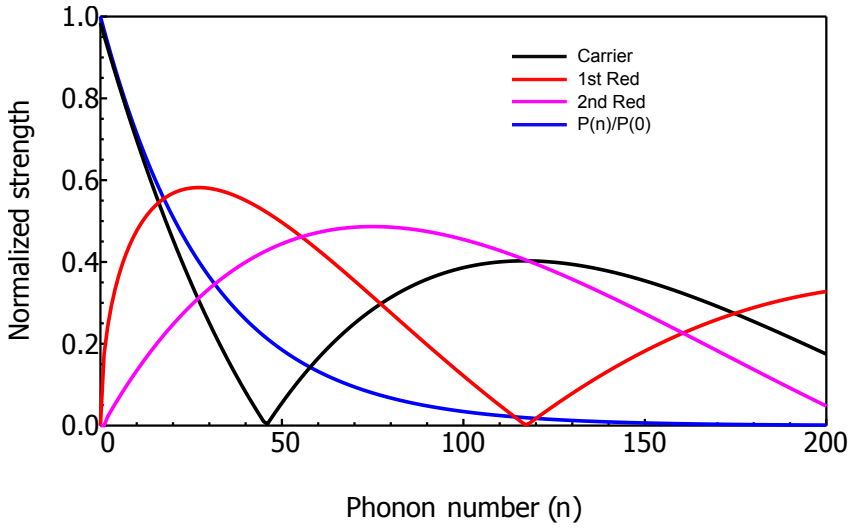


Figure 5.8: The figure shows coupling strength of the first red sideband (in red), the second red sideband (in magenta) and the carrier (in black) as a function of phonon number. Blue line corresponds to the normalised occupation in phonon state n.

In order to describe the cooling performance for the above-mentioned case, a rate equation approach is adopted. The simulated mean phonon number as a function of sideband cooling time is shown in figure 5.9 (a). The 729-nm Rabi frequency and the re-pumping rate are assumed to be 40 kHz and 20 kHz, respectively. The cooling laser is tuned to resonant with the first red sideband transition. For the sake of simplicity, the population is initialised in a specific phonon state and the mean phonon number is estimated at various values of sideband cooling times. The simulations are performed for various initial phonon states and the mean phonon numbers are estimated for as a function of cooling time. The simulations show that for low lying phonon states ($n < 110$), the normal cooling behaviour is verified. However, for the phonon states greater than 110 the population is only slowly pulled down to the ground state. This is attributed to the population trapping. As mentioned before, for the system outside the L-D regime, the diffusion effects are also expected to affect the cooling dynamics, significantly. In order to distinguish the effects due to the diffusion mechanism, another simulation is carried out at the same simulation conditions except the diffusion is neglected. The findings are shown in figure 5.9 (b). The qualitative difference between plots (a) and (b) (figure (a) where the full model is considered and (b) where the diffusion is neglected) indicate that the diffusion mechanisms slow down the cooling process as speculated before. Additionally, the lowest achievable mean phonon number is higher than without diffusion of the population. Alternatively, due to the diffusion effects, the population around the sideband minimum is not quite trapped, hence

sideband cooling is observed on a longer timescale.

In order to predict the behaviour of higher order sidebands, we also simulated the cooling dynamics for the second red sideband and it is shown in figure 5.9 (c). In this case, no population trapping is observed for $n \sim 117$, instead, the population trapping is observed at $n \sim 211$. As we have seen, population trapping is one of the consequences of systems outside the L-D regime. This population trapping gets more severe with decreasing motional frequency, i.e. increasing L-D parameter. The population trapping above the first zero of the first red sideband can be up to 65% at 100 kHz motional frequency. Hence, in this regime, we need a cooling sequence which can eliminate any sort of population trapping.

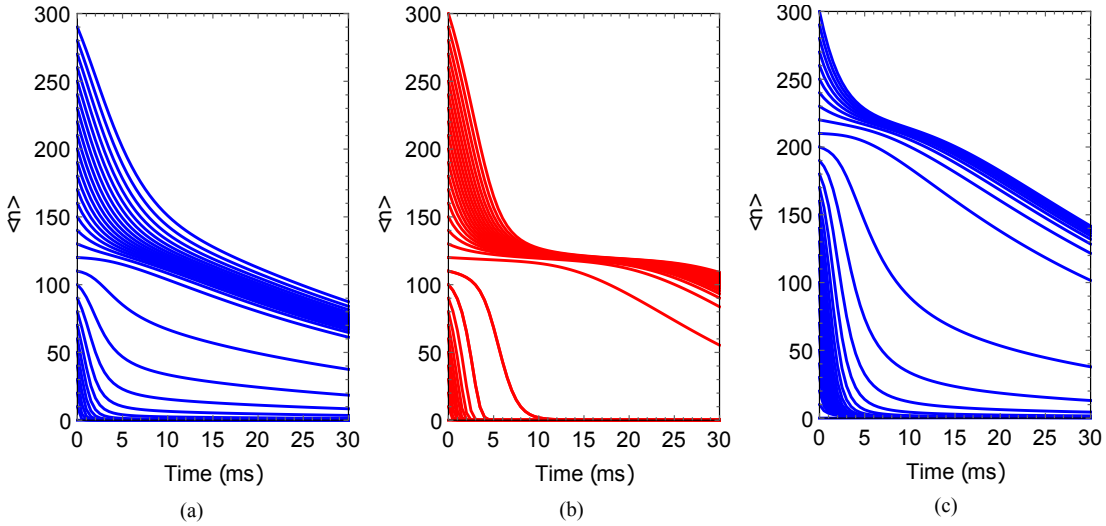


Figure 5.9: Simulated average phonon number (a) after a single stage sideband cooling on the first red sideband and (c) after a single stage cooling on the second red sideband. Curve (b) shows population dynamics after cooling at the first red sideband but without considering the diffusion during spontaneous decay of the photon from the excited state.

5.3.2 Optimisation of cooling sequence

From the discussion in the last section, it is clear that sideband cooling outside the L-D regime requires special attention. In order to avoid population trapping at the sideband minimum point, one must include sideband cooling on the higher order sidebands. At lower motional frequency, the L-D parameter is larger and hence the heating effects are severe. In figure 5.10 the strength of the first and second red sidebands are shown at 150 kHz motional frequency. It can be seen that the sideband strengths for both of the sidebands have minima at different values of n, hence switching from one to the other can be useful to avoid any population trapping.

I also introduce another scheme for sideband cooling rather that simply switching between two lowest order sidebands. In this scheme, cooling can be started at a higher order sideband (say higher than third order sidebands) and subsequently switched towards a lower order sideband once the population occupies the low n states. This scheme is expected to work efficiently as the higher order sidebands are stronger at high n and the sideband minima are observed at

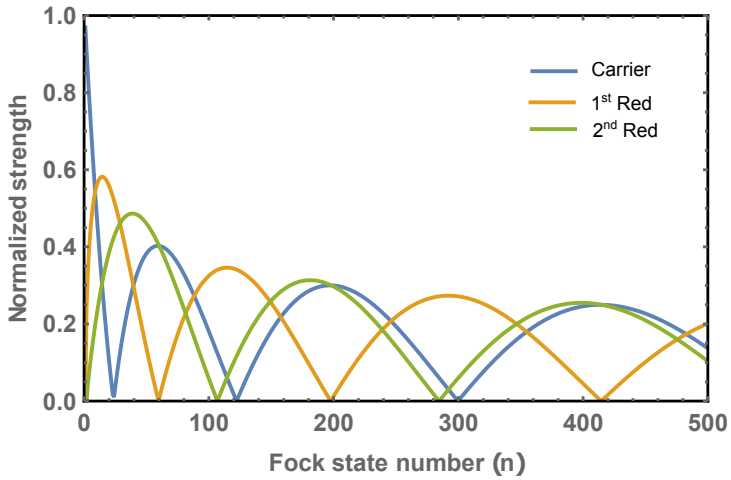


Figure 5.10: The above figure shows calculated sideband strengths as a function of phonon number at 150 kHz ion oscillation frequency. The first red sideband is shown in green and the second red sideband in orange. The blue curve indicates the carrier strength. Note that the sideband minima for both sidebands do not coincide, hence the choice of cooling on the alternate sidebands will avoid population trapping.

higher values of n. Additionally, the number of phonons removed on average in each excitation is more than one in this case. In order to illustrate the cooling behaviour, I show the product of sideband strength, change in phonon numbers (Δn) and population distribution ($P(n)$) after Doppler cooling as a function of n in figure 5.11. This represents the rate of removal of phonons after Doppler cooling for various sidebands. It can be seen that initially at high n the higher order sidebands would show better cooling in comparison to lower order ones and vice-versa for low n.

If we integrate the rate of removal of phonons for each curve, the quantity can be treated as the overall cooling rate for an individual sideband. At 150 kHz, the integral is found to be highest for the third red sideband. However, there will be 1.7% of the population population above the first minimum of the third red sideband. If we want to achieve 99.99% of the population in the ground state, we should start at the sideband for which the sideband minimum point lies further in the higher side of n. At 150 kHz motional frequency, the eighth sideband (not shown in the figure) has the first sideband minimum above the required cumulative population point. But it is pointless to cool with the eighth red sideband as the overall cooling rate will be negligible. At this stage, it is difficult to conclude which sidebands should be taken into consideration to efficiently cool the ion to its motional ground state.

However, at this stage, we can qualitatively conclude that sideband cooling will be efficient for the third red sideband but there will be some population trapping, which can be avoided by repeating the cooling sequences. At 150 kHz frequency, it is best to cool through the third red and second red sidebands until the population is dragged below the minimum of the first red sideband. We can also conclude that for efficient sideband cooling, one should find the sideband for which the overall cooling rate is maximum and cooling must be initiated at that sideband. In order to avoid population trapping, the laser frequency must be switched between the sideband

for which the overall cooling rate is highest and second highest until the population is dragged below the first minimum of the first red sideband.

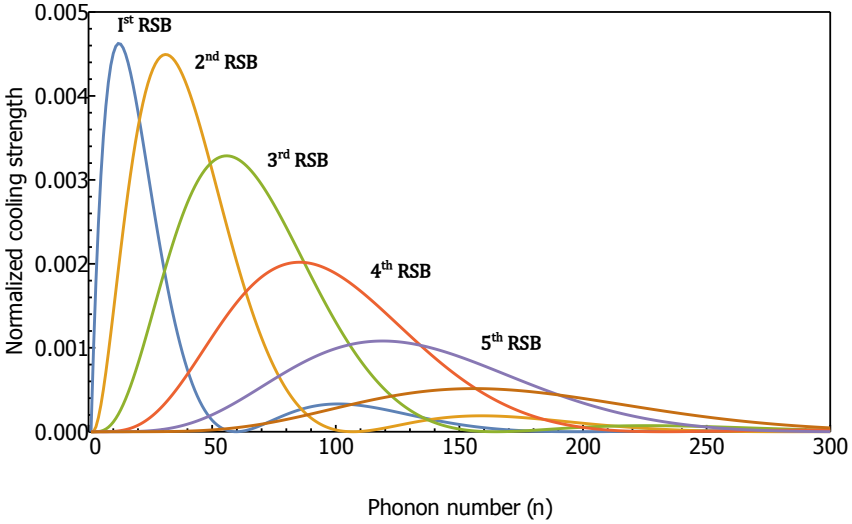


Figure 5.11: The figure shows calculated normalised cooling strength ($P(n) \times \Delta n \times \Omega_{n,n'}$) for the individual phonon state (n) at 150 kHz ion oscillation frequency after Doppler cooling. It can be seen that at high n cooling is more efficient for higher order sidebands.

5.3.3 Simulation of cooling dynamics for a single ion

Previously, I discussed optimisation of laser parameters and cooling sequences. In this section, I will show the results of the cooling limit and present the results of cooling dynamics of a single ion at two extreme motional frequencies. After Doppler cooling of a single ion in a Penning trap, a large fraction of the population resides outside the L-D regime, especially at a low motional frequency. The simulations are performed at 420 kHz and 150 kHz motional frequencies. For the simulation, the Rabi frequency and the re-pumping rate are assumed to be 40 kHz and 20 kHz respectively.

Figure 5.12 (a) indicates mean phonon number ($\langle n \rangle$) and figure (b) indicates the ground state occupancy ($P(0)$), as a function of sideband cooling time at 420 kHz motional frequency. The studies show that the $\langle n \rangle = 0.2$ if only single stage cooling is performed. The simulation also shows that lower value of the mean phonon number or higher occupancy in $n = 0$ state is observed for two-stage sideband cooling.

The simulation is also carried out at 150 kHz motional frequency. In this situation, approximately 37% of the population lies outside the first minimum of the first red sideband at the Doppler limit of a calcium ion. From the qualitative discussion in the previous section, we know that single stage cooling would not work. In this case, I choose a cooling sequence 3rd-2nd-3rd-2nd-1st-3rd-1st, where cooling is performed for 2.5 ms at each sideband and 5 ms for the last pulse. The cooling sequence is chosen on a trial and error basis. A simulated curve of the mean phonon number as a function of cooling time is shown in figure 5.13. The curve in blue corre-

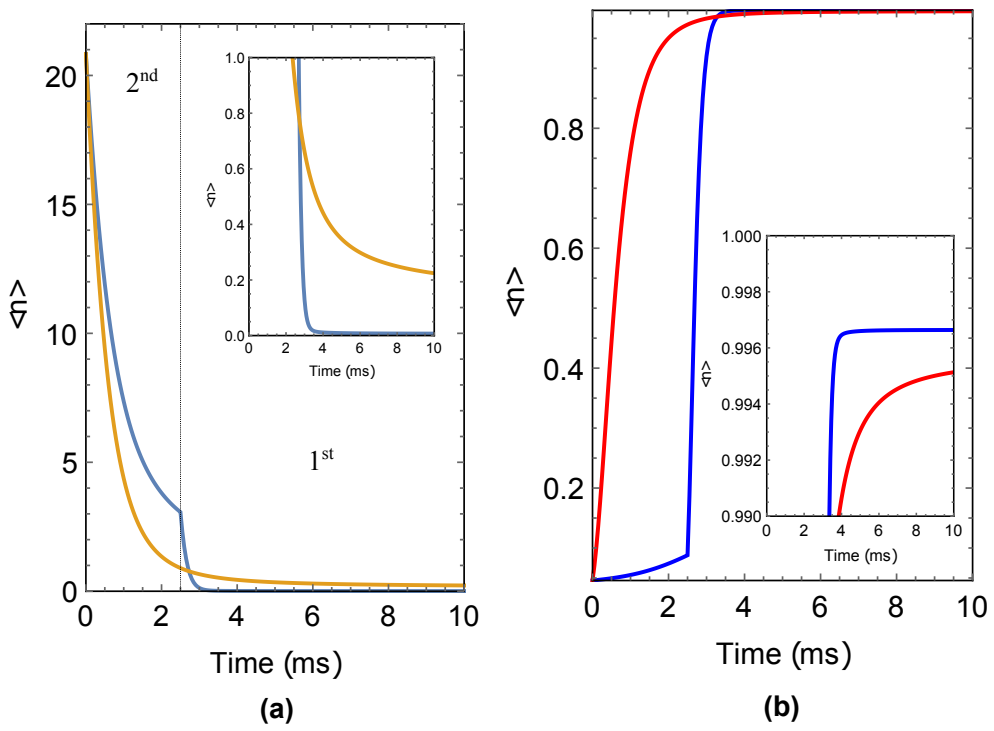


Figure 5.12: Simulated sideband cooling dynamics of a Doppler cooled ion at 420 kHz motional frequency. Figure (a) shows mean phonon number ($\langle n \rangle$) and (b) shows ground state occupancy ($P(0)$) as a function of cooling time. Sideband cooling is initiated at the second order sideband for 2.5 ms time followed by first red sideband for the rest of the time. The curves in orange and red indicate the time behaviour for single stage cooling, hence poor cooling is verified through the simulations.

sponds to multi-stage cooling and the curve in red corresponds to single-stage cooling. Clearly, the simulations show lower $\langle n \rangle$ for the multi-stage sideband cooling.

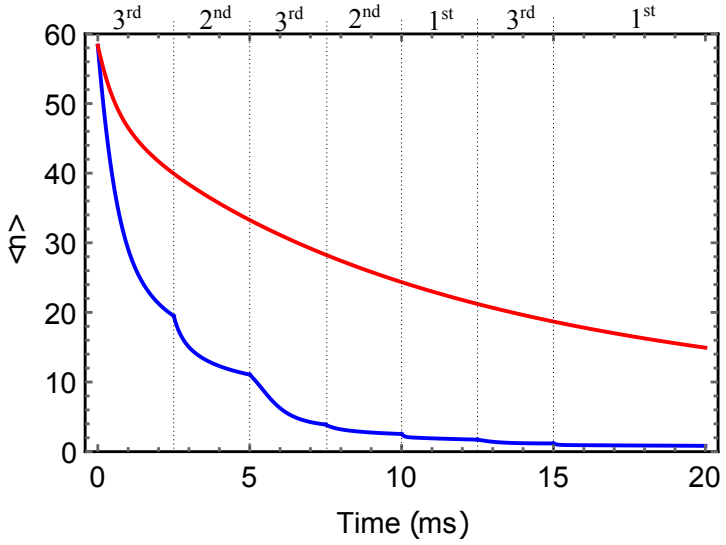


Figure 5.13: Simulated cooling dynamics of single ion at 150 kHz motional frequency. The curve in red corresponds to a single stage cooling (cooling with first red sideband) and curve in blue corresponds to multi-stage cooling (the pulse sequence is shown at the top of the frame).

Finally, the mean phonon number ($\langle n \rangle$) as a function of motional frequency is shown in figure 5.14. The laser parameters are chosen to be $\Omega_0 = \tilde{\Gamma} = 2\pi \times 40$ kHz. It can be seen that the mean phonon number increases rapidly towards lower values of the motional frequency. This can be attributed to the diffusion mechanism which increases when the motional frequency decreases. The cooling limit also depends upon the repumping rate and the rate at which 729 nm absorption takes place. To avoid off-resonant excitation, which also limits the cooling limit, one must reduce the 729-nm and 854-nm laser power for the last period of sideband cooling. In the first instance, the cooling limit is found to be inversely proportional to the square of the motional frequency at a fixed value of repumping and 729-nm absorption rates.

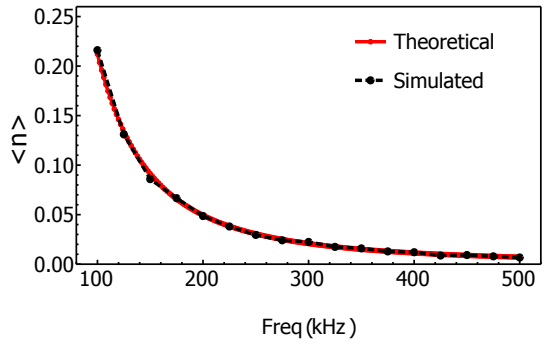


Figure 5.14: Minimum achievable $\langle n \rangle$ as a function of ion oscillation frequency after performing sideband cooling. The red continuous curve corresponds to the cooling limit that is estimated from rate equation approach and the black curve is the Monte-Carlo simulations results.

5.3.4 Cooling dynamics of a two-ion Coulomb crystal

Sideband cooling of multiple ions is significantly harder than a single ion due to the presence of multiple modes of oscillation which need to be cooled simultaneously. In this section, I study cooling dynamics of a two-ion crystal through a 2D rate equation, where excitation on a sideband of one motional mode will be associated with a carrier excitation on the other mode.

A two-ion chain

A two-ion-chain in a Penning trap can only be obtained at a low axial trapping frequency. Increasing the axial frequency above a certain value flips the crystal to a planar orientation. From the single-ion studies, it is known that at a low axial frequency the system lies outside the L-D regime, hence the chain is also expected to form a system that is outside the L-D regime. In this case, we can also avoid the population trapping by cooling on the higher order sidebands. The simulation will be performed for the axial motional modes. In this situation two motional modes are expected, namely COM and breathing motional modes.

To understand the cooling dynamics of a two-ion chain I show contour plots of sideband strengths as a function of phonon number (n), at $\omega_z = 2\pi \times 162$ kHz (which gives $\omega_B = \sqrt{3}\omega_z =$

$2\pi \times 281$ kHz). In this particular case where the L-D parameter is fairly large ($\eta_{COM} = 0.17$ and $\eta_B = 0.13$), we expect to have a large fraction of the population beyond the first minimum of the red sideband for both of the motional modes [70]. In order to bring all the population to the motional ground state, one has to target higher-order sidebands, repeatedly. A combined sideband contour plot of the first, second and third red sidebands of the COM mode along with the first and second red sidebands of the breathing mode is shown in figure 5.15 (a) - (c). Due to a smaller value of the L-D parameter for the breathing mode (i.e. $1/3^{1/4}$ times smaller than the COM mode), we expect to have less complexity for the breathing mode than the COM mode. Hence, we assume that the population can be taken to the ground state by targeting just the second and first order breathing mode sidebands, whereas for the COM case we expect to need the first, second and third order sidebands.

The combined strength for all these five sidebands is shown in figure 5.15 (d). Note that the combined plot still has a darker region, which corresponds to the carrier excitation being minimum for both of the motional modes and it also leads to population trapping. In order to avoid population trapping in such regions one needs to target inter-modulation sidebands. A plot showing one of these intermodulation sidebands (i.e. the second COM red sideband of the first breathing mode red sideband) is shown in figure 5.15 (e). The overlap of all the sidebands discussed above is shown in 5.15 (f). Qualitatively, it is clear that the cooling with the aforementioned sidebands would bring the population to the ground state of a two-ion chain.

In this case, apart from the population trapping events, we also expect heating of one motional mode while performing sideband cooling of the other mode. This is expected due to the diffusion of the population during the repumping processes. Figure 5.16 shows cooling dynamics of a two-ion chain at 162 kHz axial frequency. The laser parameters are chosen to be same as they were for the single-ion case. Intuitively, we start cooling on the breathing mode first, as it has a smaller value of the L-D parameter than for the COM mode. Due to the smaller value of the L-D parameter, the diffusion for the breathing mode will take place at a slower rate than that of the COM motional mode.

The cooling sequence is also indicated in figure 5.16. In order to cool the breathing mode first, we start with the second red sideband and then switch to the first red sideband of the transition. This way the breathing mode is ground state cooled but at the same time the COM mode is slightly heated up due to the diffusion of the population. In the second round of cooling, the laser is tuned to the third red sideband of the COM mode, followed by second and first red sidebands of the same mode. In order to eventually achieve the ground state of both modes simultaneously, some of the sidebands are repeated. In order to clear out the population from the phonon states for which cooling for both motional modes approaches zero (the common dark portion of first five plots in figure 5.15), an inter-modulation sideband is used in the cooling sequence. The simulations show the ground state cooling of a two ion chain. The experimental results for sideband cooling of a two-ion chain will be verified in chapter 6.

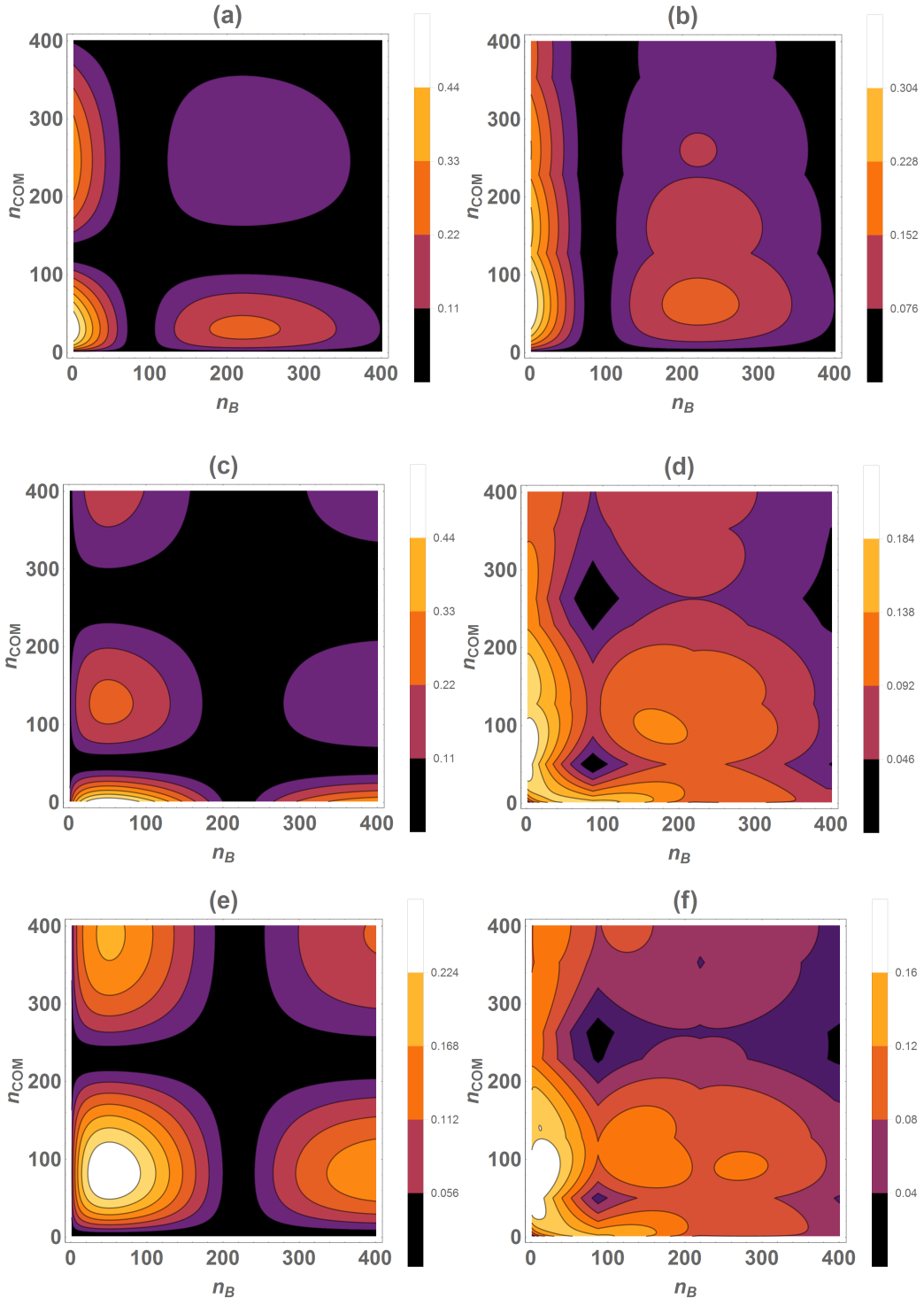


Figure 5.15: The contour plots show the strength of various sidebands as a function of phonon numbers in both axial modes for a two-ion string at 162 kHz COM frequency. Starting from the top, sideband strengths for the (a) first red sideband of COM, (b) the summation of the first three COM red sidebands, (c) first breathing red sideband, (d) sum of first three COM red and two breathing red sidebands, (e) first red breathing sideband of second red COM sideband and (f) is sum of (e) and (d).

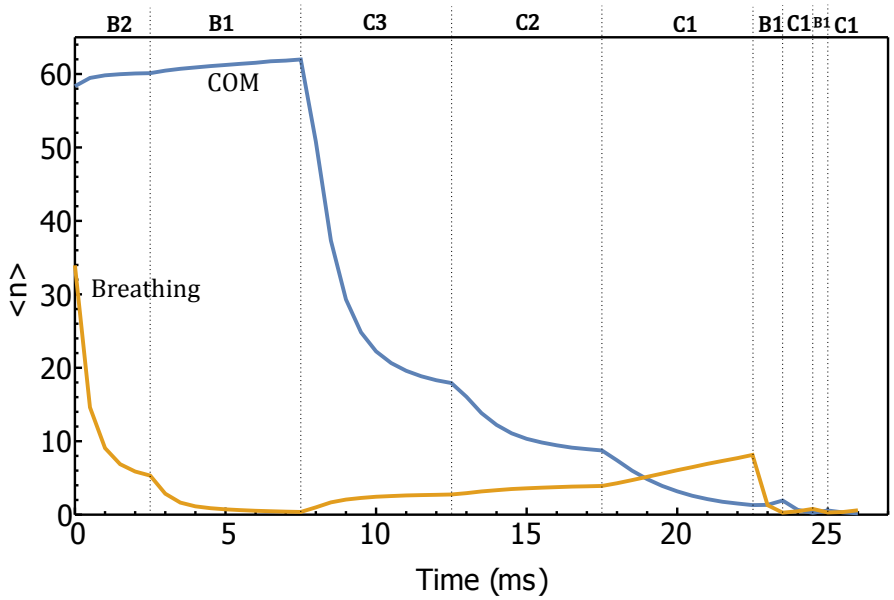


Figure 5.16: Average phonon number of the COM mode (blue) and the breathing mode (orange) as a function of time during multi-stage cooling of a two-ion chain with all sidebands included (see text).

Sideband cooling of a two-ion planar crystal

The axial motional modes for a two-ion planar crystal have been discussed in chapter 2. Sideband cooling of a planar crystal is particularly of interest due to its possible use in quantum simulation studies [25, 69]. In a two-ion planar case, the motional frequency of the out-of-phase mode (tilt mode) can be varied, as shown in equation 2.35, by changing the rotation frequency of the crystal. The rotation frequency in the radial plane of a crystal can be changed by locking the crystal to a rotating wall drive [120, 121] or by changing the perpendicular laser beam parameters (such as laser intensity, beam offset and the laser detuning) [121, 122]. The rotational frequency in a Penning trap can be varied between the magnetron frequency (ω_-) and the modified cyclotron frequency (ω_+), where the minimum separation of the ions can be obtained at $\omega_c/2$.

At first, I simulate the cooling dynamics at fixed laser cooling parameters for a two ion planar crystal in the resolved sideband case. Laser parameters for this case are chosen to be the same as for the two-ion chain. The axial motional frequency is chosen to be 346 kHz, where the tilt mode frequency can have values from 216 kHz to 346 kHz, depending upon the rotation frequency of the crystal. In the resolved sideband case, where I assume that the tilt mode is at 216 kHz and the COM mode is at 346 kHz, cooling will be simulated for both sidebands. This condition can be achieved at a crystal rotation frequency equal to the half of the cyclotron frequency ($\omega_c/2$). In this case the L-D parameter is $\eta_{COM} = 0.116$ and $\eta_{tilt} = 0.146$ for the COM and tilt motional modes, respectively. The simulated cooling dynamics is shown in figure 5.17 (a). It can be seen that both modes can be ground state cooled via implementing the third, second and first red sidebands on the tilt mode followed by the second and first on the COM mode. The simulations also show the sideband heating on the COM mode while attempting to cool the breathing mode

and vice-versa. At the end of the cooling sequence, I repeat the lower order sidebands in order to efficiently cool both motional modes to their ground state.

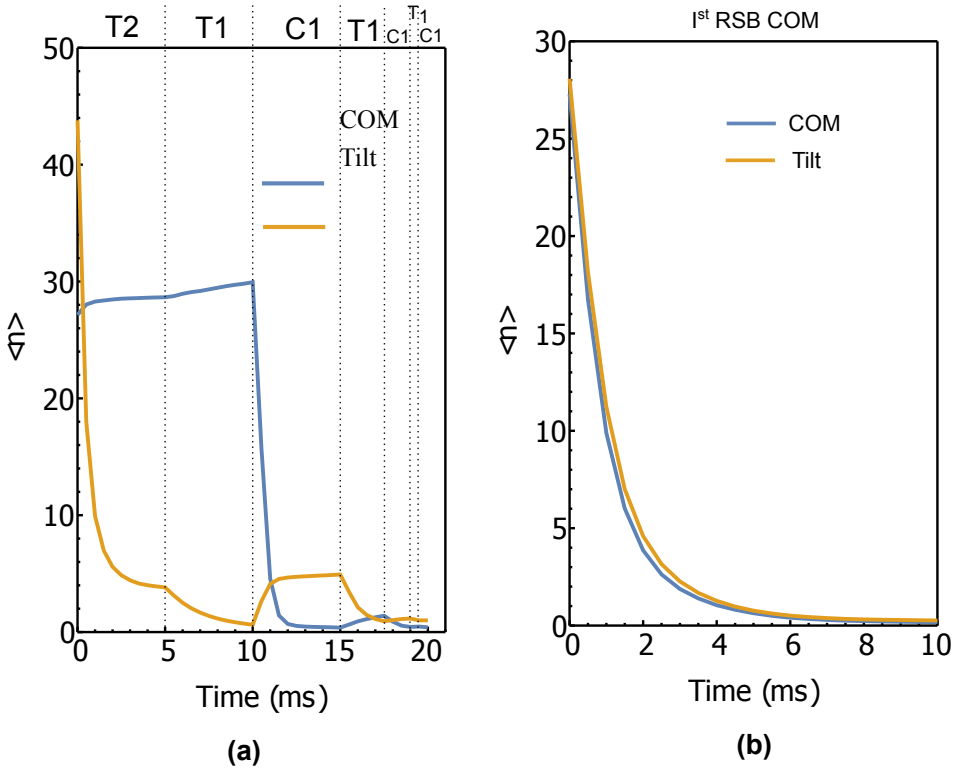


Figure 5.17: The mean phonon number ($\langle n \rangle$) as a function of sideband cooling time for the case when COM and Tilt motional modes are (a) resolved and (b) unresolved after Doppler cooling. Note that off-resonant cooling takes place for the tilt mode when the cooling laser is tuned to the COM mode of a two-ion planar crystal.

In the second case, I choose the motional frequency of the tilt motional mode to be close to the COM mode, which can be achieved by tuning the rotation frequency slightly above the magnetron frequency. For the simulations, I chose the tilt mode frequency to be 339 kHz and COM mode frequency to be 346 kHz. The L-D parameters in this case are calculated to be $\eta_{COM} = 0.116$ and $\eta_{tilt} = 0.118$. In this case, the sidebands are not expected to be well resolved after Doppler cooling, hence cooling on one of the motional modes can simultaneously cool the other mode via off-resonant excitation. The simulated cooling dynamics is shown in figure 5.17 (b). Note that by setting the cooling laser frequency to the COM mode cooling of the breathing mode is verified through the simulations. This is closer to the experimental case of sideband cooling of a planar crystal which will be discussed in chapter 6.

5.4 Sideband heating to outside the L-D regime

In this section, I present the simulation results of sideband heating. Sideband heating of an ion prepares a quantum state with a high motional quantum number (n). In order to prepare the ion outside the L-D regime, the 729-nm laser will be tuned to the blue sidebands of the transition

instead of the red sideband. To simulate this, I will adapt a Monte-Carlo approach. The ion will be initialised in the ground state of motion at 420 kHz. In figure 5.18, I show the population in different phonon states as a function of sideband heating time. The laser parameters are chosen to be same as they were for the single-ion and two-ion sideband cooling studies.

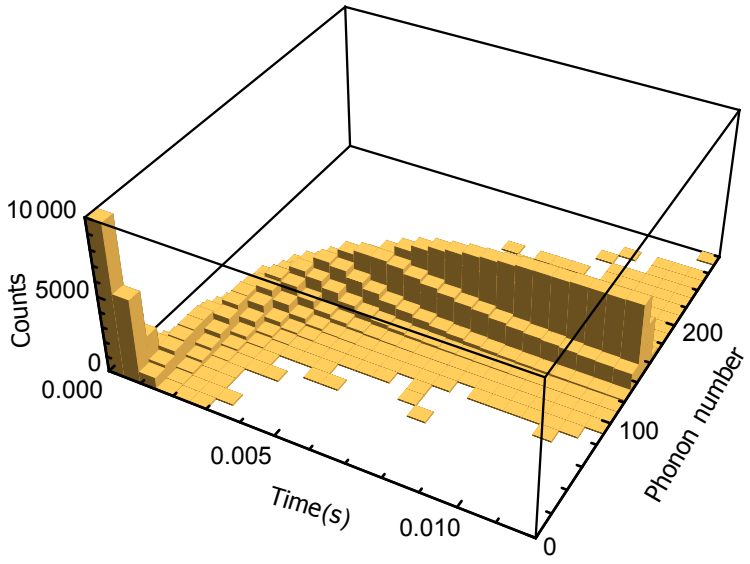


Figure 5.18: A simulated histogram plot for the population after sideband heating on the blue sideband, where time is varied from 0 ms to 12 ms. It can be seen that the population moves towards the first minimum of the blue sideband. At 420 kHz motional frequency the blue sideband minimum is observed at $n = 163$.

Simulation results are further illustrated in figure 5.19. Note that, initially, as $\langle n \rangle$ begins to increases with time, the standard deviation (spread of the population in phonon states) also increases due to the diffusion effects. Once the upper tail of the population distribution approaches near $n = 163$, the standard deviation starts to shrink and the growth of $\langle n \rangle$ slows down. This is attributed to falling blue sideband strength as a function of the phonon number. Eventually, population settles to $n \sim 150$. The further sideband heating only increases the standard deviation while maintaining the $\langle n \rangle$.

This can be contrasted with the situation where an ion is cooled to its motional ground state. In the ground state cooling case, all the population accumulates into the $n = 0$ phonon state. On the other hand, the whole population cannot be sideband heated to a single state due to the presence of diffusion outside the Lamb-Dicke regime. Nevertheless, the shrinking of the population in sideband heating case is unachievable unless around the point of blue sideband minima. These dark states are only achieved due to the effect of a large L-D parameter.

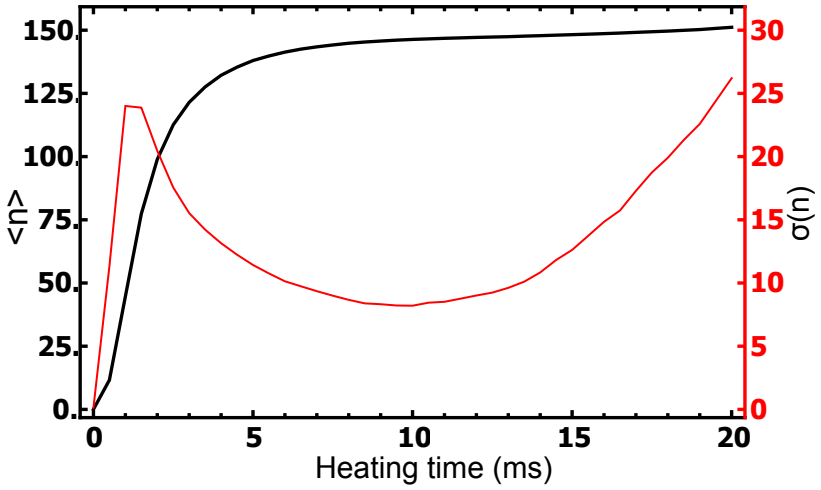


Figure 5.19: Figure shows population dynamics after sideband heating as a function of laser interaction time. Black curve represents mean phonon number ($\langle n \rangle$) and red curve represents the standard deviation around the mean value.

5.5 Summary

In this chapter, I presented the simulation studies of resolved sideband cooling in a Penning trap. The studies were performed for a multi-level atomic system in order to incorporate different Zeeman sublevels of a calcium ion in a Penning trap. The studies were conducted by employing a Monte Carlo method and in some places a rate equation approach was adapted. The cooling dynamics was described for the situations where the population lay outside the L-D regime after Doppler cooling. A multi-stage cooling sequence was devised to envisage ground state cooling of motion in such situations. The studies were further extended for two ions in a Penning trap and appropriate cooling dynamics was investigated. Additionally, through a resolved sideband heating method, a large phonon state is engineered for the application of coherent dynamics of trapped ions outside the L-D regime. These studies will be further verified experimentally in the following chapter.

Chapter 6

Experimental realisation of ground state cooling in a Penning trap

In this chapter, I will present the experimental results of ground state cooling of trapped calcium ions in a Penning trap. Previously, ground state cooling of the axial motion of a single ion has been performed in our trap [45]. After performing Doppler cooling of a single ion at a low trapping potential, the population lies outside the L-D regime, which affects the sideband cooling dynamics. Moreover, sideband cooling of radial motional modes has not been demonstrated before due to complicated motion in the radial plane. In this chapter, I will show the first ever demonstration of sideband cooling of the radial motion in a Penning trap. The experimental results of sideband cooling of multiple ions will also be presented in this chapter. Studies have only been performed along the axial direction for multiple ions. In the last section of this chapter, I present the results of sideband heating of a single ion, where the ion is prepared far outside the L-D regime by a resolved sideband heating technique.

6.1 Ground state cooling of the axial motion of a trapped calcium ion

The methodology of sideband cooling was explained in section 3.3 and the relevant level structure of a calcium has been described in chapter 5. Resolved sideband cooling is performed on a narrow linewidth transition. The S–D transition of a calcium ion is best suited for this purpose. For sideband cooling of the axial motion, the 729-nm laser beam direction is chosen to match the trap axis (say the z-axis). The laser beam induces the transition between the $m_j = -1/2$ sub-level of the $S_{1/2}$ state and the $m_j = -3/2$ sub-level of the $D_{5/2}$ state. To efficiently populate the ground state, it is essential to pre-cool the ion to its Doppler limit. Doppler cooling of a calcium ion is carried out on the S–P transition, which is a broad linewidth transition. In this case, the motional states are not resolved by the Doppler cooling laser beam. As discussed in chapter 3, in order to achieve the Doppler limit, the laser needs to be red detuned from the

transition by $\Gamma/2$, where Γ is the natural linewidth of the transition. After Doppler cooling, the trapped ion typically achieves a mean phonon number between 20 and 120. The value of the mean phonon number after Doppler cooling depends upon the value of the axial frequency.

The results will be divided into two parts, first at a low trapping potential and second at a relatively higher value of the trapping potential. At a low trapping potential, due to the large value of the L-D parameter (typically $\eta > 0.2$), the system will be considered as outside the LD regime.

6.1.1 Sideband cooling at a low trapping potential

The experimental demonstration is carried out at a 50 V trapping potential (187 kHz axial frequency). In our system, the ion is precooled by a pair of red-detuned 397-nm laser beams. The beam is focussed at the trap centre to approximately to 100 μm beam waist. The estimated laser power at the trap centre is $\sim$ 4 μW for each laser beam. In order to achieve efficient Doppler cooling, the laser intensity is required to be below the saturation intensity. In low axial frequency traps, efficient Doppler cooling also requires additional measures due to the relaxation heating. In a low-frequency ion trap, the ion is shifted away from its trap centre due to the radiation pressure. In practice, if the laser beam is turned off for any reason, the ion oscillates around the trap centre with this initial offset from the trap centre leading to additional energy of motion [91]. A similar case is observed during Doppler cooling of an ion at 50 V trapping potential in our trap. The increase in the ion's average kinetic energy eventually leads to a higher temperature than otherwise achieved. In order to obtain a lower value of temperature in our system, the 397-nm laser intensity is attenuated to less than half from its initial value.

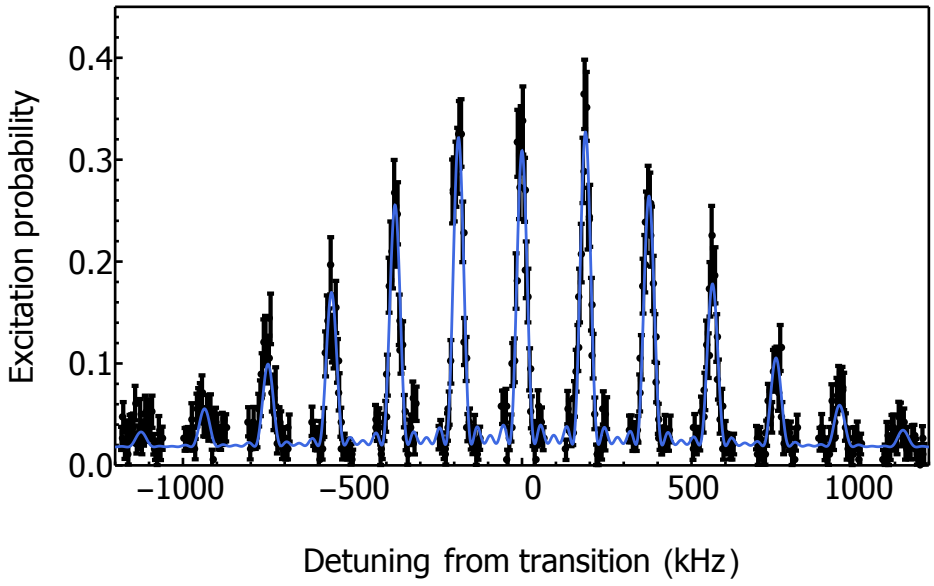


Figure 6.1: Doppler spectrum of a trapped calcium ion at 187 kHz trap frequency. The value of $\langle n \rangle$ is estimated to be 55 ± 3 by fitting the experimental data. Several sidebands are observed indicating the system is outside the L-D regime.

In order to estimate the temperature after Doppler cooling, a spectrum is recorded with the 729-nm laser beam. The trap is operated at 187 kHz axial frequency. At this frequency, $\langle n \rangle$ after Doppler cooling is expected to be 51. To avoid relaxation heating, the 397-nm laser power is reduced to one half of its normal operating value. Typically, the 397-nm laser powers are set to 1.7 μW at the trap centre for each beam. The 854-nm and 866-nm laser beams are operated at normal operating powers. The measurement involves a 12 ms Doppler cooling sequence followed by a short probe laser pulse at 729 nm. The 729-nm laser photons shelve the ion to its metastable state ($D_{5/2}$ state), depending upon the detuning from the transition. The shelving probability is estimated by detecting the state of the ion with the 397-nm laser beams. In this case, the ion scatters the photon only if the shelving did not place during the probe time. The experimental sequence is repeated 400 times before the probe laser frequency is changed to a different value and the shelving probability is estimated by comparing the dark and bright counts during the state detection.

In practice, the pre-cooling is performed for a relativity longer duration than the required time. In normal operating conditions, Doppler cooling is achieved in a time scale of 1 ms. In our system, cooling is performed for 12 ms and the collected photons are used as an indicator of the ion's state before the interaction with the 729-nm laser photons, to avoid any false readings. In practice, this additional measure indicates if the cooling lasers have become unlocked or if the ion has undergone a strong collision with the residual gas. If any of these events occur during the measurements, the state of the ion is recorded as shelved to the metastable states. This will lead a false excitation probability. In the current system, fluorescence counts during Doppler cooling are used to distinguish between actual shelving and false shelving due to collisions.

The spectrum of a Doppler cooled calcium ion is shown in figure 6.1. The recorded spectrum is fitted using a "sinc function", which includes the behaviour of all sidebands weighted by a thermal distribution function. The excited state probability for a Doppler cooled case is given as

$$P(e) = \sum_{n=0}^{\infty} \frac{\langle n \rangle^n}{(\langle n \rangle + 1)^{n+1}} \frac{\Omega_{n,n'}^2}{\Omega_{n,n'}^2 + (\omega - \Delta n\, \omega_z)^2} \sin^2 \left(\frac{1}{2} \tau \sqrt{\Omega_{n,n'}^2 + (\omega - \Delta n\, \omega_z)^2} \right), \qquad (6.1)$$

where $\langle n \rangle$ is the mean phonon number and Δn (= $n' - n$) is the sideband number. The fitting of the experimental data suggests that the mean phonon number ($\langle n \rangle$) after Doppler cooling is 55 ± 3, which is reasonably close to the theoretical Doppler limit i.e. $\langle n \rangle$ = 51 at this trap frequency.

Single-stage sideband cooling

After performing Doppler cooling, the ion is prepared for sideband cooling. The relevant laser sequence used for sideband cooling of a single ion is shown in figure 4.21. The sideband strength at this motional frequency is plotted as a function of phonon number and this is shown in figure 6.2. Interestingly, in this case, the Doppler cooling limit indicates that $\sim 26\%$ of the population lies at $n \geq 72$, which is the first red sideband minimum. A spectrum after performing the single-

stage sideband cooling of a calcium ion at 187 kHz axial frequency is shown in figure 6.3. In this case, sideband cooling is performed through the first red sideband of the transition. The fitting estimates that $\sim 84\%$ of the population is in the ground state and the remaining 16% population is trapped around the first red sideband minimum. The population trapping is also verified by the rate equation calculation; a similar approach is discussed in chapter 5. The spectrum also shows that the excitation probability for the first red sideband is zero but at the same time, the second and third red sidebands are visible, which confirms that the population is trapped at the first red sideband minimum point.

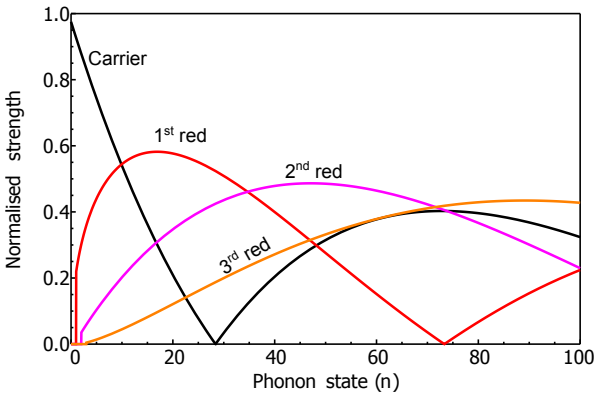


Figure 6.2: Sideband strength as a function of phonon state number of a single calcium ion at 187 kHz axial frequency. First red sideband minimum is observed at $n = 72$.

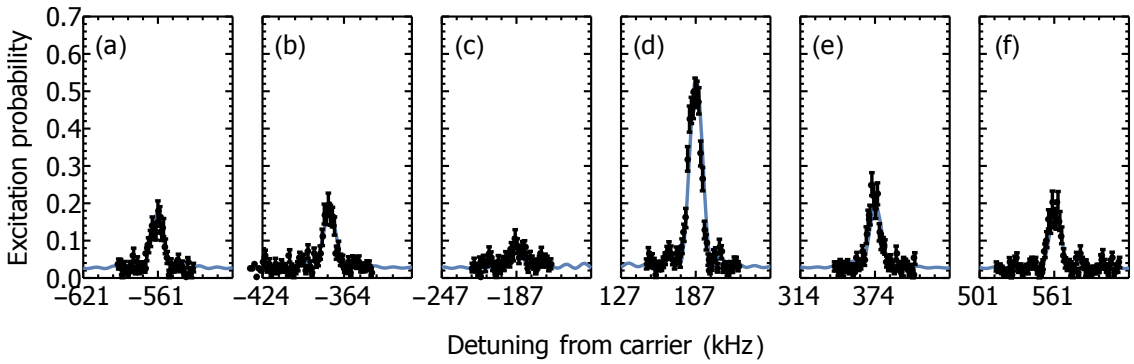


Figure 6.3: Figure showing a spectrum after 10 ms of resolved sideband cooling on the first red sideband. The first red sideband (a) is nearly zero, however, the second and third red sidebands (a, b) show excitation indicating some population is trapped near the first red sideband of the transition.

Multi-stage sideband cooling

In order to efficiently prepare the ion in the motional ground state[1], a multi-stage cooling sequence is employed. The cooling sequence is indicated in figure 6.4 a. In the previous chapter,

[1]Ideally, a ground state of motion is achieved when an ion is found in $n = 0$ for all realisations, which corresponds to $\langle n \rangle = 0$. In real systems realising a perfect ground state of motion is impossible, but rather the state is represented by a small non-zero value of the mean phonon number. In this thesis, the term “ground state cooling" will be used as a shorthand for the experimental realisations when the ion is found predominantly in the ground state of motion.

multistage sideband cooling is discussed with the simulation results. In this case, the laser is tuned to the 2nd, 3rd, 2nd, 3rd and finally the 1st order red sidebands of the transition and cooling is employed for 5 ms at each sideband. A spectrum after proper ground cooling of a single ion at 187 kHz axial frequency is shown in figure 6.4. The fitting estimates $\langle n \rangle = 0.03 \pm 0.01$, which corresponds to 97 % population in the ground state of motion. The results are also verified through simulation studies and the estimated cooling limit matches with the predicted values.

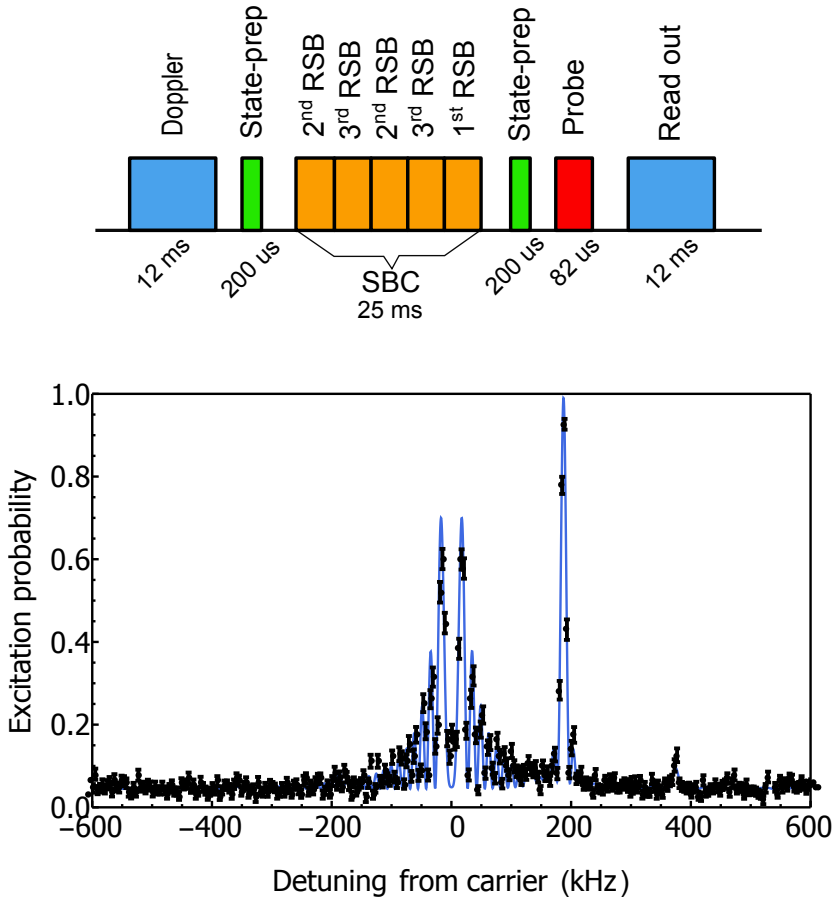


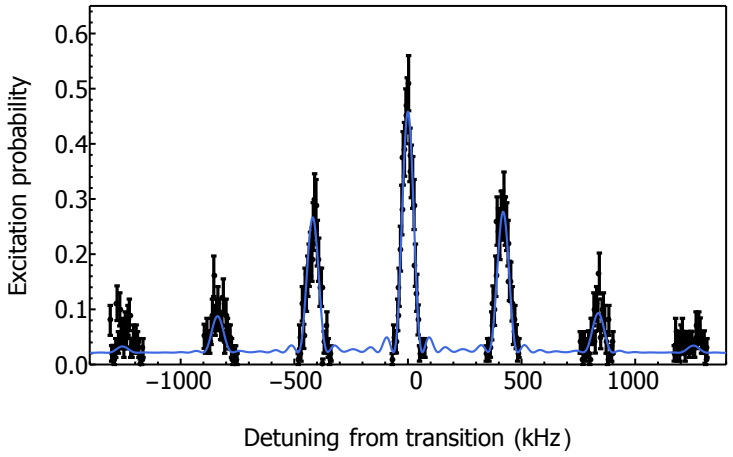
Figure 6.4: A multistage sideband cooling sequence (top). A spectrum after multi-stage sideband cooling of the axial motion at 187 kHz trap frequency is shown at the bottom of the figure. The mean phonon number is estimated to be $\langle n \rangle = 0.03 \pm 0.01$.

6.1.2 Sideband cooling at a high trapping potential

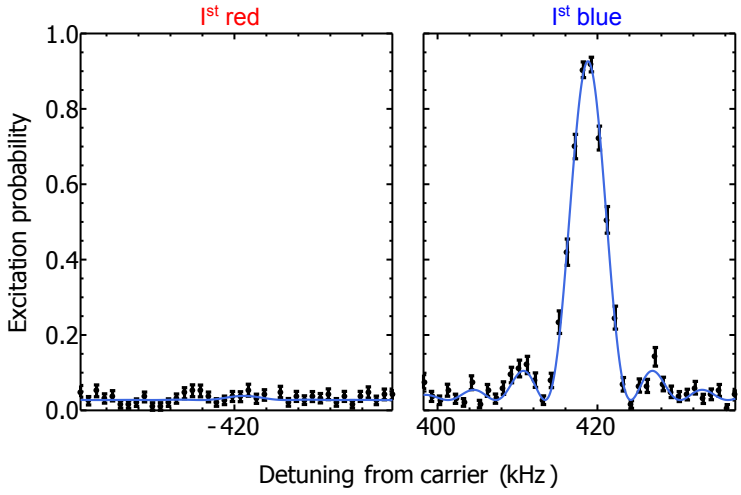
At a high trapping potential, cooling is relatively simpler due to the fact the L-D parameter is small. In order to demonstrate the ground state cooling, the trap potential is chosen to be 250 V, at which the axial frequency is $\sim$ 420 kHz in our system. The L-D parameter is calculated to be 0.15 for a trapped calcium ion at this frequency. After Doppler cooling, only 2% of the population is expected to lie outside the first red sideband minimum. Simulation studies at this trap frequency showed that even single stage cooling is sufficient to cool the ion to the

ground state. In the current demonstration of ground state cooling, a two-stage sideband cooling sequence (1st-2nd-1st red sidebands) is employed, which ensures ground state occupation to be $\sim 99\%$.

A spectrum after Doppler cooling is shown in figure 6.5a at 250 V trap potential. The fitting gives $\langle n \rangle = 24 \pm 2$. The estimated mean phonon number is found to be within the theoretically calculated Doppler limit ($\langle n \rangle = 22$). A spectrum after performing two-stage sideband cooling is shown in figure 6.5a. The fitting estimates $\langle n \rangle = 0.012 \pm 0.009$, confirming the simulation studies shown in the previous chapter.



(a)



(b)

Figure 6.5: Figure showing spectra of an ion after performing (a) Doppler cooling for 10 ms (b) sideband cooling for 20 ms at 250 V trap potential. See text for fitted results.

6.1.3 Cooling dynamics of the axial motion

The sideband cooling rate and the minimum achievable mean phonon number both depend on the 729-nm Rabi frequency and the 854-nm repumping rate. The theoretical description of the transition rates for the relevant transition has been carried out in chapter 5. The Rabi

frequency is measured by performing a Rabi flop experiment with a ground state cooled ion. A detailed analysis of the Rabi flop experiment will be carried out in chapter 7. Typically, at 40 mW of 729-nm power at the trap centre, the Rabi frequency is measured to be 40 kHz at the carrier transition. The sideband cooling results that will be presented in this thesis are acquired at roughly the same value of Rabi frequency. In some cases, the laser intensity was decreased in order to reduce the off-resonant excitation rates, which helps to obtain better cooling. Specifically, if the sidebands are located close to the carrier transition, the off-resonant excitation causes heating of the ion, which is avoided by reducing the laser power and thus reducing the off-resonant rates.

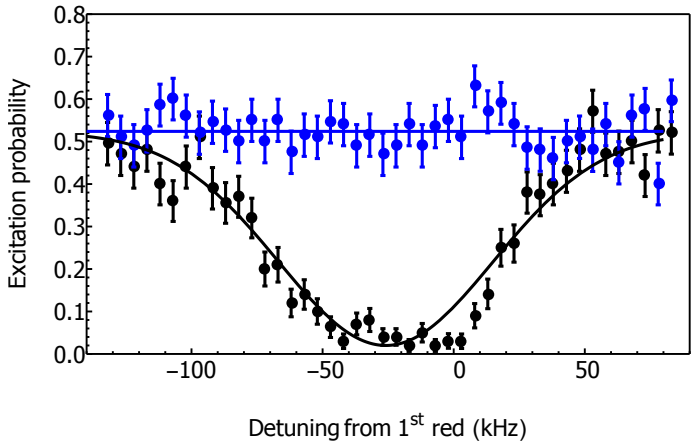


Figure 6.6: The figure shows the dip-spectrum for a ground state cooled trapped calcium ion in our Penning trap (black data points). The cooling frequency is scanned across the first red sideband and the ion is probed at a fixed value of probe frequency, usually tuned to the first red sideband of the transition. In the event of ground state cooling, a dip is noted and the point of minimum excitation is found. The blue data points are recorded after probing the ion after Doppler cooling.

In order to efficiently cool the ion, it is important to tune the 729-nm laser to the correct detuning value. In principle, the cooling laser is tuned to the first red sideband of the transition, but in reality, the AC Stark effect changes the cooling frequency. In this case, the Stark effect is caused by the repumping laser (the 854-nm laser beam). If the 854-nm laser is red detuned from the transition, then it shifts the $D_{5/2}$ level further away from its initial position and the cooling transition is further red detuned. In our experiments, the AC Stark shift is measured by the "dip-spectrum experiment". The method is similar to the sideband cooling experiment except the probe pulse is set to the first red sideband of the transition and the cooling pulse frequency is scanned across the cooling transition. The experiment requires the precise positioning of the red sideband (unshifted) at which the probe pulse is tuned to. The ion is then sideband cooled with the cooling pulse and the frequency of the cooling pulse is scanned across the cooling transition. In the event of ground state cooling, the excitation strength of the first red sideband sees a dip and the frequency of the minimum excitation is estimated. Such a spectrum is shown in figure 6.6. The experiment is carried out by acquiring two spectra alongside each other. The first spectrum is acquired after Doppler cooling of the ion and probed at the first red sideband of the transition. In this case, a constant level of excitation is observed, which sets a base level for the

other spectrum. This is denoted by the blue data points in figure 6.6. The second spectrum is acquired after 10-20 ms of sideband cooling and probed at the actual sideband position. If the sideband cooling laser frequency is scanned across the cooling transition, the excitation strength varies depending upon whether the ion is ground state cooled or not. In the event of perfect ground state cooling, the first red sideband excitation goes to almost zero. Such a spectrum is denoted by the black data points in figure 6.6. The estimated cooling frequency in this case comes to -25 kHz from the first red sideband, indicating the value of the AC Stark shift.

The other important parameter for sideband cooling is the repumping rate (Γ_{eff}). It determines the rate at which the metastable state is recycled to the $P_{3/2}$ level. In order to efficiently cool the ion, the ion needs to be repumped at an appropriate rate. Usually, a higher repumping rate leads to broadening of the transition, thus causing heating due to the off-resonant excitation. On the other hand, if the re-pumping rate is small, then the sideband cooling process takes longer, which is not ideal for many experiments. In the previous chapter, I showed that a repumping rate of roughly 10 kHz is suitable for our system. In order to estimate the cooling rate, the repumping rate has been measured experimentally. A plot showing repumping of metastable state population using the 854-nm laser beam is shown in figure 6.7.

For the current experiment, the ion is first prepared in the motional ground state and a π pulse is applied on the carrier transition to shelve the ion in the metastable state. The 854-nm laser is then switched on for a variable time and the excited state population is measured. Sideband cooling is not essential for this experiment but gives better control for shelving the ion in the metastable state. The estimated repumping rate depends upon the 854-nm detuning and the laser intensity at the trap centre. Typically, the laser beam is used at 0.6 mW of power at the trap centre, focused to a beam waist of roughly 100 μm. In this case, a detuned laser beam is advisable to avoid any heating due to broadening effects, hence a few tens of MHz detuning gives rise to roughly 13 kHz of repumping rate. In our system, prior to running the sideband cooling sequence, the repumping rate is optimised by the above mentioned method.

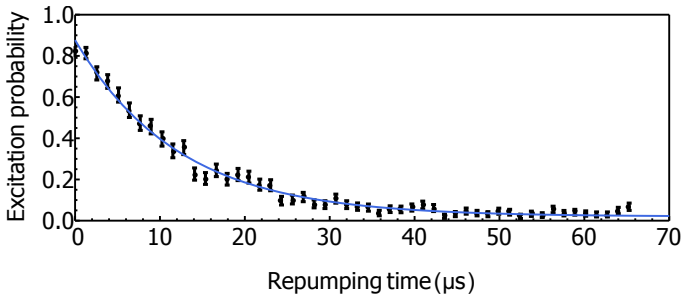


Figure 6.7: The figure shows repumping of the metastable state using 854-nm laser after optimising the laser detuning and the beam pointing at the ion. Fitting estimates the rate to be 13.0 ± 0.4 kHz.

After optimising the sideband cooling parameters, the ground state cooling of an ion at 419 kHz axial frequency is performed and the mean phonon number $\langle n \rangle$ is measured for various sideband cooling times. The measured $\langle n \rangle$ as a function of cooling time is shown in figure 6.8. The study suggests that typically 10 ms time sideband cooling is sufficient to achieve 98%

population in the ground state of motion. The study also suggests that longer cooling does not increase the ground state occupation. In our system, in most experimental studies, sideband cooling is performed for longer than the required time. The extra time is found to be helpful to account for the laser frequency and power drifts during sideband cooling.

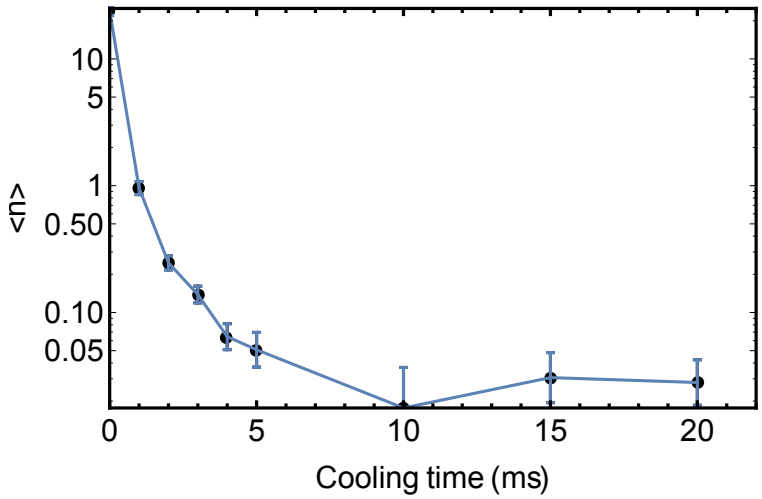


Figure 6.8: The figure shows measured $\langle n \rangle$ as a function of sideband cooling time.

6.2 Demonstration of ground state cooling of radial motional modes of a calcium ion in a Penning trap

For radial ground state cooling, the 729-nm laser beam propagates along the direction perpendicular to the magnetic field axis inducing both radial modes simultaneously. In this case, the S–D transition is also induced through the 729-nm laser light with a polarisation perpendicular to the quantisation axis. Previously, our group has examined sideband cooling of the radial motion and demonstrated preliminary results at a low axial trapping potential. At a low axial trapping potential, when $\omega_- < \Omega_0$, the magnetron sidebands are unresolved in the Doppler spectrum. In this case, ground state cooling is found to be inefficient [98]. This study implied that the ground state cooling of the modified cyclotron mode can be achieved by the resolved sideband method but the magnetron motion is not cooled to the ground state. The experimental studies showed that the magnetron motion was cooled from $\langle n \rangle \sim 1000$ from $\langle n \rangle \sim 100$. In the current thesis, those studies will be extended and the ground state cooling of both modes will be demonstrated. The studies are performed at a trapping potential of 100 V. At this trapping potential, the magnetron frequency is calculated to be 51 kHz and modified cyclotron frequency is calculated to be 677 kHz for a calcium ion in our trap.

6.2.1 Radial Doppler spectrum

Prior to sideband cooling of the radial motion, the ion is cooled through the Doppler cooling method. As discussed in chapter 3, Doppler cooling of the magnetron motion requires a gradi-

ent in laser intensity. It is found that the gradient cooling is efficient only at a low axial trapping potential and at high trapping potential (high axial frequency) the mean phonon number for the magnetron motion increases exponentially for a given beam waist and detuning. The exponential increase in the mean phonon number as a function of the axial frequency has been shown in figure 3.2. This is overcome by employing the axialisation field in the radial plane. In this case, the normal Doppler cooling on the modified cyclotron cools both modes simultaneously. In theory, no gradient cooling is required when the axialisation field is applied [123]. In practice, the gradient cooling helps to achieve better cooling along with the axialisation field. I have also carried out a preliminary simulation for the stochastic cooling process in the presence of the axialisation field and results are presented in figure 3.4. The simulation studies indicate that the simultaneous use of axialisation field and gradient cooling outperforms the gradient cooling. Cooling is expected to bring both modes to an approximately equal amplitude of motion.

After adapting the axialisation technique as described in section 3.2, the mean phonon number for the magnetron motion is reduced. Preliminary adjustments are made by estimating the radial spread using an EMCCD image. We noted that the EMCCD image showed a wider spread of the ion in the radial plane if the axialisation field is not applied. After applying an axialisation field at the ring electrode at 500 mV the spread is reduced. After preliminary adjustments, the Doppler spectrum is recorded under these conditions. The spectrum of a Doppler cooled calcium ion in our trap is shown in figure 6.9. In this experiment, the Doppler cooling laser is red-detuned by roughly $\Gamma_{397}/2$. In addition to this, the axial 397-nm laser power is reduced to 1μW for each 397-nm laser beam. This additional precaution helped in minimising the additional heating caused by the emission of photons in the radial direction. The radial 397-nm laser beams still operated at 6.5 μW each at the trap centre. A detailed description of Doppler cooling of the radial motion will be given in the thesis of Pavel Hrmo. I will only present the important results of radial cooling.

Experimental data of the Doppler spectrum is shown in figure 6.9. Several sidebands are observed in the spectrum, which suggests that the system is far outside the L-D regime. The peaks are found to be grouped together in a regular manner. The set of peaks at zero detuning correspond to the carrier transition and its magnetron sidebands. Similarly, the modified cyclotron sidebands and their respective magnetron peaks are observed in the spectrum. The spectrum is fitted with the Lorentzian peak functions corresponding to each sideband and they have been plotted as red curves. In this spectrum, the fitting of the whole spectrum is found to be computationally expensive, hence the mean phonon numbers for each mode will be estimated separately.

The mean phonon numbers are estimated separately, for each mode, by fitting the individual comb. At first, the magnetron $\langle n \rangle$ is estimated by performing a least squares fit of the carrier magnetron comb. This spectrum, along with the fitted curve, is shown in figure 6.10. The estimated value of $\langle n \rangle$ comes to be 75 ± 7. Similarly, $\langle n \rangle$ for the modified cyclotron modes has been estimated by fitting the relevant peaks. In this case, the intermodulation peaks are dropped from the spectrum and the fitting is carried out of the modified cyclotron sidebands only. The

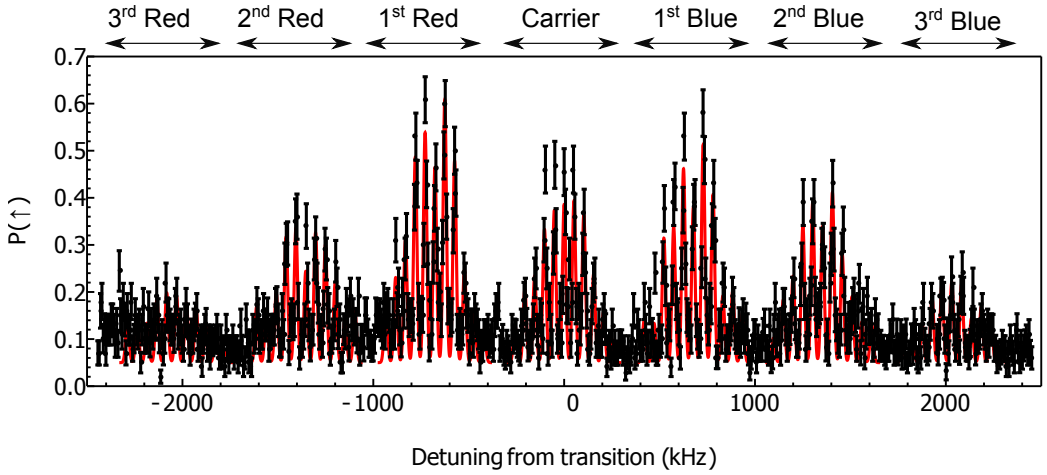


Figure 6.9: A spectrum after performing Doppler cooling of the radial motion of a trapped calcium ion in a Penning trap. The curve in red is used to indicate the relevant sideband transitions. Each comb corresponds to a modified cyclotron sideband (labelled with relevant sideband number) and it contains 11 magnetron sideband peaks in one comb.

fitted spectrum is shown in figure 6.11 and $\langle n \rangle_+$ is measured to be 51 ± 5. The values are found to agree with the simulation results discussed in section 3.2.

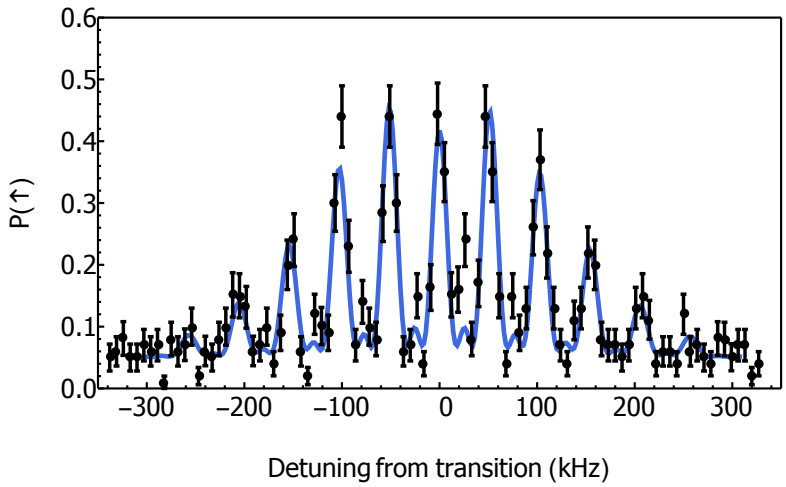


Figure 6.10: Magnetron sidebands of the carrier transition of a trapped calcium ion. The fitting is carried out in order to estimate $\langle n \rangle$ and the corresponding fitted curve is shown with the blue curve.

6.2.2 Ground state cooling of the radial motion

The above discussion of the Doppler cooled spectrum supports the possibility of ground state cooling of both modes using resolved sideband cooling. The L-D parameter is calculated to be 0.167, for both modes, suggesting that the system will be far outside the L-D regime for the case when $n \geq 18$. Following the theoretical discussion of sideband cooling of a single ion, it is

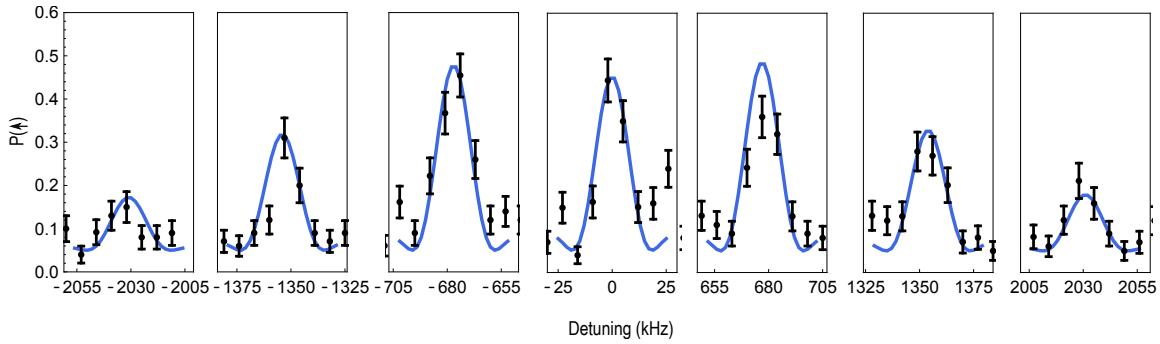


Figure 6.11: The modified cyclotron peaks are shown with black data points. The blue curve is the fit to the experimental data.

clear that a multistage cooling sequence will be essential to achieve ground state cooling of both modes. Arguably, sideband cooling of the radial modes is similar to the two-ion chain case, hence a similar treatment is performed for ground state cooling of both modes. The cooling sequence is chosen such that any population trapping is avoided. The cooling sequence is illustrated in table 6.1.

Table 6.1: Laser sequence for the radial ground state cooling without intermodulation sidebands.

Motional mode	Sideband number	Time	AOM power
Mod-C	2nd red	5 ms	100%
Mod-C	1st red	10 ms	100%
Mag	3rd blue	5 ms	100%
Mag	2nd blue	5 ms	100%
Mag	1st blue	5 ms	50%
Mod-C	2nd red	5 ms	100%
Mod-C	1st red	5 ms	100%
Mag	3rd blue	5 ms	100%
Mag	2nd blue	5 ms	100%
Mag	1st blue	5 ms	50%
Mod-C	1st red	10 ms	100%
Mag	1st blue	2 ms	50%
Mod-C	1st red	1 ms	100%

The total duration of sideband cooling is 68 ms. This is roughly seven times longer than the time required for the axial sideband cooling of a single ion. For the axial case, roughly 10 ms sideband cooling was sufficient to provide a 98% ground state population. In contrast to that, in the radial cooling case, approximately five times more phonons are removed, thus 50 ms sideband cooling time is anticipated. In addition to that, we expect some heating of one mode during sideband cooling of another, hence longer cooling is required. A similar situation is expected for a two-ion chain as discussed in the previous chapter. The cooling sequence was partially anticipated from simulation studies of a two-ion chain and partially inferred on trial and error basis.

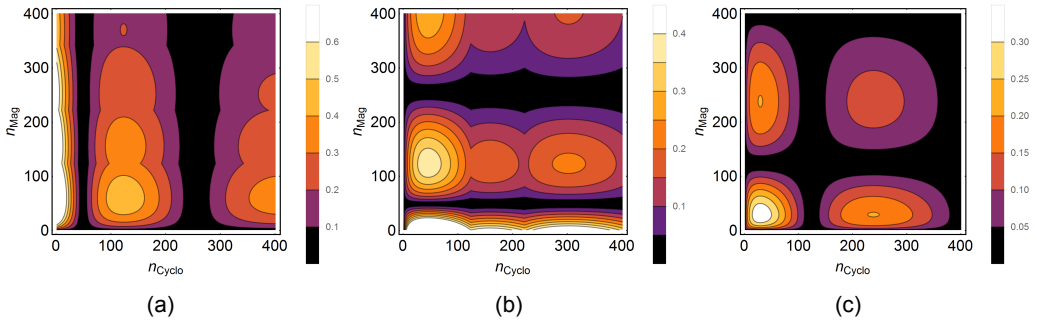


Figure 6.12: Contour plots of sideband strength for the radial motional modes, (a) 1-3 blue sidebands of magnetron mode, (b) 1-2 sidebands of breathing mode and (c) 1st blue magnetron of the 1st red modified cyclotron.

The strengths of the required sidebands are shown in figure 6.12. The contour plot in (a) shows the combined strength of the first, second and third blue sidebands of the magnetron mode. If cooling is performed with these sidebands, any population trapping at the sideband minima of the magnetron modes will be avoided. It is of utmost importance to note that sideband cooling of the magnetron mode requires the laser to be tuned to the blue sideband instead of the red sideband of the transition. A contour plot for the modified cyclotron mode is shown in figure (b), which shows the combined strength of the first and second red sidebands. In this case, cooling is realised with the first and second order sidebands only.

Additionally, population trapping is expected at the carrier minima of both sidebands, which is expected in the dark region obtained by combining the contour plots (a) and (b), i.e. $n_+ = n_- = 50$. The population trapping around those points can be avoided by performing cooling on the intermodulation sidebands as shown in contour plot (c). The plot shows the first blue magnetron sideband of the first red modified cyclotron sideband. The contour plot has sideband minima at different places than the first two, resulting in no population trapping during sideband cooling.

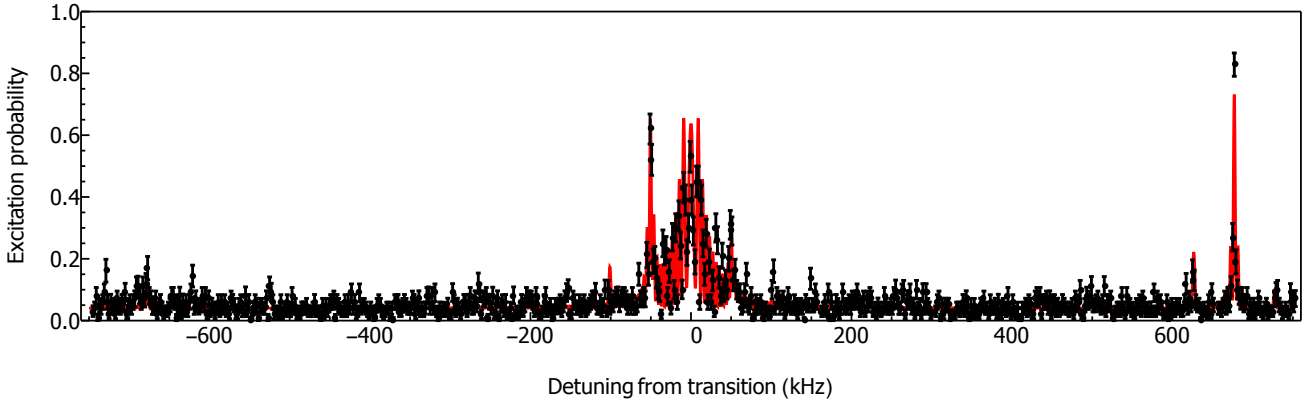


Figure 6.13: A spectrum after sideband cooling of the radial motional modes demonstrates the ground state cooling of the radial motional modes.

A sideband cooled spectrum after performing multi-stage cooling of the radial motion is shown in figure 6.13. Sideband cooling is tested with and without the intermodulation cooling pulses and it has been found to make no difference. We anticipate that in practice the population trapped in the carrier minima points is cooled through off-resonant excitation. Independently, a rate equation model is used to verify the cooling process and it is observed that cooling is achieved even without the intermodulation sidebands. The spectrum shown in figure 6.13 is clearly less complicated than the Doppler spectrum. For the modified cyclotron mode (the far distant sidebands from the carrier) the blue sideband is found to be stronger than the red sideband which signifies ground state cooling of this mode. However, for the magnetron mode, near to the carrier transition, the red sideband is found to be stronger than the blue sideband. This counter-intuitive asymmetry between magnetron sidebands demonstrates that ground state cooling of the magnetron motion has been achieved in combination with the ground state cooling of the modified cyclotron mode. The fitting suggests that the $\langle n \rangle$ is < 0.6 for the magnetron mode and < 0.4 for the modified cyclotron mode. The estimation of the exact value was difficult due to a poor least squares fitting of the spectrum.

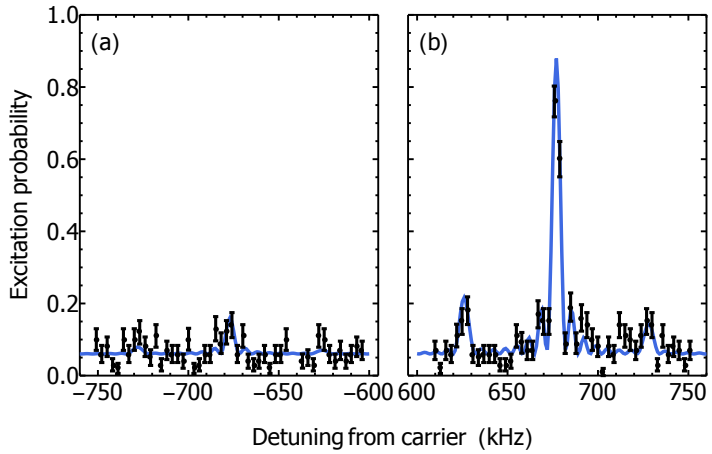


Figure 6.14: A windowed spectrum after scanning over the first order modified cyclotron modes. The blue line shows a fit to the experimental data.

Figure 6.14 a windowed spectrum after performing multistage cooling after with the same cooling sequence described above. The least squares fit is shown in blue. The mean phonon number is estimated to be 1.2 ± 0.4 for the magnetron mode and 0.14 ± 0.05 for the modified cyclotron mode. The estimated values indicate ground state cooling of modified cyclotron mode.

6.2.3 Effect of the axialisation field

The above demonstration of sideband cooling would not have worked without the axialisation field, which enormously reduced the radial temperature. However, the axialisation field itself causes issues during sideband cooling and probing of the ion. In order to avoid this, the axialisation field was kept on during Doppler cooling and it is turned off for rest of the duration. A spectrum after sideband cooling of the radial motion is shown in figure 6.15. In this case, the

axialisation field was kept on for all the time. Asymmetric red and blue peaks of the cyclotron mode verify near ground state cooling of the mode, however, some artefacts are observed around $\pm$730 kHz. These peaks correspond to the driven motion due to the axialisation field. In order to avoid the driven motion, all the radial spectroscopy results were performed without using the axialisation field during the probe and sideband cooling time. The switching of the field is carried out by an RF switch which was controlled by the experimental FPGA control system.

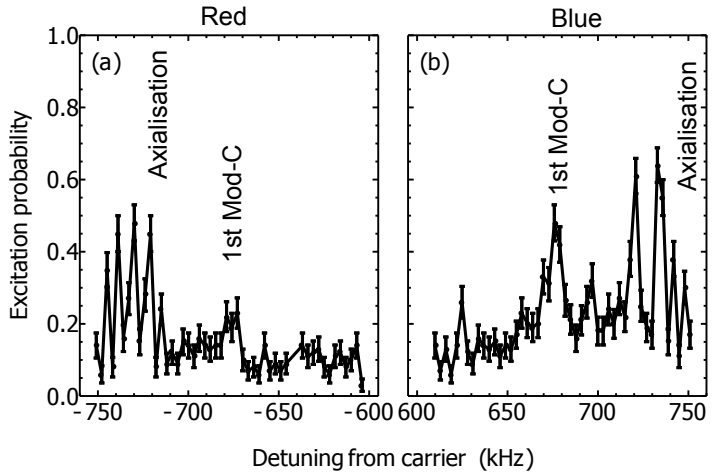


Figure 6.15: The figure shows the spectrum of a sideband cooled ion after keeping the axialisation field on during the sideband cooling and probe durations. The axialisation peaks at 730 kHz detuning are observed on both sides of the carrier transition indicating driven motion due to the axialisation field.

6.3 Sideband cooling of a two-ion Coulomb crystal

After performing ground state cooling of the axial motion of a single ion in a Penning trap, we have extended these studies for multiple trapped ions. The ground state cooling of multiple trapped ions is complicated than the single-ion case. The obvious complication arises due to the presence of multiple motional modes.

In a Penning trap, the two ions may align themselves in two different orientations with respect to the magnetic field axis. In the first situation, where the axial trapping force is weaker than the force in the radial plane, the ions align themselves in a chain configuration. The force in the axial direction in a Penning trap is provided by a DC potential, giving rise to the harmonic motion at ω_z. The relative strengths of the axial frequency and the effective radial frequency (ω_{rad}) are used to control the structure. In the second situation when $\omega_z > \omega_{rad}$ the ions align themselves in a planar arrangement. A planar crystal in the radial plane rotates about the magnetic field axis at a rotation frequency (ω_r), which is governed by the trap parameters and Doppler cooling laser parameters. A detailed discussion of two-ion Coulomb crystal can be found in chapters 2 and 5. For illustration purposes, the crystal images at two different trapping conditions are shown in figure 6.16. The relevant axial modes are also indicated in the figure.

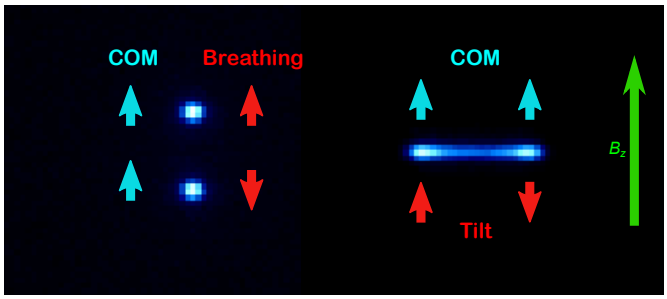


Figure 6.16: Two-ion Coulomb crystal images captured from an EMCCD camera located in the radial plane in our apparatus. On the left side a two ion chain at a low trap voltage ($U_{dc} = 50V$) showing two individual ions and on the right side a planar crystal at a high voltage ($U_{dc} = 170V$) showing a blurred disc of two ions rotating in the radial plane. The COM and the breathing/tilt motional modes are indicated for both crystal orientations.

6.3.1 Sideband cooling of a two-ion chain in a Penning trap

Sideband cooling of a two-ion chain is performed at $U_{dc} = 50$ V. In order to analyse the cooling performance, a spectrum is recorded after Doppler cooling of the crystal. Doppler cooling is performed for 23 ms. The longer cooling time was required to match the trigger and read-out times of the FPGA sequence. After Doppler cooling, the ion was probed with the 729-nm laser beam for 40 μs. The acquired spectrum is shown in figure 6.17. The laser sequence for spectroscopy of a two-ion chain is same to the single-ion case. An EMCCD camera was used to collect the scattered photons from the ions instead of the PMT, which allowed us to detect the individual ions. In order to automate the state detection with an Andor EMCCD camera, a `C#` based control was devised separately and the code is merged with the previous spectroscopy controller software.

The fitting of a two-ion Doppler spectrum was computationally expensive. The rough value of the crystal temperature was estimated from the overall width of the spectrum and it was found to be 1.5 times higher than the Doppler limit of a calcium ion. The mean phonon numbers corresponding to the COM and breathing modes are further estimated by simulating the spectrum and superimposing it with the experimental data. By minimizing the least squares difference between simulated and experimental data, the values of the mean phonon numbers are extracted to be 81 and 51 for the COM and breathing mode, respectively.

Resolved sideband cooling is performed on the crystal after optimising the pre-cooling temperature. The cooling scheme required a multi-stage cooling sequence that is examined through simulations and any population trapping is prevented. The sequence is shown in table 6.2 and it slightly differs from the one discussed in chapter 5. The scheme discussed in the simulation chapter is an optimised cooling sequence which ensures the highest occupancy with the shortest cooling time. However, the experimental run was based on a brute-force method of achieving highest occupancy in the ground state without bothering about the time taken to achieve it. The final sequence that is used for the demonstration of sideband cooling of two-ion chain comprises

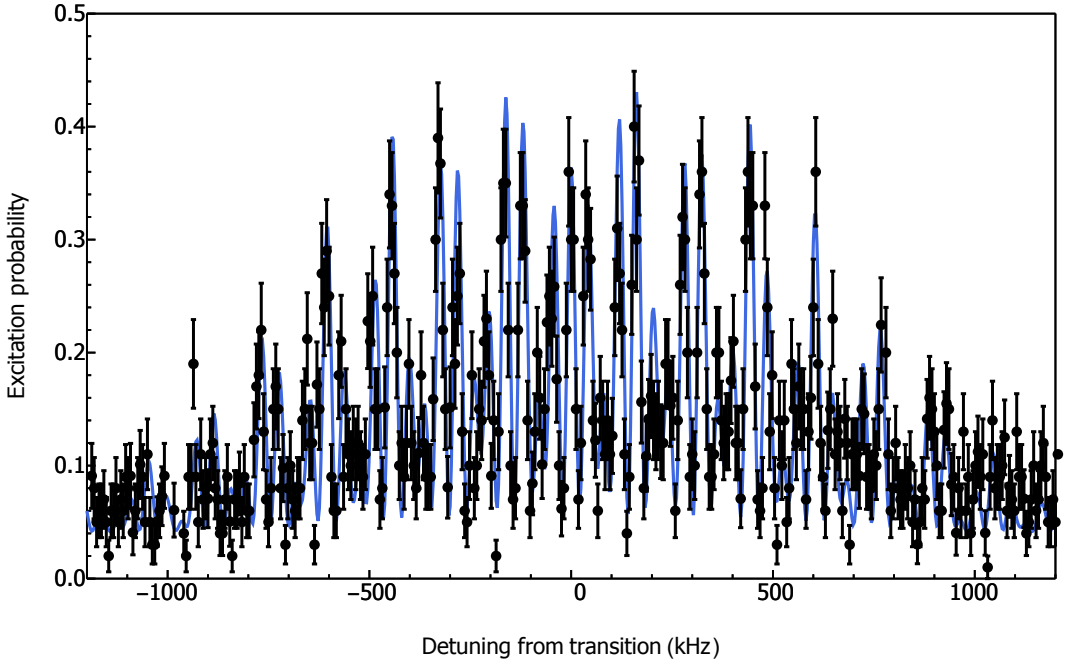


Figure 6.17: Spectrum of a two-ion Coulomb crystal in a chain configuration after 23 ms of Doppler cooling. The estimated mean phonon numbers $\langle n \rangle_{\text{com}} = 87$ and $\langle n \rangle_{\text{b}} = 51$ corresponding to COM mode and breathing modes respectively.

the red sidebands of 1$^{\text{st}}$ COM, 1$^{\text{st}}$ B, 2$^{\text{nd}}$ COM, 2$^{\text{nd}}$ B, 3$^{\text{rd}}$ COM and an intermodulation sideband.

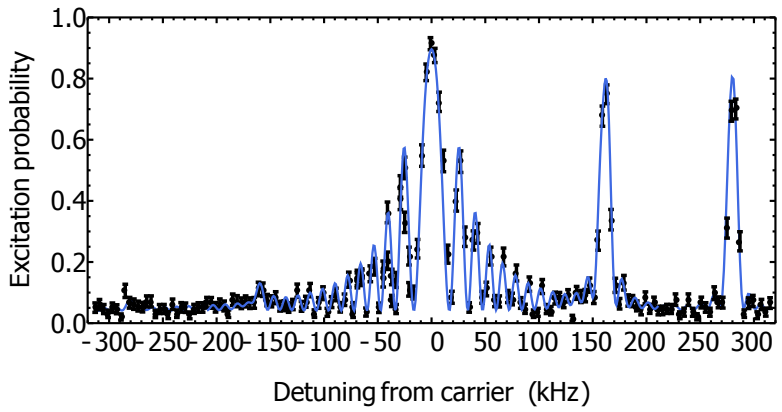


Figure 6.18: A spectrum of a two-ion chain after performing the multi-stage resolved sideband cooling for 36.4 ms. The curve in blue is the least squares fit of the experimental data.

After employing the aforementioned cooling sequence, a spectrum of two-ion Coulomb crystal is shown in figure 6.18. The spectrum clearly indicates the blue sidebands for the COM mode (at 187 kHz) and the breathing mode (at 281 kHz). However, on the red side of the transition, both sidebands disappear, verifying the ground state cooling of both modes. The fitting is carried out using a numerical model derived by solving the Schrödinger equation through numerical methods. The estimated mean phonon numbers from the fitting are $\langle n \rangle_{\text{com}} = 0.18 \pm 0.04$ and $\langle n \rangle_{\text{b}} = 0.06 \pm 0.03$ for the COM and breathing modes, respectively. In this case, a simple calculation of $\langle n \rangle$ from the ratio of the red and blue sidebands height will underestimate the

Table 6.2: Sideband cooling sequence for a two-ion chain.

Sideband number	Time (μs)	
2^{nd} COM	500	$\times 15$
2^{nd} Breathing	500	
3^{rd} COM	300	
1^{st} Breathing	200	
2^{nd} COM 1^{st} Breathing	500	
1^{st} Breathing	200	$\times 2$
2^{nd} COM	500	
1^{st} COM	500	
2^{nd} COM 1^{st} Breathing	500	
2^{nd} COM 1^{st} Breathing	500	$\times 1$
1^{st} COM	2000	
1^{st} Breathing	500	

value due to the entanglement effect thus the numerical fitting model was necessary.

6.3.2 Sideband cooling of a two-ion planar crystal

Sideband cooling was also demonstrated in a planar configuration for two ions in a Penning trap. The Doppler spectroscopy is performed in the same manner as previous cases. A spectrum after performing Doppler cooling for 10 ms is shown in figure 6.19. After Doppler cooling of the crystal in unresolved mode case, the ions were interrogated with the 729-nm laser beam for 22 μs. The spectrum looks less cluttered than a two-ion chain situation. The trapping is performed at 180 V trapping potential, which yields the axial frequency $\omega_z = 355$kHz. In a planar configuration, two motional modes along the axial direction are expected, namely the COM mode and tilt mode. The frequency of the tilt mode can be varied by changing the rotation frequency of the crystal. In figure 6.19, the sidebands are spaced at the COM frequency, suggesting the modes are unresolved. The theory of planar crystal suggests that the tilt mode and the COM modes have the same frequency if the crystal rotation frequency is equal to the magnetron or modified cyclotron frequency.

In principle, the tilt mode can be resolved by changing the rotation frequency of the crystal, which is varied by the 397-nm laser parameters. The crystal rotation frequency is severely affected by the laser detuning and intensity fluctuations. In our experimental apparatus, the Doppler cooling laser is stabilised to 1 MHz linewidth. Also, various ambient conditions affect the beam pointing at the ions, hence the rotation frequency is not found to be constant throughout the duration of the spectroscopy and sideband cooling demonstrations. The system is found to be more stable if it is operated at a higher axialisation potential (typically 2 to 4 V) and the Doppler cooling laser beam is further red detuned from the transition, which in turn reduces the spacing between tilt mode and COM mode sidebands.

In current experimental demonstration, two PMT's were used to detect the fluorescence of

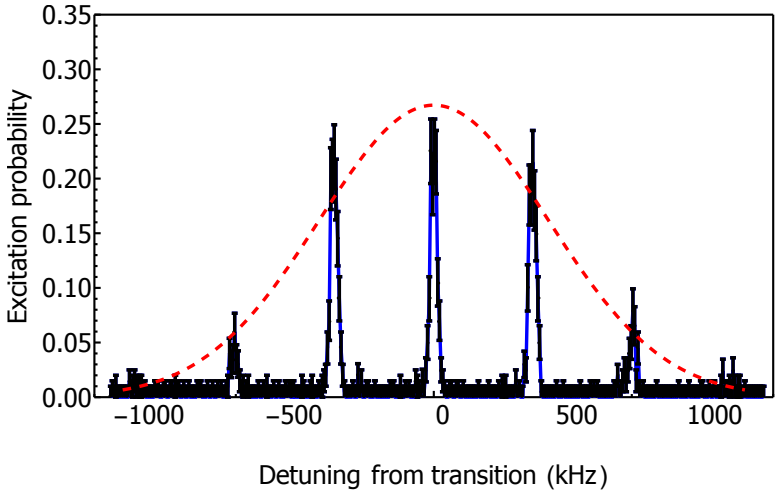


Figure 6.19: A Doppler spectrum of a two-ion planar crystal at 180 V trapping potential. The peaks correspond to both ions in the excited state. Each peak contains a COM and a breathing sideband transition.

the ions. The crystal rotates along the magnetic field direction thus individual ion detection was not possible using the EMCCD. The same can be anticipated from figure 6.16, where the two ions in planar configuration show a blurred image due to the rotation of the crystal. In this case, the PMT data are analysed for excitation of both ions. The count histogram of the PMT indicates three distinct peaks. The PMT counts for this case are shown in figure 6.20, where each bin corresponds to the counts during 12 ms of readout time. If both ions are shelved in the metastable state, only background counts are detected. The threshold method was used to distinguish the peaks and the excitation probability is estimated for both ions in the excited state. The Doppler spectrum in unresolved motional modes case is difficult to fit. An upper limit of $\langle n \rangle < 30$ is estimated by superimposing a Gaussian envelope on the experimental data.

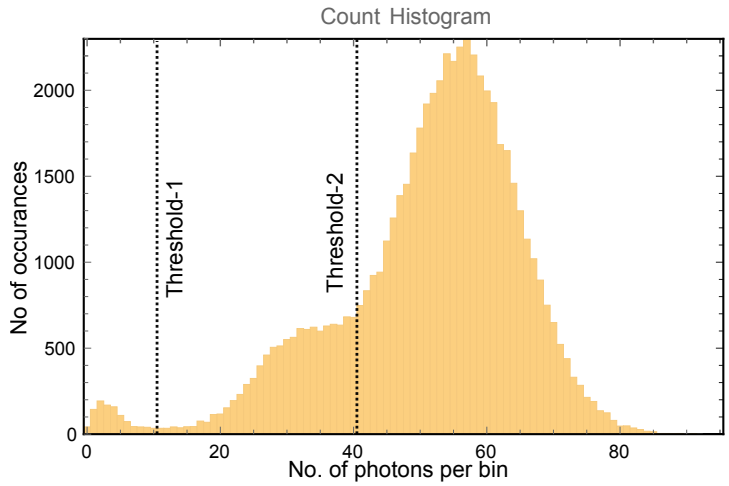


Figure 6.20: A histogram of the PMT data used for the state detection of two ions. The counts in the left side of threshold-1 correspond to both ions in the metastable states and the counts between threshold-1 and threshold-2 correspond to one of the two ions metastable state.

After performing Doppler cooling of the crystal, resolved sideband cooling is employed on the system. The study is performed at $U_{dc} = 180$ V, hence a smaller L-D parameter is expected than that of a two-ion chain. In this case, cooling does not require us to consider the higher order sidebands into the cooling sequence. Just to avoid any issues, cooling was performed with a 2^{nd} red sideband cooling pulse along with the 1^{st} red sideband. Cooling was performed for 25 ms at the COM sidebands only and the other mode was off-resonantly cooled. The cooling dynamics was also verified through the simulation studies as discussed in section 5.3.4. A spectrum after sideband cooling is shown in figure 6.21. The fitting estimated that $\langle n \rangle < 0.2$ for both motional modes. In this figure, the peaks on the left and right side of the carrier transition are artefacts and observed due to the rotation of the crystal. It is anticipated that the peaks are observed due to non-uniform beam pointing and non-zero beam angle from the trap axis. The peaks as such do not limit the coherent control. On the other hand, these peaks provide additional information to estimate the tilt mode frequency. The relation between of tilt mode and rotation mode frequencies can be seen in equation 2.35.

For the current experiment, the rotation frequency of the crystal is measured to be 111 kHz and at which the tilt mode frequency comes to be $\omega_{\text{tilt}} \sim 348$ kHz. Additionally, the rotation frequency is estimated through crystal size measured using an EMCCD image. The measurement is described in appendix D. The rotation frequencies at various trapping voltages have been measured and the values are shown in figure 6.22. For comparison, the magnetron frequency is also calculated and the rotation frequency is found to be roughly 10 kHz higher than the magnetron frequency.

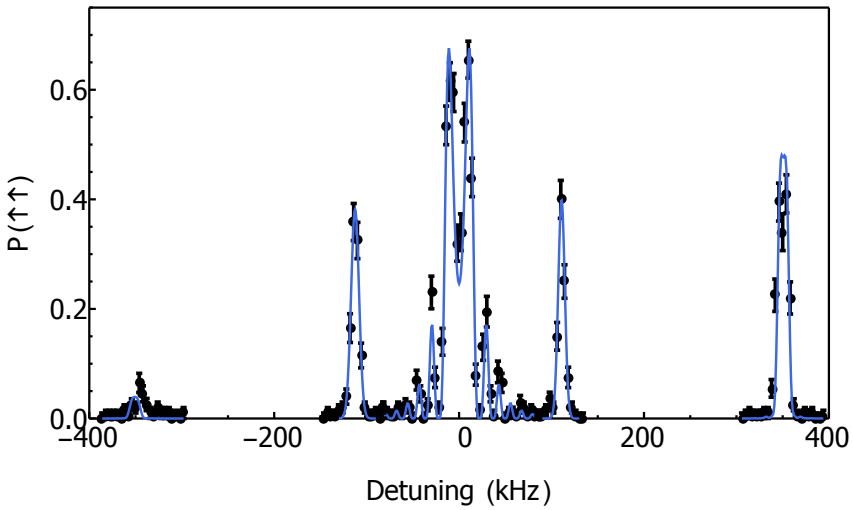


Figure 6.21: A spectrum of a two-ion planar crystal after performing resolved sideband cooling for 25 ms. The tilt mode and COM mode sidebands are found to be overlapping. The peaks at ± 110 kHz are artefacts due to the rotation of the crystal about the magnetic field axis.

Furthermore, results are also shown for a resolved sideband case. The experiment was performed at the same trapping and laser cooling conditions as before. In order to resolve the motional modes in the spectrum, the spectroscopy probe intensity is reduced to a few mW at the trap. The laser interaction time is adjusted in order to obtain a near π pulse for the blue

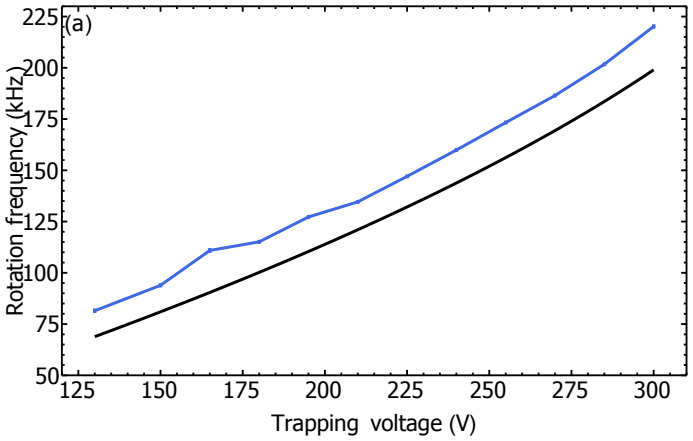


Figure 6.22: Measured rotation frequency of a two-ion planar crystal in a Penning trap at different values of the trap voltages (in blue). For comparison, the magnetron frequency of a single ion is calculated at 1.86 T magnetic field and the rotation frequency is found to be approximately 10 kHz higher than the magnetron frequency.

sidebands for both modes. The spectrum is shown in figure 6.23. The spectrum clearly reveals two distinct peaks. The mean phonon number for both sidebands is estimated to be < 0.2 by fitting the experimental data.

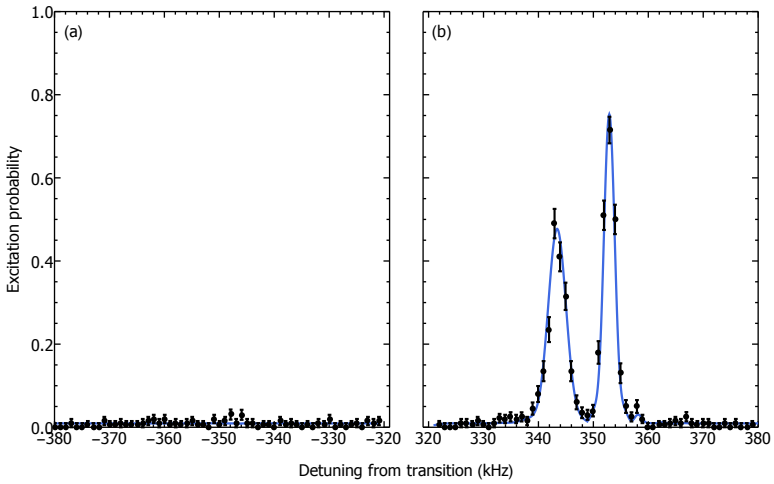


Figure 6.23: Spectrum of sideband cooled two-ion planar crystal at 180 V trapping voltage. The tilt mode and COM mode peaks are resolved in this case and a fitting of the experimental data is carried out (curve in blue) measuring $\langle n \rangle < 0.2$.

6.4 Sideband cooling of a multi-ion Coulomb crystal

After demonstrating sideband cooling of two ions, we extend the studies for multiple ions. In a Penning trap, planar crystals are of main interest due to their use in quantum simulations. Planar crystals are observed if the radial confining force is weaker than the axial confining force. In general, the structure can be changed from a linear chain to a planar configuration by changing the trapping potential. Such a structural change is demonstrated in figure 6.24 for hundreds of

ions. In the current studies I show the experimental demonstration with only a small number of ions in a planar configuration. The motional modes and their frequencies of a planar crystal along the axial direction can be solved by numerical methods [75]. The detailed discussion of motional frequencies and more results of sideband cooling of a crystal can be found in an upcoming thesis of Vincent Jarlaud.

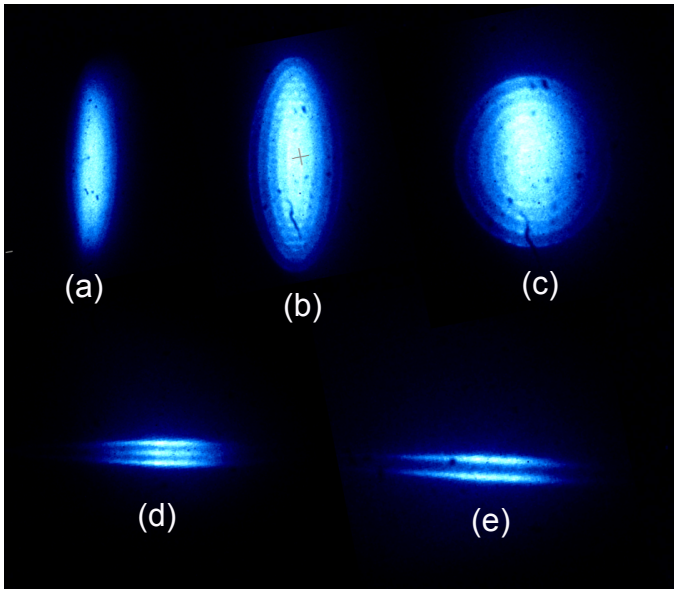


Figure 6.24: Structural change in ion Coulomb crystals from (a) to (e) in increasing order of trapping potential in a Penning trap.

6.4.1 Ground state cooling of a three-ion Coulomb crystal

A three-ion planar crystal in a Penning trap forms an equilateral triangle geometry where all three ions reside at an equal distance from the trap centre. A top-down and side-on schematic view of a three-ion Coulomb crystal is shown in figure 6.25. The current experimental arrangement does not allow us to image the crystal through top-down imaging and images can be only taken from side-ways, thus a blurred image is expected.

The motional modes of the three-ion Coulomb crystal are expressed in terms of three normal modes of motion. The expected modes are illustrated in figure 6.26. In this case, one COM and two degenerate tilt modes are expected. In this case also, the COM frequency is same as a single-ion axial mode frequency and the tilt motional mode frequency depends upon the rotation frequency of the crystal.

A spectrum after sideband cooling of a three-ion Coulomb crystal is shown in figure 6.27. The spectrum is constructed for overall photon counts of 400 repeats. Each repeat contains the photon counts taken over 12 ms duration. In this case, the experimental system does not provide sufficient contrast between individual peaks in the histogram count data, as observed for a single-ion and two-ion cases, thus the excitation probability of an individual ion cannot be

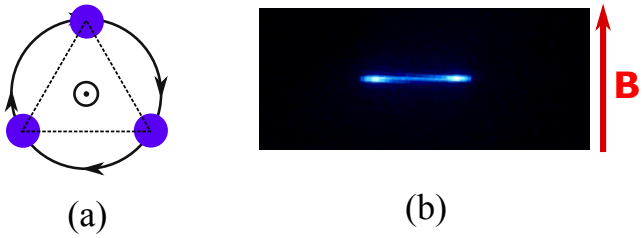


Figure 6.25: Schematic of a three-ion planar Coulomb crystal in a Penning trap: (a) top view where crystal is rotating in clockwise direction under the influence of rotating forces due to laser beam and magnetic field, (b) side-on view where due to the rotation of the crystal the image will be blurred.

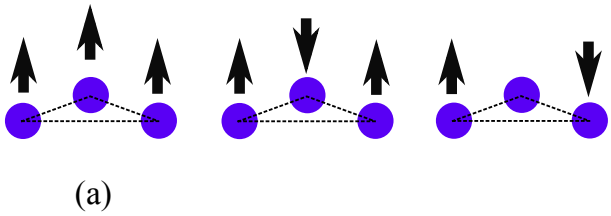


Figure 6.26: Axial motional modes of a three-ion planar Coulomb crystal, (a) COM mode and (b), (c) two orthogonal tilt motional modes.

measured. The experiment was performed at 210 V trapping potential, which gives the COM frequency to be 379 kHz. A large asymmetry between the blue and the red sideband of motion verifies the ground state cooling of both modes. In the spectrum, various other sidebands are visible, which are seen due to the radial artefacts. The peaks have been identified and they have been labelled accordingly in the figure.

For this particular set of experiments, sideband cooling is performed on first, second and first red sidebands of the COM mode for a total 30 ms (10 ms for each sideband). The other motional mode is cooled off-resonantly and the ground state cooling is achieved for both modes. In order to stabilise the crystal structure, an axialisation potential is applied between the segments of the ring electrode at 4 V of amplitude. In order to estimate the mean phonon number, each axial sideband peak is fitted using a Lorentzian peak model and the peak height is measured. The mean phonon number is roughly estimated by comparing the heights of the red and blue sidebands of the transition. For the current spectrum, the mean phonon number for the COM mode and tilt mode are estimated to be $\langle n \rangle \leq 0.1$ and $\langle n \rangle \leq 0.5$, respectively.

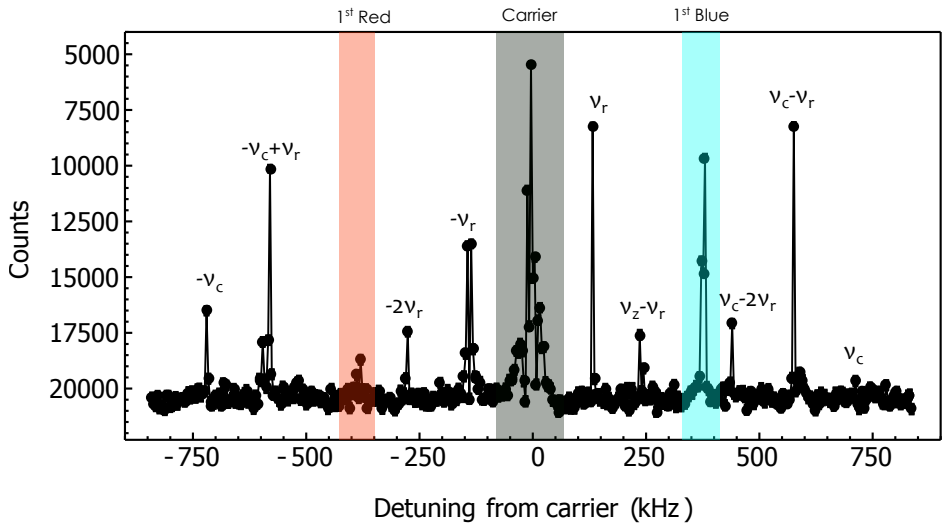


Figure 6.27: The figure shows a spectrum of a three-ion planar crystal in a Penning trap after performing ground state cooling for 30 ms. The important peaks in inverted plot of photon counts are labelled in the figure for illustration purpose.

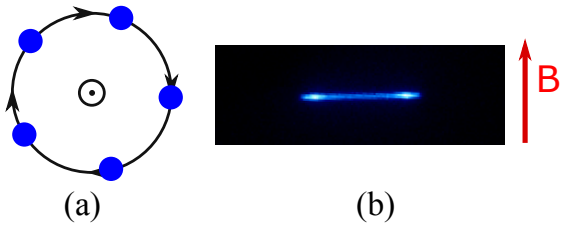


Figure 6.28: A crystal structure of a five-ion planar Coulomb crystal in a Penning trap. For our system the structure is experimentally realised at 210 V axial potential and the corresponding COM frequency is calculated to be 384 kHz.

6.4.2 Sideband cooling of a five-ion Coulomb crystal

Sideband cooling of axial motional modes of a five-ion crystal is demonstrated at 210 V axial potential. A spectrum after performing resolved sideband cooling for 20 ms is shown in figure 6.29. The corresponding crystal structure is shown in figure 6.28. The asymmetry between the red and the blue sideband in the spectrum confirms the near ground state cooling of all five axial modes. In this case, we do not have a direct model to fit the sidebands hence it is difficult to estimate the mean phonon numbers. All five modes are expected to be closely spaced to the COM sidebands, as indicated with dotted lines. The spectrum includes the red, carrier and blue sidebands of the transitions. The radial artefacts are not shown in the spectrum for clarity.

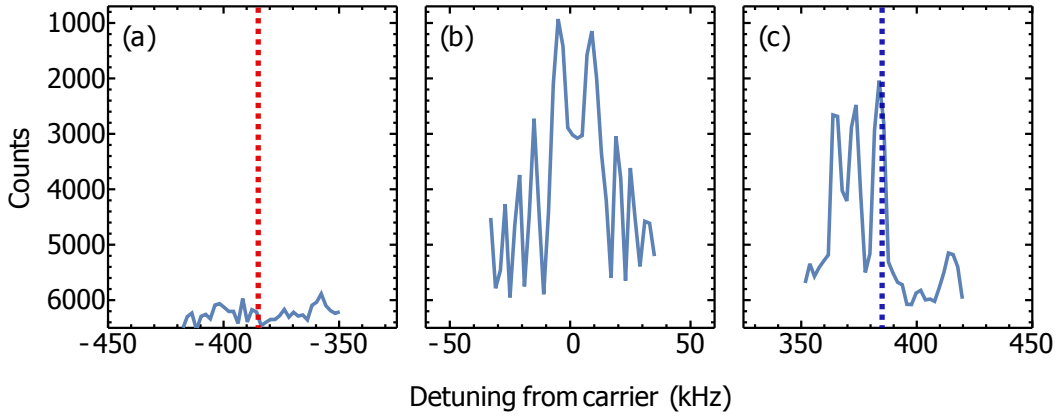


Figure 6.29: A spectrum after two-stage sideband cooling (2nd and 1st red) of a five-ion Coulomb crystal in a Penning trap. All the axial modes are found to be within the comb of the first blue sideband. The motional modes are cooled off-resonantly while performing resonant cooling on the COM mode. The COM sidebands are marked with the red and blue dotted lines in spectrum (a) and (c) and the carrier peak is shown in spectrum (b).

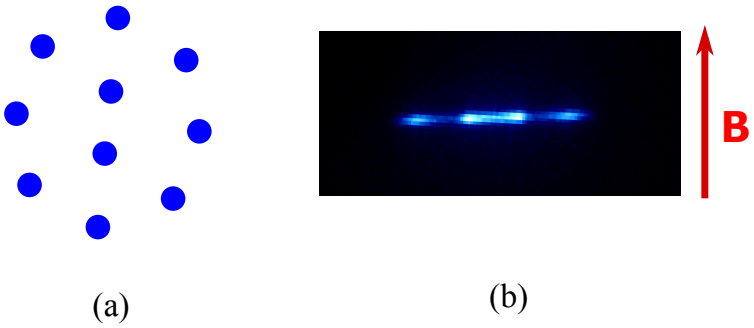


Figure 6.30: A ten-ion planar Coulomb crystal in our Penning trap (a) viewed along the trap axis (b) in the radial plane. The image is blurred due to the rotation of the crystal about the magnetic field axis.

6.4.3 Sideband cooling of a ten-ion Coulomb crystal

Sideband cooling of a ten-ion Coulomb crystal is demonstrated at 210 V axial trapping voltage and a spectrum is shown in figure 6.31. The red, blue and carrier sidebands have been labelled. Sideband cooling is performed for total of 31 ms after cooling on various first and second order red sidebands, resonantly and off-resonantly. A large asymmetry indicates the ground state cooling for all axial motional modes which have been found grouped close to the first red and the first blue COM motional sidebands. The remaining peaks observed are due to the rotation of the crystal. A crystal structure and the EMCCD image are shown in figure 6.30.

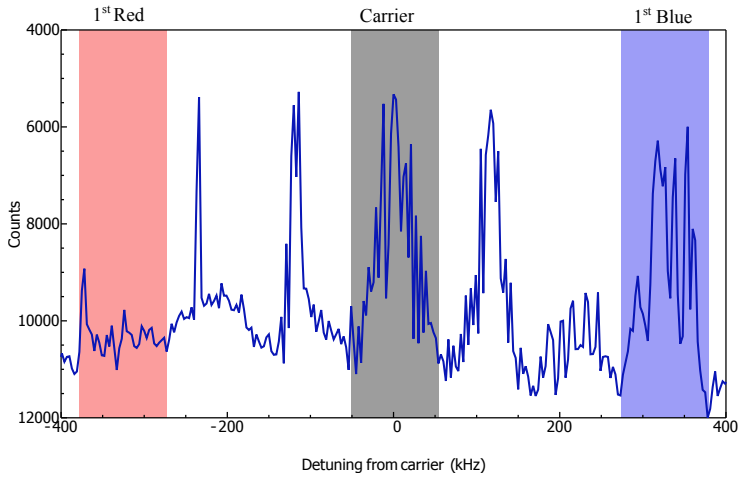


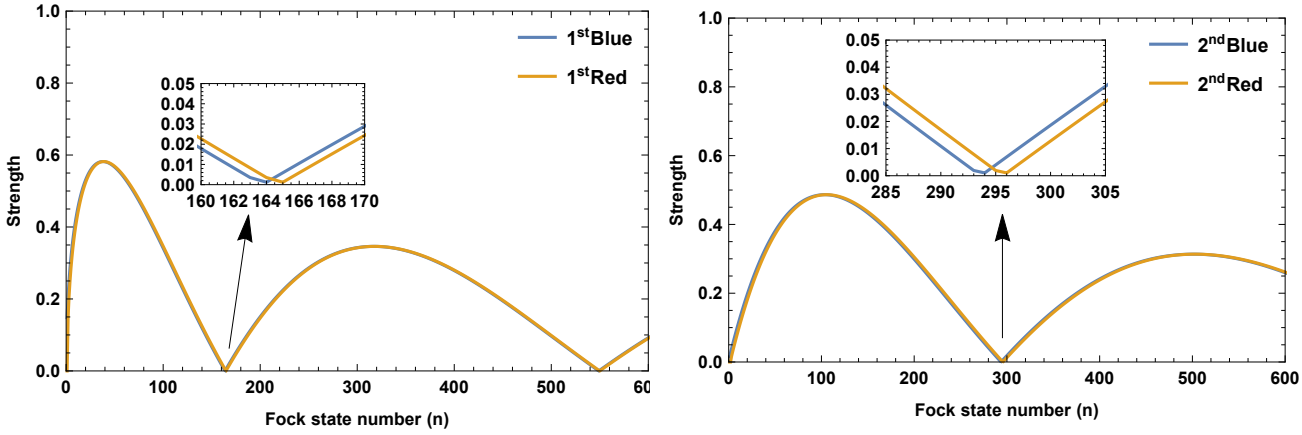
Figure 6.31: A spectrum after ground state cooling of a ten-ion planar Coulomb crystal in a Penning trap. The two-stage sideband cooling sequence is used for 31 ms and the asymmetry between the red and blue sideband signifies the ground state cooling.

6.5 Sideband heating: preparing an ion outside the L-D regime

In this section, I will present the results of sideband heating of a single ion. These studies will be used to demonstrate the coherent control of a system far outside the L-D regime. In chapter 5, we discussed the case of sideband heating of an ion after tuning the 729-nm laser to a blue sideband of the transition. In order to verify those studies, an experimental demonstration is carried out with a ground state cooled trapped calcium ion in our apparatus at 419 kHz axial frequency. The sideband heating is performed on the first blue axial sideband. After following the discussion from the previous chapter, the process is expected to prepare the ion near the first sideband minimum point, which is indicated in figure 6.32a. At this frequency, the first blue sideband minimum point is obtained at $n = 163$, which gives $\sqrt{(2n+1)}\eta \sim 25$. For this situation, the system will be prepared far outside the L-D regime.

The experiment is demonstrated by performing 20 ms of sideband cooling followed by 10 ms of sideband heating of the axial motion. The spectrum is shown in figure 6.33a. In this spectrum, the first red and first blue sidebands are weak in comparison to the other sidebands. The spectrum is fitted to a non-thermal type of distribution and the mean phonon number is estimated to be $\langle n \rangle = 145 \pm 2$ with a spread of $\Delta n = 17$. The fitting model is given in appendix E. The estimated mean phonon number is lower than the actual blue sideband minima point ($n = 163$), which is anticipated due to shorter sideband heating duration. Longer heating is expected to move the population to a higher value of the mean phonon number but at the cost of a larger spread of the population, which is not useful for us. The same can be inferred from the simulation studies shown in figure 5.19.

Similarly, we perform the sideband heating of an ion through a second order sideband and prepare the ion at the phonon state where the second order sideband is minimum. The second blue and the second red sideband strength as function of phonon number at 419 kHz axial

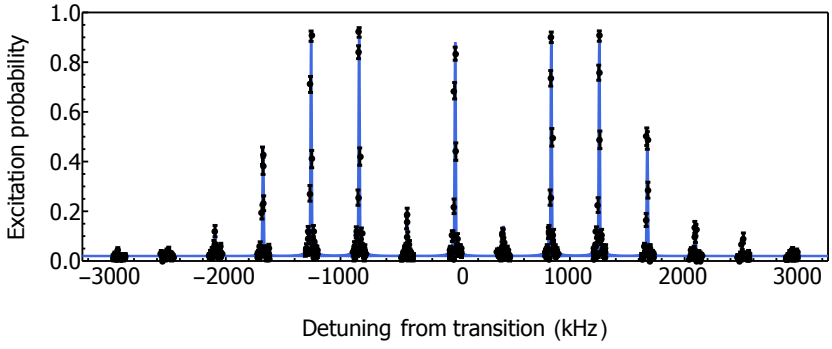


(a) (b)

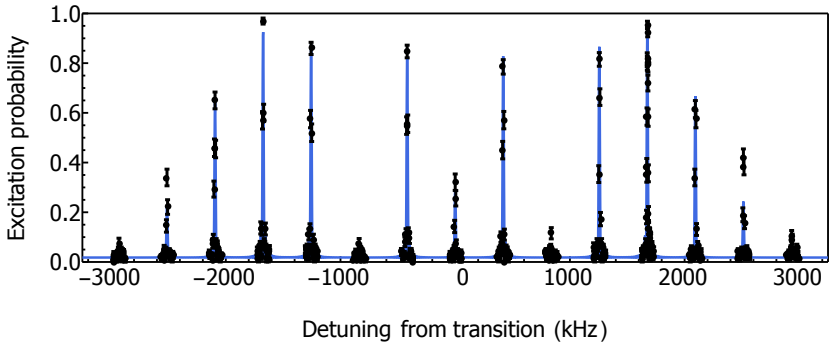
Figure 6.32: Calculated plots of sideband strengths (a) 1st red and 1st blue sidebands (b) 2nd red and 2nd blue sidebands at 419 kHz trapping frequency.

frequency can be seen in figure 6.32b. In this case, the sideband minimum is expected at $n = 294$. Experimentally, the sideband heating is performed in two steps. In the first step, the ion is prepared at the first blue sideband minimum point using the first blue sideband transition for 10 ms of sideband heating. The second step prepares the ion in the second blue sideband minimum point after 10 ms of sideband heating. The spectrum acquired after two-stage heating is shown in figure 6.33b. The experimental data points are fitted with a model assuming a Gaussian probability distribution function in phonon space. The spectrum is found to be fitting well to the distribution functions and the fitting gives $\langle n \rangle = 288 \pm 2$, with a spread around the mean point Δn = 14. The spectrum also shows that the second blue and second red sideband are weaker than other sidebands.

The above studies are of particular interest for coherent control with a higher order sideband. So far, coherent control has been demonstrated within the L-D regime, where the higher-order sidebands are not observed or are weakly observed. The higher order sidebands are evident if the system is prepared outside the L-D regime. Our studies indicate that coherent control can be realised even with the 6^{th} order sideband. In order to verify it, we perform a Rabi flop experiment on the 4^{th} red sideband of the transition after preparing the ion at $\langle n \rangle = 288$. The Rabi flops of the 4^{th} red sideband are shown in figure 6.34, indicating a clear of sinusoidal pattern. The experimental demonstration is equivalent to a laser ion interaction of a two-level system, where the two levels are realised with $|g, n\rangle$ and $|e, n-4\rangle$. Also from the previous studies, it is clear that the sideband heating does not prepare the ion in a definite phonon state, rather a Gaussian distribution around a mean phonon state is achieved. The occurrence of a sinusoidal pattern is expected due to the fact that the strength of the fourth order sideband is roughly constant around the second blue sideband minimum point. Further discussion of coherent control will be carried out in chapter 7.



(a)



(b)

Figure 6.33: Spectrum after sideband heating (a) 1st stage sideband heating (b) 2nd stage sideband heating of a trapped calcium ion.

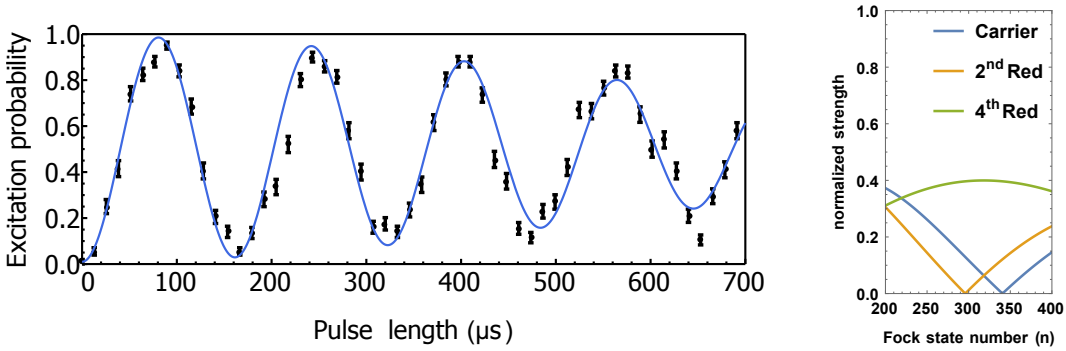


Figure 6.34: Rabi oscillations of the 4^{th} red sideband of transition after preparing the ion at $\langle n \rangle$ = 288. The transition strength of the carrier, first red and the fourth red sideband is shown on the right side.

6.6 Adiabatic ground state cooling of a trapped ion in a Penning trap

Previously, sideband cooling outside the L-D regime has been demonstrated using a multi-stage cooling sequence. In an extension to that, I present the results of ground state cooling of an ion by the means of adiabatic cooling. In this demonstration, the ion is first ground-state cooled at a relatively high motional frequency and then the trap potential is reduced adiabatically,

maintaining the ground state occupancy. At a higher trapping frequency, typically a single stage cooling sequence is sufficient.

In order to carry out the experiment, a DC switch is installed in the system and controlled using a TTL pulse generated by the experimental control system. The schematic of the switch control is shown in figure 6.35. The switching of the trap supply must be slow enough to maintain the ground state population. Previous studies of adiabatic cooling suggest that in order to maintain the ground state population the trap frequency must be changed at $\dot{\nu_z} \ll 2\pi\nu_z^2$ [67, 124], where ν_z is the trap frequency and $\dot{\nu_z}$ is the rate of change of trap frequency. The time constant of the circuit in our system is measured to be 7 μs (see figure 6.36). The value of the time constant implies that the adiabatic nature is maintained if the motional frequency is changed from 420 kHz to 180 kHz. In order to achieve cooling for even lower axial frequency, an additional 10 nF capacitor is installed in the circuit and the time constant is increased to 45 μs, for which the adiabatic nature is maintained down to 60 kHz trap frequency.

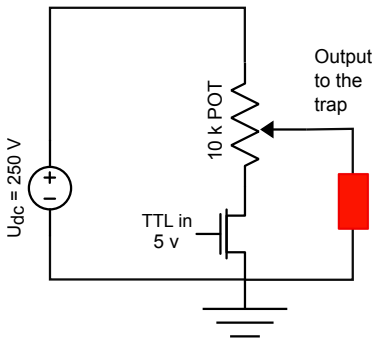


Figure 6.35: Schematic of the electrical circuit used to demonstrate the adiabatic cooling in our trapping system. The MOSFET is enabled by a 5 V TTL pulse controlling the potential division at a 100 kΩ POT.

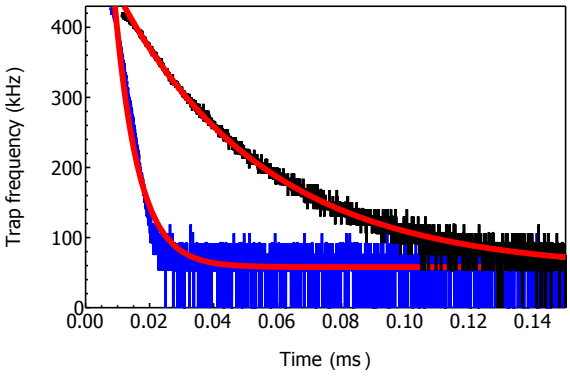


Figure 6.36: Measurement of time constant of the electrical circuit used to decrease the trapping voltage adiabatically, (black data points) with additional 10 nF capacitor and (blue data points) no additional capacitor in the circuit. The measured time constant is 45 μs and 7 μs with and without a capacitor in the circuit.

In this process, we observed that if the trap potential is changed in an adiabatic manner, the

ground state population is maintained. Spectroscopy of the ion is performed to verify this. A spectrum before and after the adiabatic cooling is shown in figure 6.37. Sideband cooling is performed at 419 kHz axial frequency. The mean phonon numbers from fits to the spectra are found to be 0.01 ± 0.01 and 0.03 ± 0.02 at 419 kHz and 195 kHz, respectively. In the spectrum, the apparent change in the height of the blue sidebands is attributed to the difference in the L-D parameter for both cases, which depends on the trap frequency. In the current demonstration, the probe time is chosen to be same at both trap frequencies.

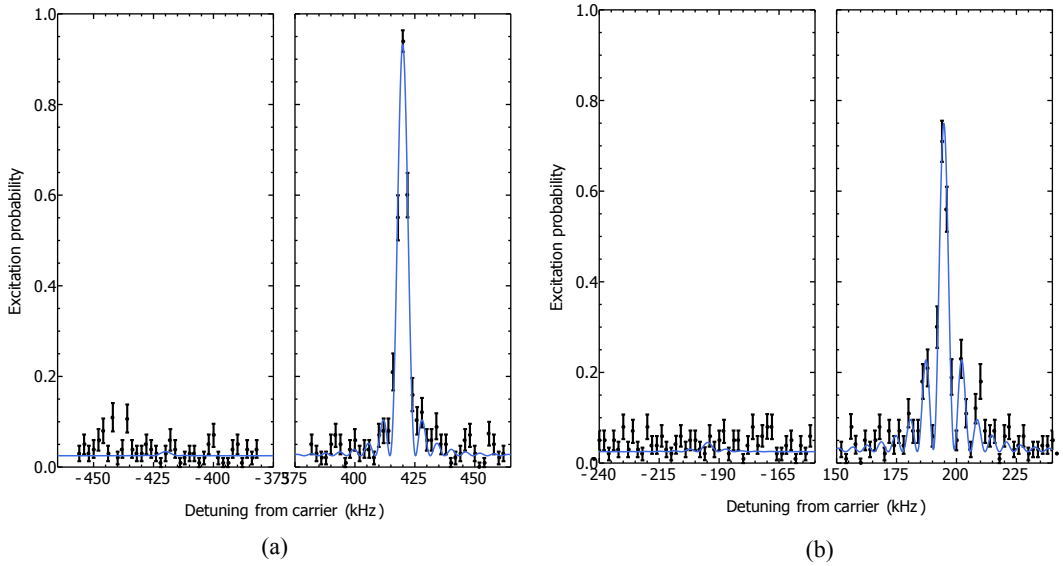


Figure 6.37: The first red and first blue sidebands of a trapped calcium ion (a) before and (b) after decreasing the trap potential from 250 V to 50.4 V. Sideband cooling is performed at 250 V and the asymmetry of the red and blue sidebands is maintained after changing the voltage to 50.4 V.

Furthermore, the experimental studies are verified at various values of the trap voltages. Like the previous study, sideband cooling is performed at 419 kHz and eventually the trap is relaxed to achieve cooling at lower trap frequencies. The demonstration is carried out between 66 kHz and 377 kHz trap frequencies and the estimated mean phonon values are shown in figure 6.38. The experimental results are compared with the simulated cooling limit as shown in figure 5.14. The simulated cooling limit is calculated by a rate equation model, which considers a multi-stage cooling sequence. The experimental results show the adiabatic cooling process achieves a mean phonon number lower than that from the multistage cooling methods at the same trap frequency. Furthermore, the experimental sequence for the adiabatic cooling is much simpler than what would be required for a multi-stage cooling method. Sideband cooling through adiabatic means is found to be more efficient and will have great use when a large L-D parameter is required. The technique is used in chapter 7 to demonstrate coherent control at a low trap potential.

At lower values of the axial frequencies, the mean phonon number is found be slightly higher than before changing the trap frequency. This is expected due to a small DC offset at the trap centre caused by patch potentials in the trap electrodes. Any patch potential is expected to move the ion position while lowering the trapping force. For illustration purpose, a curve at $1/\nu_z^2$ is

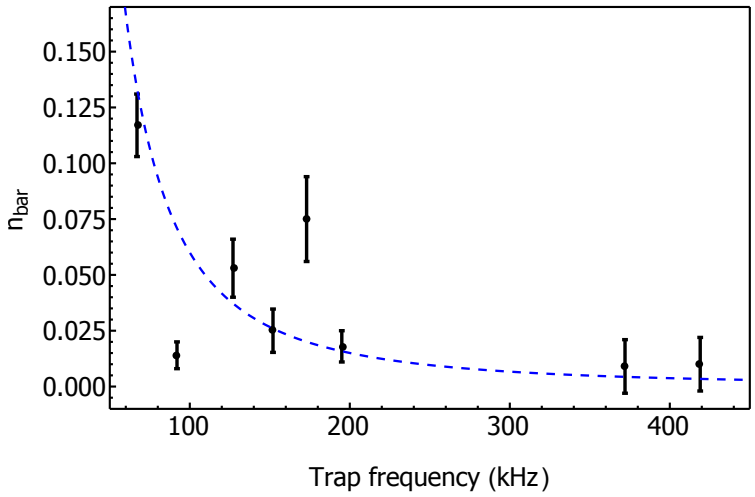


Figure 6.38: Measured mean phonon number at different axial frequencies of a trapped calcium ion in a Penning trap after employing the adiabatic cooling, The ion is cooled at 419 kHz and the trap frequency is decreased down to 66 kHz and the ground state cooling is maintained.

plotted along with the experimental data in figure 6.38. We anticipate that the ion may also be heated the frequency dependent residual noise.

6.7 Summary

In this chapter, I have presented the experimental results for resolved sideband cooling of ions in a Penning trap. Sideband cooling has been demonstrated for the axial motion for up to ten ions in a Penning trap. The ground state occupation has been achieved up to 98% for a single-ion case. The studies have been extended to the radial motional modes and the ground state cooling of the magnetron and the modified cyclotron motion has been accomplished. Additionally, a single ion is prepared in a high phonon state, typically $n = 290$, through resolved sideband heating of the axial motion. In order to avoid a complicated cooling sequence, ground state cooling has been demonstrated using the adiabatic cooling method, where cooling is performed at a high value of the trapping potential and the trap potential is reduced adiabatically in order to maintain ground state cooling at a low axial frequency. These studies will be further used to demonstrate coherent control with trapped ions in the following chapter.

Chapter 7

Coherent control using trapped atomic ions

In this chapter, I will present the experimental results of quantum coherent control using trapped calcium ions in our Penning trap. In the first section, I will present experimental results of optical coherence after preparing a single ion in the ground state of motion. Coherent control with multiple ions will be presented in a later section of the chapter. Comparative studies of optical coherence time with Rabi oscillations and Ramsey interference measurements will be shown for a ground state cooled ion. In a subsequent section, I will show the improvement of optical coherence time with a dynamical decoupling scheme. In the last section of the chapter, I will present the experimental results of coherent manipulation between different motional states of a trapped ion using the 729-nm transition.

7.1 Quantum coherence in a two-level trapped atomic ion

A theory of quantum coherence in two-level atoms has been briefly discussed in chapter 2. A detailed discussion of quantum coherence in trapped ions can be seen in references [79, 125]. The optical coherence time, or more precisely the measured linewidth of the atomic transition, is a prerequisite for the stability of current atomic clocks [126] and high fidelity quantum gates [22, 63]. In principle, atomic coherence times can be up to several minutes but experimental decoherence effects, such as magnetic field noise or linewidth of the laser system, limit the coherence time of the qubit to a few μs to ms.

7.1.1 Demonstration of Rabi oscillations with a trapped calcium ion in a Penning trap

A two-level atomic system shows periodic oscillations of the population between the ground and excited states when interrogated with an oscillatory radiation field. Generally, these oscillations

fade away due to the dephasing effects in the system. In trapped ions, the main cause of dephasing occurs due to the occupation of the ions in different motional states. For a single ion, the dephasing is observed due to its interaction with a thermal bath, which occurs mainly due to the interaction between an ion and a Doppler cooling laser beam.

The experimental realisation involves trapping and laser cooling of a calcium ion followed by probing the ion with the 729-nm laser radiation. In the Doppler cooling case, the ion is prepared in the $S_{1/2,-1/2}$ electronic state and the 729-nm laser is tuned to the carrier of the $S_{1/2} \leftrightarrow D_{5/2}$ transition. After interrogation with the laser radiation for a few μs, the state of the ion is detected and the individual data point is constructed. The experimental sequence is indicated in figure 7.1. Each experimental data point contains 400 repeats of such an experimental sequence. In the sideband cooling case, the ion is prepared in the ground state of motion after Doppler cooling.

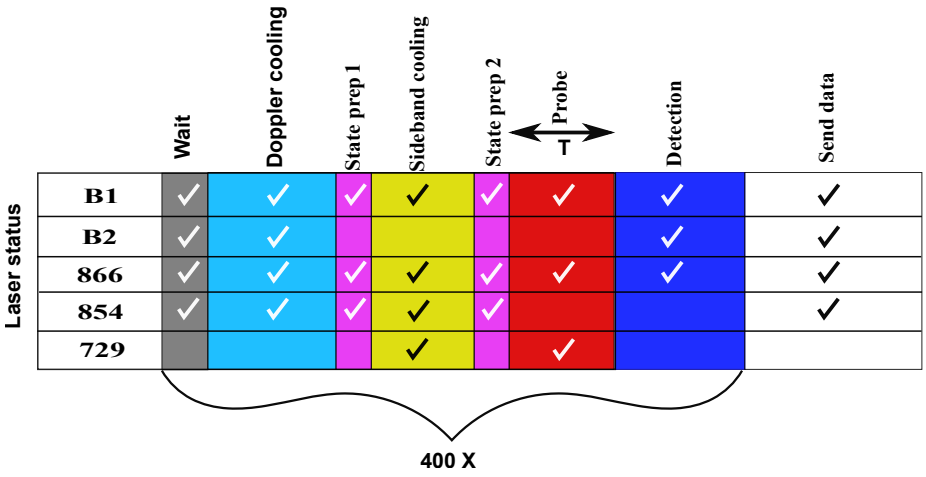


Figure 7.1: A schematic of the laser sequence used in the Rabi oscillation experiment with a ground state cooled ion. In the Doppler cooling case the “sideband cooling" and “state prep-2" is eliminated from the sequence.

Experimentally, after Doppler cooling, a trapped ion is found in different motional states at each repeat of the experiment. The statistical mixture of different phonon states after Doppler cooling leads to an incoherent sum of Rabi frequencies, hence the oscillations fade away as a function of laser-ion interaction time. A Rabi spectrum for a trapped calcium ion after Doppler cooling is shown in figure 7.2. In this case, the laser is tuned to the carrier of the $S_{1/2} \leftrightarrow D_{5/2}$ transition. The laser beam is aligned along the axial direction. An expression for the excited state probability as a function of laser interaction time is shown in equation 2.88. The fitting of the experimental data is carried out with the model derived from equation 2.88 and the mean phonon number ($\langle n \rangle$) is estimated to be 25 ± 1. The estimated Rabi frequency of the transition is estimated to be 19 ± 0.1 kHz from the fit.

Trapped ion systems, provide a near pure quantum state if the ions are cooled to their ground state of vibration. A Rabi plot after ground state cooling of a trapped calcium ion in a Penning trap is shown in figure 7.3. Note that the oscillations are distinctively visible indicating a good

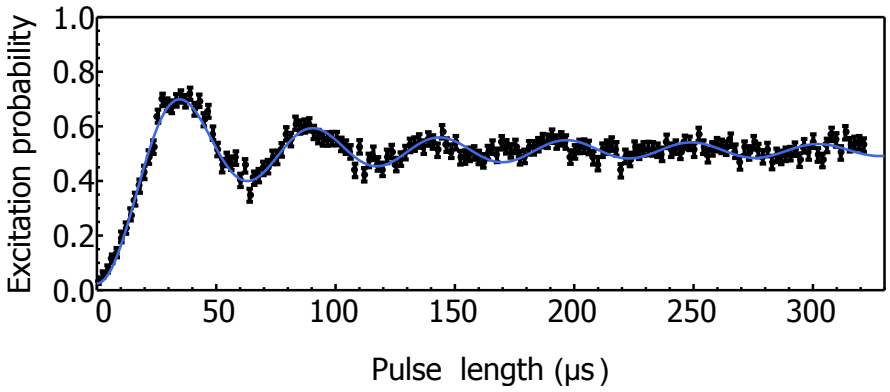


Figure 7.2: Rabi oscillations after Doppler cooling of a single ion in a Penning trap at 419 kHz axial motional frequency and $\langle n \rangle = 25$.

level of quantum coherence in the system. In a ground state cooled trapped ion system, the level of quantum coherence diminishes with time due to the experimental decoherence such as magnetic field noise, laser frequency noise, and laser intensity noise.

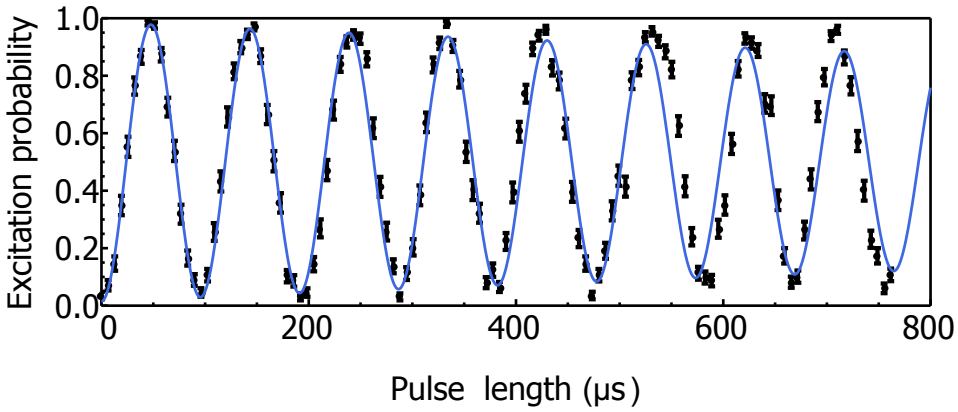


Figure 7.3: Rabi flops signifying the quantum coherence in a trapped ion system after performing ground state cooling. The coherence time is observed to be 1.4 ± 0.2 ms. The ion is trapped and Doppler cooled at 419 kHz axial frequency and the resolved sideband cooling is performed for 10 ms to prepare in the ground state of motion.

7.1.2 Decay of the visibility

In a pure quantum system, the evolution of a two-level system with resonant electromagnetic drive indicates sinusoidal population transfer between the two levels, illustrating the ability to perform coherent control with the quantum system. In reality, the visibility of the sinusoidal patterns diminishes with time. Often the decay is caused by ambient perturbations. The loss of optical coherence is shown in figure 7.4 for a trapped calcium ion in a Penning trap. In this experiment, an ion is interrogated with a resonant drive tuned to the carrier transition after performing ground state cooling.

After comparing the sinusoidal patterns in figure 7.3 and 7.4, a higher decay rate is seen

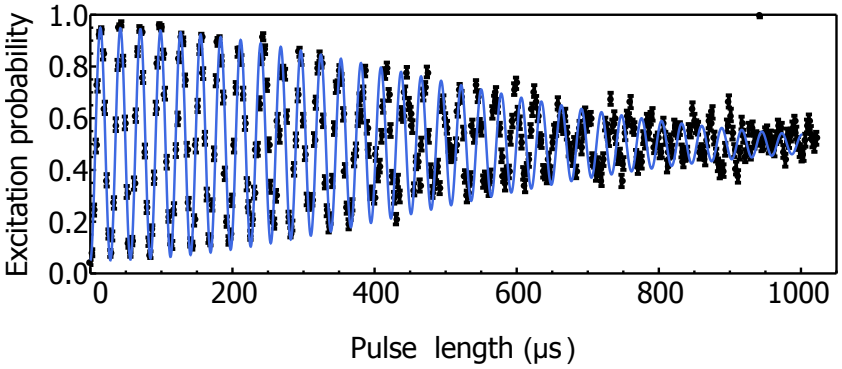


Figure 7.4: Figure showing diminished Rabi flops as a function of laser interaction time. The diminished flops indicate decoherence in the system.

for the second plot. However, both experiments were performed with a single ion and at the same axial frequency. The ion was prepared in the vibrational ground state with approximately the same mean phonon number for both experiments. Quantitatively, in the second plot, we observe a higher number of flops after interrogating for 800 μs than the first one. The qualitative comparison of both plots indicates that the decoherence rate depends upon the value of the Rabi frequency, which depends upon the absolute laser intensity. In order to support the observation, the Rabi flops were acquired at much lower Rabi frequency and the results are presented in figure 7.5. The estimated coherence time (the time after which the visibility goes to $1/e$ from its value at $t = 0$) comes to be 3200 μs. On the other hand, when a higher value of the Rabi frequency is chosen (in figure 7.4), the coherence time is measured to be 750 μs. The enhancement can be understood if the Rabi frequency noise, due to the laser intensity noise, is assumed to be in proportion to the actual value of the Rabi frequency.

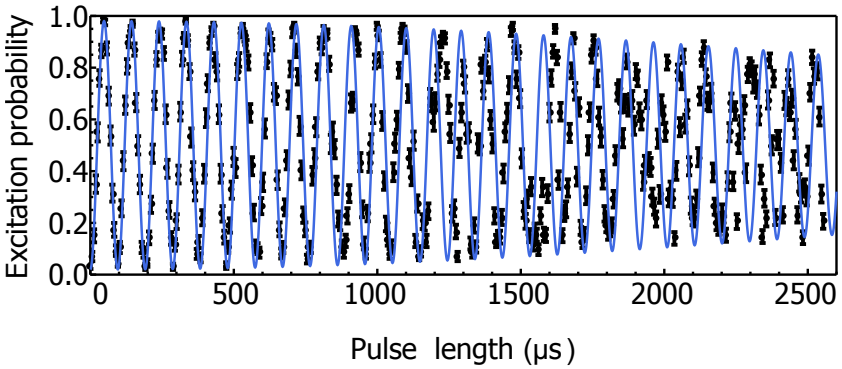


Figure 7.5: Rabi flops after ground state cooling of the axial motion of a single ion at 419 kHz axial frequency. The Rabi frequency is significantly reduced and the optical coherence time is enhanced to 3200 μs.

In the Doppler cooled case, as shown in figure 7.2, the decay of the flops visibility with time is attributed to the thermal dephasing phenomena. A similar thermal dephasing or rather an irregular pattern is observed due to improper ground state cooling. The relevant experimental result is shown in figure 7.6. In this special case, the irregular patterns are observed due to population trapping during sideband cooling. In chapter 6, the experimental studies of population

trapping have been shown, where single-stage cooling has indicated the inability to bring all the population to the ground state of motion. Here, the experimental data was taken at 187 kHz axial frequency and resolved sideband cooling/probing is carried out along the axial direction.

In this case, approximately 78% of the population occupies the ground state and the remaining population is trapped at $n = 73$. The system is expected to follow two types of distributions. The part of the population cooled to the ground state follows a thermal distribution function and the trapped population follows a Gaussian distribution function. These two distributions have different Rabi frequencies, which is expected from equation 2.84. The summed oscillations at two different frequencies from a beat output, which is observed in figure 7.6. The fitting of the experimental data is carried out after incorporating two types of distributions and respective Rabi frequencies. The study indicates quantum coherence with two distinct types of distributions and the fitting of the data also verifies population trapping as discussed in chapters 5 and 6.

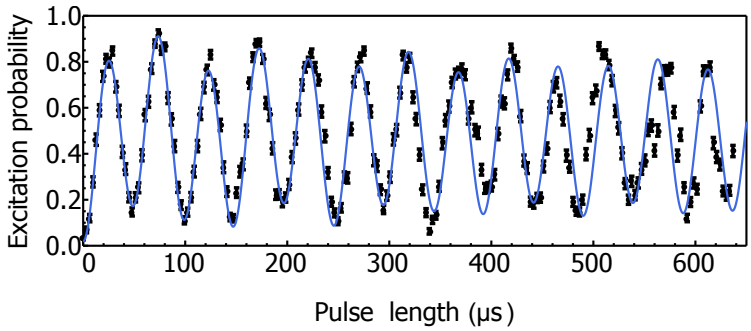


Figure 7.6: Rabi flops after improper ground state cooling of a single ion at 187 kHz axial frequency. An irregular sinusoidal pattern is observed due to population trapping at around $n = 73$.

Additionally, one common problem noted in the above experimental results is that they show some irregularities during the latter half of the laser interaction time. We believe that these irregularities arise due to slow drifts of the carrier transition. These drifts are expected due to slow drifts of the reference cavity mode or perhaps magnetic field drifts. These systematic errors have been discussed in section 4.5.2. The current experimental arrangement does not allow us to track and change the carrier frequency in between one set of Rabi flop experiments. However, a fresh experimental run is always carried out after measuring the clock transition, which eliminates the error for the next experimental run. In future such irregularities can be eliminated by characterising the clock transition and correcting for it during each experimental run.

7.2 Source of errors/dephasing in the optical qubit

In quantum systems, the visibility of quantum coherence decays with time due to various noise sources present in the system. In this section, I will discuss plausible sources of error in our

optical qubit.

7.2.1 Decoherence due to radiative decay of the metastable state

In a two-level system, often, the ground electronic state is treated as a stable state and the excited electronic state is treated as a long-lived state. In a calcium ion optical qubit, the ground state ($S_{1/2}$) is infinitely long lived, but the metastable state ($D_{5/2}$) has a finite lifetime. The population of the excited state decays to the ground electronic state in approximately 1 s [107], thus putting a fundamental limit to the coherence time of the system. Often, long lived atomic states are chosen to enhance the fundamental limit of the coherence time. Specifically, the octupole transition in Yb^+ provides one of the best optical qubits having > 650 days of radiative lifetime [127]. In our system, the coherence time is measured to be 3.2 ms through Rabi oscillations, which is much shorter than the radiative lifetime of the optical qubit, hence we can assume that the radiative lifetime does not limit the coherence time of the optical qubit in our system.

7.2.2 Decoherence due to magnetic field noise

In atomic systems, where the atomic states are strongly sensitive to the magnetic field, the transition frequency changes with ambient fluctuations in the magnetic field. In most atomic systems, the primary source of decoherence is caused by magnetic field noise [63]. In our system, the $S_{1/2,-1/2} \leftrightarrow D_{5/2,-3/2}$ transition is one of the least magnetically sensitive transitions. The first order drift for this transition is -15.9 kHz/μT, which can induce significant decoherence in the qubit state. The second order shift is reasonably small (~ 0.034 kHz/μT^2), which can be neglected for the noise calculation. The superconducting magnet system provides some sort of magnetic shielding. The exact level of magnetic shielding for our system is not known. The transition linewidth measurement as shown in figure 4.12 gives an upper bound of such noise levels. Additionally, we observe some slow drifts of the carrier transition perhaps due to the magnetic field change. The specification of the magnet suggests that the field drift is of the order of 0.1 ppm/h, which results in a drift of 1.5 kHz per hour. The overall change of the carrier transition is measured to be approximately 1.5 kHz/day (see figure 4.13), which is much smaller than the hourly drifts specified by the magnet manufacturer. We believe that the carrier frequency variation due to magnetic field drift is partially cancelled out by the cavity mode drift (729-nm laser frequency drift).

7.2.3 Decoherence due to frequency or phase noise in the probe laser

In optical systems, another basic kind of decoherence is caused by laser frequency and phase noise. The laser detuning from the carrier transition is an important parameter contributing to the rotation of the Bloch vector, thus any noise limits the control of coherent manipulation. In our system, the laser is believed to have a linewidth < 1 kHz [91], but a precise measurement of

the laser linewidth could not carried out. Apart from the frequency stability, the phase stability of the laser was never studied before in our system. The only measurement we ever carried out was using a single trapped ion and measuring the linewidth of the transition. In this measurement, the measured linewidth may have some contribution due to some other line broadening mechanism, such as magnetic field noise. If we believe that the only source of noise in our qubit is due to the probe laser frequency noise then the linewidth comes to be roughly 530 Hz. [1]

Additionally, we expect some error in our qubit due to laser frequency drifts. The measurements discussed in this thesis using a trapped calcium ion clock transition do not explicitly determine whether the drifts are caused by the magnetic field or the laser frequency. In principle, both drift rates can be individually estimated by measuring two different Zeeman clock transitions i.e. $S_{1/2,-1/2} \leftrightarrow D_{5/2,-3/2}$ and $S_{1/2,-1/2} \leftrightarrow D_{5/2,-5/2}$. In this case, both transitions have different magnetic field sensitivity but the same laser drifts if they are probed with a common laser source. In our system, these measurements are impossible to carry out. In our case, the frequency spacing between the aforementioned transitions is a few tens of GHz, which cannot be spanned with any AOM. Such measurements of the clock transitions are often carried out in Paul traps, where only a weak magnetic field is applied to specify the quantisation axis and the frequency change between the Zeeman transitions is provided by an AOM.

7.2.4 Laser intensity noise

The Rabi frequency of the transition depends upon the amplitude of the electric field or intensity of the laser radiation at the ion. Any intensity fluctuation in the laser beam thus affects the Rabi frequency. Primarily, in Rabi flop experiments, the dephasing is expected due to the laser intensity noise in our probe laser. These errors are broadly characterised into three categories. The first one is referred to the direct laser intensity fluctuations, which are caused by variation in ambient conditions such as temperature or mechanical effects. A passive stabilisation system reduces the intensity noise on the laser source driven by such ambient effects. Additionally, an active feedback loop for intensity fluctuations reduces the noise in the laser beam. The second type of Rabi frequency noise is identified in terms of polarization induced intensity noise. In our system, the laser beam travels through various fibres and optical components before reaching to the trap centre, thus any change in the polarisation angle of the laser beam cannot be disregarded. This change in the polarisation angle manifests itself as intensity noise after passing through a polarising beam splitter (PBS). The third type of noise is due to the position of the beam at the ion. In reality, if a tightly focused laser beam is shone to the ion then any vibrations in the system lead to intensity noise at the ion. In our system, the first and second types of intensity noise are actively suppressed by a home built intensity stabilisation system, which suppresses intensity noise below 0.2% of the total intensity. The third type of noise does not impose any limitation on our measurements while performing coherent control on a single ion qubit, due to its wider waist size of the beam at the trap centre (typically larger than 100 μm).

[1] Please refer to figure 4.12 and the relevant section for the transition linewidth measurements.

7.2.5 Thermal dephasing

Rabi flops have been shown for a Doppler cooled ion in figure 7.2 and the apparent dephasing has been noted. In contrast to that, for a ground state cooled ion, a clear sinusoidal Rabi pattern is observed. In reality, the ground state cooling is expressed in terms of a thermal phonon distribution function, where a smaller attained value of the mean phonon number ($\langle n \rangle$) is preferred for better coherent control. The severity of the thermal dephasing increases with increasing value of the L-D parameter. For the sake of illustration, a simulated visibility plot for the carrier Rabi flops as a function of probe time at various values of $\langle n \rangle$ is shown in figure 7.7. In the simulation, the Rabi frequency is chosen to be 40 kHz and the motional frequency is assumed to be 419 kHz. Moreover, due to the large dependency of the sideband Rabi frequency on the motional state number, coherent control with sidebands is found to be more affected by thermal dephasing. The following figure also indicates a revival of the visibility at 1.2 ms, which is attributed due to the in-phase summation of different Rabi flops corresponding to different phonon states.

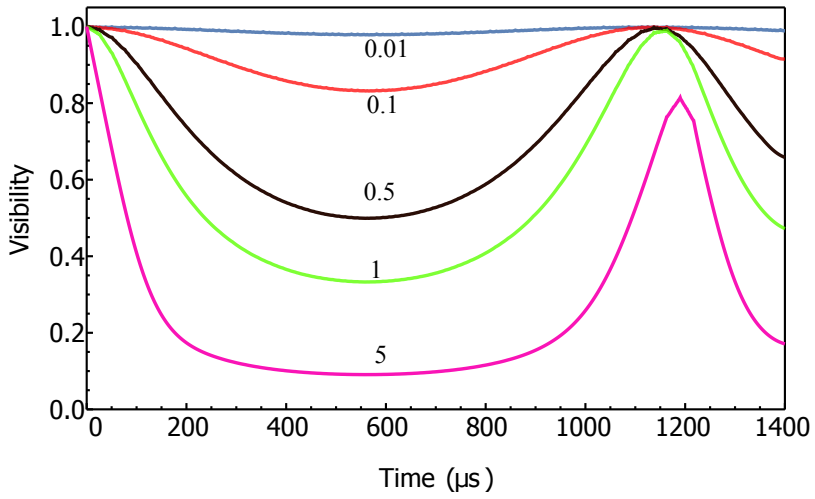


Figure 7.7: Simulated visibility of Rabi oscillations at various values of $\langle n \rangle$ at the carrier transition. The simulation is carried out at 40 kHz Rabi frequency and 419 kHz axial frequency for a trapped calcium ion. The reduction in the visibility is seen as $\langle n \rangle$ increases.

7.2.6 Pulse-timing error

In our system, when the FPGA control was added to the experimental control, the tick length was kept to 640 ns. This smallest tick length in time prevented us from applying laser pulses with accurate pulse widths while performing coherent control in our system. In order to overcome the issue, we often carried out the measurements with reduced Rabi frequencies, hence longer probe times. Very recently, we modified the FPGA control and changed the time step to 40 ns from 640 ns. This lessened the aforementioned problem, however, due to some unknown technical reasons, we were unable to reduce the time offset below 720 ns. This issue does not currently limit us while performing any coherent control in our system.

7.2.7 Loss of information in optical qubits

As with solid-state qubits [128], the qubit noise or decoherences in the trapped ion system are characterised into two types: the first is due to the relaxation of the qubit state (T_1 decay) and the second due to the dephasing (T_2 decay) [129]. In a trapped ion system, the T_1 coherence time (radiative decay time), is very long, hence it does not limit the coherence time of the system. It is the T_2 coherence time which is short and limits the coherence time of the system. In our system, magnetic field noise, laser frequency and intensity noise contribute to T_2 type decoherences.

7.2.8 Estimation of qubit coherence time for our system

The aforementioned noise sources will be divided into two main categories. The first category will be called qubit detuning noise (Δ) and the second one will be incorporated into Rabi frequency noise (δ_Ω). For the time being, decoherence due to changes in the trap frequency will be ignored. After including these terms, the excited state probability as a function of laser interaction time is given as

$$P(\uparrow) = \sum_{n=0}^{n_f} \frac{n_b^n}{(n_b+1)^{n+1}} \frac{[(\delta_\Omega + \Omega_0)\tilde{\Omega}_n]^2}{[(\delta_\Omega + \Omega_0)\tilde{\Omega}_n]^2 + \Delta^2} \sin\left(\sqrt{[(\delta_\Omega + \Omega_0)\tilde{\Omega}_n]^2 + \Delta^2}\,\frac{\tau}{2}\right), \tag{7.1}$$

where Ω_0 is the Rabi frequency of the transition and τ is the probe time. The Rabi and detuning noise is included in terms of δ_Ω and Δ. Using this functional form, simulated Rabi flops at 17 kHz and 30 kHz Rabi frequencies are shown in figure 7.8. The noise corresponding to the Rabi frequency is assumed to be 0.5% of the actual value and the standard deviation of the carrier detuning is assumed to be $\sigma_\delta = 700$ Hz. Computer generated random numbers are called for 400 times for the simulation and the flops are constructed. For the simulation, the noise forms are assumed to follow a normal distribution function.

Simulations suggest that the estimated coherence time decreases with increasing Rabi frequency[2]. After fitting the visibility of the simulated flops, the coherence time is found to be $\approx 1/(\delta_\Omega)$, where δ_Ω is the standard deviation of Rabi frequency noise in units of radian/s. Separately, simulations are also performed for various values of detuning error. They suggest that the estimated coherence time in Rabi flop measurements mainly depends upon the Rabi frequency noise in the limit $\sigma_\delta \ll \Omega_0$.

[2]In these simulations, the noise parameters are chosen to be slightly higher than estimated from the various measurements. Please refer to chapter 4 for more about error estimation in our system.

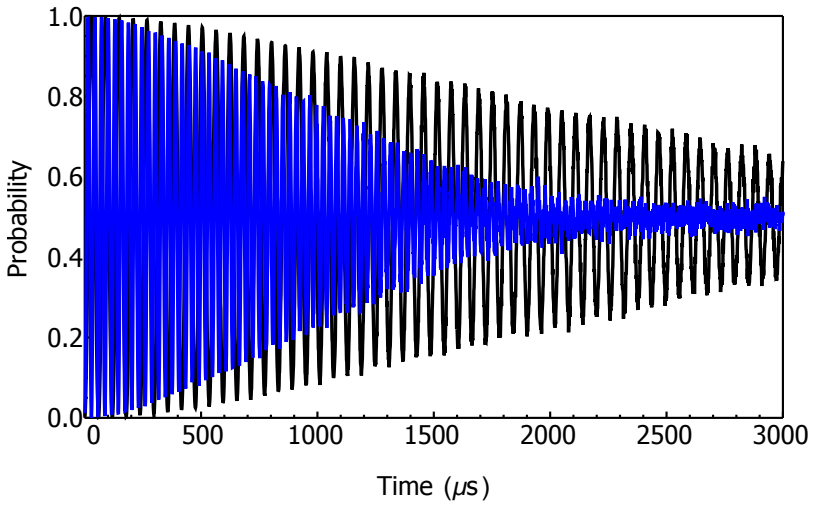


Figure 7.8: Simulated Rabi flops of the carrier transition at 17 kHz (in Black) and 35 kHz (in Blue) Rabi frequencies after ground state cooling ($n_b = 0.03$). In the simulation, the standard deviation of Rabi frequency noise is assumed to be 0.5% of the actual value. Similarly, the laser detuning noise is taken into account with $\sigma_\delta = 700$ Hz.

7.3 Estimation of optical coherence time with Ramsey interference experiment

The optical coherence time of a quantum system can also be estimated from a Ramsey interference experiment [130–132]. A typical Ramsey interference experiment is performed with two $\pi/2$ pulses (two short laser pulses in our case), successively, with a fixed wait period. Initially, the system is prepared in one of the two quantum states. The first $\pi/2$ pulse is used to create a superposition of states $|g\rangle$ and $|e\rangle$ and the second pulse is used to measure the phase evolution during the wait time.

The coherent evolution of a two-level atom in a Ramsey experiment can be illustrated by Bloch vector rotation in the Bloch sphere [133] and is shown in figure 7.9. After the Bloch vector is initiated along the north pole, the first $\pi/2$ pulse transforms the vector into the equatorial plane. During the waiting period, the vector acquires some phase $\phi = \Delta \times T$, where Δ is the laser detuning and T is the waiting period (typically $T \gg \tau$, where τ is the pulse duration). The second $\pi/2$ pulse rotates the Bloch vector depending upon the acquired phase and aligns the vector along the north or south poles or in intermediate regions. The experiment ends with measuring the population in the state $|g\rangle$ and a spectrum is constructed.

In the Ramsey scheme, the laser interaction time is very short. The laser intensity noise therefore does not limit the coherence time, whereas it was found to be limiting the Rabi coherence time. In our system, the Ramsey experiment is performed on a ground state cooled calcium ion. The laser beam is aligned along the axial direction to induce the S-D transition. Typically, the $\pi/2$ pulse lengths are chosen for zero detuning and the laser frequency is varied at a given waiting time. For a fixed value of the wait time (T), the acquired phase $\Delta \times T$ changes with laser

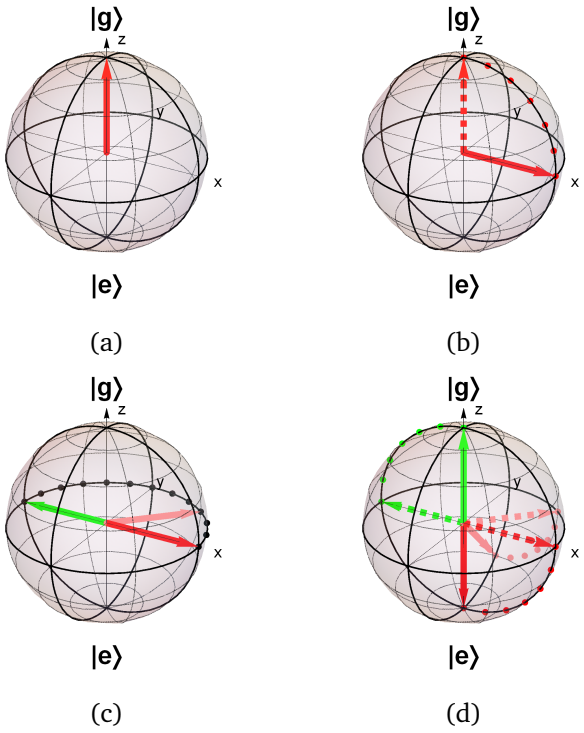


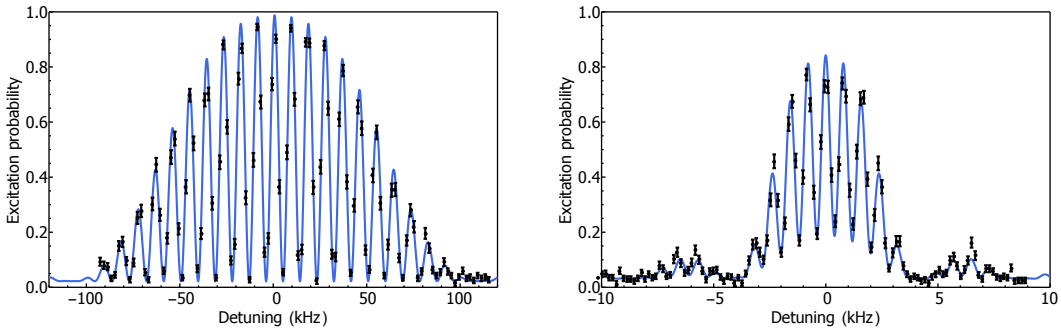
Figure 7.9: The figure shows an illustration of a Ramsey experiment in Bloch representation. From top-left, (a) the vector is initially prepared along the north pole of the Bloch sphere, (b) the first $\pi/2$ pulse rotates it about the $y-$axis into the equatorial plane. During the wait time, T, the free evolution of the Bloch vector causing dispersion is indicated in (c) and the final state of the vector due to the rotation with second $\pi/2$ is indicated in (d). The trajectory during the free evolution of the vector is indicated in black filled circles and various other trajectories during the laser interaction time are shown in red, green and pink colours.

detuning, which gives rise to constructive and destructive interference fringes. An interference pattern for a ground state cooled calcium ion is shown in figure 7.10a. The current measurement was carried out at 419 kHz axial frequency and waiting time (T) of 100 μs. The spectrum is constructed by changing the probe frequency, simultaneously for both $\pi/2$ pulses. The figure indicates full visibility, confirming no reduction in visibility due to decoherence effects. The fitting is carried out with an expression for excitation probability as a function of waiting time (T), laser detuning (Δ), Rabi frequency (Ω) and the probe duration (τ). The expression for the excitation probability is given as

$$P(\uparrow) = \frac{4\Omega^2}{b^2}\sin^2\left(\frac{b\,\tau}{2}\right)\left(\cos\left(\frac{b\,\tau}{2}\right)\cos\left(\frac{\omega\,\mathrm{T}}{2}\right) - \frac{\Delta}{b}\sin\left(\frac{b\,\tau}{2}\right)\sin\left(\frac{\Delta\,\mathrm{T}}{2}\right)\right)^2, \tag{7.2}$$

where $b = \sqrt{\Omega^2 + \Delta^2}$. From the above expression, the spacing between the interference fringes can be deduced as $1/(\mathrm{T} + \tau)$ Hz.

Similarly, the Ramsey experiment is performed at longer waiting times, where the decoherence effects are expected to affect the visibility of the interference fringes. Such a spectrum at 1 ms waiting time is shown in figure 7.10b. In this case, the visibility is reduced due to the frequency noise in our qubit. The fitting of the spectrum is not possible due to no simple expres-



(a) (b)

Figure 7.10: Ramsey interference fringes acquired for a ground state cooled trapped calcium ion in our Penning trap, (a) at 100μs and (b) at 1 ms waiting period.

sion for the excitation probability as a function of the decoherence processes being available. However, to explain the findings, I have overlayed the experimental spectrum with a simulated curve for the excitation probability. The parameters for the simulations are chosen from the corresponding experimental observations. The expression is taken directly from equation 7.2 after making a slight modification to incorporate the frequency noise in the system. The noise parameters in the simulated curve are adjusted to exactly match the experimental curve. The noise parameters that are gathered from the simulated curve are also compared with the frequency noise estimated from the lineshape measurement as shown in figure 4.12 and are found to be comparable.

7.4 Enhancement of optical coherence time

The coherence time of a two-level atomic system can be extended by various dynamical decoupling methods previously discussed in references [134–136]. The techniques discussed in the above references use multiple π pulses, generally inserted between two Ramsey pulses, at various time intervals. In this thesis, I will only present the results of the extension of optical coherence time in our system by employing a spin-echo technique and Uhrig Dynamical Decoupling (UDD) techniques.

7.4.1 Spin-echo

The spin-echo technique, sometimes called Hahn's spin-echo technique [137], is widely used to correct various errors in quantum systems. This technique has been previously demonstrated on a range of quantum systems including in trapped ion systems to eliminate errors due to qubit frequency noise [54, 131]. In a Ramsey experiment, as discussed previously, dispersion of the spin vector takes place at long waiting times due to the detuning noise and thus reduces the visibility of the Ramsey interference fringes. In Hahn's spin-echo technique, such phase evolution in the system is exactly reversed and corrected if a π pulse is inserted at half of the

period of the Ramsey waiting time.

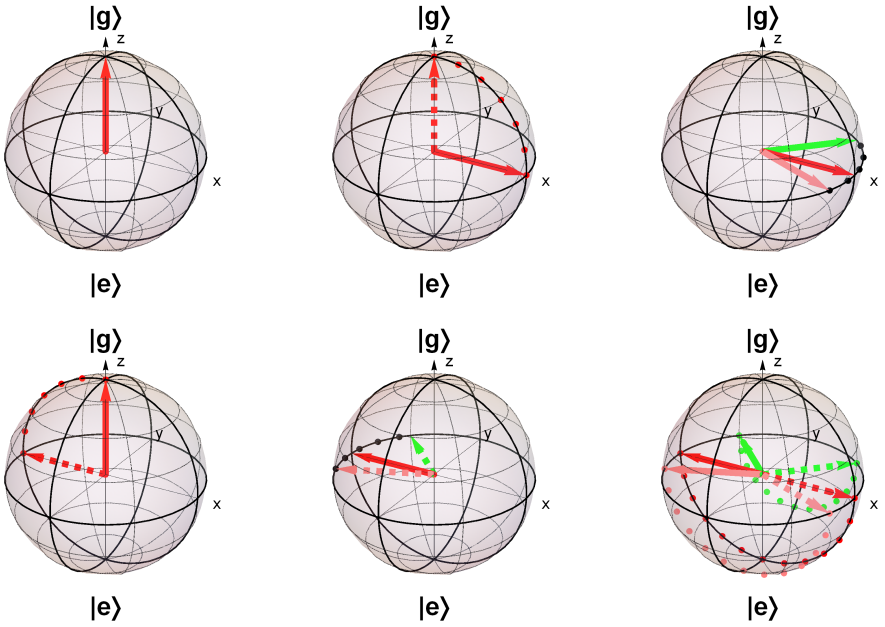


Figure 7.11: Plots show phase evolution of the Bloch vector in a spin-echo experiment. From top left in a clockwise manner, first, second and third plots illustrate the evolution of the vector after first $\pi/2$ pulse. The fourth plot indicates rotation of three dispersed-Bloch vectors after applying a π pulse. The fifth plot illustrates the refocusing of the vectors which then are later aligned back to the north pole by second $\pi/2$ pulse, which is indicated in the sixth plot.

In our system, the technique is implemented with a ground state cooled trapped calcium ion. Cooling and coherent manipulation are performed along the axial direction. For efficient coherent control, the $\pi/2$ and π pulses are measured through the Rabi flop experiment performed at the carrier transition. After preparing the ion into a pure quantum state $|g\rangle$, a $\pi/2$ pulse is used to prepare the superposition of states $|g\rangle$ and $|e\rangle$. For a given waiting period (T) in the Ramsey sequence, a π pulse is inserted at $T/2$. The population evolution is measured with the second $\pi/2$ pulse. The scheme can be illustrated with Bloch vector rotation as a result of the application of the required laser pulses. Such an illustration is shown in figure 7.11. In this figure, the first three Bloch spheres exactly resemble the Ramsey experiment, as discussed in the previous section and seen in figure 7.9. The fourth sphere (bottom right) illustrates the rotation of the Bloch vectors for various laser detunings under the operation of a π pulse. After applying a π pulse, the vectors are refocussed in the equatorial plane after a period $T/2$. The second $\pi/2$ pulse rotates the vectors about the $y-$axis aligning it exactly along the north pole, hence showing no population excitation under a correct spin-echo sequence.

The aforementioned scheme is employed at various waiting times and the phase scan plots are generated by changing the phase of the second $\pi/2$ pulse. The second $\pi/2$ pulse rotates the vector along the $z-$axis and the projection of the vector along the $z-$axis is measured. Depending upon the phase of the second $\pi/2$ pulse, a sinusoidal pattern is observed and is shown in figure 7.12. For comparison, the Ramsey phase scan plots are also shown alongside of the spin-echo plots. It is noticeable that in the Ramsey phase scan plots the system shows complete

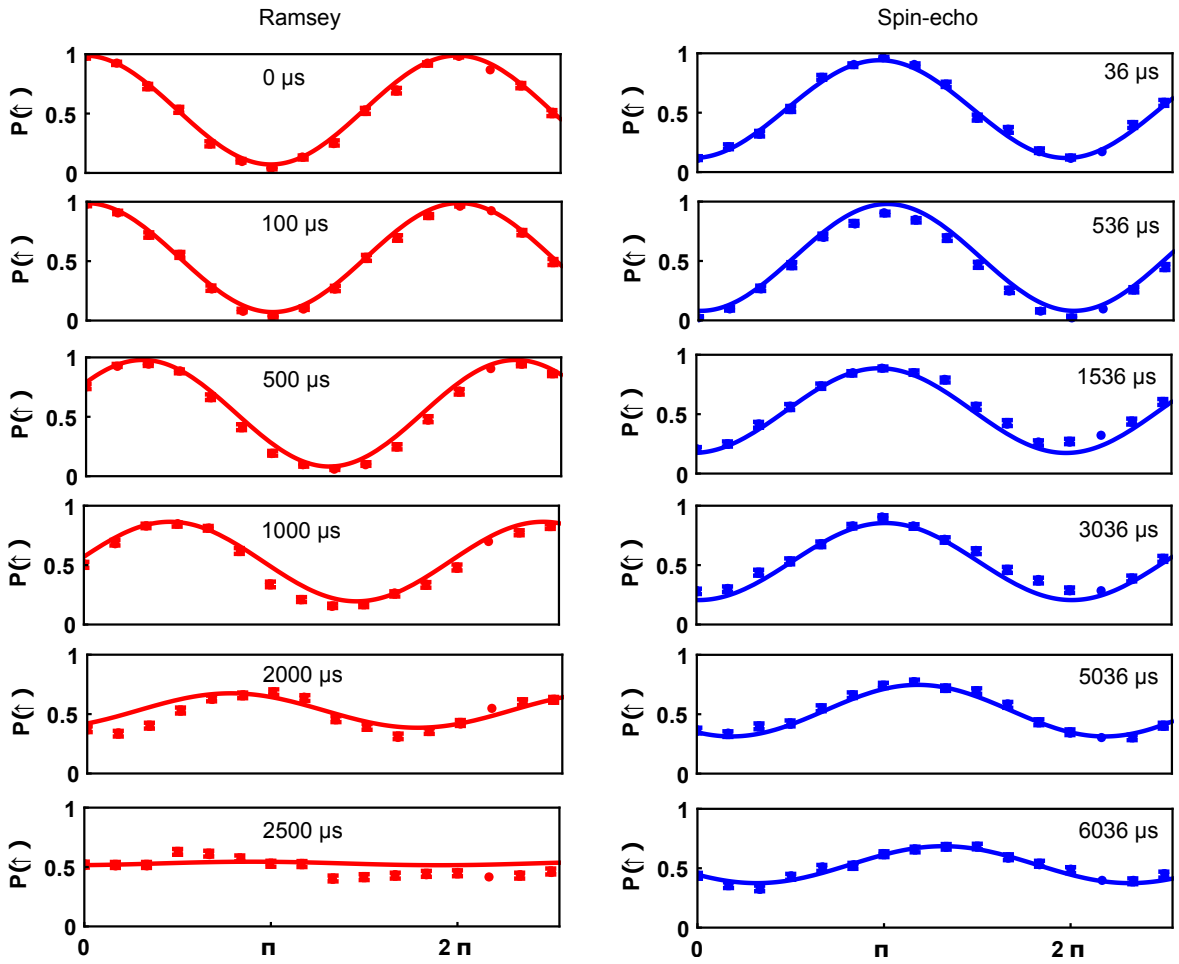


Figure 7.12: Plots showing a sinusoidal variation of the population in state $|e\rangle$ as a function of the applied phase (the phase of the second $\pi/2$ pulse with respect to first one) at different waiting times after applying the spin-echo sequence (in blue). The Ramsey phase scan plots (in red) are shown in order to compare the results.

dephasing at 2.5 ms waiting time. However, after inserting a π pulse, the sinusoidal behaviour is still clearly observed after 6 ms, confirming the enhancement of the optical coherence time in our system. Additionally, the fitted curves sometimes slightly differ from the experimental data points. This is expected due to small error bars estimated for the experimental data points. In our case, the error model does not include any systematic errors such as laser intensity drift and slow drifts in the laser frequency or phase. In reality, these factors affect the coherent manipulation. Simultaneous measurements of such parameters will help in getting better experimental data in the future.

7.4.2 Theory of dynamical decoupling in quantum systems

A quantum system in the presence of classical decoherence effects is expressed in terms of a Hamiltonian [103]

$$H = \frac{1}{2}[\omega + \beta(t)]\sigma_z, \tag{7.3}$$

where ω is the frequency spacing between the internal states of the atom, $|e\rangle$ and $|g\rangle$, and $\beta(t)$ is time-dependent noise variable used to denote frequency noise in the system. After applying a first $\pi/2$ pulse in the Ramsey experiment, the time evolution state vector in the laboratory frame is expressed as

$$|\psi\rangle = \frac{1}{\sqrt{2}}[e^{-i\omega t/2}e^{(-\frac{i}{2}\int_0^t \beta(t')\mathrm{d}t')}|e\rangle + ie^{i\omega t/2}e^{(\frac{i}{2}\int_0^t \beta(t')\mathrm{d}t')}|g\rangle]. \tag{7.4}$$

After making the rotating wave approximation in the above equation, time evolution of the state $|\psi(t)\rangle$ can be interpreted in terms of the Bloch vector rotation in the equatorial plane. This quantum state is prone to so-called "T_2 decoherence" effects, and any random phase evolution of the state limits the coherent control in the system. In this situation, the time-dependent noise variable simply randomises the phase acquisition during Bloch vector rotation.

In a purely random phase acquisition scenario (i.e. $\langle\beta(t)\rangle = 0$), the system will be observed as completely dephased if $\sqrt{\langle\phi_\beta^2\rangle} = \pi$, where $\phi_\beta = \int_0^t \beta(t')\mathrm{d}t'$. In any quantum system, the information is lost due to such dephasing events and this leads to an error in any qubit operation. Hahn in his paper [137] introduced the idea of protecting the quantum system against such dephasing mechanisms by inserting a π pulse in between two Ramsey pulses. A simple spin-echo technique only protects the system against any time independent frequency noise. The basic concept of the dynamic decoupling techniques (or multi π spin-echo techniques) is derived from Hahn's spin-echo method. In these multi-π spin-echo techniques [135, 136], the timing of π pulses are derived from a "filter function" designed specifically to suppress any higher order time dependent components of the detuning noise.

In this chapter, I will show the results of enhancement of an optical qubit coherence time after employing the UDD scheme. Detailed theory and experimental demonstrations of the UDD scheme in trapped ion systems can be found in references [134, 135, 138]. For the sake of completeness, I will briefly discuss the theory of the UDD scheme. Here, I will follow the same aprroach as in reference [138]. Say the time-dependent detuning noise is expressed as polynomial of order $(n-1)$ of time t

$$\beta(t) = \sum_{k=0}^{n-1} a_k t^k, \tag{7.5}$$

where a_k is an arbitrary coefficient determining the random nature of the noise. Mathematically, after integrating the frequency noise term in time, the phase error (ϕ_β) is determined. Rotation of the Bloch vector by a π angle is mathematically equivalent to assigning a $+1$ or a -1 prefac-

tor to the detuning term. The cumulative phase cancels out if these rotations are carried out at appropriate intervals [134]. In the above reference, the Bloch vector rotations are carried out at π_x angles where the first $\pi/2$ rotation is along the $y-$axis [3]. Our experimental demonstration is carried out without changing the rotation axis, hence the mathematical treatment will differ from the aforementioned references. The current treatment will also agree with the experimental demonstration of the spin-echo technique that is discussed in the previous section. After performing $n-\pi_y$ rotations between the first and second $\pi/2_y$ pulses, at time intervals $t_{i=1,n}$, the total phase noise can be expressed as

$$\begin{aligned}\phi_\beta &= \sum_{j=0}^{n}\left(\pi+(-1)^j\int_{t_j}^{t_{j+1}}\beta(t)\mathrm{d}t\right), \\ &= \sum_{j=0}^{n}\left(\pi+(-1)^j\int_{t_j}^{t_{j+1}}\sum_{k=1}^{n}a_{k-1}t^{k-1}\mathrm{d}t\right), \\ &= \sum_{j=0}^{n}\left(\pi+(-1)^j\left[\sum_{k=1}^{n}a_{k-1}\frac{t^k}{k}\right]_{t_j}^{t_{j+1}}\right), \\ &= n\pi+\phi_{err},\end{aligned} \tag{7.6}$$

where $t_0=0$ is the time of the first $\pi/2$ pulse and $t_{n+1}=T$ is the second $\pi/2$ pulse. In the above equation, the constant phase term $n\pi$ will be left as such and the main aim will be to make the phase noise term $\phi_{err}=0$. After rearranging the coefficients of the polynomial in the expression, the total phase is expressed as

$$\phi_\beta = mod(n,2)\pi+\sum_{k=1}^{n}\frac{a_{k-1}}{k}\left[(-1)^n-2\sum_{j=1}^{n}(-1)^j t_j^k\right], \tag{7.7}$$

where $mod(n,2)=1$ for an odd number of pulses and $mod(n,2)=0$ for an even number of pulses. For any choice of a_k, the phase error can be made zero if $(-1)^n-2\sum_{j=1}^{n}(-1)^j t_j^k=0$ for $k=1,..,n$. This condition is met for the coefficient values given as [138]

$$t_j=\sin^2\left(\frac{\pi j}{2(n+1)}\right), \tag{7.8}$$

which determines the pulse timing of the j_{th} π pulse.

This scheme is expected to work if the π pulses are instantaneous and there is no phase accumulation during their use. To demonstrate the scheme, I will first show the simulation results. The phase dynamics under an arbitrary phase relaxation noise of polynomial order three is shown in figure 7.13a. In this figure, the phase initially diverges but after the application of four π pulses, the phases acquisition becomes zero. The scheme has also been illustrated by employing five π pulses and the simulated phase evolution is shown in figure 7.13b. The corresponding noise model is shown in figure 7.14, where the coefficients for the noise model

[3] From the experimental point of view, the angle of rotations do not make sense without choosing a proper basis set and the phase difference between laser pulses. As a rule of thumb, the $z-$axis is assigned for the projection to the internal states of the ion. The first $\pi/2$ laser pulse is used to determine the $y-$axis and the 90-degree phase difference between the first and subsequent laser pulses determines the third axis.

have been chosen arbitrarily. The simulation shows that the final phase acquisition is π in this case, however, the time-dependent part is zero.

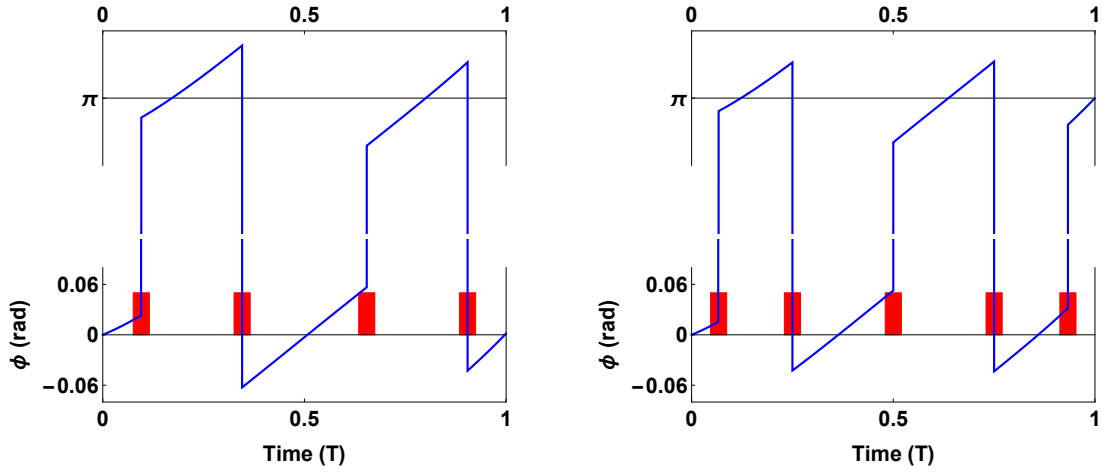


Figure 7.13: Simulated curves (in blue) for the phase evolution of the state $\frac{1}{2}(|g\rangle + i\,|e\rangle)$ under the application of an arbitrary detuning noise after applying (a) 4 π pulses and (b) 5 π pulses (indicated by red vertical bars) at intervals determined by the UDD scheme, and showing the cancellation of random phase acquisition.

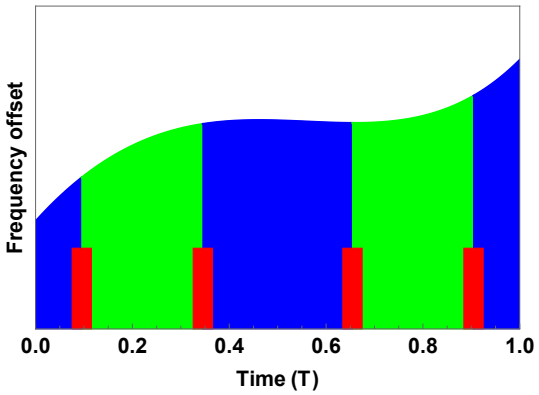


Figure 7.14: Figure showing time variation of the qubit frequency, assuming an arbitrary 4^{th} order polynomial as a noise model that is also used in the simulation. Green and blue shaded area indicate negative and positive phase acquisitions of a Bloch vector.

The above scheme is further illustrated for multiple iterations where the coefficients are randomly chosen. The simulated phase evolution after employing a five-π UDD scheme is shown in figure 7.15. In this particular plot, for clarity, I have dropped the constant term, π phase, which comes due to an odd number of π rotations. The noise is completely cancelled out at time T indicating the full noise correction. An important features the UDD technique is that it only cancels out the noise of $n-1$ order polynomials if $n\pi$ pulses are implemented.

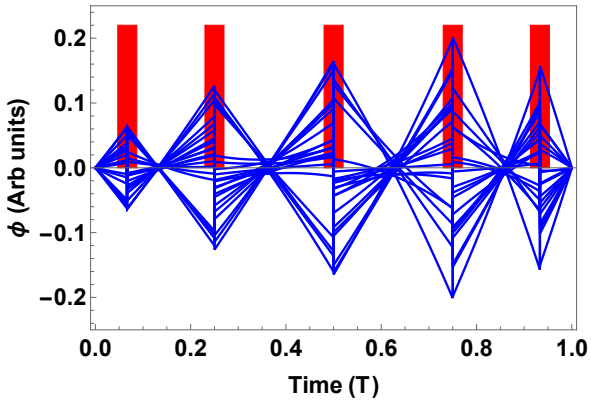


Figure 7.15: Figure indicating elimination of the random phase acquisition of the Bloch vector after implementing a five-π-pulse UDD scheme. The method is tested for 20 random cases where the 4^{th} order noise polynomial is assumed to take random coefficients, illustrating the experimental situation with a single ion following random time-dependent noise.

7.4.3 Experimental demonstration of the UDD scheme

Previously, the UDD technique has been demonstrated in a trapped ion system by Biercuk et al., for $\sim$ 1000 Be^{+} ions [103] and by Szwer et al. for a single trapped calcium ion [139]. In this thesis, the aim of demonstrating the UDD technique is to characterise our Penning trap system against any background perturbations. For the sake of simplicity, we only apply up to three π pulses and observe a significant improvement in the optical coherence time. The sequence is tested with a ground state cooled trapped calcium ion in our Penning trap. The pulse widths are calculated first by performing a Rabi flop experiment. The pulse spacing is calculated from the time-function given in equation 7.8. The experimental results are shown in figure 7.16, showing roughly an order of magnitude improvement of the optical coherence time. After the addition of each π pulse, the initial visibility (at $t = 0$) is reduced due to the decoherence during the pulse operation time. In reality, the UDD scheme eliminates the error during the waiting time (T). The scheme does not eliminate any error during the pulse operations, hence the reduced visibility is expected.

7.5 Demonstration of spin-coherence with multiple ions

7.5.1 Two-ion chain

In the previous chapter, I showed the results of sideband cooling of a two-ion chain. In order to ground state cool the ion, a multi-stage cooling sequence is employed and both modes, COM and breathing, were cooled to their ground state of motion. In this section, I will present experimental measurements of spin coherence in the two-ion chain configuration. In this configuration, individual ion detection is possible with an EMCCD, hence the Rabi flops can be measured individually. In our system, the laser beam excites both ions simultaneously. Rabi oscillations on the carrier transition for one of the two ions are shown in figure 7.17. The decoherence rate is

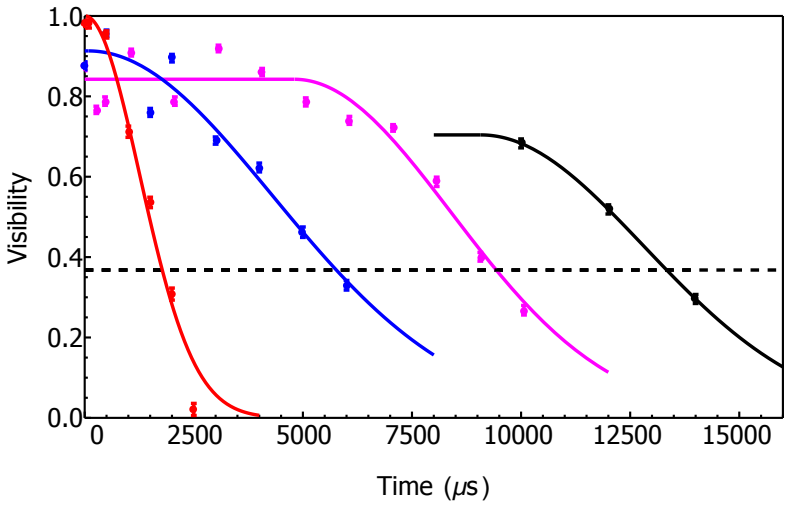


Figure 7.16: Experimental demonstration of enhancement of optical coherence time after employing a UDD technique. The data points in red, blue, magenta and black correspond to 0, 1, 2 and 3 π pulses inserted consecutively in a Ramsey phase scan experiment.

inserted into the fitting function from the intensity noise measurements and the fitting is carried out in order to estimate the Rabi frequency for one of the two ions. The Rabi frequency is estimated to be 14.2 ± 0.1 kHz for the first ion. The fitting has been carried out for the second ion as well and the estimated Rabi frequency comes to be 14.0 ± 0.1 kHz, which agrees with the ion one measurement.

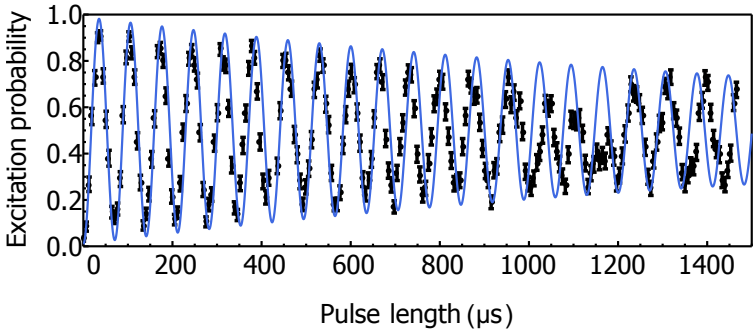


Figure 7.17: Carrier Rabi flops of a two ion chain. In this case, the measurements are presented for only one of the two ions.

Furthermore, Ramsey interference fringes for both ions were acquired on the carrier transition. The fitted experimental data is shown in figure 7.18. The black data points along with the blue fitted curve correspond to the first ion and the red data points along with the orange fitted curve correspond to the second ion. Between the spectra, a small mismatch is observed. The mismatch comes about due to the magnetic field difference at the ion-1 and ion-2 positions. In an ideal case, where the system has no magnetic field gradient, there should be no mismatch between the Ramsey fringes. The corresponding shift in the carrier frequency is estimated to be 2.2 ± 0.3 kHz and the magnetic field difference between ion-1 and ion-2 is calculated to be 0.2 μT.

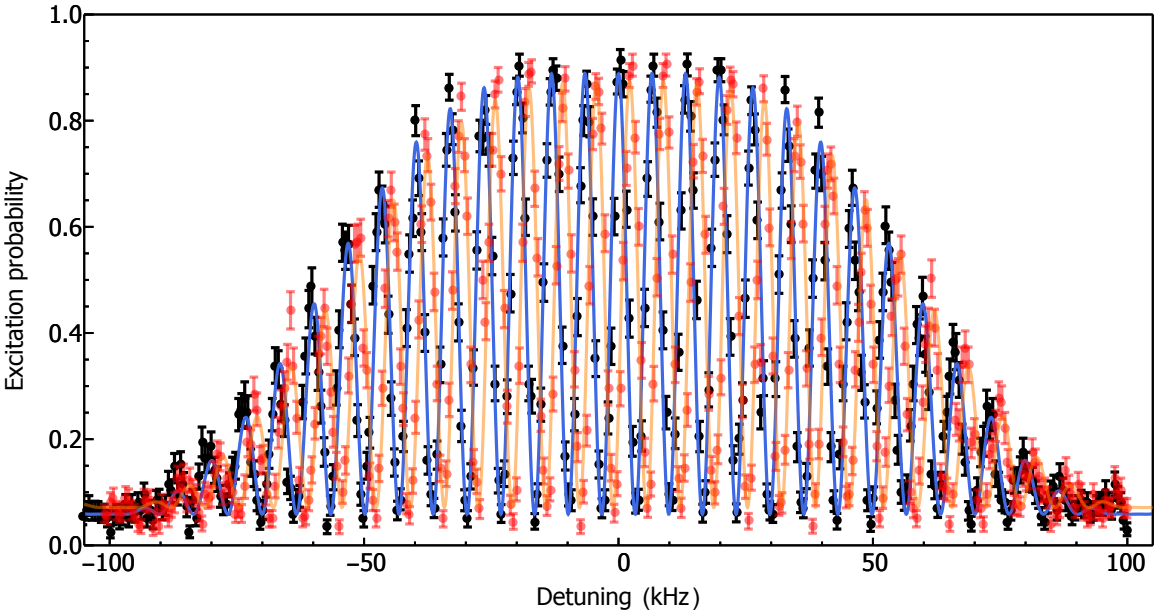


Figure 7.18: Ramsey interference pattern with two ground state cooled ions in a Penning trap. The wait time is 139.52 μs and the pulse length 9.6 μs. Red data points correspond to ion-2 and black data points correspond to ion-1 shelving probabilities as a function of laser detuning.

A phase scan experiment was performed after preparing ion-1 and ion-2 in the superposition of ground and excited electronic states with the help of a carrier $\pi/2$ laser pulse. The excited state population of each individual ion is measured after a 219.5 μs wait time through a Ramsey sequence. The phase of the second $\pi/2$ pulse is varied with respect to the first and the individual ion state is read-out. Due to a difference in the transition detuning, each ion acquires an offbeat phase. The wait time is chosen such that the phase difference between ion-1 and ion-2 is π. The experimental plot is shown in figure 7.19, indicating two sinusoidal patterns out of phase from each other. The plot shows an intriguing situation where both ions evolve out of phase for a global 729-nm probe beam. The studies are important for the system characterisation. In this case, the PMT data does not show any sign of periodicity due to the averaging effect.

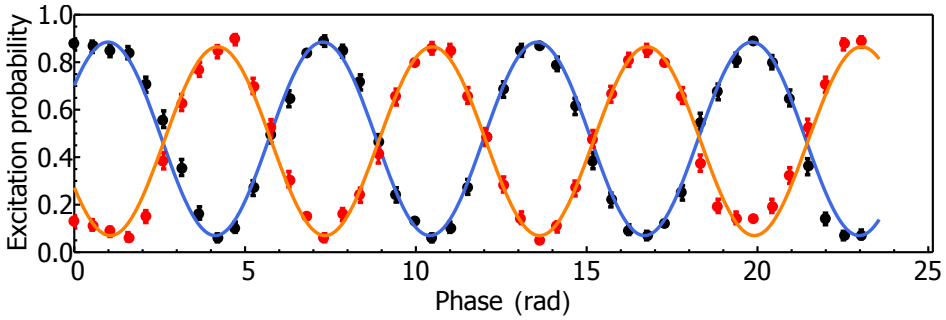


Figure 7.19: Ramsey phase scan with a two-ion chain, the blue curve corresponds to ion-1 and the red curve corresponds to ion-2. The waiting time is chosen to be 219.5 μs between two $\pi/2$ pulses.

Moreover, Rabi flops for a two-ion chain on the COM blue sideband are shown in figure 7.20. In this case, a global 729-nm laser beam is used to induce the transition for both ions. The ions

were ground state cooled to $\langle n \rangle < 0.3$ at 187 kHz COM frequency. The data points in black correspond to ion-1 and data points in red correspond to ion-2. In this particular experiment, the laser is tuned to the blue sideband transition of ion-1 and ion-2 is off-resonantly driven. Due to the different laser detuning of ion-1 and ion-2, the Rabi flop excitation probabilities evolve differently for both ions. The results were further verified by simulation studies with a two-ion Rabi model. The simulation is carried out by numerical simulations of the Hamiltonian given in equation 2.108, which includes the entanglement and different detuning of the individual ions. The simulated Rabi flops are shown with the experimental data and they match with the experimental observation. The simulation parameters are chosen from the experimental measurements carried out independently.

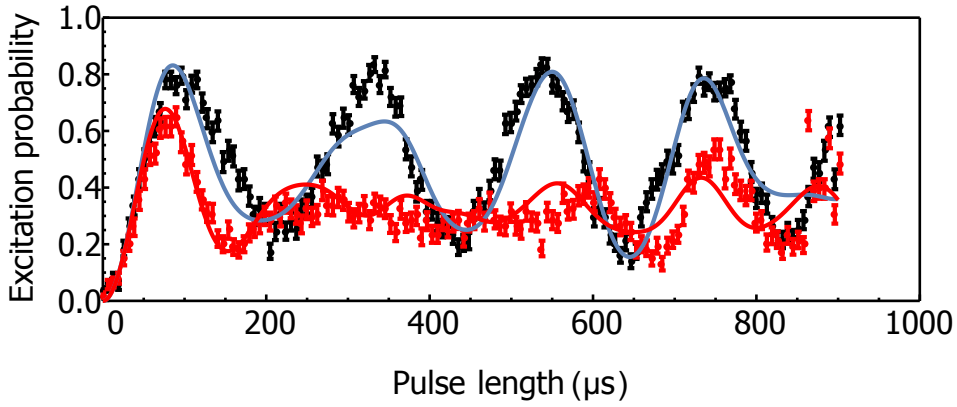


Figure 7.20: Rabi flops of a two-ion chain on the first blue sideband of the transition.

7.5.2 Two-ion planar crystal

Similarly, we perform the Rabi flop experiment with two ions in a planar orientation. In this configuration, individual ion detection is not possible using the EMCCD, which can only distinguish ions axially, and not in the radial plane, hence it cannot resolve their positions. For the current experiment, PMT data was used and the excited state population is estimated by post-processing of the experimental data. The PMT data for two ions shows three distinct peaks indicating three distributions as shown in figure 6.20. The first peak arises due to both ions being dark. The second peak arises due to one ion being dark and the other being bright. The third peak arises due to both ions being bright. If the first threshold is chosen between one ion being bright and both ions being dark, the $|ee\rangle$ probability can be estimated. The second threshold is chosen between both ions being bright and only one ion being bright, which gives rise to $|eg\rangle + |ge\rangle$ excitation probability. The post-processed two-ion planar Rabi flops are shown in figure 7.21. In this figure, the data points in black indicate the $|ee\rangle$ excitation probability and the data points in red correspond to the cumulative excitation probability of the states $|eg\rangle$ and $|ge\rangle$. The experimental data points are then fitted with the expressions for relevant excitation

probabilities, which are given as

$$P(|ee\rangle) = \sin^4\left(\frac{\Omega_{n,n}t}{2}\right), \tag{7.9}$$

$$P(|eg\rangle + |ge\rangle) = \frac{1}{2}\sin^2\left(\frac{\Omega_{n,n}t}{2}\right), \tag{7.10}$$

where $\Omega_{n,n}$ is the Rabi frequency of the carrier transition. The best-fitted curves for both excitation probabilities are shown along with the experimental data. The estimated Rabi frequency of the transition comes to be 29.6 ± 0.3 kHz. The spectrum is taken for 200 μs, which is much shorter than the coherence time of the Rabi experiments (typically 2 ms), hence the decoherence effects are neglected in the fit. Also, in this case, the detuning due to the magnetic field gradient is not expected to play any role due to the ions rotating about the trap axis so that any effect will be averaged with time.

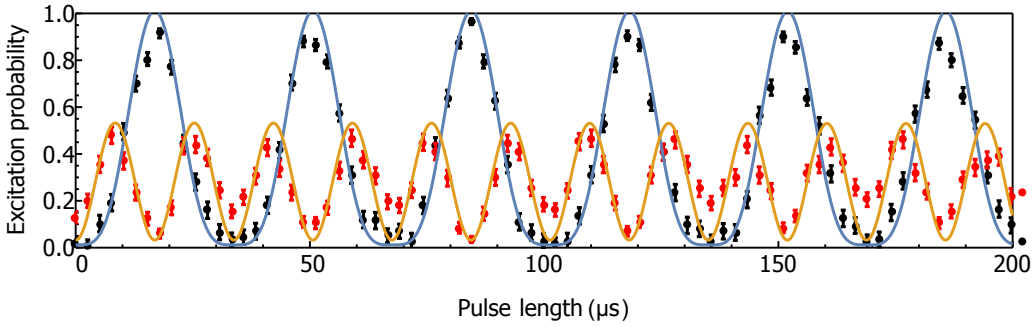


Figure 7.21: Rabi flops with two calcium ions in a planar orientation in the Penning trap. The data points in black show the probability of both ions being dark and the data points in red indicate the probability of one ion being dark and the other ion being bright.

7.5.3 Three-ion planar crystal

We also demonstrate a Rabi flop experiment with three ground state cooled ions in a planar configuration in the Penning trap. Sideband cooling has been demonstrated in chapter 6. In this section, the results of the Rabi flop experiment on the carrier transition of the three ion crystal are presented. The experiment is performed at 210 V of trapping potential. The axial COM mode frequency for this case is of approximately 385 kHz. The remaining two degenerate modes have a motional frequency approximately 377 kHz. The corresponding Rabi flops at the carrier transition are shown in figure 7.22. As in the two-ion planar case, the spatial resolution of three ions in planar configuration was not possible with the EMCCD, hence the PMT counts will be used for the state detection of the ions. Furthermore, in this case, we are not able to resolve the fluorescence levels for the individual states, hence the total photon counts were used to illustrate the results. The periodicity of the oscillations is clearly visible in the spectrum, indicating highest florescence level when none of the ions were shelved and the lowest fluorescence level when all of them are shelved to the metastable state with the 729-nm laser radiation. The Rabi frequency of the transition comes to be 68 kHz. In this case, the Rabi flops are found to decay faster than

the coherence time previously measured in our system. This is attributed to the large intensity noise on the laser beam and poor ground state cooling of the ions.

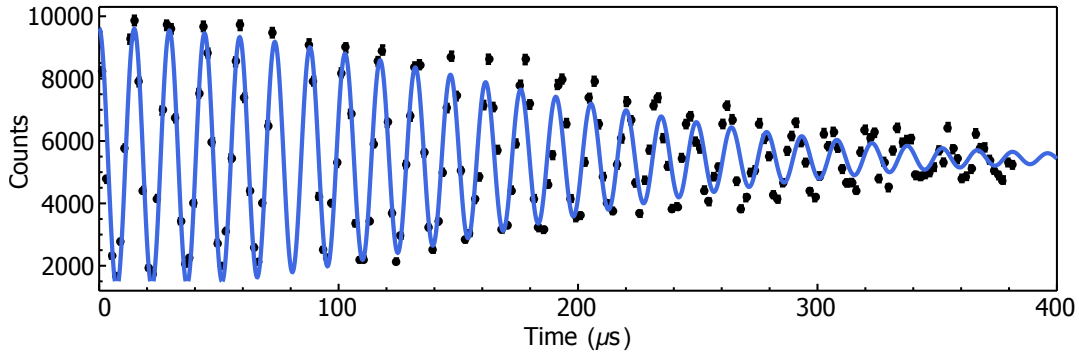


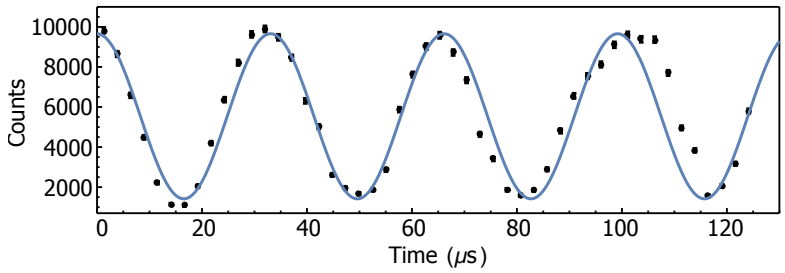
Figure 7.22: Rabi oscillations with three ground state cooled ions in our Penning trap.

7.5.4 Multi-ion planar crystals

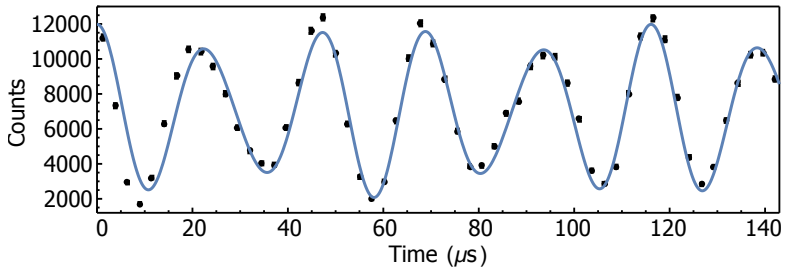
Coherent control has been demonstrated with a larger number of ions in our trap. In this section, I will show the results for five, six and ten ions. For the five-ion case, the axial COM frequency is chosen to be 385 kHz. The corresponding Rabi flops are presented in figure 7.23a after performing near ground state cooling of the ions. Similarly, six-ion and ten-ion Rabi oscillations are acquired at 356 kHz COM frequency and the results are presented in figure 7.23b and figure 7.23c, respectively. The last two plots show the beat-output of different Rabi frequencies of the trapped ions, which is expected due to the Gaussian shape of the probe beam. Assuming that the laser beam is focussed at the trap centre the central ionsare illuminated with more intensity than the outer ions, leading to different Rabi frequencies for central and outer ions. In the six-ion case, the central ion is illuminated more than the remaining five ions. Fitting of the experimental data suggests that the central ion Rabi frequency is approximately 60 kHz and the outer ions have a Rabi frequency of approximately 42 kHz. Similarly, for the ten-ion case, the inner and outer ions have different Rabi frequencies, which are estimated to be 48 kHz and 30 kHz, respectively. These results are presented here for demonstration purposes only, hence a coherence time measurement was not carried out using these results.

7.6 Coherent evolution of population between motional states

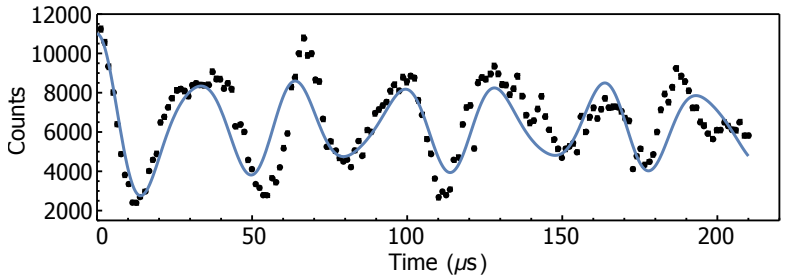
A motional state superpositions can be used to measure the motional coherence in trapped ion systems [140]. A ground state cooled ion is an ideal realisation of a pure Fock-state. Using appropriate laser pulses, one can create a superposition of motional states. In this section, I will present the results of the motional coherence with a ground state cooled ion. I will also extend the studies to an ion which is prepared in a high-n state via a sideband heating technique. A Ramsey equivalent experiment will be performed between two motional states. In this situation, a motional superposition will be realised in one of the two electronic states of the trapped ion in



(a)



(b)



(c)

Figure 7.23: Rabi flops for (a) five, (b) six and (c) ten ground state cooled ions in the Penning trap on the carried transition. The experimental demonstrations are carrier out for planar crystals, where the ions are cooled to $\langle n \rangle < 0.5$ through a resolved sideband cooling technique.

order to eliminate the optical decoherence effects. It is advantageous to prepare the ion in the ground electronic state to avoid radiative decay of the metastable state of the ion. A motional superposition in the ground electronic state is denoted by

$$|\psi\rangle = |g\rangle\,(a\,|n\rangle + b\,|n'\rangle), \tag{7.11}$$

where a and b are the coefficients of the state vectors $|n\rangle$ and $|n'\rangle$. The superposition will be realised in the ground electronic state with the combination of appropriate laser pulses.

7.6.1 Demonstration of $n = 0$ and $n = 1$ superposition

A motional superposition can be created by applying carrier and sideband laser pulses to a ground state cooled ion. A pulse sequence used to demonstrate the Ramsey experiment with $n = 0$ and $n = 1$ motional states is illustrated in figure 7.24. The experimental sequence required a $\pi/2$ pulse at the carrier transition followed by a π pulse tuned to the first red sideband of the

transition. The phase acquisition of the superposition state is then measured after a waiting period (T). For measurement of the phase evolution, the sequence is applied in the reverse and the excited state population ($P(e)$) is measured. In the experiment, the ion is first prepared in the ground state of motion by resolved sideband cooling technique followed by a short laser pulse in order to prepare the ion in the electronic ground state. The population of the ion is found in the ground or excited electronic state depending upon the phase acquisition during the wait time. The experiment was performed in two parts, in the first part the phase of the last carrier pulse is varied with respect to the first carrier pulse and the excited state population ($P(e)$) was measured. In the second part, the free-evolution time is varied and the $P(e)$ as a function of time was measured at zero phase difference between the laser pulses.

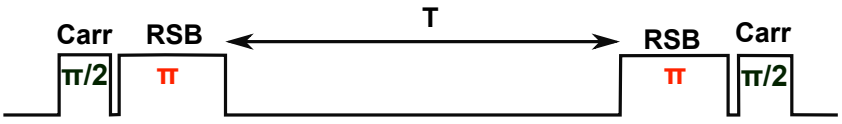


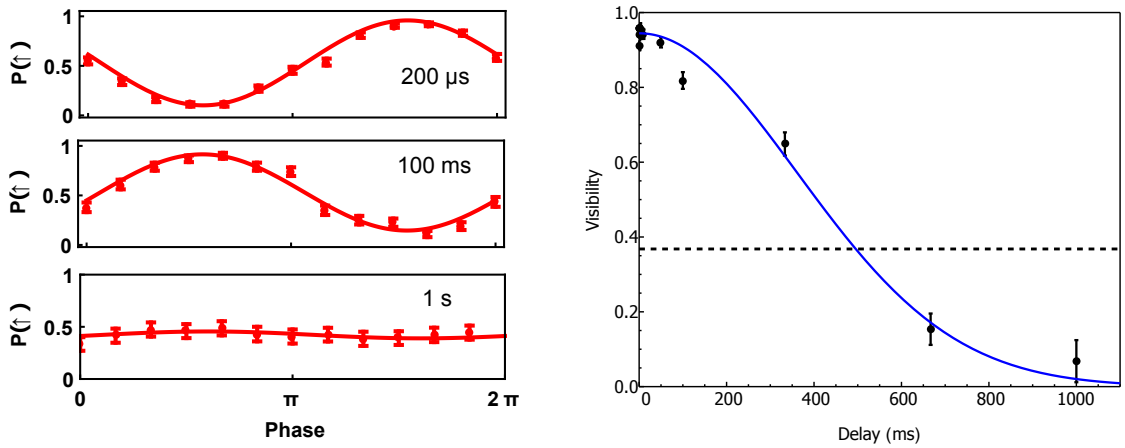
Figure 7.24: The schematic of the laser pulses used to prepare and detect the motional superposition in states $n = 0$ and $n = 1$.

Experimental results of 1-0 motional state superposition are shown in figure 7.25a for various wait periods. The experiment was performed at 419 kHz axial frequency. In order to measure the visibility of the superposition, the phase of the second $\pi/2$ laser pulse is varied at a fixed waiting time. The resultant sinusoidal patterns are fitted with a sine function and the visibility is estimated. The probability of the ion being in the excited electronic state as a function of the phase difference between first and second carrier pulses is expressed as

$$P(|e\rangle) = \frac{1}{2}\left[1 + \cos(\omega_z(T + \tau_r) + \phi_c)\right] \tag{7.12}$$

where ϕ_c is the phase difference between first and last carrier laser pulses. The time τ_r, the pulse duration of the first red sideband pulse, is inserted in the expression to include the effects of the finite laser pulse duration. In reality, due to decoherence effects, the visibility of the sinusoidal pattern diminishes as a function of waiting time. The figure indicates that the sinusoidal patterns diminish completely at $T = 1$ s, indicating the loss of motional coherence at that time. Figure 7.25b shows the visibility at various times estimated from the sinusoidal plots. The motional coherence time of the system is measured to be 510 ± 20 ms. The measured motional coherence time suggests a high level of quantum coherence in our system. To our knowledge, the measured value of the motional coherence time is highest in any trapped ion system. The estimated value is also found to be in agreement with the heating rates measured in our system [45].

In the second part of the experiment, instead of the phase (ϕ_c), the free-evolution time is varied for $\phi_c = 0$. In this experiment, the time is increased in small steps after a fixed duration interval ($T + t$). During the free-evolution time, the population oscillates between ground and excited electronic states at the axial frequency (ω_z). The experimental demonstration of mo-



(a) (b)

Figure 7.25: Plots in (a) show the sinusoidal variation of $P(e)$ as a function of ϕ_c at various values of the waiting time (T). Figure (b) shows the estimated value of the visibility at different times (T), indicating the loss of visibility due to the motional dephasing effects. Fitting is carried out with a half Gaussian function to measure the coherence time of the system.

tional coherence at $T = 0$ is shown in figure 7.26. The fitting is carried out with a sine function and the frequency of the system is estimated to be 420.0 ± 1.5 kHz, consistent with the trap frequency at 250 V in our system.

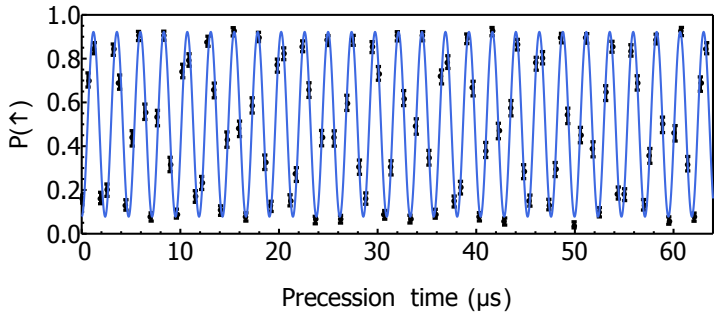


Figure 7.26: Experimental demonstration of the motional free-precession with a ground state cooled trapped calcium ion at 419 kHz axial frequency. The laser pulses are kept phase synchronous with each other and the waiting time is varied in 640 ns incrementations from $T = 0$. The sinusoidal pattern is fitted with equation 7.12.

7.6.2 Demonstration of the $n = 0$ and $n = 2$ superposition

A motional superposition was created between the $n = 0$ and $n = 2$ phonon states and the coherence time was measured using the phase scan technique. In this experiment, the superposition state is created using two laser pulses. The first, a $\pi/2$ pulse tuned to the first blue sideband of the transition, creates a superposition of $|g, 0\rangle$ and $|e, 1\rangle$ states. The second, a π pulse tuned to the red sideband of the transition, creates the superposition between $|g, 0\rangle$ and $|g, 2\rangle$ states. In this situation, the phase of the superposition state, $|g\rangle\,(a\,|0\rangle + b\,|2\rangle)$, evolves at $2\omega_z$ frequency. After some waiting time, the laser sequence is reapplied in the reverse order.

The phase of the second blue pulse (ϕ_b) is then varied with respect to the first laser pulse. The population in the ground and excited electronic states depends upon the phase of the final laser pulse and the phase acquired during the waiting time. The phase scan plots show the sinusoidal variation of the excited state population as a function of the applied phase (ϕ_b) and the visibility of the sinusoidal plots are measured at various waiting times (T). Measured visibilities for the 0-2 motional superposition as a function of waiting time are shown in figure 7.27. The motional coherence time for 0-2 motional superposition is estimated to be 530 ± 10 ms, which is same as for the 0-1 case.

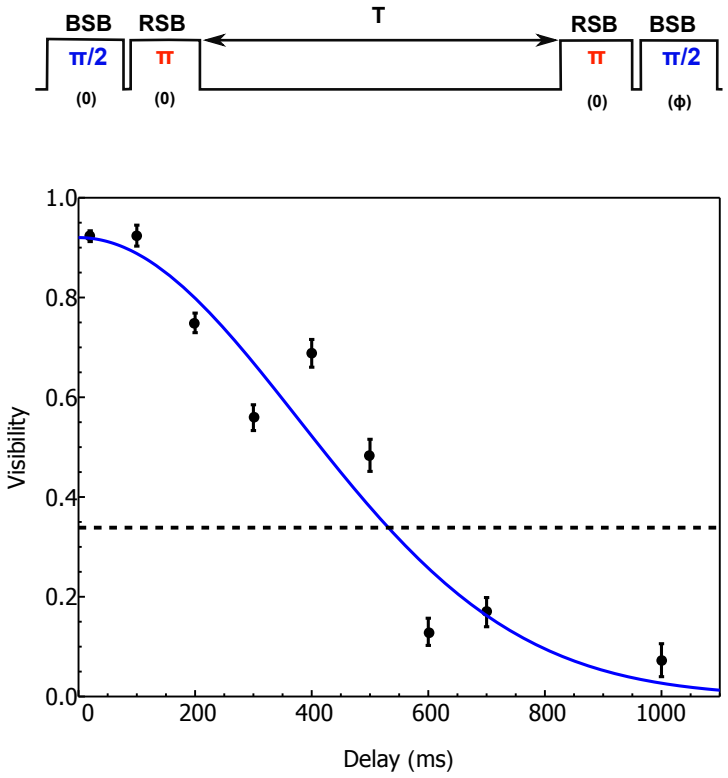


Figure 7.27: Motional Ramsey sequence to demonstrate 0-2 motional superposition of a ground state cooled ion (top) and plot showing visibility as a function of waiting time (bottom) at 419 kHz axial frequency.

Studies of 0-1 and 0-2 motional superpositions show an approximate 500 fold increase in motional over optical coherence time. Due to short laser interaction times, in motional superposition cases the studies are not limited by spin dephasing effects, thus they are irrelevant for the measurements.

7.6.3 Demonstration of the phonon-echo with a trapped ion system

In the motional superposition studies, dephasing is introduced from the trap electrodes or sometimes due to heating of the ion due to some unknown reasons. As we saw in section 7.4.1, the effect of decoherence in spin systems is greatly reduced by implementing the spin-echo technique. In the motional case, such a scheme can also be implemented with appropriate choice

of laser pulses. The scheme is expected to eliminate the effect of motional frequency noise in the system. A laser sequence that is used to demonstrate the spin-echo type technique in the motional superposition is shown in figure 7.28. The first set of laser pulses creates a superposition of states $|g,0\rangle$ and $|g,2\rangle$. The second set of laser pulses flips the population between the motional states $n = 0$ and $n = 2$. The final set of laser pulses (applied in reverse order to the first set) is used to project the population onto the electronic states. Finally, state detection of the ion is carried out using the usual state readout technique and the excited state population is measured.

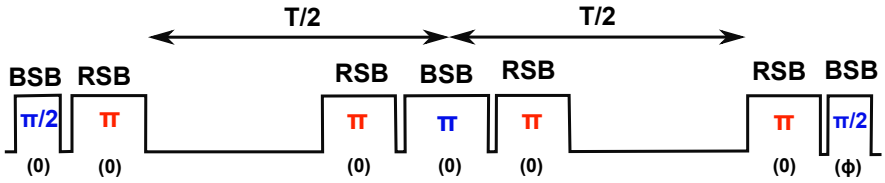


Figure 7.28: Laser pulses used to demonstrate phonon-echo of a ground state cooled calcium ion in our system. Three π pulses (RSB, BSB and RSB, respectively), are inserted at $T/2$ reverting the motional decoherence effects during the second half of the motional Ramsey.

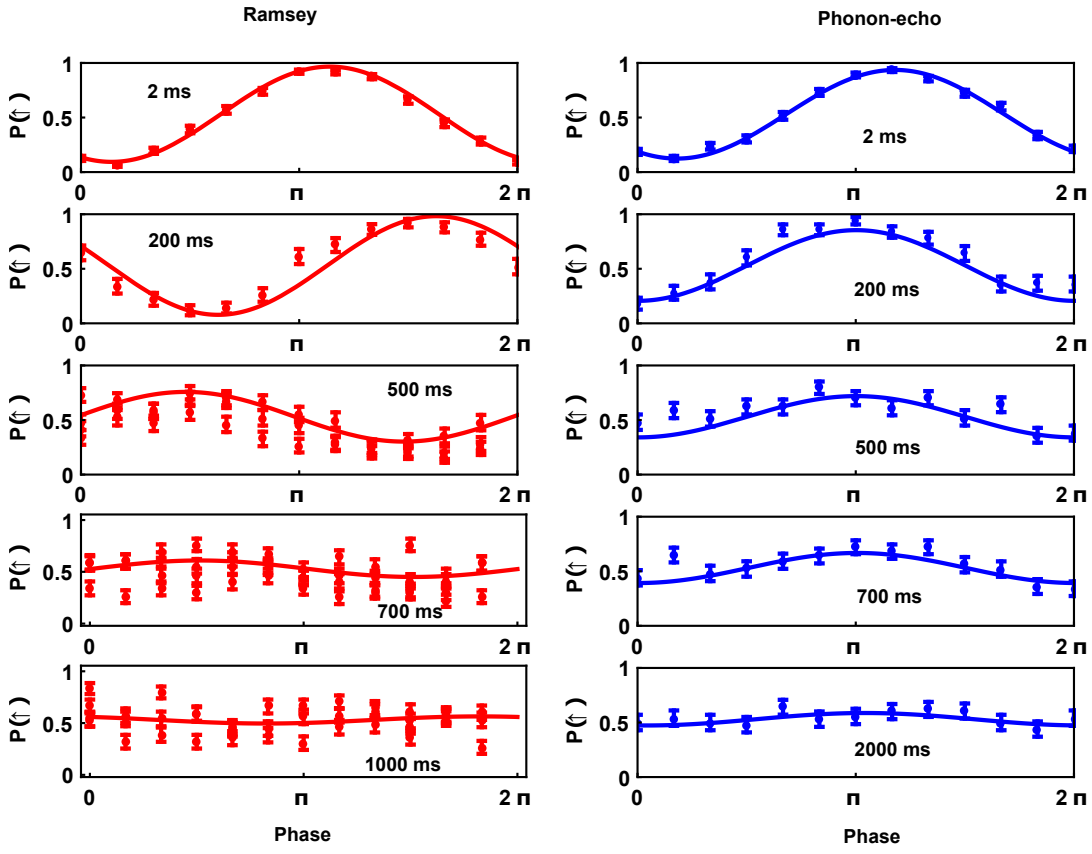


Figure 7.29: Phase scan plots for various waiting times corresponding to the motional Ramsey experiment (in red) and phonon-echo experiment (in blue).

Phase scan plots for the phonon-echo experiment at various values of waiting time (T) are shown in figure 7.29 along with the phonon Ramsey phase scan plots. The phase scan plots in red correspond to the 0-2 Ramsey experiment and the phase scan plots in blue correspond to the 0-2 phonon-echo experiment. The red curves start at a random initial phase, however, this is not observed for blue curves. As we discussed in the spin-echo case, the technique eliminates the time-independent laser frequency noise. The same argument is valid in the motional case, where the phonon-echo eliminates the trap frequency noise. The corresponding enhancement of the motional coherence time is also noted after implementing the phonon-echo sequence.

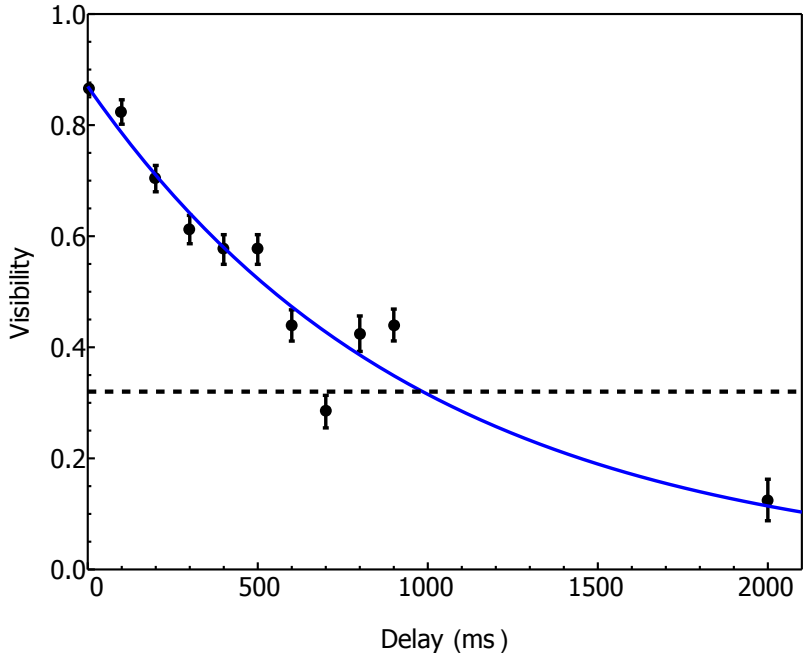


Figure 7.30: Phase scan visibility as a function of waiting time after performing a phonon-echo scheme in the 0-2 motional superposition. The fit gives a motional coherence time of the order of 1 second.

Experimental verification of the enhancement of the motional coherence time after implementing the phonon-echo scheme is shown in figure 7.30. The fit suggests that the coherence time of the system is 1000 ± 50 ms, which is a two-fold improvement on the phonon-Ramsey coherence time for a 0-2 motional superposition. It is expected that the enhancement occurs due to the elimination of the constant frequency noise in the trap supply. In this case, fitting is carried out with an exponential decay model instead of the half Gaussian model used for the Ramsey case. The phonon-echo is not prone to any dephasing due to heating of the ion, which follows an exponential decay function [66]. The measurements are also consistent with heating rates measurements carried out in section 7.8.2.

7.6.4 Demonstration of 0-1-2 motional superposition

In addition to a superposition of two motional states, a triple-state superposition experiment is demonstrated with a ground state cooled trapped calcium ion in the Penning trap. The su-

perposition state is realised using the laser sequence indicated in figure 7.31. The first laser pulse, with proper selection of pulse length ($2\pi/3.3$), transfers $2/3$ of the population to the state $|e,0\rangle$. The second laser pulse, a $\pi/2$ pulse tuned to the first red sideband, transfers $1/3$ of the population to the state $|g,1\rangle$. Subsequently, a π pulse tuned to second red sideband transfers the remaining 1/3 population to the state $|g,2\rangle$. The final superposition state can be expressed as

$$\psi(t) = \frac{1}{\sqrt{3}} |g\rangle \left(|0\rangle + e^{i\omega_z t} |1\rangle + e^{2i\omega_z t} |2\rangle \right) \tag{7.13}$$

where ω_z is the axial frequency.

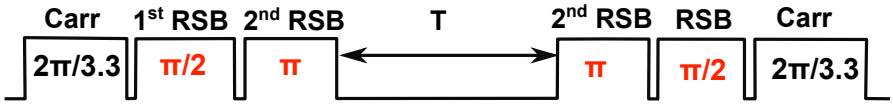


Figure 7.31: Laser sequence used to demonstrate the triple-slit interference pattern with motional states of the ion.

A derivation of the triple slit interference patterns is carried out by applying the equivalent operators for the laser pulses that are used in the experiment. The ion is initially prepared in the state $|g,0\rangle$. The steps followed for the derivation are illustrated here.

$$|g,0\rangle \xrightarrow[2\pi/3.3]{\text{Carrier}} \frac{1}{\sqrt{3}}\left(|g,0\rangle - i\sqrt{2}\,|e,0\rangle \right) \tag{7.14}$$

$$\xrightarrow[\pi/2]{\text{RSB1}} \frac{1}{\sqrt{3}}\left(|g,0\rangle + i\,|g,1\rangle - i\,|e,0\rangle \right) \tag{7.15}$$

$$\xrightarrow[\pi]{\text{RSB2}} \frac{1}{\sqrt{3}}\left(|g,0\rangle + i\,|g,1\rangle + |g,2\rangle \right) \tag{7.16}$$

$$\xrightarrow{\text{Wait T}} \frac{1}{\sqrt{3}}\left(|g,0\rangle + i\,|g,1\rangle\, e^{i\omega_z T} + |g,2\rangle\, e^{2i\omega_z T} \right) \tag{7.17}$$

$$\xrightarrow[\pi]{\text{RSB 2}} \frac{1}{\sqrt{3}}\left(|g,0\rangle + i\,|g,1\rangle\, e^{i\omega_z T} + i\,|e,0\rangle\, e^{2i\omega_z T} \right) \tag{7.18}$$

$$\xrightarrow[\pi/2]{\text{RSB 1}} \frac{1}{\sqrt{3}}\left(|g,0\rangle + \frac{i}{\sqrt{2}}\,|g,1\rangle\, e^{i\omega_z T} + \frac{i}{\sqrt{2}}\,|e,0\rangle\, e^{i\omega_z T} \right. \tag{7.19}$$

$$\left. + \frac{i}{\sqrt{2}}\,|e,0\rangle\, e^{2i\omega_z T} - \frac{i}{\sqrt{2}}\,|g,1\rangle\, e^{2i\omega_z T} \right). \tag{7.20}$$

The last $2\pi/3.3$ carrier pulse gives rise to a superposition between $|g,0/1\rangle$ and $|e,0/1\rangle$ states and the state is expressed as

$$\psi(T) = \frac{1}{\sqrt{9}}\Big(|g,0\rangle \left[1 + e^{i\omega_z t} + e^{2i\omega t}\right] + |g,1\rangle \left[\frac{i}{\sqrt{2}} e^{i\omega_z T} - \frac{i}{\sqrt{2}} e^{2i\omega_z T}\right] \tag{7.21}$$

$$+ |e,0\rangle \left[-i\sqrt{2} + \frac{i}{\sqrt{2}} e^{i\omega_z T} + \frac{i}{\sqrt{2}} e^{2i\omega_z t} \right] + |e,1\rangle \left[e^{i\omega_z T} - e^{2i\omega_z T} \right] \Big).$$

After taking the projection of the state on the eigenstates $|e,0\rangle$ and $|e,1\rangle$, the amplitude of the projection is calculated, which gives the probability

$$P(e) = \frac{1}{9}\big[5 - 3\cos(\omega_z T) - 2\cos(2\omega_z T)\big], \tag{7.22}$$

of the ion being in the excited state as a function of the wait time (T). After inserting some arbitrary phases during the preparation of the superposition, the expression is given as

$$P(e) = \frac{1}{9}\big[5 - 2\cos(\omega_z T + \phi_1) - \cos(-\omega_z T + \phi_1 - \phi_2) - 2\cos(2\omega_z T + \phi_2)\big], \tag{7.23}$$

where ϕ_1 and ϕ_2 are the phases between the laser pulses and some additional phase acquired during the preparation of the motional superposition.

A triple slit interference has been previously realised with atomic states [141] or with three physically separated slits [142, 143]. In our system, a ground state cooled ion is prepared in a superposition of three motional states, and the phonon triple-slit interference is realised. The phase acquisition of the motional wave-packet during its stay in the motional states 0, 1 and 2 is noted as a function of excitation probability between the internal states of the ion. The time evolution of the excited state population as a function of the waiting time is shown in figure 7.32. The plot indicates two frequency components of 127 kHz and 254 kHz. To reduce the complexity of the fitting, the fitting model is chosen as

$$P(e) = \big[A - B\cos(\omega_z T + \phi_1) - \frac{B}{2}\cos(-\omega_z T + \phi_1 - \phi_2) - B\cos(2\omega_z T + \phi_2)\big], \tag{7.24}$$

where the coefficients are found using the least-square fitting method. The experiment is performed at a low trapping frequency thus the ground state cooling is carried out by the adiabatic cooling technique.

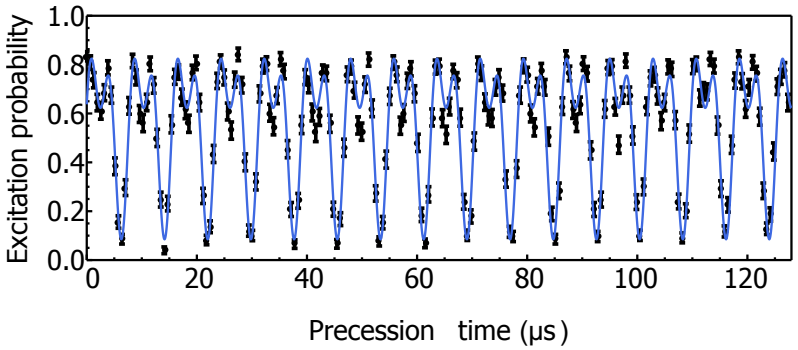
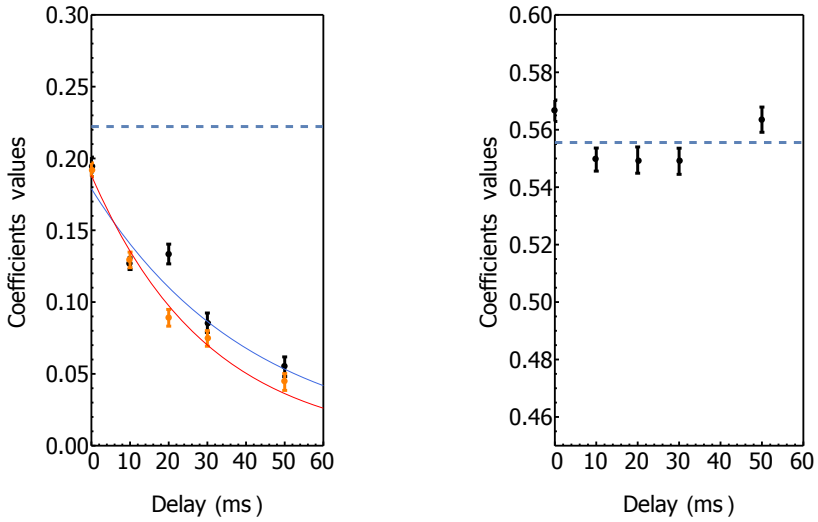


Figure 7.32: Free precession of population in state $|e\rangle$ in the triple slit experiment, indicating superposition of two frequencies ω_z and $2\omega_z$.

Furthermore, the studies were extended for various waiting times. In this case, the free-precession data was acquired after some initial waiting times (after inserting a gap of a few tens of milliseconds), and the coefficients were found by fitting the experimental data. The variation of the coefficients is shown in figure 7.33. We expect that the ω_z and $2\omega_z$ time-dependent parts

dephase differently, hence the terms are fitted with two independent coefficients. Figure 7.33 (a) shows the time variation of the ω_z component (black data points) and $2\omega_z$ component (orange data points). The fitting of the data is carried out with an exponential model and the coherence time is estimated to be 41 ± 3 ms for the ω_z component and 30 ± 2 ms for the $2\omega_z$ component. Figure 7.33 (b) shows the time-independent coefficient in equation 7.24. The dotted lines are plotted to show their actual values as given in equation 7.23. Note that the measured coefficients differ slightly from the theoretically calculated values, which is caused by systematic errors in laser pulses and detunings.



(a) (b)

Figure 7.33: Loss of the visibility of the triple-slit interference pattern with wait time. In figure (a), black data points are the measured values of the coefficients of the ω_z component and the orange data points are the coefficient values of the $2\omega_z$ component. The solid curves are fitted to the experimental data points. Figure (b) shows the data points of the time-independent term in equation 7.23.

7.6.5 Motional superposition of high-n motional states

An interesting motional superposition is demonstrated after preparing the ion in a high-n state through a sideband heating technique. In high-n states, the sideband strength of the higher order sidebands increases, hence it is possible to coherently manipulate the quantum states using higher order sidebands. In this case, the ion is initially prepared in the $n \sim 150$ phonon state at 420 kHz axial frequency. In order to prepare the ion in such a high-n state, resolved sideband heating technique is implemented, where the 729-nm laser is tuned to the first blue sideband of the transition. This technique prepares the ion in a state very close to the first blue sideband minima point. A more detailed description of the sideband heating method can be found in chapters 5 and 6. The laser sequence which is used to prepare and detect the motional superposition with high phonon-number is shown in figure 7.34. The first laser pulse ($\pi/2$ carrier pulse) creates a superposition of $|g, n\rangle$ and $|e, n\rangle$, followed by the second laser pulse ($\pi/2$ third-red sideband pulse) creates the superposition $|g, n\rangle$, $|e, n\rangle$,$|g, n+3\rangle$ and $|e, n-3\rangle$. The

resultant state is expressed as

$$|\psi\rangle = (a\,|g,n\rangle + b\,|e,n\rangle + c\,|g,n+3\rangle + d\,|e,n-3\rangle), \tag{7.25}$$

where a, b, c and d are the coefficients of the respective state vectors. After creating the superposition of the internal state and external states of the ion, the state is detected after some waiting time (T) by projecting it onto the excited and the ground state of the ion. During the waiting time, the system acquires some phase which is seen as the time variation of the excited state population ($P(e)$) as a function of waiting time. The time evolution of the state vectors can be measured by following the algebra of the state vector and laser sequence that is used to perform the experiment. The excited state probability as a function of free-evolution time comes to be

$$P(e) = \frac{1}{8}\big[5 - 2\cos(3\omega_z(T+t)) + \cos(6\omega_z(T+t))\big], \tag{7.26}$$

where the parameters have the usual meaning. Note that the expression indicates two frequency components, one at $3\omega_z$ and the second at $6\omega_z$. After including the phase of the respective laser pulses, the more general expression is given as

$$P(e) = \frac{1}{8}\big[4 + \cos(\phi_c) + \cos(6\omega_z t + 2\phi_t - \phi_c + 2\phi_r) - 2\cos(3\omega_z t + \phi_t - \phi_c + \phi_r)\cos\phi_r\big], \tag{7.27}$$

where ϕ_c, ϕ_r are the phase differences between the carrier pulses and third red pulses, respectively. The extra phase, ϕ_t, is included to account for the phase acquisition during time T. The expression further simplifies if the optical decoherence in the system is assumed. After the optical coherence time the excited state population comes to be

$$P(e) = \frac{1}{2} - \frac{1}{4}\cos(3\omega_z t + \phi_r - \phi_c - \phi_t), \tag{7.28}$$

which indicates that the $6\omega_z$ component drops out of the expression due to dephasing of the ground and excited electronic states. The remaining expression averages out at around $P(e) = 0.5$ and contains an oscillatory component at $3\omega_z$.

The experiment is performed at various waiting times T and the free-evolution time (t) is varied in steps of 40 ns. Plots showing the time evolution of the population in the excited state ($P(e)$) as a function of free-precession time are shown in figure 7.35. The data points in red and orange are taken at phase $\phi_c = 0$ and $\phi_c = \pi$, respectively. The data points are then fitted with the theoretical model discussed in equation 7.27. The experimental data indicates both frequency components ($3\omega_z$ and $6\omega_z$) are present within the optical coherence time. However, outside the optical coherence time, the data shows time variation with only the $3\omega_z$ frequency component.

The visibility of the high-n superposition is extracted from the plots and shown in figure 7.36 as a function of T. The figure indicates intriguing results of motional and spin coherence effects. In this experiment, the superposition state is composed of spin and motional eigenstates, hence the interference of both quantum effects is expected. At initial waiting times, the visibility is

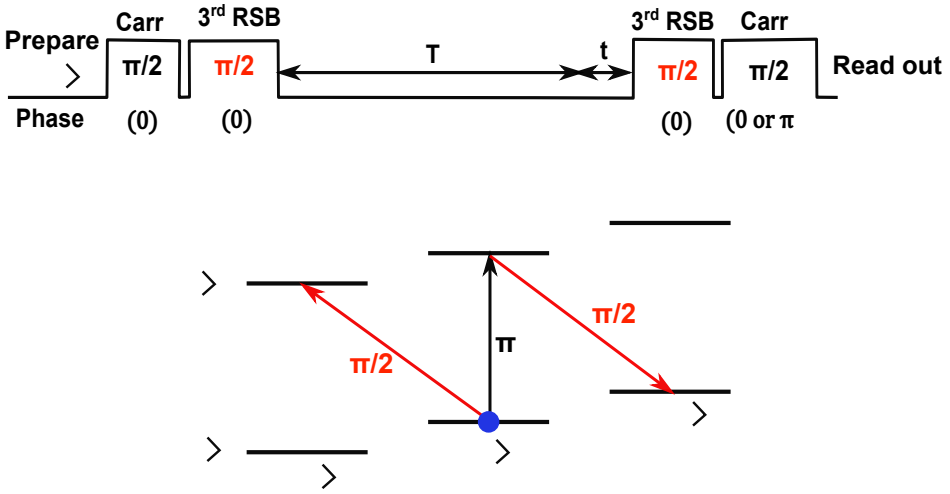


Figure 7.34: Laser sequence used to create motional superposition at high phonon state (top), and (bottom) an illustration of how the superposition state, $\frac{1}{\sqrt{4}}(|g,n\rangle + |e,n\rangle + |g,n+3\rangle + |e,n-3\rangle$, is generated from the above laser pulses.

highest and it drops down to approximately 0.5 at 1 ms. During the first 1 ms, the system dephases against the spin decoherence effects. However, at later times, only motional coherence contributes to the sinusoidal variation at $3\omega_z$. The system completely dephases after the motional coherence time. The estimated optical coherence time is found to be 500 ± 50 μs, which is not consistent with previously measured optical coherence time [4]. The motional coherence time is measured to be 100 ± 10 ms, which is also shorter than the 0-1 motional coherence time. In this case, the superposition is created for $\Delta n = 3$ so we expect this change [63].

A motional superposition was also created after preparing the ion near the minimum of the second blue sideband. In this case, the ion is initially heated to the first blue sideband minima, followed by the second stage of sideband heating where the ion is heated to the second blue sideband minima. We expect the resultant phonon state to be n ~288. To perform coherent manipulation of the motional states, a $\pi/2$ pulse tuned to the first red sideband is used, which creates the superposition of $|g,n\rangle$ and $|e,n-1\rangle$. Subsequently, a second $\pi/2$ pulse, tuned to the third red sideband, creates a superposition state which is denoted by

$$|\psi\rangle = \frac{1}{2}\big(\,|g,n\rangle + |e,n-3\rangle + |e,n-1\rangle + |g,n+2\rangle\,\big). \tag{7.29}$$

The resultant state then acquires phase during the free-evolution time (T). The laser sequence used in the experiment is similar to that shown in figure 7.34, the only difference being that the

[4]This reduction in the optical coherence time is observed very recently. We believe that the optical coherence time is decreased due to some additional laser frequency noise that was added to our frequency locking system. In September 2016 our superconducting magnet was recharged, which changed the magnetic field by approximately 0.5 % from its previous value. This required a new 729-nm laser frequency to induce the carrier transition. The change in the laser frequency was not possible to bridge with the scanning AOM, hence, the reference cavity mode was changed and the laser was locked to some other cavity mode. Somehow, this alteration in the locking system did not give us the same optical coherence time as before.

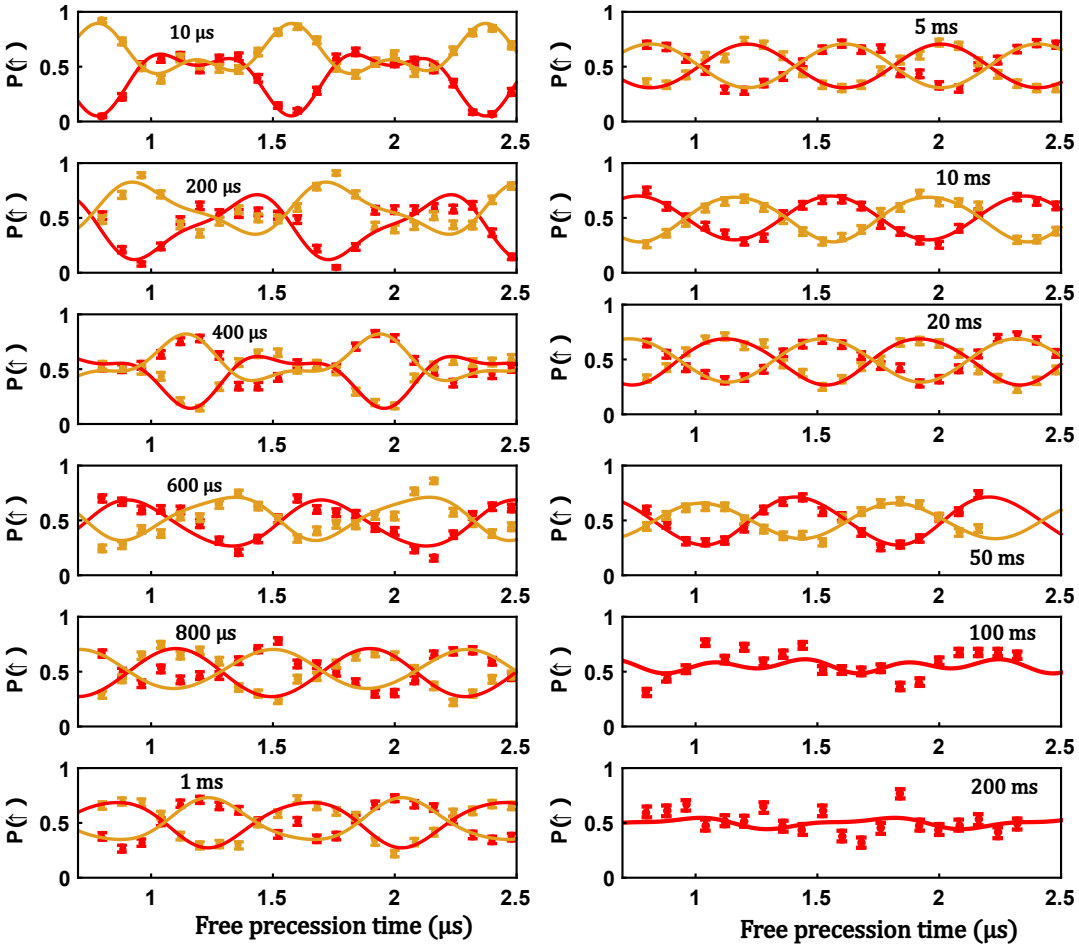


Figure 7.35: Plots showing the time evolution of the excited state population for several values of waiting time, after creating the motional superposition at $n \sim 150$. Orange and red curves indicate the time evolution of state vectors for $\phi_c = 0$ and π, respectively. For $T < 1$ ms, the optical and motional coherence both contribute to give full visibility of the plots. At later times, only the motional coherence contributes to the sinusoidal oscillations.

carrier laser pulse is replaced by a first red sideband pulse. The excited state population as a function of the waiting time $(T + t)$ is expressed as

$$P(e) = \frac{1}{8}\big[5 - 2\cos(2\omega_z(T+t)) + \cos(4\omega_z(T+t))\big], \tag{7.30}$$

where the laser pulses are assumed to be phase synchronised with respect to each other. The global phase is omitted by assuming zero phase acquisition for the $|g, n\rangle$ and $|e, n-1\rangle$ states. After inserting the relevant laser phases into expression, it becomes similar to equation 7.27 after replacing $3\omega_z$ with $2\omega_z$. Figure 7.37 shows the variation of the amplitude of the motional superposition as a function of free evolution time. The fitting is carried out with two decay rates, one for the optical dephasing and the second for the motional dephasing effects. The fitting model is given in appendix E. We find $\tau_{optical} = 620 \pm 100$ μs and $\tau_{motional} = 270 \pm 30$ ms. The spin dephasing time is found to be the same as the optical coherence time as measured in

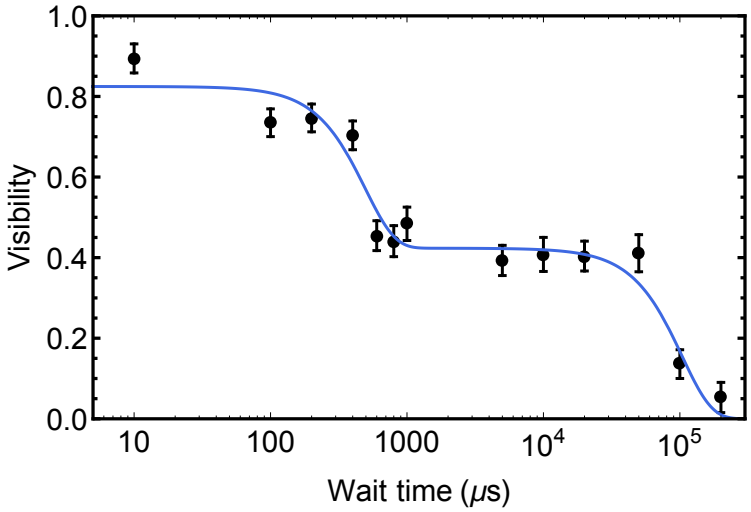


Figure 7.36: Coherence time measurement using motional superposition of high n motional states. The plot shows two kind of quantum coherence effects. The spin coherence effects are observed at short waiting times ($T < 1$ ms) and the motional coherence effects are observed at long waiting times ($T > 1$ ms).

the previous section.

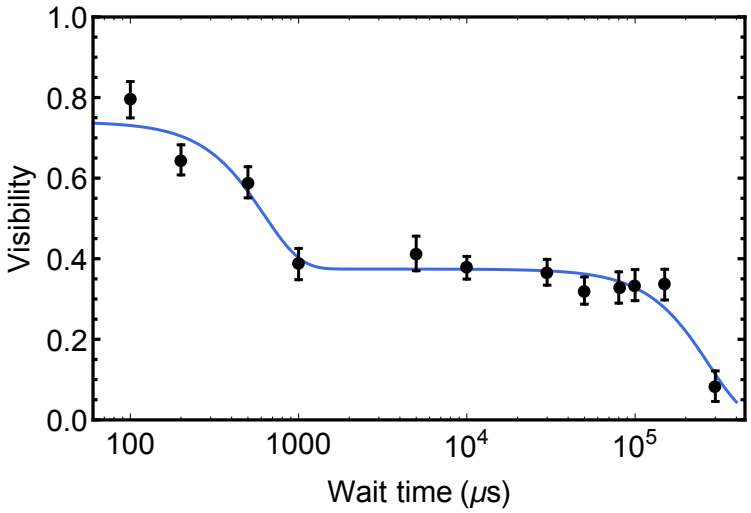


Figure 7.37: Plot showing the loss of the visibility as a function of waiting time when the superposition is created with the first red sideband and the third red sideband pulses for a sideband heated ion. The superposition is demonstrated after preparing the ion in the $n \sim 288$ state via a two-stage sideband heating technique.

The motional coherence time for $n \sim 288$ is measured slightly higher than that for $n \sim 150$. In the previous experiment, $\Delta n = 3$ however this experiment was performed for $\Delta n = 2$. The study indicates that the coherence time varies with Δn not with the phonon state number. Additionally, in chapter 6 we saw that the state prepared after sideband heating is not a pure Fock state, but rather has some spread around the first and second blue sideband minima. The spread of the population is not a problem if the sideband strength is roughly constant over the Fock states of interest. In reality, this causes some systematic reduction in the visibility. This is noted at $T = 0$ in plots 7.36 and 7.37, where the visibility is measured to be 0.8 instead of 1.

For the current discussion, we are interested in the coherence times, thus the systematic errors are ignored.

7.7 Experimental demonstration of coherent state of motion

The coherent state is a minimum uncertainty state of a quantum harmonic oscillator and is a close analogue to the classical harmonic oscillator. After preparing the ion in its the motional and electronic ground states, a bichromatic laser radiation is used to construct the state α. The interaction of an ion with the bichromatic radiation field is explained below. The sum of two classical light fields generated by two light sources is expressed as

$$\mathbf{E} = E_1\hat{x}\cos(\omega_{l1}t - kz) + E_2\hat{x}\cos(\omega_{l2}t - kz) \tag{7.31}$$

where E_i is the amplitude and ω_{li} is the frequency of the applied electric field. In this case, the direction of propagation of the laser beam creating the bichromatic fields is assumed to be along the z axis and the polarisation is assumed to be directed along the x axis. Let us assume that both fields have the same amplitude, E_0. In order to simplify the expression, let us assume that the two laser beams have $\omega_{l1} = \omega_l - \omega_d$ and $\omega_{l2} = \omega_l + \omega_d$, then the combined field is expressed as

$$\mathbf{E} = 2E_0\hat{x}\cos(\omega_l t - kz)\cos(\omega_d t). \tag{7.32}$$

The equivalent Hamiltonian for the field interacting with an atom of dipole operator $\mathbf{D}$ is given as

$$H = -\mathbf{E}\cdot\mathbf{D}. \tag{7.33}$$

After following the usual definition of the dipole operator D, the Hamiltonian simplifies to

$$H = \hbar\Omega(\sigma_+ + \sigma_-)\left[\mathrm{e}^{i(\omega_l t - kz)} + \mathrm{e}^{-i(\omega_l t - kz)}\right]\cos(\omega_d t), \tag{7.34}$$

where the parameters have been defined earlier. The Hamiltonian in the interaction picture, and after making the rotating wave approximation, simplifies to

$$H_{int} = \hbar\omega\big(\sigma_+\mathrm{e}^{-i\Delta t}\mathrm{e}^{i\eta(\tilde{a}+\tilde{a}^\dagger)} + \sigma_-\mathrm{e}^{i\Delta t}\mathrm{e}^{-i\eta(\tilde{a}+\tilde{a}^\dagger)}\big)\cos(\omega_d t) \tag{7.35}$$

where $\Delta = \omega_l - \omega_0$ and $\tilde{a}$ is the lowering operator in the interaction picture. After assuming $\Delta = 0$ and $\omega_d = \omega_z + \delta$, which implies the laser has two sidebands around the carrier at frequencies $\pm(\omega_z + \delta)$, the Hamiltonian is expressed as

$$H_{int} = \hbar\omega\big(\sigma_+\mathrm{e}^{i\eta(\tilde{a}+\tilde{a}^\dagger)} + h.c.\big)\cos(\omega_z t + \delta t). \tag{7.36}$$

For the case when $\delta = 0$, the above interaction Hamiltonian implies a classical force term giving rise to the displacement operator $D = \mathrm{e}^{\alpha^* a - \alpha a^\dagger}$ for harmonic motion with frequency ω_z [144]. If this Hamiltonian is applied to a ground state cooled ion, it creates a coherent state of motion. The above Hamiltonian in resolved sideband terms is expressed as

$$H_{int} = \frac{\hbar\omega}{2}\left(\sigma_+ \mathrm{e}^{-i\omega_z t}\mathrm{e}^{i\eta(\tilde{a}+\tilde{a}^\dagger)} + h.c.\right) + \frac{\hbar\omega}{2}\left(\sigma_+ \mathrm{e}^{i\omega_z t}\mathrm{e}^{i\eta(\tilde{a}+\tilde{a}^\dagger)} + h.c.\right), \tag{7.37}$$

where the first term in the right hand side of the expression is equivalent to excitation of the first blue sideband and the second term is equivalent to excitation of the first red sidebands. This implies that if laser radiation is applied simultaneously to the red and blue sidebands of the transition, a coherent state of motion can be created in trapped ion systems.

The schematic of the laser sequence used to create a coherent state of motion is shown in figure 7.38. Experimentally, the coherent state is constructed by using a bichromatic laser beam. For a fixed duration of the bichromatic interaction, the population resides in a superposition of the states $|g\rangle$ and $|e\rangle$. For a near ideal realisation, a short 854-nm laser pulse is added in the sequence, which prepares the ion in the state $|g, \alpha\rangle$ (only to some approximation [144]).

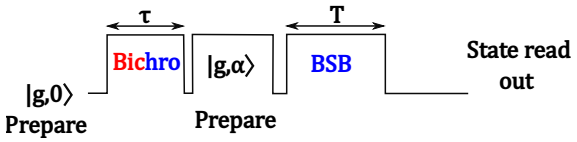


Figure 7.38: Schematic of the laser pulses used to prepare the coherent state of motion. The first state-preparation pulse is required for ground state cooling and preparing the ion in its electronic ground state. The second state-preparation pulse indicates a short 854-nm laser pulse that is used to prepare the ion in the electronic ground state.

In order to carry out frequency analysis of the coherent state, the probe laser is tuned to the blue sideband of the 729-nm transition and a Rabi-flop experiment is performed [5]. The time evolution of the excited state population as a function of laser interaction time is shown in figure 7.39. The experimental data points are then fitted to a model expressed as

$$P(\uparrow) = \sum_{n=0}^{n_{max}} \frac{\exp[-\langle n\rangle]\,\langle n\rangle^n}{n!} \sin\left(\frac{\tau}{2}\Omega_{n,n+1}\right), \tag{7.38}$$

where $\langle n\rangle$ is the mean phonon number, τ is the laser interaction time and $\Omega_{n,n+1}$ is the blue sideband Rabi frequency for the motional state n.

For the experimental demonstration, the bichromatic laser radiation was applied for 150 μs after ground state cooling of the ion. The mean phonon number ($\langle n\rangle$) for the coherent state produced is measured to be 3.30 ± 0.06. In this experiment, a fascinating and unique effect of quantum coherence is observed. The quantum coherence is observed to disappear after 100 μs and the revival of quantum coherence is observed after 400 μs, verifying the quantum behaviour

[5] In principle, the Rabi flops can be observed on the carrier transition too but the BSB is preferred due to its dependency on n.

of a coherent state of motion (n).

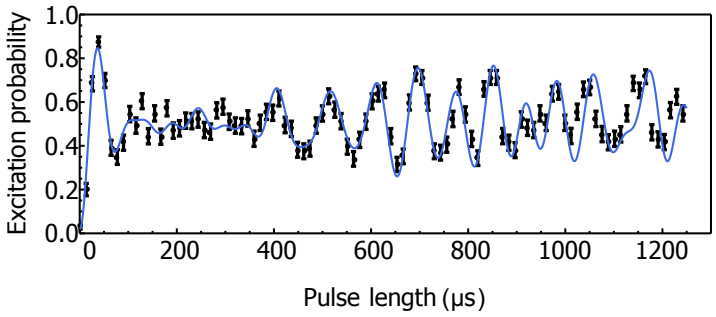


Figure 7.39: Time evolution of the excitation probability as a function of laser interaction time with the blue sideband of the transition after generating a coherent state of motion.

Also, for the Rabi oscillation curve shown in figure 7.39, the frequency analysis is achieved by fitting $P(n)$ with individual coefficients for each motional state. The extracted occupation probability from the blue sideband Rabi-flop fit is shown in figure 7.40. The distribution is found to be in agreement with the Poissonian model of the occupation probability expected for a coherent state of motion.

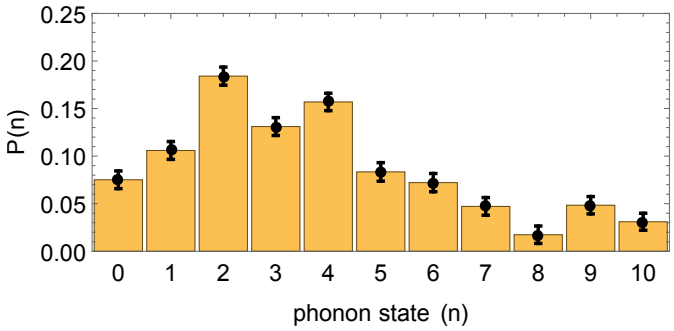


Figure 7.40: Occupation probability in each phonon state after frequency analysis of the Rabi flops as shown in figure 7.39.

7.7.1 Demonstration of a forced harmonic oscillator using a trapped ion system

Additionally, some intriguing effects are observed when the bichromatic radiation is slightly detuned from the sideband frequencies. The Hamiltonian for this is given in equation 7.36. The forced term due to the laser field is defined as

$$F = F_0 \cos(\omega_z t + \delta t), \tag{7.39}$$

where δ is the detuning of the bichromatic radiation from the sideband transitions ($\omega_d = \pm(\omega_z + \delta)$). In this case, if the laser is detuned by a few hundreds of Hz from each sideband, the radiation drives the oscillator to a high mean phonon number, and after some time the oscillator is driven back to the ground state of motion. The effect is identical to a situation in which a classical

harmonic oscillator is driven by a detuned force which periodically changes the amplitude of the motion.

In the first set of experiments, the bichromatic interaction time is varied and simultaneously the probability of the ion being in the excited electronic state is measured for a given probe time. For a fixed probe time, the ion changes its electronic state depending upon the Rabi frequency of the particular motional state (n). If the probe time is set to be a π pulse for a given transition at $n = 0$, it does not remain a π pulse if the motional state is changed, hence the excitation probability varies with bichromatic interaction time. The evolution of the excitation probability with bichromatic interaction time for a fixed carrier pulse ($\tau_{n=0} = 4\pi$) is shown in figure 7.41 (black data points). In the same figure, the time evolution of the excitation probability for a fixed duration of laser pulse tuned to the first blue sideband transition ($\tau_{n=0} = \pi$), is indicated by red points.

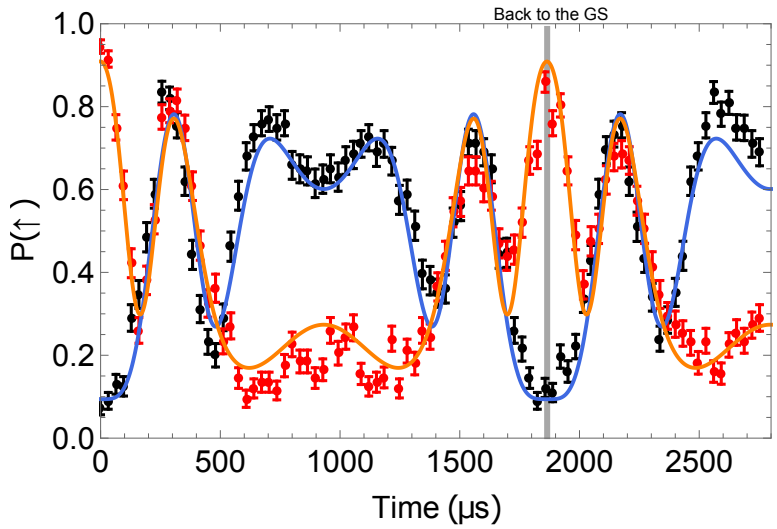


Figure 7.41: Collapse and revival of population in the ground motional state as a function of bichromatic drive time. The excitation probability is measured at various drive times and fixed probe lengths. The revival of the ground state population is observed at approximately 1900 μs.

The experimental data points are then fitted with a model which takes into account the time variation of the mean phonon number and the corresponding change in the Rabi frequency for a given transition. The model used for the fitting is expressed as

$$P(\uparrow) = \sum_{n=0}^{\infty} \frac{e^{-\langle n\rangle_t}\,\langle n\rangle_t^n}{n!} \sin^2\left(\frac{1}{2}\tau_{probe}\Omega_{n,n'}\right) \tag{7.40}$$

where $\langle n\rangle_t = \langle n\rangle_{max} \sin^2(\pi\delta t)$ is the time-varying mean phonon number of the quantum harmonic oscillator and the parameter $\langle n\rangle_{max}$ is used to estimate the maximum change in the mean phonon number due to the bichromatic drive.

The best-fitted plots of the time-varying excitation probabilities for the carrier and the first blue sideband transitions are shown in figure 7.41, along with the experimental data. The estimated value of the detuning (δ) comes to be 536 ± 1 Hz and the maximum value of the

mean phonon number is estimated to be 49.7 ± 0.2. The corresponding amplitude of motion comes to be 760 nm at 419 kHz axial frequency. In this plot, the full reflection to the ground state of motion is observed at 1865 μs. To precisely estimate the mean phonon number at the highest amplitude point, another experiment is performed where spectroscopy is carried out for a known bichromatic interaction time and at a given probe time. The spectrum after bichromatic interaction time of 1 ms is shown in figure 7.42. The fitting is carried out by considering a Poisson type distribution of the occupation probability and the value of the $\langle n \rangle$ is estimated. The estimated $\langle n \rangle$ at the highest amplitude point is found to be 48.7 ± 0.6, which is broadly consistent with the above findings. This is the largest coherent state of motion that we realised in our system.

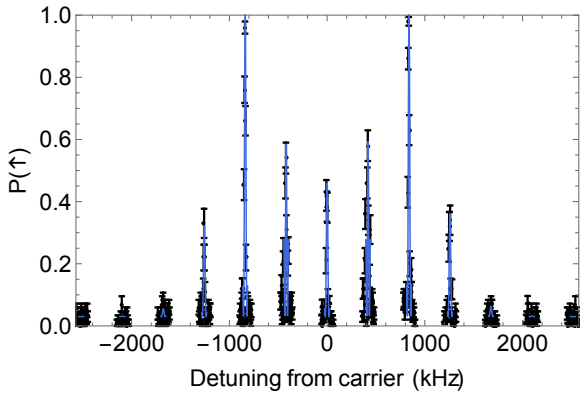


Figure 7.42: Spectrum after preparing a coherent state of motion with a bichromatic drive. The fitting suggests that the mean phonon number is 48.7 ± 0.6, and the population around the mean point follows a Poissonian distribution.

In the third set of experiments, Rabi flops are acquired for the carrier and the first blue sideband transitions after 1 ms of bichromatic field interaction. The data is presented in figure 7.43. Note that the Rabi flops for the first blue sideband transition (shown with red data points) indicate periodic behaviour, however, the carrier Rabi flops (shown with black data points) are not observed to be oscillatory in nature. This is attributed to the difference in the carrier strength for different n states. Moreover, the behaviour can be understood by looking at the plot of the sideband strengths at 419 kHz axial frequency shown in the right panel of figure 7.43. Note that the carrier strength varies drastically for the phonon distribution at $\langle n \rangle = 49$, however, the blue sideband strength is relatively constant around these phonon states. Consequently, the different frequency components in the carrier Rabi experiment introduce dephasing and hence the excitation strength averages out to 0.5 for this case.

In another experiment, we set the detuning to be approximately 1.4 kHz and measure $\langle n \rangle$ for various durations of the bichromatic field. The experimental findings are shown in figure 7.44 for interaction times of 0, 352 and 704 μs, respectively. The classical drive, in this case, creates the largest amplitude of motion at $t = 352$ μs, which is half the revival time $(1/\delta)$. For this case, the measured value of $\langle n \rangle$ is 6.31 ± 0.14. Subsequently, at time $t = 704$ μs the ground state population is reconstructed, confirming the revival of the population with the classical drive. Furthermore, revival and collapse are observed at integer and half-integer durations of 704 μs, and the data is presented in figure 7.45.

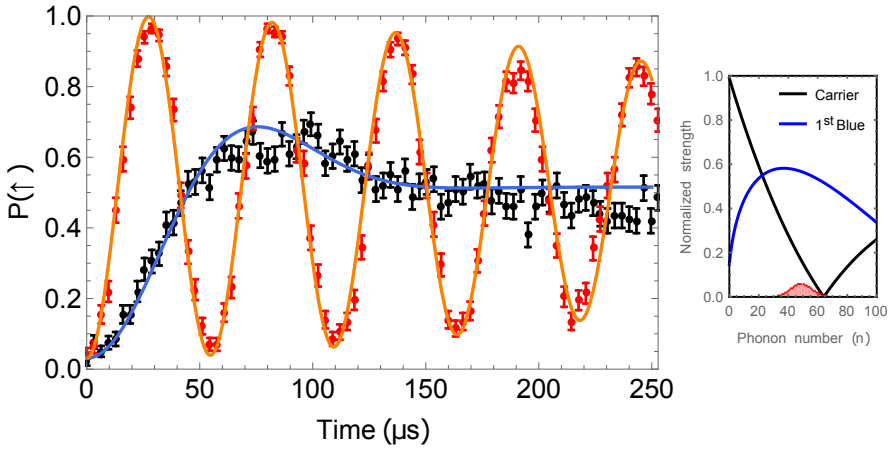


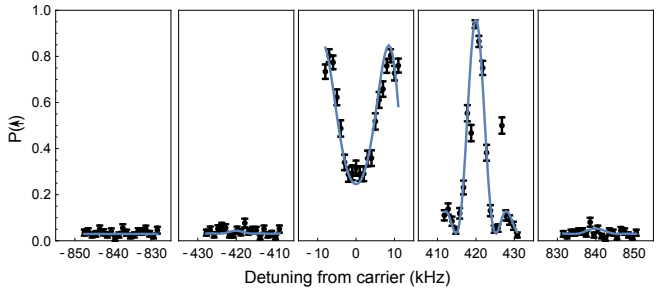
Figure 7.43: Rabi oscillation of the carrier transition (black data points) and at the first blue sideband (red data points) after preparing the ion at $\langle n \rangle$ =49 through bichromatic driving. The estimated Rabi frequency is 32 kHz. On the right, the sideband strength around $\langle n \rangle = 49$ for the carrier and blue sideband is shown, indicating a steep change in the Rabi frequency for the carrier transition leading to dephasing.

For this case, fitting is not performed, however for illustration purposes, the experimental data is superimposed with simulated results. A sinusoidal curve (in red) is drawn to indicate the periodicity in the revival and collapses after every 704 μs. Additionally, the equation of motion for an equivalent classical oscillator is solved by numerical methods. The system is assumed to be subjected to a similar driving force as estimated from the experimental results and a damping term included. The normalised strength of the drive and damping is varied to exactly overlay the experimental points. The estimated value of the normalised driving term comes to be 61.5/μs^2 and the equivalent damping is estimated to be 560 Hz in the normalised displacement units.

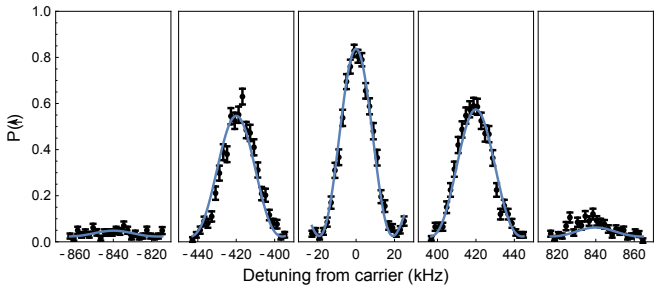
7.7.2 Experimental demonstration of a squeezed state of motion

A squeezed state of motion in a trapped ion system is realised by applying a parametric drive potential at the trap electrodes or by illuminating the ions with a standing laser field beating at twice the trap frequency [145]. In our system, the experimental demonstration of a squeezed state of motion is carried out with the help of bichromatic laser radiation. The laser beam interacts with the ion in a travelling wave configuration and it is tuned to the second red and the second blue sidebands of the transition. In an ideal situation, the scheme must populate the even phonon states [78] and the probability distribution must follow a squeezed state distribution as shown in equation 2.69. The experiment is carried out at 419 kHz axial frequency. Before applying the bichromatic interaction, the ion is prepared in the electronic ground state and motional ground state. After a fixed bichromatic interaction time, Rabi oscillations on the blue sidebands (BSB) are recorded. The theoretical model for the time evolution of the squeezed state is expressed as

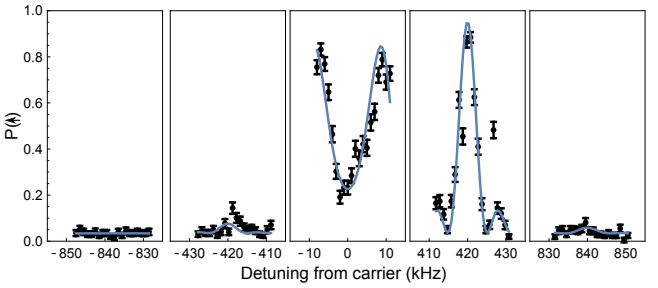
$$P(\uparrow) = \sum_{n=0}^{nmax} \frac{(2n)!\tanh^{2n}(r)}{(2^n n!)^2 \cosh(r)} \sin^2\left(\frac{\tau}{2}\Omega_{2n,2n+1}\right), \tag{7.41}$$



(a)



(b)



(c)

Figure 7.44: Spectra of a trapped calcium ion after driving it with a bichromatic radiation for (a) 0 μs, (b) 352 μs and (c) 704 μs. Each windowed spectrum contains two red sidebands, two blue sidebands and a carrier transition. In spectra (a) and (c) the dip at the carrier transitions indicate that the probe time is longer than the π pulse time.

where τ is the laser interaction time for the first BSB. The Rabi frequency of the blue sideband is denoted by $\Omega_{2n,2n+1}$. The model assumes occupation of the even phonon states during the bichromatic interaction time.

The Rabi flops on the first blue sidebands, after preparing the squeezed state of motion in our system, are shown in figure 7.46. The bichromatic radiation is applied for 900 μs at $\pm 2\omega_z$. Unlike the coherent state of motion, the squeezed state is not identifiable from the Rabi flops. However, the fitting of the spectrum with a proper model gives rise to the squeezing parameter, $\xi(= e^{2r})$. The fitting of the experimental data gives squeezing parameter to be 35 ± 2, which corresponds to $\langle n \rangle = 8.1 \pm 0.5$. The fitting is carried out for even phonon states only and the fitted curve is shown in blue. In principle, the odd states are not get occupied in this case, however, the incoherent repumping by the 854-nm laser may slightly populate the odd states. Occupation probability of the odd states is negligible however if the experiment is performed within the L-D regime.

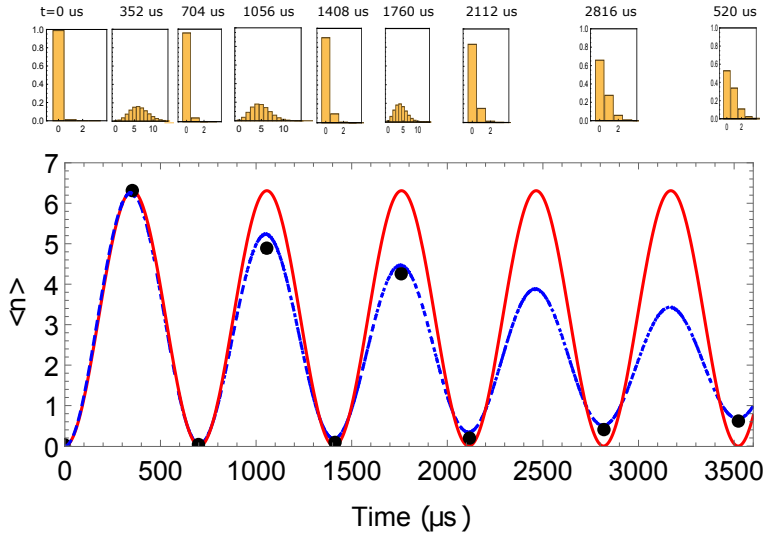


Figure 7.45: Periodic collapse and revival of the population in the ground state as a function of bichromatic interaction time. The period is observed to be 704 μs. The bottom plot shows $\langle n \rangle$ as a function of bichromatic interaction time and the various sub-plots at the top indicate the phonon distributions corresponding to each data point in the bottom curve.

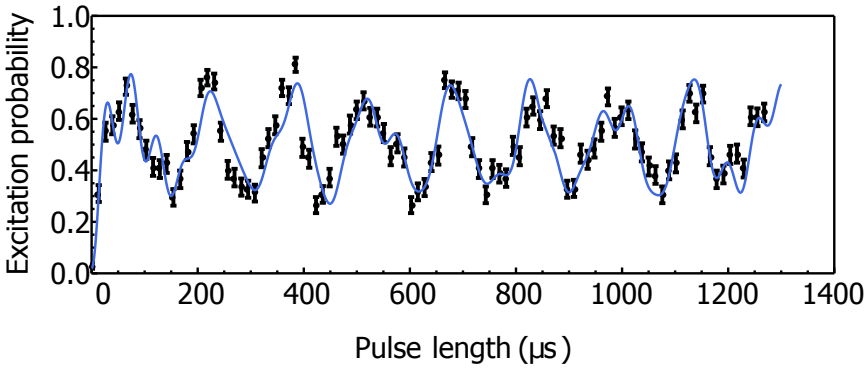


Figure 7.46: Rabi oscillations of the blue sideband after bichromatic interaction of 900 μs. Bicromatic radiation was tuned to the second red and second blue sideband transition. The fitting is carried out with three different cases. See text for more detail.

The population in each individual motional state is extracted by independently fitting the experimental Rabi data. The fitting is carried out by allowing the occupation probability in the individual phonon states to be free parameters. In order to simplify the fitting procedure, the ion is assumed to reside in the even phonon states only. The estimated value of $P(n)$ is shown in figure 7.47 with red circles. The curve in black corresponds to the estimated value of $P(n)$ for $\langle n \rangle = 8.1$ as estimated previously. The expression used to estimate the value of $P(n)$ is given in 2.69. The individual phonon state fitting is not very reliable due to insufficient information from the Rabi plot. However, for the sake of completeness, the experiment verifies demonstration of the squeezed state of motion in our system. Additional analysis of the squeezed state of motion is presented in appendix F.

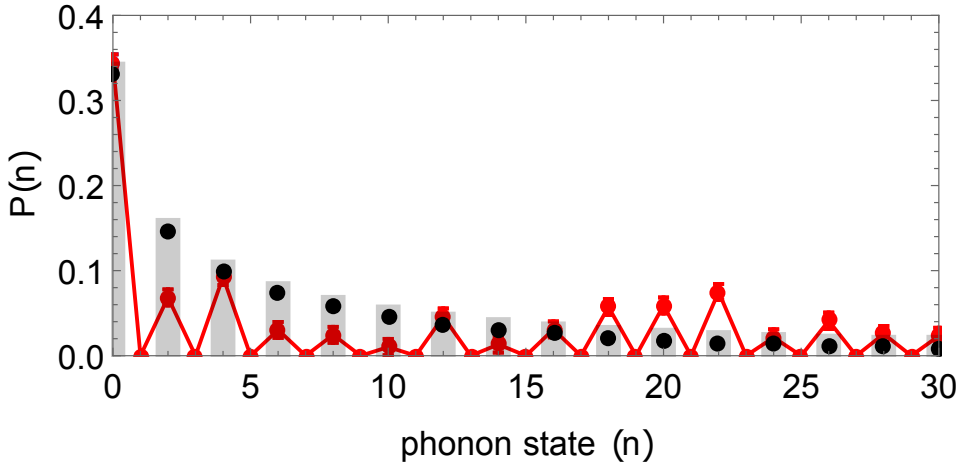


Figure 7.47: Occupancy distribution analysis of the squeezed state of motion. The black data points with grey vertical bars represent the occupation probability estimated at $\langle n \rangle = 8.1$. The circles in red indicate the individual phonon state occupation after fitting with the individual phonon state occupancy as a free parameter. In both cases, only even phonon states are taken for the fit.

7.8 Dephasing of the motional superposition

In trapped ion systems, the motional coherence time is a very important factor limiting the fidelity of any quantum control. In the previous section, I have shown the measurements of the motional coherence time in our system signifying a high level of motional coherence. In this section, I will further verify the motional coherence time measurements through some supplementary measurements that were carried out in our system.

7.8.1 Stability of the trap power supply

Dephasing of the motional superposition is directly related to the stability of the trap supply. A direct measurement of the trap power supply was carried out using a 6.5 digit Agilent 34401A digital voltmeter and the stability plot is shown in figure 7.48. The measurement was carried out at 250 V, which is a normal operating potential in our system. The standard deviation of the trapping voltage noise is measured to be $\sim$ 1 mV, which corresponds to σ_{ω_z} =0.8 Hz at ω_z = 419 kHz. The corresponding value of the estimated coherence time comes to be approximately 0.5 s. The estimated coherence time of our system agrees with the value measured in the 0-1 motional superposition experiment.

7.8.2 Heating rate measurements

Heating of trapped ions affects the ability to manipulate quantum systems [63]. In RF traps, generally, the micromotion and noise on the trap electrodes cause heating of a trapped ion. A more specific reason for the heating mechanism of a trapped ion is still unclear [66]. In a Pen-

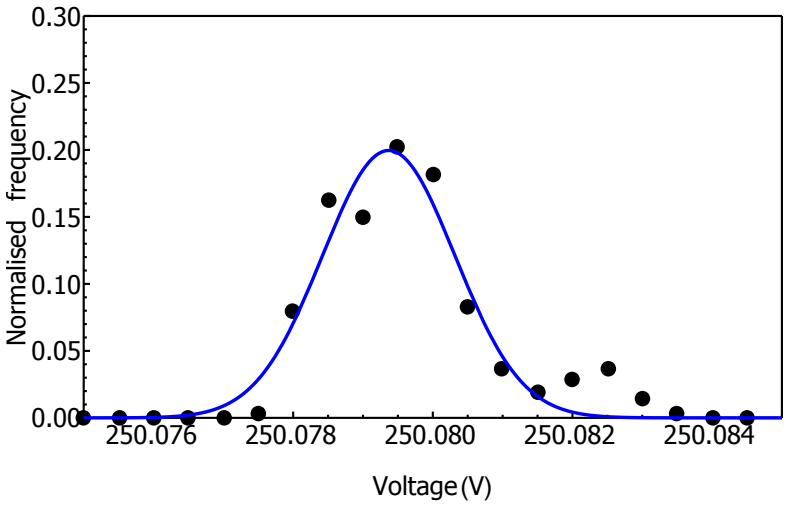


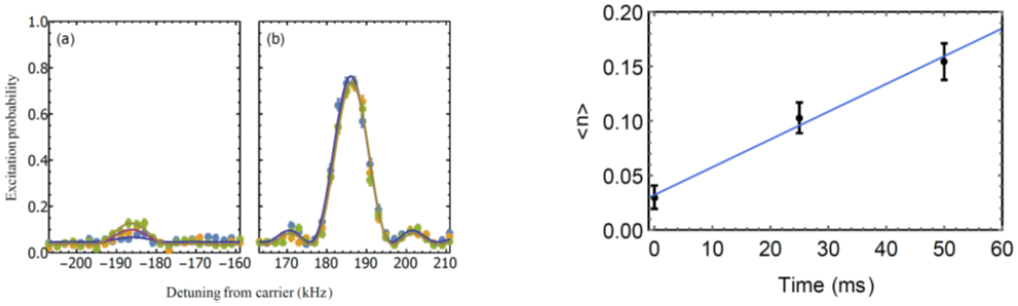
Figure 7.48: The figure shows the stability of the trap power supply at 250.079 V. The measurements were taken for 2 hours at 1 Hz acquisition rate.

ning trap, no RF field is present, hence, heating is expected due to patch potentials or trapping potential instability. There is no specific explanation as to whether the heating mechanism affects the entangled state or not. However, if the motional state is changed due to heating, the coherent manipulation differs due to the change in Rabi frequency. In this section, I will present heating rate measurements with a calcium ion in the Penning trap. The measurements are carried out with one and two ground state cooled ions. After preparing the ions in the motional ground state, spectroscopy is performed at various waiting times and the ground state occupation is measured. If the ion changes phonon number during this waiting time, the red sidebands of the spectrum become visible, indicating a reduction in the ground state occupation. By noting the rate of change of the mean phonon number with time, the heating rate can be estimated for a particular motional mode.

7.8.3 Heating rates of a single ion

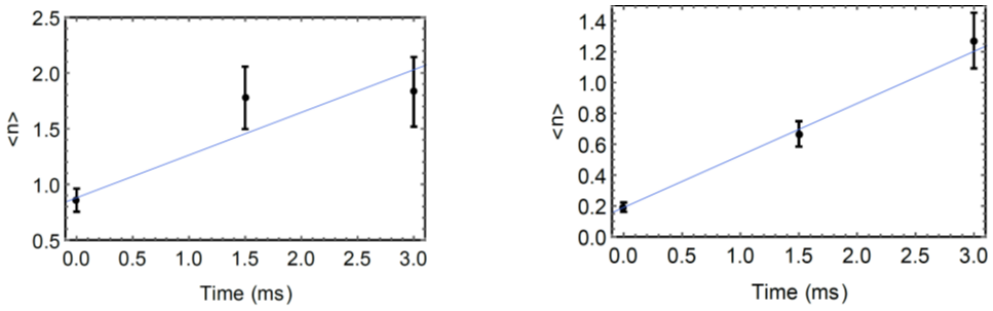
Previously, the heating rate of a trapped calcium ion at 420 kHz was measured to be 0.3 ± 0.2 phonons/s [45], estimating sub-hertz heating rates. As a rule of thumb, heating rates vary with the ion oscillation frequency, assuming that the system has Johnson noise [66]. Recently, we reassessed the heating rates in our trap and they were found to be consistent with our previous measurements at 420 kHz axial frequency. We also measured the heating rates at 186 kHz ion oscillation frequency along the axial direction and the results will be presented in this section. A plot showing spectra after various waiting times at 187 kHz axial frequency is shown in figure 7.49. The single ion heating rates at this frequency are estimated to be 2.5 ± 0.5 phonons/s, a slightly higher value than that measured at 420 kHz axial frequency.

The radial motion in a Penning trap is unique due to two types of circular motion. In chapter 6, I have presented the experimental demonstration of ground state cooling of the radial motional modes. In extension to those studies, the heating rate measurement is carried out for



(a) (b)

Figure 7.49: Heating rate measurements of the axial motion at 187 kHz axial frequency. In figure (a), spectra are shown after 0, 25ms and 50 ms of ground state cooling of the axial motion. In figure (b), the estimated mean phonon number as a function of the waiting time is shown. A linear fit is carried out of the data points giving rise to the heating rates of 2.5 ± 0.5 phonons/s.



(a) (b)

Figure 7.50: Heating rate measurement of the radial motional modes at 100 V trapping potential. In figure (a), the data points show $\langle n \rangle$ for the magnetron motion at 51 kHz. Similarly, figure (b) shows the heating rate of the modified cyclotron mode at 678 kHz.

the radial modes. The measurement is performed at 100 V trap potential which corresponds to 51 kHz and 678 kHz frequencies of the magnetron and modified cyclotron modes, respectively. After preparing the ion in the motional ground state, the mean phonon number is estimated after waiting times of 0, 1.5 and 3 ms. The estimated mean phonon numbers at these times are shown in figure 7.50. The linear fit of the experimental data implies a heating rate of 380 ± 100 phonons/s for the magnetron motion and 340 ± 40 phonons/s for the modified cyclotron motion.

The measured heating rates for the radial motional modes are found to be two orders of magnitude higher than that of the axial mode. One possible reason for the higher heating rates is due to the differential noise on the split ring electrodes. Axialisation requires a quadrupole field in the radial plane, which is produced by a circuit which provides four individual outputs at the required phases and amplitudes. We expect that the noise in the radial plane is higher because of this additional circuit, however, the same noise is not seen to affect the axial motion. In the current apparatus, a direct measurement of the differential noise at the trap electrodes is not possible due to the inaccessibility of the trap assembly. In future, a direct measurement of electrical noise at the ring segments can be performed to determine the reason for the higher heating rates.

7.8.4 Heating rates with a two-ion chain

The heating rate was also measured for the COM and breathing modes of two ions. In the Penning trap, a chain configuration is attained at a low trap potential (typically at 50 V). A measurement of the heating rate of a two-ion chain is performed at 162 kHz COM frequency and the results are shown in figure 7.51. The rate of change in mean phonon number is measured to be 15 ± 10 phonons/s. On the other hand, the breathing mode heating rate is measured to be 0.5 ± 0.4 phonons/s, which is consistent with the axial heating rate measurement of a single ion. In principle, the reason for different heating rates can be explained by the nature and response of the electric field noise in the trap. The COM mode is expected to respond to the symmetric electric field noise in the spatial extension of the ions, however the breathing mode responds to the asymmetric field noise. On the other hand, the trap frequency for the COM is smaller than the breathing mode. Assuming that the system has Johnson noise, we expect more heating of the COM mode than the breathing mode. We have also performed heating rate measurements for two ions in a planar configuration and found to be consistent with the single-ion axial heating rate measurements.

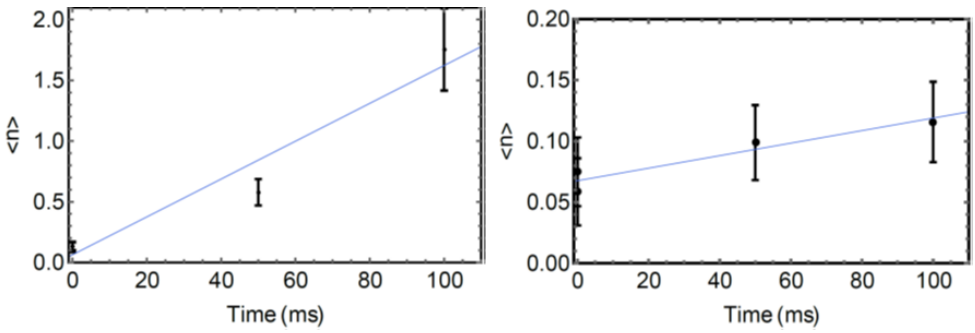


Figure 7.51: Heating rate measurement of COM and breathing modes at 162 kHz COM mode frequency.

7.9 Summary

In this chapter, I have shown studies related to coherent control of trapped ions in our trap. Coherent manipulation was performed on a calcium ion system using a narrow linewidth laser beam. The studies included Rabi oscillations and Ramsey interference measurements with a single ion. The optical coherence time is found to vary with the type of noise dominant for a particular type of experimental measurement. The measurements suggest the optical coherence time of the system is of the order of 1 ms. Coherence time of the system was further enhanced using the spin-echo and UDD techniques by an order of magnitude. The coherent control was demonstrated for multiple ions after preparing them in their vibrational ground states.

Coherent studies were also carried out for motional states of a trapped ion, revealing a high level of motional coherence. The results were supported by a low rate of heating in our system. Additionally, motional coherence was demonstrated for a sideband heated ion. The studies

showed distinct sources of decoherence, the first due to decoherence in electronic state and the second due to decoherence of the motional states. The motional coherence time is measured to be three orders of magnitude higher than that of the optical qubit.

Chapter 8

Conclusion

In this thesis, I have discussed experimental and theoretical studies of laser cooling in a Penning trap. The studies demonstrate coherent control of trapped ions within and outside the L-D regime. Previous studies of coherent control using trapped ions in other systems were performed within the L-D regime. Sideband cooling and coherent manipulation of the quantum states using a laser beam were demonstrated with a single calcium ion trapped in a Penning trap. The studies were also extended to a larger number of ions and the results have been presented in this thesis. The experimental control system has been discussed in previous theses [91, 98, 146]. Nevertheless, the experimental apparatus has been modified since then to make it suitable for sideband cooling of the radial modes and to perform coherent manipulation on trapped ions. Furthermore, a home built intensity noise eating system was installed, which provided better coherent control of the trapped ions. The appropriate modifications and new installations in the experimental apparatus have been presented in this thesis.

8.1 Summary of thesis achievements

This thesis has presented the simulation studies of resolved sideband cooling in a Penning trap. The cooling scheme has been devised by performing test simulations for a system outside the L-D regime for one and two ions. The studies were further used to carry out the experimental demonstration of resolved sideband cooling of the ions in our trap. In the presence of such a large magnetic field, the previous theory of resolved sideband cooling was not appropriate to fully understand the cooling dynamics. The requirement of a multistage cooling scheme has been discussed and appropriate cooling sequences were examined in order to predict the cooling performance in our system.

The experimental demonstration of ground state cooling of the axial mode of a single ion has been shown. A multistage sideband cooling sequence is employed to realise ground state cooling of a system where the population initially lay far outside the L-D regime. The studies have been extended for a two-ion chain, where ground state cooling of the axial modes was impossible

without performing sideband cooling on multiple sidebands. Cooling has been demonstrated for up to ten ions in a planar configuration. These studies are crucial to enabling high fidelity quantum simulations using multiple ions.

The first ever demonstration of ground state cooling of the radial motional modes has been presented in this thesis. Due to the complicated radial motion and negative energy magnetron modes in the system, cooling was difficult to attain. In this case, sideband cooling is performed using the blue sideband of the magnetron transition. However, the modified cyclotron mode was cooled through a conventional cooling way. In these studies, the system lay outside the L-D regime, hence a multi-stage cooling scheme was employed.

Additionally, for special cases, an adiabatic cooling technique is employed for the axial motion. These experimental studies were used in performing coherent control for a system beyond the L-D regime. Such studies have not been performed before to our knowledge. A special state of high phonon number is prepared through a sideband heating technique. In this instance, the system is prepared far beyond the L-D regime via sideband heating on a first blue and second blue sidebands of the transition.

Finally, this thesis has demonstrated coherent control of trapped ions in a Penning trap. The enhancements of the optical coherence time of a single ion qubit in a Penning trap was observed by employing the spin-echo and UDD techniques. Furthermore, the motional superposition of a ground state cooled ion in a Penning trap has been presented, indicating a high level of quantum coherence in our system. Additionally, interesting quantum control was demonstrated by superimposing electronic and motional quantum states together with a trapped calcium ion. This particular study was performed in a high phonon state, which was realised through a sideband heating technique. The superposition of three low lying Fock states was demonstrated, analogous to the three slit interference of photons. The interference pattern was only feasible due to a great level of coherent control in our system. Additionally, I have presented experimental studies of coherent and squeezed states of motion. The coherent studies between motional states are consistent with the heating rate measurements in our system.

In summary, in this thesis, I have presented the experimental studies of sideband cooling and coherent control with trapped ions in a Penning trap. The studies indicate a remarkable level of coherent control in our system. These were the first ever studies in a Penning trap. The coherent studies also have been performed beyond the L-D regime. The overall idea of these studies was to demonstrate coherent studies in a Penning trap and show their usability in quantum computation and quantum simulations. The experimental results were reasonably competitive with the other groups in ion trapping community. All the experimental demonstrations were performed in three years of my PhD. To start with, sideband cooling of a single ion along the axial direction, both within and outside the L-D regime, was performed in the first year of my PhD. Then after coherent control between internal states of a ground state cooled ion was demonstrated and the coherence time of an optical qubit in a Penning trap was measured. Later the studies were extended to a small ICC initially up to two ions and later extended to ten ions. In the second year, we performed studies of a motional coherence time in our system and

verified a high level of motional coherence in our trapping system. Sideband heating of an ion and radial cooling is performed in the final year of my PhD.

8.2 Applications

The key studies of sideband cooling of small ICC's in a Penning trap have potential applications for of studying quantum effects in ICC's. Quantum simulation has been performed with Doppler cooled ions in Penning traps, however, sideband cooling of ions will improve the simulation performance. Furthermore, the low heating rates of planar two-ion crystals indicate a high level of isolation between motional modes. Interestingly, the ions in a two-ion planar crystal rotate at a few tens of m/s about the magnetic field axis, which in addition to ground state cooling and low heating rates indicate near perfect isolation between the normal modes of motion. The sideband cooling of the planar crystal has potential application in QEC and QI based studies in a Penning trap [10].

The theoretical and simulation studies of sideband cooling outside the L-D regime can be used to obtain efficient ground state cooling of trapped ions and the studies are applicable to any other similar type of apparatus. The Penning trap is best used in confining non-neutral plasma and in precision studies with highly charged ions. In many cases, the direct cooling of highly charged ions or elementary particles such as protons and antiprotons is not possible. In those cases, cooling of some other ion is used to sympathetically cool the ion of interest. The current studies of laser cooling have potential applications in utilising such tools to minimise uncertainties in high precision measurements [147].

8.3 Outlook

The efficiency of sideband cooling of the radial motion will be further enhanced if cooling is performed on the $S_{1/2,-1/2} \leftrightarrow D_{5/2,-5/2}$ transition. This forms a closed cycle for sideband cooling and the population decay to a $S_{1/2,1/2}$ will drastically reduce due to selection rules. A back-of-the-envelope calculation suggests that approximately 99% of the population will directly come to the desired ground electronic state ($m_j = -1/2$). Previously, for the cooling transition used in our system, approximately 33% percent of the population was repumped by one of the two 397-nm laser beams. The relevant energy diagram is shown in figure 8.1. On the other hand, this transition cannot be coupled through a laser beam along the trap axis, hence cooling of the axial motional modes will not work through this transition.

The key results of this thesis are motional coherence studies. Some of the studies discussed in this thesis were possible because of a large L-D parameter. The demonstration of a three-state superposition was possible with a second order red sideband, which is not observed if the system is within the L-D regime. The experimental results showed superposition effects of the ω_z and $2\omega_z$ frequency components, confirming the coherence between three motional states.

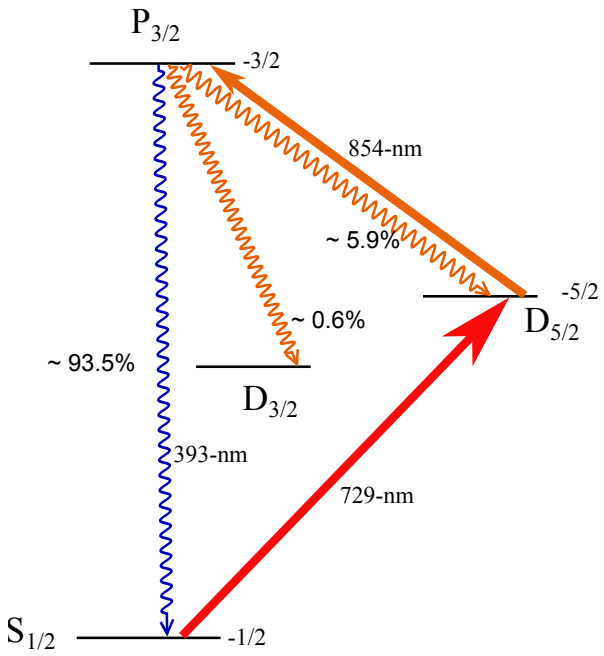


Figure 8.1: An alternative sideband cooling transition for the radial motional modes. This transition will reduce heating due to the 397-nm repumping laser which is essential to prepare the ion in the $m_j = -1/2$ sublevel of the ground electronic state. This cooling transition will be helpful in getting more efficient cooling of the radial motion.

However, these studies can be further extended to observe any multipath quantum coherence through the moments method as discussed in reference [148] and new physical implications can be tested [142]. The results discussed in this thesis are unique and a phenomenological model of motional coherence time can be formulated by performing detailed studies in this direction. Additionally, coherent studies at high n states can be used to test quantum computation outside the L-D regime. A proposal of quantum computation outside the L-D regime in an RF trap using optimal control theory has been presented collectively by Richard Thompson and Florian Mintert from our group. The plan in their proposal is to perform quantum computation of trapped ions in such a regime and devise a protocol to suppress any unwanted effects by utilising optimal control of laser pulses [149, 150].

Bibliography

[1] P. Benioff. Quantum Mechanical Models of Turing Machines That Dissipate No Energy. *Physical Review Letters*, 48(23):1581–1585, jun 1982. URL: https://link.aps.org/doi/10.1103/PhysRevLett.48.1581.

[2] R. P. Feynman. Simulating physics with computers. *International Journal of Theoretical Physics*, 21(6-7):467–488, jun 1982. URL: http://link.springer.com/10.1007/BF02650179.

[3] P. W. Shor. Polynomial-Time Algorithms for Prime Factorization and Discrete Logarithms on a Quantum Computer. *SIAM Journal on Computing*, 26(5):1484–1509, oct 1997. URL: http://epubs.siam.org/doi/10.1137/S0097539795293172.

[4] C. Bennett and P. Shor. Quantum information theory. *IEEE Transactions on Information Theory*, 44(6):2724–2742, 1998. URL: http://ieeexplore.ieee.org/document/720553/.

[5] T. D. Ladd, F. Jelezko, R. Laflamme, Y. Nakamura, C. Monroe, and J. L. O'Brien. Quantum computers. *Nature*, 464(7285):45–53, 2010. URL: http://dx.doi.org/10.1038/nature08812.

[6] M. H. Devoret and R. J. Schoelkopf. Superconducting Circuits for Quantum Information: An Outlook. *Science*, 339(6124):1169–1174, mar 2013. URL: http://www.sciencemag.org/cgi/doi/10.1126/science.1231930.

[7] P. Schindler, D. Nigg, T. Monz, J. T. Barreiro, E. Martinez, S. X. Wang, S. Quint, M. F. Brandl, V. Nebendahl, C. F. Roos, M. Chwalla, M. Hennrich, and R. Blatt. A quantum information processor with trapped ions. *New Journal of Physics*, 15(12):123012, dec 2013. URL: http://stacks.iop.org/1367-2630/15/i=12/a=123012?key=crossref.cde36010c3c4d16e566cc4e802de2091.

[8] E. Knill and R. Laflamme. Theory of quantum error-correcting codes. *Physical Review A*, 55(2):900–911, feb 1997. URL: https://link.aps.org/doi/10.1103/PhysRevA.55.900.

[9] P. W. Shor. Scheme for reducing decoherence in quantum computer memory. *Physical Review A*, 52(4):R2493–R2496, oct 1995. URL: https://link.aps.org/doi/10.1103/PhysRevA.52.R2493.

[10] J. F. Goodwin, B. J. Brown, G. Stutter, H. Dale, R. C. Thompson, and T. Rudolph. Trapped-ion quantum error-correcting protocols using only global operations. *Physical Review A*, 92(3):032314, sep 2015. URL: https://link.aps.org/doi/10.1103/PhysRevA.92.032314.

[11] D. G. Cory, M. D. Price, W. Maas, E. Knill, R. Laflamme, W. H. Zurek, T. F. Havel, and S. S. Somaroo. Experimental Quantum Error Correction. *Physical Review Letters*, 81(10):2152–2155, sep 1998. URL: https://link.aps.org/doi/10.1103/PhysRevLett.81.2152.

[12] E. Knill. Quantum computing with realistically noisy devices. *Nature*, 434(7029):39–44, mar 2005. URL: http://www.nature.com/doifinder/10.1038/nature03350.

[13] P. Schindler, J. T. Barreiro, T. Monz, V. Nebendahl, D. Nigg, M. Chwalla, M. Hennrich, and R. Blatt. Experimental Repetitive Quantum Error Correction. *Science*, 332(6033):1059–1061, may 2011. URL: http://www.sciencemag.org/cgi/doi/10.1126/science.1203329.

[14] M. D. Reed, L. Dicarlo, S. E. Nigg, L. Sun, L. Frunzio, S. M. Girvin, and R. J. Schoelkopf. Realization of three-qubit quantum error correction with superconducting circuits. *Nature*, 482(7385):382–385, 2012. URL: http://dx.doi.org/10.1038/nature10786.

[15] K. R. Brown, J. Kim, and C. Monroe. Co-designing a scalable quantum computer with trapped atomic ions. *npj Quantum Information*, 2(1):16034, nov 2016. URL: http://www.nature.com/articles/npjqi201634.

[16] J. I. Cirac and P. Zoller. A scalable quantum computer with ions in an array of microtraps. *Nature*, 404(6778):579–581, apr 2000. URL: http://www.nature.com/articles/35007021.

[17] B. Lekitsch, S. Weidt, A. G. Fowler, K. Mølmer, S. J. Devitt, C. Wunderlich, and W. K. Hensinger. Blueprint for a microwave trapped ion quantum computer. *Science Advances*, 3(2):e1601540, feb 2017. URL: http://advances.sciencemag.org/lookup/doi/10.1126/sciadv.1601540.

[18] D. Kielpinski, C. Monroe, and D. J. Wineland. Architecture for a large-scale ion-trap quantum computer. *Nature*, 417(6890):709–711, jun 2002. URL: http://www.nature.com/articles/nature00784.

[19] R. Blatt and C. F. Roos. Quantum simulations with trapped ions. *Nat. Phys.*, 8(4):277–284, 2012. URL: http://dx.doi.org/10.1038/nphys2252.

[20] H. Häffner, C. F. Roos, and R. Blatt. Quantum computing with trapped ions. *Physics Reports*, 469(4):155–203, 2008. URL: http://dx.doi.org/10.1016/j.physrep.2008.09.003.

[21] A. M. Steane. The Ion Trap Quantum Information Processor. *Applied Physics B*, 64:623–642, 1997. URL: http://arxiv.org/abs/quant-ph/9608011.

[22] T. P. Harty, D. T. C. Allcock, C. J. Ballance, L. Guidoni, H. A. Janacek, N. M. Linke, D. N. Stacey, and D. M. Lucas. High-Fidelity Preparation, Gates, Memory, and Readout of a Trapped-Ion Quantum Bit. *Physical Review Letters*, 113(22):220501, nov 2014. URL: https://link.aps.org/doi/10.1103/PhysRevLett.113.220501.

[23] R. C. Thompson. Ion Coulomb crystals. *Contemporary Physics*, 56(1):1–17, jan 2015. URL: http://dx.doi.org/10.1080/00107514.2014.989715.

[24] J. W. Britton, B. C. Sawyer, A. C. Keith, C.-C. J. Wang, J. K. Freericks, H. Uys, M. J. Biercuk, and J. J. Bollinger. Engineered two-dimensional Ising interactions in a trapped-ion quantum simulator with hundreds of spins. *Nature*, 484(7395):489–492, apr 2012. URL: http://www.nature.com/doifinder/10.1038/nature10981.

[25] K. Kim, M.-S. Chang, S. Korenblit, R. Islam, E. E. Edwards, J. K. Freericks, G.-D. Lin, L.-M. Duan, and C. Monroe. Quantum simulation of frustrated Ising spins with trapped ions. *Nature*, 465(7298):590–593, jun 2010. URL: http://www.nature.com/articles/nature09071.

[26] N. F. Ramsey. Experiments with Separated Oscillatory Fields and Hydrogen Masers(Nobel Lecture). *Angewandte Chemie International Edition in English*, 29(7):725–733, jul 1990. URL: http://doi.wiley.com/10.1002/anie.199007251.

[27] M. Knoop, N. Madsen, and R. C. Thompson. Chapter 1: Physics with Trapped Charged Particles. *Physics with Trapped Charged Particles*, pages 1–24, mar 2014. URL: http://www.worldscientific.com/doi/abs/10.1142/9781783264063_0001.

[28] C. Champenois, M. Marciante, J. Pedregosa-Gutierrez, M. Houssin, M. Knoop, and M. Kajita. Ion ring in a linear multipole trap for optical frequency metrology. *Physical Review A*, 81(4):043410, apr 2010. URL: https://link.aps.org/doi/10.1103/PhysRevA.81.043410.

[29] F. Schmidt-Kaler, H. Häffner, S. Gulde, M. Riebe, G. Lancaster, T. Deuschle, C. Becher, W. Hänsel, J. Eschner, C. Roos, and R. Blatt. How to realize a universal quantum gate with trapped ions. *Applied Physics B*, 77(8):789–796, dec 2003. URL: http://link.springer.com/10.1007/s00340-003-1346-9.

[30] J. Pedregosa, C. Champenois, M. Houssin, and M. Knoop. Anharmonic contributions in real RF linear quadrupole traps. *International Journal of Mass Spectrometry*, 290(2-3):100–105, 2010. URL: http://dx.doi.org/10.1016/j.ijms.2009.12.009.

[31] J. J. Bollinger, D. J. Wineland, and D. H. E. Dubin. Non-neutral ion plasmas and crystals, laser cooling, and atomic clocks. *Physics of Plasmas*, 1(5):1403–1414, may 1994. URL: http://aip.scitation.org/doi/10.1063/1.870690.

[32] S. Mavadia, J. F. Goodwin, G. Stutter, S. Bharadia, D. R. Crick, D. M. Segal, and R. C. Thompson. Control of the conformations of ion Coulomb crystals in a Penning trap. *Nature Communications*, 4:2571, oct 2013. URL: http://www.nature.com/doifinder/10.1038/ncomms3571.

[33] M. Charlton, S. Jonsell, L. V. Jørgensen, N. Madsen, and D. P. van der Werf. Antihydrogen for precision tests in physics. *Contemporary Physics*, 49(1):29–41, jan 2008. URL: http://www.tandfonline.com/doi/abs/10.1080/00107510802038448.

[34] T. Hänsch and A. Schawlow. Cooling of gases by laser radiation. *Optics Communications*, 13(1):68–69, jan 1975. URL: http://linkinghub.elsevier.com/retrieve/pii/0030401875901595.

[35] D. J. Wineland and H. G. Dehmelt. Proposed $10^{14}\Delta\nu < \nu$ laser fluorescence spectroscopy on Tl^{+} mono-ion oscillator. *Bulletin of the American Physical Society*, 20:637, 1975.

[36] W. Neuhauser, M. Hohenstatt, P. Toschek, and H. Dehmelt. Optical-Sideband Cooling of Visible Atom Cloud Confined in Parabolic Well. *Physical Review Letters*, 41(4):233–236, jul 1978. URL: https://link.aps.org/doi/10.1103/PhysRevLett.41.233.

[37] D. J. Wineland, R. E. Drullinger, and F. L. Walls. Radiation-Pressure Cooling of Bound Resonant Absorbers. *Physical Review Letters*, 40(25):1639–1642, jun 1978. URL: https://link.aps.org/doi/10.1103/PhysRevLett.40.1639.

[38] F. Diedrich, E. Peik, J. M. Chen, W. Quint, and H. Walther. Observation of a Phase Transition of Stored Laser-Cooled Ions. *Physical Review Letters*, 59(26):2931–2934, dec 1987. URL: https://link.aps.org/doi/10.1103/PhysRevLett.59.2931.

[39] W. D. Phillips. Nobel Lecture: Laser cooling and trapping of neutral atoms. *Reviews of Modern Physics*, 70(3):721–741, jul 1998. URL: https://link.aps.org/doi/10.1103/RevModPhys.70.721.

[40] W. M. Itano and D. J. Wineland. Laser cooling of ions stored in harmonic and Penning traps. *Physical Review A*, 25(1):35–54, jan 1982. URL: https://link.aps.org/doi/10.1103/PhysRevA.25.35.

[41] F. Diedrich, J. C. Bergquist, W. M. Itano, and D. J. Wineland. Laser Cooling to the Zero-Point Energy of Motion. *Physical Review Letters*, 62(4):403–406, jan 1989. URL: https://link.aps.org/doi/10.1103/PhysRevLett.62.403.

[42] C. F. Roos, D. Leibfried, A. Mundt, F. Schmidt-Kaler, J. Eschner, and R. Blatt. Experimental Demonstration of Ground State Laser Cooling with Electromagnetically Induced Transparency. *Physical Review Letters*, 85(26):5547–5550, dec 2000. URL: https://link.aps.org/doi/10.1103/PhysRevLett.85.5547.

[43] J. Eschner, G. Morigi, F. Schmidt-Kaler, and R. Blatt. Laser cooling of trapped ions. *Journal of the Optical Society of America B*, 20(5):1003, may 2003. URL: https://www.osapublishing.org/abstract.cfm?URI=josab-20-5-1003.

[44] C. Monroe, D. M. Meekhof, B. E. King, S. R. Jefferts, W. M. Itano, D. J. Wineland, and P. Gould. Resolved-Sideband Raman Cooling of a Bound Atom to the 3D Zero-Point Energy. *Physical Review Letters*, 75(22):4011–4014, nov 1995. URL: https://link.aps.org/doi/10.1103/PhysRevLett.75.4011.

[45] J. F. Goodwin, G. Stutter, R. C. Thompson, and D. M. Segal. Resolved-Sideband Laser Cooling in a Penning Trap. *Physical Review Letters*, 116(14):143002, apr 2016. URL: https://link.aps.org/doi/10.1103/PhysRevLett.116.143002.

[46] R. Lechner, C. Maier, C. Hempel, P. Jurcevic, B. P. Lanyon, T. Monz, M. Brownnutt, R. Blatt, and C. F. Roos. Electromagnetically-induced-transparency ground-state cooling of long ion strings. *Physical Review A*, 93(5):053401, may 2016. URL: https://link.aps.org/doi/10.1103/PhysRevA.93.053401.

[47] J. I. Cirac and P. Zoller. Quantum Computations with Cold Trapped Ions. *Physical Review Letters*, 74(20):4091–4094, may 1995. URL: https://link.aps.org/doi/10.1103/PhysRevLett.74.4091.

[48] A. Sørensen and K. Mølmer. Quantum Computation with Ions in Thermal Motion. *Physical Review Letters*, 82(9):1971–1974, mar 1999. URL: https://link.aps.org/doi/10.1103/PhysRevLett.82.1971.

[49] G. Kirchmair, J. Benhelm, F. Zähringer, R. Gerritsma, C. F. Roos, and R. Blatt. Deterministic entanglement of ions in thermal states of motion. *New Journal of Physics*, 11(2): 023002, feb 2009. URL: http://stacks.iop.org/1367-2630/11/i=2/a=023002?key=crossref.be3fc247c634554dc69f59ebce95a834.

[50] C. Monroe, D. M. Meekhof, B. E. King, W. M. Itano, and D. J. Wineland. Demonstration of a Fundamental Quantum Logic Gate. *Physical Review Letters*, 75(25):4714–4717, dec 1995. URL: https://link.aps.org/doi/10.1103/PhysRevLett.75.4714.

[51] F. Schmidt-Kaler, H. Häffner, M. Riebe, S. Gulde, G. P. T. Lancaster, T. Deuschle, C. Becher, C. F. Roos, J. Eschner, and R. Blatt. Realization of the Cirac–Zoller controlled-NOT quantum gate. *Nature*, 422(6930):408–411, mar 2003. URL: http://www.nature.com/articles/nature01494.

[52] C. A. Sackett, D. Kielpinski, B. E. King, C. Langer, V. Meyer, C. J. Myatt, M. Rowe, Q. A. Turchette, W. M. Itano, D. J. Wineland, and C. Monroe. Experimental entanglement of four particles. *Nature*, 404(6775):256–259, mar 2000. URL: http://www.nature.com/articles/35005011.

[53] G. Milburn, S. Schneider, and D. James. Ion Trap Quantum Computing with Warm Ions. *Fortschritte der Physik*, 48(9-11):801–810, sep 2000. URL: http://onlinelibrary.wiley.com/doi/10.1002/1521-3978(200009)48:9/11%3C801::AID-PROP801%3E3.0.CO;2-1/abstract.

[54] D. Leibfried, B. DeMarco, V. Meyer, D. Lucas, M. Barrett, J. Britton, W. M. Itano, B. Jelenković, C. Langer, T. Rosenband, and D. J. Wineland. Experimental demonstration of a robust, high-fidelity geometric two ion-qubit phase gate. *Nature*, 422(6930):412–415, mar 2003. URL: http://www.nature.com/articles/nature01492.

[55] D. M. Meekhof, C. Monroe, B. E. King, W. M. Itano, and D. J. Wineland. Generation of Nonclassical Motional States of a Trapped Atom. *Physical Review Letters*, 76(11):1796–1799, mar 1996. URL: https://link.aps.org/doi/10.1103/PhysRevLett.76.1796.

[56] R. J. Glauber. Coherent and Incoherent States of the Radiation Field. *Physical Review*, 131 (6):2766–2788, sep 1963. URL: https://link.aps.org/doi/10.1103/PhysRev.131.2766.

[57] J. Alonso, F. M. Leupold, Z. U. Solèr, M. Fadel, M. Marinelli, B. C. Keitch, V. Negnevitsky, and J. P. Home. Generation of large coherent states by bang–bang control of a trapped-ion oscillator. *Nature Communications*, 7:11243, apr 2016. URL: http://www.nature.com/doifinder/10.1038/ncomms11243.

[58] C. Monroe, D. M. Meekhof, B. E. King, and D. J. Wineland. A "Schrodinger Cat" Superposition State of an Atom. *Science*, 272(5265):1131–1136, may 1996. URL: http://www.sciencemag.org/cgi/doi/10.1126/science.272.5265.1131.

[59] P. Jurcevic, B. P. Lanyon, P. Hauke, C. Hempel, P. Zoller, R. Blatt, and C. F. Roos. Quasiparticle engineering and entanglement propagation in a quantum many-body system. *Nature*, 511(7508):202–205, jul 2014. URL: http://www.nature.com/articles/nature13461.

[60] I. Buluta and F. Nori. Quantum Simulators. *Science*, 326(5949):108–111, oct 2009. URL: http://www.sciencemag.org/cgi/doi/10.1126/science.1177838.

[61] E. A. Martinez, C. A. Muschik, P. Schindler, D. Nigg, A. Erhard, M. Heyl, P. Hauke, M. Dalmonte, T. Monz, P. Zoller, and R. Blatt. Real-time dynamics of lattice gauge theories with a few-qubit quantum computer. *Nature*, 534(7608):516–519, jun 2016. URL: http://www.nature.com/articles/nature18318.

[62] C. Muschik, M. Heyl, E. Martinez, T. Monz, P. Schindler, B. Vogell, M. Dalmonte, P. Hauke, R. Blatt, and P. Zoller. U(1) Wilson lattice gauge theories in digital quantum simulators. *New Journal of Physics*, 19(10):103020, oct 2017. URL: http://stacks.iop.org/1367-2630/19/i=10/a=103020?key=crossref.fc0b12f01b2bc17282de90c5f55183a7.

[63] D. Wineland, C. Monroe, W. Itano, D. Leibfried, B. King, and D. Meekhof. Experimental issues in coherent quantum-state manipulation of trapped atomic ions. *Journal of Research of the National Institute of Standards and Technology*, 103(3):259, may 1998. URL: http://nvlpubs.nist.gov/nistpubs/jres/103/3/j33win.pdf.

[64] Y. Wang, M. Um, J. Zhang, S. An, M. Lyu, J.-N. Zhang, L.-M. Duan, D. Yum, and K. Kim. Single-qubit quantum memory exceeding ten-minute coherence time. *Nature Photonics*, 11(10):646–650, oct 2017. URL: http://www.nature.com/articles/s41566-017-0007-1.

[65] C. J. Myatt, B. E. King, Q. A. Turchette, C. A. Sackett, D. Kielpinski, W. M. Itano, C. Monroe, and D. J. Wineland. Decoherence of quantum superpositions through cou-

pling to engineered reservoirs. *Nature*, 403(6767):269–273, jan 2000. URL: http://www.nature.com/doifinder/10.1038/35002001.

[66] M. Brownnutt, M. Kumph, P. Rabl, and R. Blatt. Ion-trap measurements of electric-field noise near surfaces. *Reviews of Modern Physics*, 87(4):1419–1482, dec 2015. URL: https://link.aps.org/doi/10.1103/RevModPhys.87.1419.

[67] G. Poulsen, Y. Miroshnychenko, and M. Drewsen. Efficient ground-state cooling of an ion in a large room-temperature linear Paul trap with a sub-Hertz heating rate. *Physical Review A*, 86(5):051402, nov 2012. URL: https://link.aps.org/doi/10.1103/PhysRevA.86.051402.

[68] M. Bohman, A. Mooser, G. Schneider, N. Schön, M. Wiesinger, J. Harrington, T. Higuchi, H. Nagahama, C. Smorra, S. Sellner, K. Blaum, Y. Matsuda, W. Quint, J. Walz, and S. Ulmer. Sympathetic cooling of protons and antiprotons with a common endcap Penning trap. *Journal of Modern Optics*, 65(5-6):568–576, mar 2018. URL: https://www.tandfonline.com/doi/full/10.1080/09500340.2017.1404656.

[69] J. G. Bohnet, B. C. Sawyer, J. W. Britton, M. L. Wall, A. M. Rey, M. Foss-Feig, and J. J. Bollinger. Quantum spin dynamics and entanglement generation with hundreds of trapped ions. *Science*, 352(6291):1297–1301, jun 2016. URL: http://www.sciencemag.org/cgi/doi/10.1126/science.aad9958.

[70] G. Stutter, P. Hrmo, V. Jarlaud, M. K. Joshi, J. F. Goodwin, and R. C. Thompson. Sideband cooling of small ion Coulomb crystals in a Penning trap. *Journal of Modern Optics*, 65(1):64–74, jan 2018. URL: https://arxiv.org/pdf/1705.08518.pdfhttps://www.tandfonline.com/doi/full/10.1080/09500340.2017.1376719.

[71] S. Earnshaw. On the Nature of the Molecular Forces which Regulate the Constitution of the Luminiferous Ether, 1842. URL: http://www.mit.edu/~kardar/research/seminars/Casimir2010/pdf/EarnshawPaper.pdf.

[72] W. Paul. Electromagnetic traps for charged and neutral particles. *Reviews of Modern Physics*, 62(3):531–540, jul 1990. URL: https://link.aps.org/doi/10.1103/RevModPhys.62.531.

[73] G. Werth, V. N. Gheorghe, and F. G. Major. *Charged Particle Traps*, volume 37 of *Springer Series on Atomic, Optical, and Plasma Physics*. Springer-Verlag, Berlin/Heidelberg, 2005. ISBN 3-540-22043-7. URL: http://link.springer.com/10.1007/b137836.

[74] D. James. Quantum dynamics of cold trapped ions with application to quantum computation. *Applied Physics B: Lasers and Optics*, 66(2):181–190, feb 1998. URL: http://link.springer.com/10.1007/s003400050373.

[75] C.-C. J. Wang, A. C. Keith, and J. K. Freericks. Phonon-mediated quantum spin simulator employing a planar ionic crystal in a Penning trap. *Physical Review A*, 87(1):013422, jan 2013. URL: https://link.aps.org/doi/10.1103/PhysRevA.87.013422.

[76] C. Cohen-Tannoudji, B. Diu, and F. Laloe. *Quantum Mechanics - Vol I*. 2006. ISBN 0471569526. URL: http://scholar.google.com/scholar?hl=en&btnG=Search&q=intitle:Quantum+mechanics,+vol.1#3.

[77] F. Crimin, B. M. Garraway, and J. Verdú. The quantum theory of the Penning trap. *Journal of Modern Optics*, 65(4):427–440, feb 2018. URL: https://www.tandfonline.com/doi/full/10.1080/09500340.2017.1393570.

[78] D. Leibfried, D. M. Meekhof, C. Monroe, B. E. King, W. M. Itano, and D. J. Wineland. Experimental preparation and measurement of quantum states of motion of a trapped atom. *Journal of Modern Optics*, 44(11-12):2485–2505, nov 1997. URL: http://journalsonline.tandf.co.uk/Index/10.1080/095003497152627.

[79] D. Leibfried, R. Blatt, C. Monroe, and D. Wineland. Quantum dynamics of single trapped ions. *Reviews of Modern Physics*, 75(1):281–324, mar 2003. URL: https://link.aps.org/doi/10.1103/RevModPhys.75.281.

[80] B. W. Shore and P. R. Berman. Theory of Coherent Atomic Excitation. *Physics Today*, 44(12):71–72, dec 1991. URL: http://physicstoday.scitation.org/doi/10.1063/1.2810362.

[81] H. Häffner, S. Gulde, M. Riebe, G. Lancaster, C. Becher, J. Eschner, F. Schmidt-Kaler, and R. Blatt. Precision Measurement and Compensation of Optical Stark Shifts for an Ion-Trap Quantum Processor. *Physical Review Letters*, 90(14):143602, apr 2003. URL: https://link.aps.org/doi/10.1103/PhysRevLett.90.143602.

[82] S. H. Autler and C. H. Townes. Stark Effect in Rapidly Varying Fields. *Physical Review*, 100 (2):703–722, oct 1955. URL: https://link.aps.org/doi/10.1103/PhysRev.100.703.

[83] G. Morigi, J. Eschner, J. I. Cirac, and P. Zoller. Laser cooling of two trapped ions: Sideband cooling beyond the Lamb-Dicke limit. *Physical Review A*, 59(5):3797–3808, may 1999. URL: https://link.aps.org/doi/10.1103/PhysRevA.59.3797.

[84] D. J. Wineland and W. M. Itano. Laser cooling of atoms. *Physical Review A*, 20(4):1521–1540, oct 1979. URL: https://link.aps.org/doi/10.1103/PhysRevA.20.1521.

[85] G. Savard, S. Becker, G. Bollen, H.-J. Kluge, R. Moore, T. Otto, L. Schweikhard, H. Stolzenberg, and U. Wiess. A new cooling technique for heavy ions in a Penning trap. *Physics Letters A*, 158(5):247–252, sep 1991. URL: http://linkinghub.elsevier.com/retrieve/pii/0375960191910082.

[86] C. Lichtenberg, G. Marx, G. Tommaseo, P. Ghosh, and G. Werth. Axialisation, cooling and quenching of Ba+ ions in a Penning trap. *The European Physical Journal D - Atomic, Molecular and Optical Physics*, 2(1):29–32, may 1998. URL: http://www.springerlink.com/openurl.asp?genre=article&id=doi:10.1007/s100530050106.

[87] R. J. Hendricks, E. S. Phillips, D. M. Segal, and R. C. Thompson. Laser cooling in the Penning trap: an analytical model for cooling rates in the presence of an axializing field. *Journal of Physics B: Atomic, Molecular and Optical Physics*, 41(3):035301,

feb 2008. URL: http://stacks.iop.org/0953-4075/41/i=3/a=035301?key=crossref.c106fe5f4b125266be487e74e02094f1.

[88] D. J. Wineland, J. Dalibard, and C. Cohen-Tannoudji. Sisyphus cooling of a bound atom. *Journal of the Optical Society of America B*, 9(1):32, 1992. URL: https://www.osapublishing.org/abstract.cfm?URI=josab-9-1-32.

[89] H. J. Metcalf and P. van der Straten. *Laser Cooling and Trapping*. Graduate Texts in Contemporary Physics. Springer New York, New York, NY, 1999. ISBN 978-0-387-98728-6. URL: http://link.springer.com/10.1007/978-1-4612-1470-0.

[90] G. Morigi, J. Eschner, and C. H. Keitel. Ground State Laser Cooling Using Electromagnetically Induced Transparency. *Physical Review Letters*, 85(21):4458–4461, nov 2000. URL: https://link.aps.org/doi/10.1103/PhysRevLett.85.4458.

[91] J. F. Goodwin. *Sideband Cooling to the Quantum Ground State in a Penning Trap*. PhD thesis, Imperial College London, 2015. URL: https://spiral.imperial.ac.uk/handle/10044/1/27249.

[92] G. Morigi, J. I. Cirac, M. Lewenstein, and P. Zoller. Ground-state laser cooling beyond the Lamb-Dicke limit. *Europhysics Letters (EPL)*, 39(1):13–18, jul 1997. URL: http://stacks.iop.org/0295-5075/39/i=1/a=013?key=crossref.a9594d8392bb5738db8657171ae19c40.

[93] D. R. Crick. *Manipulation of Ca^+ Ions in Penning Traps*. PhD thesis, Imperial College London, 2009. URL: https://spiral.imperial.ac.uk/handle/10044/1/5467.

[94] J. J. Sakurai. *Modern Quantum Mechanics Revised Edition*. jan 1995.

[95] D. R. Crick, S. Donnellan, D. M. Segal, and R. C. Thompson. Magnetically induced electron shelving in a trapped Ca^+ ion. *Physical Review A*, 81(5):052503, may 2010. URL: https://link.aps.org/doi/10.1103/PhysRevA.81.052503.

[96] C. Cohen-Tannoudji, B. Diu, and F. Laloe. *Quantum Mechanics, Vol. II*. 1973.

[97] Wolfram. Wolfram ThreeJSymbol. URL: http://reference.wolfram.com/language/ref/ThreeJSymbol.html.

[98] G. Stutter. *Quantum dynamics of small numbers of ions in a Penning trap*. PhD thesis, Imperial College London, 2015. URL: https://spiral.imperial.ac.uk/handle/10044/1/31473.

[99] S. Bharadia. *Towards Laser Spetroscopy of Highly Charged Ions: Dynamics of $^{40}Ca^+$ Ions in a Penning Trap*. PhD thesis, Imperial College London, 2011. URL: https://spiral.imperial.ac.uk/handle/10044/1/9138.

[100] L. S. Brown and G. Gabrielse. Geonium theory: Physics of a single electron or ion in a Penning trap. *Reviews of Modern Physics*, 58(1):233–311, jan 1986. URL: https://link.aps.org/doi/10.1103/RevModPhys.58.233.

[101] K. Blaum, Y. N. Novikov, and G. Werth. Penning traps as a versatile tool for precise experiments in fundamental physics. *Contemporary Physics*, 51(2):149–175, mar 2010. URL: http://www.tandfonline.com/doi/abs/10.1080/00107510903387652.

[102] S. Narayanan, N. Daniilidis, S. A. Möller, R. Clark, F. Ziesel, K. Singer, F. Schmidt-Kaler, and H. Häffner. Electric field compensation and sensing with a single ion in a planar trap. *Journal of Applied Physics*, 110(11):114909, dec 2011. URL: http://aip.scitation.org/doi/10.1063/1.3665647.

[103] M. J. Biercuk, H. Uys, J. W. Britton, A. P. VanDevender, and J. J. Bollinger. Ultrasensitive detection of force and displacement using trapped ions. *Nature Nanotechnology*, 5(9): 646–650, sep 2010. URL: http://www.nature.com/articles/nnano.2010.165.

[104] C. J. Hawthorn, K. P. Weber, and R. E. Scholten. Littrow configuration tunable external cavity diode laser with fixed direction output beam. *Review of Scientific Instruments*, 72(12):4477–4479, dec 2001. URL: http://aip.scitation.org/doi/10.1063/1.1419217.

[105] S. D. Saliba, M. Junker, L. D. Turner, and R. E. Scholten. Mode stability of external cavity diode lasers. *Applied optics*, 48(35):6692–700, 2009. URL: http://www.osapublishing.org/viewmedia.cfm?uri=ao-48-35-6692&seq=0&html=true.

[106] H. Talvitie, A. Pietiläinen, H. Ludvigsen, and E. Ikonen. Passive frequency and intensity stabilization of extended-cavity diode lasers. *Review of Scientific Instruments*, 68(1):1–7, jan 1997. URL: http://aip.scitation.org/doi/10.1063/1.1147810.

[107] P. A. Barton, C. J. S. Donald, D. M. Lucas, D. A. Stevens, A. M. Steane, and D. N. Stacey. Measurement of the lifetime of the $3d^2 2D_{5/2}$ state in $^{40}Ca^+$. *Physical Review A*, 62(3): 032503, aug 2000. URL: https://link.aps.org/doi/10.1103/PhysRevA.62.032503.

[108] E. D. Black. An introduction to Pound–Drever–Hall laser frequency stabilization. *American Journal of Physics*, 69(1):79–87, jan 2001. URL: http://aapt.scitation.org/doi/10.1119/1.1286663.

[109] T. Okoshi, K. Kikuchi, and A. Nakayama. Novel method for high resolution measurement of laser output spectrum. *Electronics Letters*, 16(16):630, 1980. URL: http://digital-library.theiet.org/content/journals/10.1049/el_19800437.

[110] J. Liu. *Configurations of Ion Coulomb Crystals in a Penning Trap*. PhD thesis, Imperial College London, 2014.

[111] C. Ospelkaus, U. Warring, Y. Colombe, K. R. Brown, J. M. Amini, D. Leibfried, and D. J. Wineland. Microwave quantum logic gates for trapped ions. *Nature*, 476(7359):181–184, aug 2011. URL: http://www.nature.com/articles/nature10290.

[112] F. Beck. Theory and Simulation of Ground-State Laser Cooling in a Penning Trap. Technical Report September, Imperial College London, 2014.

[113] J. I. Cirac, R. Blatt, P. Zoller, and W. D. Phillips. Laser cooling of trapped ions in a standing wave. *Physical Review A*, 46(5):2668–2681, 1992. URL: http://pra.aps.org/abstract/PRA/v46/i5/p2668_1%5Cnhttp://pra.aps.org/abstract/PRA/v46/i5/p2668%7B_%7D1.

[114] I. Marzoli, J. I. Cirac, R. Blatt, and P. Zoller. Laser cooling of trapped three-level ions: Designing two-level systems for sideband cooling. *Physical Review A*, 49(4):2771–2779, apr 1994. URL: https://link.aps.org/doi/10.1103/PhysRevA.49.2771.

[115] D. Stevens, J. Brochard, and A. M. Steane. Simple experimental methods for trapped-ion quantum processors. *Physical Review A*, 58(4):2750–2759, oct 1998. URL: https://link.aps.org/doi/10.1103/PhysRevA.58.2750.

[116] M. Lindberg and S. Stenholm. The master equation for laser cooling of trapped particles. *Journal of Physics B: Atomic and Molecular Physics*, 17(16):3375–3389, aug 1984. URL: http://stacks.iop.org/0022-3700/17/i=16/a=019?key=crossref.3dc7169b0583e855aec079c85c50cc3b.

[117] S. Stenholm. The semiclassical theory of laser cooling. *Reviews of Modern Physics*, 58(3):699–739, jul 1986. URL: https://link.aps.org/doi/10.1103/RevModPhys.58.699.

[118] L. Mandel. Distribution of atomic momentum in resonance fluorescence. *Journal of Optics*, 10(2):001, mar 1979. URL: http://stacks.iop.org/0150-536X/10/i=2/a=001?key=crossref.d37c7a7cd541e6f36c64a600fe584098.

[119] A. W. Vogt, J. I. Cirac, and P. Zoller. Collective laser cooling of two trapped ions. *Physical Review A*, 53(2):950–968, feb 1996. URL: https://link.aps.org/doi/10.1103/PhysRevA.53.950.

[120] X.-P. Huang, J. J. Bollinger, T. B. Mitchell, W. M. Itano, and D. H. E. Dubin. Precise control of the global rotation of strongly coupled ion plasmas in a Penning trap. *Physics of Plasmas*, 5(5):1656, 1998. URL: http://scitation.aip.org/content/aip/journal/pop/5/5/10.1063/1.872834.

[121] S. Bharadia, M. Vogel, D. M. Segal, and R. C. Thompson. Dynamics of laser-cooled Ca^+ ions in a Penning trap with a rotating wall. *Applied Physics B*, 107(4):1105–1115, jun 2012. URL: http://link.springer.com/10.1007/s00340-012-4871-6.

[122] M. Asprusten, S. Worthington, and R. C. Thompson. Theory and simulation of ion Coulomb crystal formation in a Penning trap. *Applied Physics B*, 114(1-2):157–166, 2014. URL: http://link.springer.com/10.1007/s00340-013-5708-7.

[123] E. S. Phillips, R. J. Hendricks, A. M. Abdulla, H. Ohadi, D. R. Crick, K. Koo, D. M. Segal, and R. C. Thompson. Dynamics of axialized laser-cooled ions in a Penning trap. *Physical Review A*, 78(3):032307, sep 2008. URL: https://link.aps.org/doi/10.1103/PhysRevA.78.032307.

[124] G. Poulsen and M. Drewsen. Adiabatic cooling of a single trapped ion. oct 2012. URL: http://arxiv.org/abs/1210.4309.

[125] C. Roos. Controlling the quantum state of trapped ions. 2000. URL: http://cds.cern.ch/record/784342?ln=en.

[126] C. Schwedes, T. Becker, J. von Zanthier, H. Walther, and E. Peik. Laser sideband cooling with positive detuning. *Physical Review A*, 69(5):053412, may 2004. URL: https://link.aps.org/doi/10.1103/PhysRevA.69.053412.

[127] D. Church. Collision measurements and excited-level lifetime measurements on ions stored in Paul, Penning and Kingdon ion traps. *Physics Reports*, 228(5-6):253–358, jun 1993. URL: http://linkinghub.elsevier.com/retrieve/pii/037015739390030H.

[128] A. Shnirman, G. Schön, I. Martin, and Y. Makhlin. Low- and High-Frequency Noise from Coherent Two-Level Systems. *Physical Review Letters*, 94(12):127002, apr 2005. URL: https://link.aps.org/doi/10.1103/PhysRevLett.94.127002.

[129] M. Foss-Feig, K. R. A. Hazzard, J. J. Bollinger, A. M. Rey, and C. W. Clark. Dynamical quantum correlations of Ising models on an arbitrary lattice and their resilience to decoherence. *New Journal of Physics*, 15(11):113008, nov 2013. URL: http://stacks.iop.org/1367-2630/15/i=11/a=113008?key=crossref.4e5b68b9e8b82beb02a996ac4cb8e105.

[130] N. F. Ramsey. A Molecular Beam Resonance Method with Separated Oscillating Fields. *Physical Review*, 78(6):695–699, jun 1950. URL: https://link.aps.org/doi/10.1103/PhysRev.78.695.

[131] D. Vion, A. Aassime, A. Cottet, P. Joyez, H. Pothier, C. Urbina, D. Esteve, and M. Devoret. Rabi oscillations, Ramsey fringes and spin echoes in an electrical circuit. *Fortschritte der Physik*, 51(45):462–468, may 2003. URL: http://doi.wiley.com/10.1002/prop.200310063.

[132] A. D. Ludlow, M. M. Boyd, J. Ye, E. Peik, and P. O. Schmidt. Optical atomic clocks. *Reviews of Modern Physics*, 87(2):637–701, jun 2015. URL: https://link.aps.org/doi/10.1103/RevModPhys.87.637.

[133] J. P. Lee, A. J. Bennett, J. Skiba-Szymanska, D. J. P. Ellis, I. Farrer, D. A. Ritchie, and A. J. Shields. Ramsey interference in a multilevel quantum system. *Physical Review B*, 93(8):085407, feb 2016. URL: https://link.aps.org/doi/10.1103/PhysRevB.93.085407.

[134] M. J. Biercuk, H. Uys, A. P. VanDevender, N. Shiga, W. M. Itano, and J. J. Bollinger. Experimental Uhrig dynamical decoupling using trapped ions. *Physical Review A*, 79(6):062324, jun 2009. URL: https://link.aps.org/doi/10.1103/PhysRevA.79.062324.

[135] G. S. Uhrig. Exact results on dynamical decoupling by π pulses in quantum information processes. *New Journal of Physics*, 10(8):083024, aug 2008. URL: http://stacks.iop.org/1367-2630/10/i=8/a=083024?key=crossref.a8d458bce66f3a58376105964236faf9.

[136] Ł. Cywiński, R. M. Lutchyn, C. P. Nave, and S. Das Sarma. How to enhance dephasing time in superconducting qubits. *Physical Review B*, 77(17):174509, may 2008. URL: https://link.aps.org/doi/10.1103/PhysRevB.77.174509.

[137] E. L. Hahn. Spin Echoes. *Physical Review*, 80(4):580–594, nov 1950. URL: https://link.aps.org/doi/10.1103/PhysRev.80.580.

[138] D. J. Szwer, S. C. Webster, A. M. Steane, and D. M. Lucas. Keeping a single qubit alive by experimental dynamic decoupling. *Journal of Physics B: Atomic, Molecular and Optical Physics*, 44(2):025501, jan 2011. URL: http://stacks.iop.org/0953-4075/44/i=2/a=025501?key=crossref.366d7eb5ffcbdeb0c25f567053c55e2c.

[139] D. Szwer. High Fidelity Readout and Protection of a $^{43}Ca^{+}$ Trapped Ion Qubit. *Thesis*, pages 1–240, 2010. URL: https://ora.ox.ac.uk/objects/uuid:21178e0f-637e-46b8-8448-3cbce78460ff.

[140] Q. A. Turchette, C. J. Myatt, B. E. King, C. A. Sackett, D. Kielpinski, W. M. Itano, C. Monroe, and D. J. Wineland. Decoherence and decay of motional quantum states of a trapped atom coupled to engineered reservoirs. *Physical Review A*, 62(5):053807, oct 2000. URL: https://link.aps.org/doi/10.1103/PhysRevA.62.053807.

[141] A. C. Dada, T. S. Santana, A. Koutroumanis, Y. Ma, S.-I. Park, J. Song, and B. D. Gerardot. Experimental triple-slit interference in a strongly driven V-type artificial atom. *Physical Review B*, 96(8):081404, aug 2017. URL: https://link.aps.org/doi/10.1103/PhysRevB.96.081404.

[142] U. Sinha, C. Couteau, T. Jennewein, R. Laflamme, and G. Weihs. Ruling Out Multi-Order Interference in Quantum Mechanics. *Science*, 329(5990):418–421, jul 2010. URL: http://www.sciencemag.org/cgi/doi/10.1126/science.1190545.

[143] O. S. Magaña-Loaiza, I. De Leon, M. Mirhosseini, R. Fickler, A. Safari, U. Mick, B. McIntyre, P. Banzer, B. Rodenburg, G. Leuchs, and R. W. Boyd. Exotic looped trajectories of photons in three-slit interference. *Nature Communications*, 7:13987, dec 2016. URL: http://www.nature.com/doifinder/10.1038/ncomms13987.

[144] G. Kirchmair. *Quantum non-demolition measurements and quantum simulation*. PhD thesis, University of Innsbruck, 2010.

[145] J. I. Cirac, A. S. Parkins, R. Blatt, and P. Zoller. "Dark" squeezed states of the motion of a trapped ion. *Physical Review Letters*, 70(5):556–559, feb 1993. URL: https://link.aps.org/doi/10.1103/PhysRevLett.70.556.

[146] S. Mavadia. *Motional Sideband Spectra and Coulomb Crystals in a Penning Trap*. PhD thesis, Imperial College London, 2013. URL: https://spiral.imperial.ac.uk/handle/10044/1/14490.

[147] M. Bohman, A. Mooser, G. Schneider, N. Schön, M. Wiesinger, J. Harrington, T. Higuchi, H. Nagahama, C. Smorra, S. Sellner, K. Blaum, Y. Matsuda, W. Quint, J. Walz, and S. Ulmer. Sympathetic cooling of protons and antiprotons with a common endcap Penning trap. *Journal of Modern Optics*, 65(5-6):568–576, mar 2018. URL: https://www.tandfonline.com/doi/full/10.1080/09500340.2017.1404656.

[148] K. von Prillwitz, Ł. Rudnicki, and F. Mintert. Contrast in multipath interference and quantum coherence. *Physical Review A*, 92(5):052114, nov 2015. URL: https://link.aps.org/doi/10.1103/PhysRevA.92.052114.

[149] J. Werschnik and E. K. U. Gross. Quantum optimal control theory. *Journal of Physics B: Atomic, Molecular and Optical Physics*, 40(18):R175–R211, sep 2007. URL: http://stacks.iop.org/0953-4075/40/i=18/a=R01?key=crossref.60cbe8e8974d26529807617c70f0badd.

[150] F. Haddadfarshi and F. Mintert. High fidelity quantum gates of trapped ions in the presence of motional heating. *New Journal of Physics*, 18(12):123007, dec 2016. URL: http://stacks.iop.org/1367-2630/18/i=12/a=123007?key=crossref.930cce36a98a5c2febdce848c3dc66f7.

[151] K. Husimi. Miscellanea in Elementary Quantum Mechanics, II. *Progress of Theoretical Physics*, 9(4):381–402, apr 1953. URL: https://academic.oup.com/ptp/article-lookup/doi/10.1143/ptp/9.4.381.

Appendix A

Quantum dynamics of a harmonic oscillator

A.1 Axial motion

The number states of a harmonic oscillator can be constructed from the ground state by applying a raising operator. The algebraic form of this operation is expressed as

$$|n_z\rangle = \frac{(a_z^\dagger)^{n_z}}{\sqrt{n_z!}} |0\rangle \,, \tag{A.1}$$

where $|n_z\rangle$ is the oscillator state with a quantum number n_z. From operator method of a harmonic oscillator, we know that

$$a_z |0\rangle = 0. \tag{A.2}$$

From here we can express the ground state wavefunction as $\psi_0(z) = \langle z|0\rangle$. After expressing the lowering operator in position and momentum vector form

$$\frac{1}{\sqrt{2}} \left(\frac{z}{z_1} + z_1 \frac{\mathrm{d}}{\mathrm{d}z} \right) \psi_0(z) = 0, \; z_1 = \sqrt{\frac{\hbar}{m\omega_z}}, \tag{A.3}$$

we can simply deduce the expression of the harmonic oscillator wavefunction, which is comes out to be

$$\psi_0(z) = \frac{1}{\sqrt{z_1 \sqrt{\pi}}} \exp(\tfrac{-z^2}{2z_1^2}). \tag{A.4}$$

The wavefunction corresponding to n_z^{th} quantum state can be constructed from equation A.1,

and it is expressed as

$$\begin{aligned}\psi_{n_z}(z) &= \frac{1}{\sqrt{n_z!2^{n_z}}}\left(\frac{z}{z_1}-z_1\frac{\mathrm{d}}{\mathrm{d}z}\right)^{n_z}\psi_0(z),\\ &= \frac{1}{\sqrt{n_z!2^{n_z}z_1\sqrt{\pi}}}\left(\frac{z}{z_1}-z_1\frac{\mathrm{d}}{\mathrm{d}z}\right)^{n_z}\exp\left(-\frac{z^2}{2z_1^2}\right).\end{aligned} \tag{A.5}$$

After following the recursion relationship of Hermite polynomial [76], the wave function simplifies to

$$\psi_{n_z}(z) = \frac{1}{\sqrt{n_z!2^{n_z}z_1\sqrt{\pi}}}H_{n_z}(\tfrac{z}{z_1})\exp\left(-\frac{z^2}{2z_1^2}\right). \tag{A.6}$$

A.2 Radial motion

Similarly, the radial wave function can be constructed by adapting a similar approach. Let us first write the raising and lowering operators in differential forms. In cylindrical coordinates, the radial raising and lowering operators can be written as,

$$\begin{aligned}a_- &= \frac{e^{-i\phi}}{2}\left(\frac{\rho}{r_1}+r_1\frac{\partial}{\partial\rho}-\frac{ir_1}{\rho}\frac{\partial}{\partial\phi}\right),\\ a_-^\dagger &= \frac{e^{i\phi}}{2}\left(\frac{\rho}{r_1}-r_1\frac{\partial}{\partial\rho}-\frac{ir_1}{\rho}\frac{\partial}{\partial\phi}\right),\\ a_+ &= \frac{e^{i\phi}}{2}\left(\frac{\rho}{r_1}+r_1\frac{\partial}{\partial\rho}+\frac{ir_1}{\rho}\frac{\partial}{\partial\phi}\right),\\ a_+^\dagger &= \frac{e^{-i\phi}}{2}\left(\frac{\rho}{r_1}-r_1\frac{\partial}{\partial\rho}+\frac{ir_1}{\rho}\frac{\partial}{\partial\phi}\right),\end{aligned} \tag{A.7}$$

where subscripts $+$ and $-$ correspond to the cyclotron and magnetron motion, respectively. The parameter r_1 is defined as $\sqrt{\hbar/m\omega_1}$. In this case, the ground state wave function can be calculated in a rotating frame, where the motion will be interpreted in terms of two independent oscillators with frequency ω_1. After following similar approach as discussed in the previous section, the ground state wavefunction is given as

$$\Xi_{0,0}(x',y') = \frac{1}{r_1\sqrt{\pi}}\exp\left(-\frac{x'^2+y'^2}{2r_1^2}\right). \tag{A.8}$$

This expression can be written in the laboratory frame after making the following transformation

$$\Xi_{0,0}(\rho,\phi) = e^{-i\frac{\omega_c.L_z}{2\hbar}}\Xi_{0,0}(x',y'), \tag{A.9}$$

where L_z is the angular momentum operator and it has been defined in chapter 2. Subsequently, the radial ground state wavefunction comes out to be

$$\Xi_{0,0}(\rho,\phi) = \frac{1}{r_1\sqrt{\pi}}e^{-\frac{\rho^2}{2r_1^2}} \tag{A.10}$$

and after applying raising and lowering operators in differential forms, the generalised wave-function is given as

$$\Xi_{n_+,n_-}(\rho,\phi) = \frac{1}{\sqrt{n_+!n_-!}}(a_-^\dagger)^{n_-}a_+^\dagger)^{n_+}\Xi_{0,0}(\rho,\phi). \tag{A.11}$$

The detailed properties of the a_+ and a_- in the cylindrical coordinates is discussed in reference [76], after following the same treatment I can write

$$\begin{aligned}\Xi_{n_+,n_-}(\rho,\phi) &= \frac{1}{\sqrt{n_+!n_-!}}(a_-^\dagger)^{n_-}a_+^\dagger)^{n_+}\Xi_{0,0}(\rho,\phi),\\ &= \frac{1}{r_1\sqrt{\pi n_+!n_-!}}(a_-^\dagger)^{n_-}a_+^\dagger)^{n_+}e^{-\frac{\rho^2}{2r_1^2}}.\end{aligned} \tag{A.12}$$

The solution here is in the form of raising and lowering operator and can be analytically solved in Mathematica. The radial wave-function can be simplified in the form of associated Laguerre polynomial. A more general treatment of the radial motion is carried out by [151] and discussed in [73].

Appendix B

Electric quadrupole transitions

In section 2.4, I assumed that the atomic ion has a dipole moment **D**. However, in this thesis, I am mainly interested in S-D transition of a calcium ion, which is an electric quadrupole transition. In a quadrupole transition, electromagnetic field gradient couples to the quadrupole moment of the atomic state and induces transition [79]. The interaction Hamiltonian for this case given as

$$H_Q = \sum_{i,j} Q_{ij} \frac{\partial \mathrm{E_j}}{\partial r_i}, \tag{B.1}$$

where $\mathbf{r} = (x, y, z)$ is the position vector and $\mathbf{E} = E_0 \cos(\omega_L t - \mathbf{k}.\mathbf{r})\hat{\epsilon}_L$ is the electric field vector of the electromagnetic radiation. The electric quadrupole moment is a tensor quantity and it is expressed as

$$Q_{ij} = e_- \frac{1}{2}\left(r_i r_j - \frac{1}{3}\delta_{ij} r^2\right), \tag{B.2}$$

where e_- is electron's electric charge. Let us assume that the plane electromagnetic wave is travelling along the z-axis then the interaction Hamiltonian simplifies to

$$H_Q = \frac{1}{2} e_- E_0 (\epsilon_L.\mathbf{r}) kz \sin(\omega_L t - kz). \tag{B.3}$$

After introducing the projection operator $|e\rangle\langle e| + |g\rangle\langle g| = \mathbb{1}$, the Hamiltonian H_Q in operator form is given as

$$\begin{aligned} H_Q &= \frac{1}{2} e_- E_0 \langle e| (\epsilon_L.\mathbf{r}) kz |g\rangle \cos(\omega_L t - kz + \pi/2)(|e\rangle\langle g| + |g\rangle\langle e|), \\ &= \hbar\Omega_0 \cos(\omega_L t - kz)(\sigma_+ + \sigma_-) \\ &= \frac{\hbar\Omega_0}{2}(e^{i(\omega_L t - kz)} + e^{-i(\omega_L t - kz)})(\sigma_+ + \sigma_-), \end{aligned} \tag{B.4}$$

where $\Omega_0 = \frac{1}{2\hbar} e_- E_0 \langle e| (\epsilon_L.\mathbf{r}) kz |g\rangle$ is the Rabi frequency of a quadrupole transition. Also we made a choice to neglect the phase $\pi/2$ in the expression. The above interaction Hamiltonian (H_Q) is exactly same as shown in equation 2.77. The remaining expressions of the dipole transition case are valid here too.

Appendix C

Circuit diagram for intensity noise eater

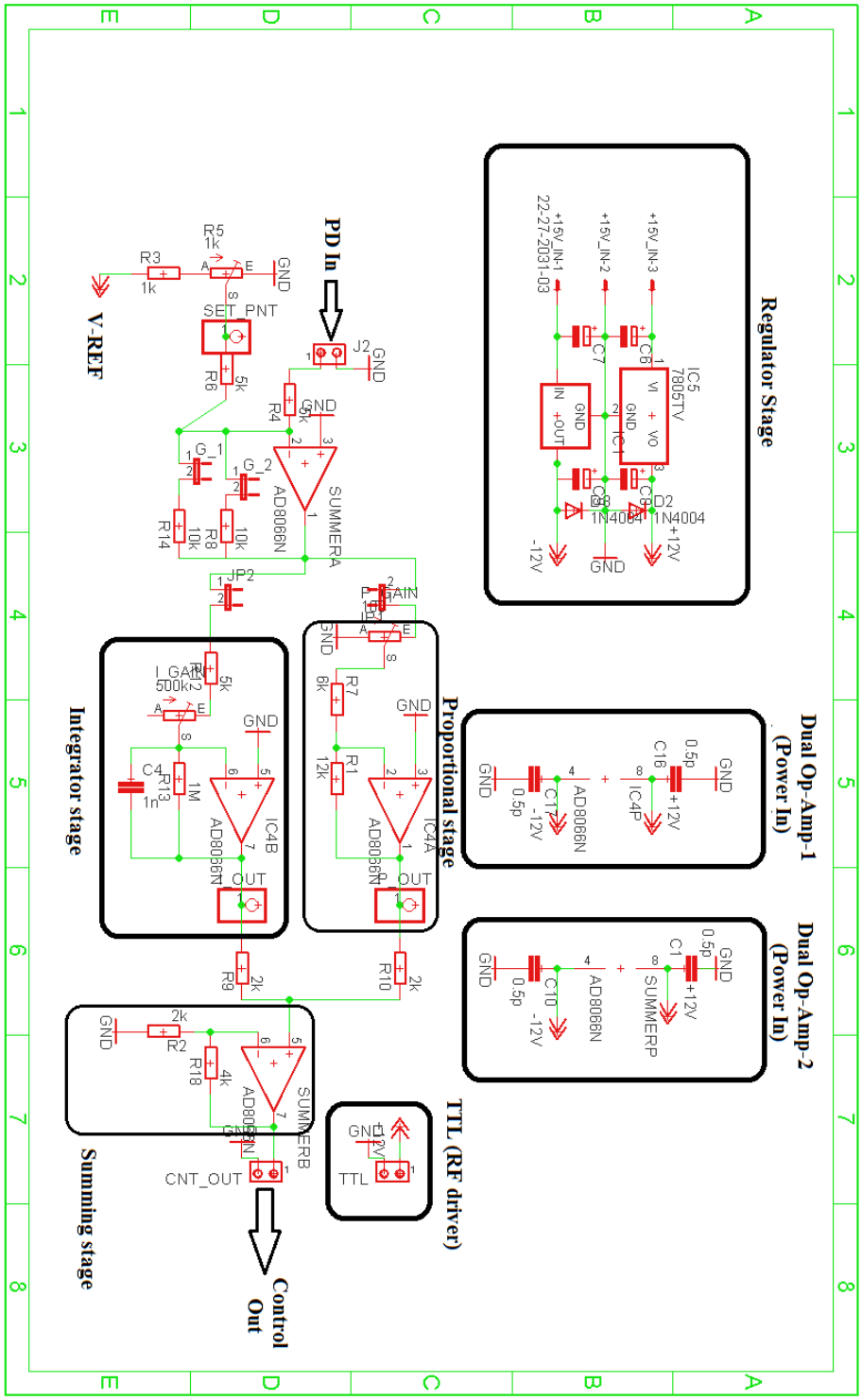


Figure C.1: Electronic circuit for the 729-nm noise eater system.

Appendix D

Calibration of trap frequency and ion spacing in our apparatus

The axial frequency of an ion in a Penning trap depends upon the applied potential, the mass of the ion and the characteristic trap dimension (d_0). For an ideal Penning trap, d_0 is expressed in terms of the ring electrode radius. However, in an cylindrical Penning trap, it is empirically estimated. In our system, in order to estimate the d_0 parameter, the motional frequency is measured through spectroscopy at various values of trap potentials. A plot is shown in figure D.1 to indicate the dependence of trap frequency on the applied potential. The d_0 is estimated from the fit and is comes out to be 18.6 mm.

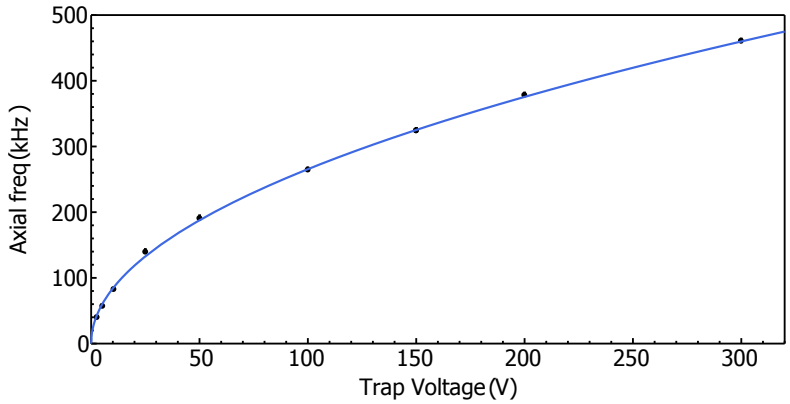


Figure D.1: Measured trap frequency as a function of the trapping voltage in our Penning trap.

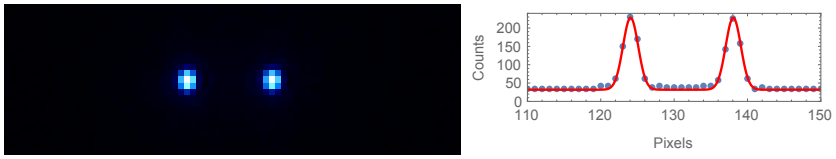


Figure D.2: A two-ion chain at 40.04 V trapping potential in our trap.

The rotation frequency of a two-ion planar crystal at 180 V is also estimated from the

EMCCD image. At first, the camera resolution is calibrated by taking a two-ion chain image taken at 40.04 V. The trap frequency at this operating potential comes out to be 168.2 kHz. The ion spacing is measured to be 14 pixels, which is shown in figure D.3. The pixel size is then converted into actual dimensions by comparing the trapping force and Coulomb repulsion between the ions. After performing some algebra, the camera resolution is estimated to be $1.31 \times 10^{-6} \mu$m/pixel.

At 180 V axial potential, the spread of the planar crystal is measured to be 23 pixels (= 30 μm) and corresponding rotation frequency is calculated to be 114 kHz. In this case, the Tilt mode frequency comes out to be 343 kHz.

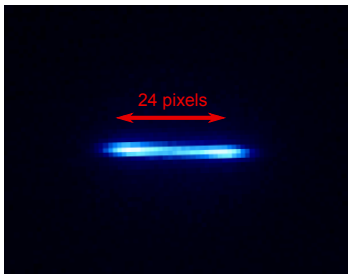


Figure D.3: A two-ion planar crystal at 180 V trapping potential in our trap.

Appendix E

Distribution functions and excited state probabilities

For the Doppler cooling and sideband cooling cases, the occupation probability as a function of phonon number n is expressed in the form of a thermal distribution function [78]. The excitation probability for these cases is given as

$$P(e) = \sum_{n=0}^{\text{nmax}} \left(\sum_{\Delta\text{n}=-7}^{-7} \frac{\langle n \rangle^n}{(\langle n \rangle + 1)^{n+1}} \frac{{\Omega^2}_{n,n'}}{\tilde{\Omega}^2_{n,n'}} \sin^2 \left(\frac{1}{2} \tau \, \tilde{\Omega}_{n,n'} \right) \right), \tag{E.1}$$

where $\langle n \rangle$ is the mean phonon number and $\tilde{\Omega}_{n,n'} = \sqrt{\Omega^2_{n,n'} + (\omega_l - (n'-n)\omega_z)^2}$.

In sideband heating case, the population distribution is approximated by a Gaussian distribution function. This is an approximate expression that was anticipated from the simulation studies discussed in chapter 5. In this case, the S–D shelving probability is expressed as

$$P(e) = \sum_{n=0}^{\text{nmax}} \left(\sum_{\Delta\text{n}=-7}^{-7} \frac{e^{-\frac{(n-\mu)^2}{2\sigma^2}}}{\sqrt{2\pi}\sigma} \frac{{\Omega^2}_{n,n'}}{\tilde{\Omega}^2_{n,n'}} \sin^2 \left(\frac{1}{2} \tau \, \tilde{\Omega}_{n,n'} \right) \right). \tag{E.2}$$

Fitting function for motional and optical coherence times in high n superposition case is given as

$$V = A_o \exp\left(-\frac{t^2}{\tau_o^2} \right) + A_m \exp\left(-\frac{t^2}{\tau_m^2} \right) \tag{E.3}$$

where τ_o and τ_m are the optical and motional coherence times. A_o and A_m are the visibilities at $t = 0$.

Appendix F

Squeezed state miscellany

The squeezed state results presented in chapter 7 has some issues due to the system not being so within the L-D regime. During the repumping cycle, approximately half of the population is brought to the electronic ground state in order to detect the squeezed state of motion. During which the motional state is not preserved and eventually odd phonon states are populated. For those experimental data, the estimated population in the all phonon state is calculated and shown in figure F.1. Curve in black represents the population in only even phonon states and curve in blue shows the calculated population in all phonon states for the experimental conditions in our system. Calculation suggests that approximately 17% of the total population is occupied in the odd states, which is not negligible.

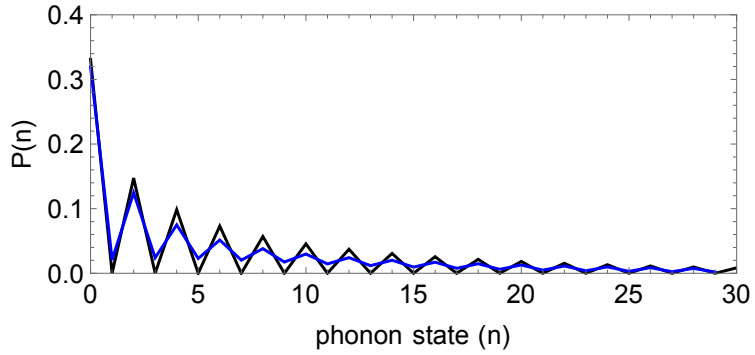


Figure F.1: The calculated population in different phonon states for the experimental data presented in figure 7.46. Black curve corresponds to the ideal situation where no odd phonon states are populated and blue curve corresponds to the situation where odd states are populated during repumping cycle.

Frequency analysis of the experimental data presented in figure 7.46 is also carried out independently after taking all phonon states into account and the occupancy as a function of phonon state is shown in figure F.2 is carried out and corresponds to the squeezed state data. The analysis is completely unreliable for the case when occupancies in all phonon states are chosen as free parameters.

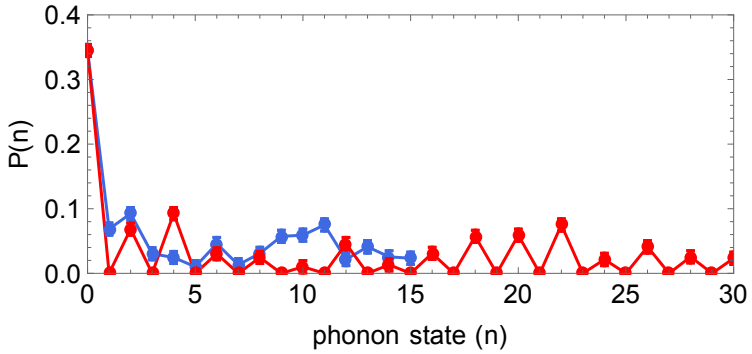


Figure F.2: Frequency analysis of the experimental data in figure 7.46 and corresponding estimated population in different phonon states. Red data points when only even states and blue data points when both even and odd states are taken into consideration.